Rational Design of Hole Transport Materials: Tools and Structure-Packing-Property Relationships

Présentée le 7 septembre 2020

à la Faculté des sciences de base
Laboratoire de design moléculaire computationnel
Programme doctoral en chimie et génie chimique

pour l'obtention du grade de Docteur ès Sciences

par

Kun-Han LIN

Acceptée sur proposition du jury

Prof. K. Sivula, président du jury
Prof. A.-C. Corminboeuf, directrice de thèse
Dr D. Andrienko, rapporteur
Dr C.-P. Hsu, rapporteuse
Prof. U. Röthlisberger, rapporteuse

École
polytechnique
fédérale
de Lausanne

2020

Intuition has to lead knowledge,

but it can't be out there alone.

—Bill Evans

To my wife and my family.

Acknowledgements

First of all, I would like to thank Prof. Clémence Corminboeuf for her support and guidance for all these years. As the only material scientist in LCMD group, I am always inspired by the meaningful discussion with her, where she offers me very different perspectives to my research. I am particularly grateful to her that she gives me a lot of freedom to explore the interesting world of organic semiconductors.

In these four years, I have received many helps from a lot of people. I would like to give my special thanks to Dr. Antonio Prlj, my best friend and colleague. At the beginning of my research, we almost discussed every single day, which helped me gradually shape my research direction. In addition, his serious and responsible attitude toward science has deeply influenced me. I especially miss the time that we discussed about science and life during the walk from BCH building to Migros. I wish him a successful career in academia. I would like to thank Dr. Alberto Fabrizio and Raimon Fabregat, who always bring laughter to this lab. Moreover, they always inspire and support me and my research. In addition, I would like to thank Boodsarin Sawatlon and Veronika Juraskova for being always very thoughtful. From time to time, they bring their delicious homemade delicacies to the office, which save me many times from afternoon hunger. In addition, it is my pleasure to meet new generation of PhD students, Terry Blaskovits, Simone Gallarati and Ksenia Briling. I wish them a successful PhD.

I am lucky that I met many nice and talented postdocs in LCMD. I thank Dr. Anya Gryn'ova and Dr. Matthew Wodrich, who provided me so many helps on my scientific writing. I thank Dr. Jian-Hao Li, who is the other Taiwanese in LCMD group, for being very helpful especially at the beginning of my PhD. Dr. Benjamin Meyer is the nicest guy that I have ever met, who is always very kind and helpful. I wish him enjoy his life and current job. Special thanks go to Dr. Sergi Vela and Dr. Maria Fumanal, who have always been very inspiring and helpful. We have very good time in Morges. In addition, I acknowledge previous and new LCMD members: Dr. Giulia Mangione, Dr. Stepan Ruzicka, Dr. Marc Hamilton Dr. Shubhajit Das. Special thanks goes to Daniel Jana and Véronique Bujard, my PhD can't be so smooth without their technical and administrative supports.

I had a pleasure to collaborate with many experimentalists during my PhD. My first collaboration with my 12-year friend, Shang-Jung Wu, was amazing. I learned a lot about the applications of carbon nanotubes in biotechnology, which is a completely different field. I really enjoyed the collaboration with my friend, Dr. Nikita Drigo, where we explored interesting properties of his synthesized acridine-based

Abstract

The growing demand for low-cost, large-scale and flexible electronics has led to a boost in research on organic semiconductors (OSC). Understanding structure-packing-property relationships (SPPR) and the role of molecular building blocks in charge transport enables the development of effective rational design strategies, which helps in accelerating the search of promising of OSCs. Therefore, the original work presented in this thesis addresses these two aspects, with a focus on organic hole transport materials (HTM) utilized in perovskite solar cells.

In the first part of this thesis, we place emphasis on revealing the SPPR of triphenylamine (TPA)-based HTMs utilizing multi-scale simulations involving molecular dynamics, density-functional theory and kinetic Monte-Carlo techniques. In the first example, we investigated the role of heteroatoms, presence of hexyl chains and substitution positions on charge transport for truxene derivatives. In particular, the impact of the presence of hexyl chain on hole mobility (μ) was identified, where hexyl-substituted truxene compounds possess hole mobilities an order of magnitude lower than those of their bare-core counterparts. The lower mobility originates primarily from the steric effect of hexyl chains, which prevents the truxene dimer from adopting a face-to-face arrangement. Due to the crucial role of the hexyl chain, we further investigated the effect of alkyl chain length on charge transport. As the alkyl chain is elongated, the reorganization energy (λ) remains unchanged, while the electronic coupling (V) and energetic disorder (σ) decrease simultaneously. Since V decreases much faster than σ does, μ gradually decreases with increasing alkyl chain length. Finally, we reveal the underlying mechanism of the multiarm effect on μ. By increasing the number of carbazole arms substituted on the TPA core, all transport parameters are decreased, which overall leads to an increase in μ.

The second part focuses on the development of a fragment-based decomposition scheme for reorganization energy (FB-REDA) and electronic coupling (FB-ECDA). The total λ of a molecule is partitioned into fragment reorganization energies utilizing local fragment vibrational modes. We demonstrate the usefulness of FB-REDA by successfully reduce the λ of a dopant-free HTM (TPA1PM, $\lambda = 213$ meV) by nearly 50% (TPD3PM, $\lambda = 108$ meV) using rational design strategies based on the FB-REDA results. Similarly, the total V between two molecules in a dimer was decomposed into fragment-fragment electronic coupling terms using FB-ECDA. Combined with percolation and dimer composition analysis, we successfully established the relationship between molecular packing and electronic coupling for two series of molecules.

Keyword

Organic semiconductors, hole transport materials, perovskite solar cells, charge transport, reorganization energy, electronic coupling, charge mobility, multi-scale simulations, kinetic Monte-Carlo, fragment-based decomposition, molecular building blocks

Résumé

La demande croissante pour les dispositifs électroniques à faible coût et à grande échelle a stimulé la recherche dans le domaine des semi-conducteurs organiques (SCO). La compréhension du *rapport* entre la *structure*, l'*organisation* à l'état solide et les *propriétés* des matériaux (RSOP), ainsi que du rôle joué par les «blocs de construction» moléculaires au sein des phénomènes de transport de charges mènent à l'élaboration des stratégies de design efficaces. Celles-ci permettant ainsi d'accélérer la recherche de nouveaux SCOs prometteurs. Par conséquent, les travaux présentés dans cette thèse portent sur ces deux aspects, où une emphase particulière a été placée sur les matériaux transporteurs de trous d'électrons (MTT) utilisés au sein des cellules solaires de type pérovskite.

Dans la première partie de cette thèse, nous nous penchons sur le RSOP des MTT à base du triphénylamine (TPA) en utilisant des simulations moléculaires multi-échelle comprenant la dynamique moléculaire, la théorie de la fonctionnelle de la densité et la méthode de Monte-Carlo cinétique. Dans un premier temps, nous avons investigué le rôle joué par les hétéroatomes, la présence de chaînes hexyle et les sites de fonctionnalisation chimique sur les propriétés de transport des charges chez les dérivés du truxène. L'impact des chaînes hexyle sur la mobilité des trous d'électrons (μ) a été identifié, où les dérivés du truxène substitués avec des chaînes hexyle possèdent des mobilités de trou un ordre de grandeur plus faible que les systèmes ayant un cœur truxène non-substitué. Cette baisse de mobilité de charges provient principalement de l'effet stérique des chaînes hexyles, qui empêchent les interactions intermoléculaires de type face-à-face. Étant donné le rôle décisif de la chaîne hexyle, dans un deuxième temps nous avons poursuivi notre investigation en étudiant l'effet de la longueur de la chaîne alkyle sur le transport des charges. On remarque qu'en augmentant la longueur de la chaîne, le couplage électronique (V) et le désordre énergétique (σ) diminuent simultanément, tandis que l'énergie de réorganisation (λ) reste constante. Puisque V diminue beaucoup plus rapidement que σ, μ décroit graduellement en augmentant la longueur de la chaîne alkyle. Dans un troisième temps, nous avons révélé le mécanisme sous-jacent de l'effet des multiples branches latérales sur μ. En effet, en augmentant le nombre de substituants carbazole latéraux sur le noyau TPA, on observe une décroissance de tous les paramètres gouvernant le transport des charges, ce qui mène à une augmentation de μ.

La deuxième partie de cette thèse concerne l'élaboration d'outils permettant de décomposer en contributions fragmentaires l'énergie de réorganisation (FB-REDA) et le couplage électronique (FB-ECDA). L'énergie de réorganisation totale d'une molécule est cloisonnée en énergie de réorganisation des fragments en utilisant des modes de vibration locaux. Nous démontrons l'utilité de FB-REDA en

l'appliquant à un MTT (TPA1PM, λ = 213 meV) afin de réduire sa λ de presque 50% (TPD3PM, λ = 108 meV) en utilisant des stratégies de design basées sur les résultats obtenus avec FB-REDA. De même, le V entre deux molécules d'un dimère a été décomposé en termes de couplage entre fragments en utilisant FB-ECDA. En unissant ces résultats avec l'analyse de la percolation et de la composition des dimères, nous avons établi la relation entre l'organisation moléculaire à l'état solide et le couplage électronique pour deux séries de molécules.

Mots-clés

semi-conducteurs organiques, matériaux transporteurs de trous d'électrons, cellules solaires de type pérovskite, transport de charges, énergie de réorganisation, couplage électronique, mobilité de charge, simulations multi-échelle, méthode de Monte-Carlo cinétique, décomposition à base de fragments, blocs de construction moléculaires

Contents

x

List of Figures

List of Supporting Figures

Chapter 1　Introduction

Developments in semiconductor technology over more than 50 years have profoundly impacted our daily lives. In 1965, Gordon Moore predicted[1] based on an empirical estimation, that the density of transistors on an integrated circuit would double approximately every two years. Although numerous predictions about the end of Moore's Law have been made, this estimation has continued to be remarkably accurate and, without exaggeration, has defined the trajectory of the technology. The enormous success of the semiconductor industry, to date, has mainly been based on technologies involving crystalline silicon and other inorganic materials. Notably, this has led to high-performance computing with ever-growing computational power, Si-based solar cells with high power conversion efficiency (PCE), as well as light-weight and low-cost portable electronic devices. In recent years, emerging technologies requiring large-area and flexible semiconductors with solution processability (*e.g.*, roll-to-roll processing or inkjet printing),[2] which is generally less suited for conventional inorganic semiconductors, has increased demand for another type of materials, organic semiconductors.[3–7]

Organic semiconductors, like their inorganic counterparts, are semiconductors but rather than being constructed of inorganic compounds, are composed of organic materials. Although generally showing smaller charge mobility (10^{-10}~10 $cm^2V^{-1}s^{-1}$),[8] which is a crucial property for various applications, organic semiconductors exhibit several notable advantages over the inorganic counterparts including: flexibility, capability of large-scale thin-film manufacturing, and solution processability.[9] Furthermore, the versatility in organic synthesis enables "tailor-made" organic functional materials by selecting and combining "molecular LEGOs"[10,11] into the appropriate configurations. Not surprisingly, these advantages have attracted tremendous research interest in search of promising organic semiconductors for various optoelectronic applications, such as organic photovoltaics (OPV)[12,13] and organic light-emitting diode (OLED) displays,[14,15] over the last few decades.

Based on molecular weight, organic semiconductors can be divided into two main groups: small molecules and (conjugated) polymers.[16] Moreover, they can be further categorized into two major subclasses, crystalline and amorphous semiconductors, based on their morphologies. As compared to polymers, small molecules exhibit well-defined chemical structures, monodispersity, and good synthetical reproducibility.[17] Among different organic small molecules, planar conjugated molecules usually show poor solubility in common organic solvents and tend to form aggregates via π–π stacking.[18] Therefore, thermal evaporation deposition techniques are often needed to produce homogenous

crystalline films for molecules of this type.[19] Due to the ordered molecular packing in the crystalline phase, small-molecule based crystalline organic semiconductors (SMCOS) usually exhibit high charge mobility (> 10 cm^{2}V^{-1}s^{-1}) as compared to their amorphous counterparts.[20] Conversely, small molecules with bulky groups or solubilizing groups (*e.g.*, long alkyl chains) tend to well dissolve in common solvents, which enables large-scale deposition of amorphous and homogeneous thin films.[21] However, small-molecule based amorphous organic semiconductors (SMAOS), due to their disordered nature, possess relatively low charge mobility (10^{-10} to 10^{-3} cm^{2}V^{-1}s^{-1}).[22] For this reason, SMCOS are more widely used in applications where high charge mobility is crucial, such as organic field-effect transistors; on the other hand, SMAOS are extensively adopted in large-area optoelectronic applications (*e.g.*, OLED and OPV).

In first half of the thesis, we place emphasis on charge transport properties of SMAOS, with a specific focus on SMAOS as hole transport materials (HTM) incorporated in perovskite solar cells (PSC).[23–26] Due to the high PCE ($> 20\%$), solution processability and relatively low production cost, perovskite solar cells are considered to be promising next-generation photovoltaic technology.[27,28] The hole transport materials are vital in PSCs, which significantly reduces the electron-hole recombination rate at the interface, leading to improved PCE.[29] This is supported by the fact that no HTM-free PSC with high PCE has been demonstrated to date.[30] In spite of the crucial role of HTMs, the current state-of-the-art hole transport material, Spiro-OMeTAD, is far from ideal.[31] The principle shortcoming of Spiro-OMeTAD is its poor hole mobility (~10^{-5} cm^{2}V^{-1}s^{-1}), where lithium dopant (Li-TFSI), despite being harmful for the long-term stability of PSCs, is needed to enhance the charge career concentration and hence the hole mobility.[32] Consequently, many efforts have been made to identify novel dopant-free HTMs with reasonably high hole mobility (10^{-4} - 10^{-3} cm^{2}V^{-1}s^{-1}).[26]

While rational design strategies help in accelerating the search pace of promising candidates for dopant-free HTMs, such strategies require a thorough understanding of structure-packing-property relationship (SPPR)[33] that remain lacking. Early pioneering work by Bässler,[34] the Gaussian disorder model, and its extended versions by others[35–37] adequately capture the dependence of charge mobility of disordered organic semiconductors on external electric field, density of states, temperature and carrier concentration observed experimentally based on empirical fitting parameters. Despite these efforts, the SPPR is missing in these models, which renders them unable to predict charge mobility from molecular properties.[38] On the other hand, theoretical approaches recently developed allow the direct computation of charge transport parameters (electronic couplings, reorganization energies and site energies) from molecular structures *ab initio*, thus enabling the *in-silico* prediction of the charge transfer rate between molecules in a charge-transfer complex.[39] The missing link, the relation between molecular packing and charge transport properties, relies on computational protocols that take the morphology (molecular packing) effect into account.

Recent developments in multiscale simulation protocols and toolkits offer an opportunity for establishing the missing link between molecular packing and the other two aspects.[40–44] This is achieved by performing charge dynamics simulations on a simulated morphology, which is usually generated via classical molecular dynamics (MD). Various methods and treatments have been proposed for computing the charge transfer rates and the associated parameters, resulting in different flavors of multiscale approaches. Among these protocols, the Charge Transport Toolkit within Versatile Object-oriented Toolkit for Coarse-graining Applications (VOTCA-CTP)[40,45–47] developed by Andrienko *et al.* serves as an integrated computational workflow, which significantly reduces the barrier of the multiscale modeling of microscopic transport. For this reason, we investigated the SPPR of various HTMs utilizing VOTCA, providing insights for future rational design and proposing high-performance HTM candidates in the first half of the thesis.

In addition to the SPPR, another key ingredient of rational design for organic semiconductors is the knowledge of contributions from molecular building blocks (moieties) to the target properties. From a computational viewpoint, this can be achieved by developing a fragment-based decomposition analysis tool, which has been widely adopted for various quantities. For example, the concept of fragment decomposition has been exploited in molecular orbital analysis,[48] functional group symmetry-adapted perturbation theory[49,50] and fragment-based excited-state analysis,[51] providing useful insight into molecular design and enabling a better understanding of the target molecular systems. However, such computational protocols for charge transport parameters remain lacking, which motivated us to develop fragment-based decomposition analysis tools for two of the most important charge transport parameters, reorganization energy and electronic coupling. The second half of the thesis is dedicated to these decomposition schemes.

The material of the thesis is organized as follows.

In **Chapter 2**, the theoretical background of charge transport mechanism in organic semiconductors and the computational protocol for charge dynamics simulation using kMC techniques are discussed in detail. The **Chapter 3-6** are published as articles in peer-reviewed journals. The whole thesis (**Chapter 3-7**) are divided into two parts.

In the first half, from **Chapter 3** to **Chapter 5**, multiscale simulations involving molecular dynamics, density-functional theory and kinetic Monte-Carlo simulations are utilized to investigate the SPPR of different HTMs.

In **Chapter 3**, we investigated the properties crucial for perovskite solar cells applications of truxene derivatives. Truxene and its derivatives have been extensively employed for various applications and are considered as promising dopant-free hole transport materials (HTMs) in perovskite solar cells (PSCs). Yet, a systematic exploration of their performance for this specific application remained lacking. Multiscale simulations were used to investigate the key structure−property relationships of truxene

derivatives featuring distinct variations to the parent core. Specifically, the role of heteroatoms, hexyl side chains, and substitution site on the most relevant electronic, transport, and stability properties to high-performing PSCs were assessed. In particular, the hexyl side chains have a huge impact on the molecular packing and hole mobility, where the compounds substituted with hexyl chains exhibit hole mobilities one order of magnitude lower than the bare analogues. Finally, our findings demonstrate that each of the considered truxenes are potential alternatives to the current state-of-the-art HTM Spiro-OMeTAD.

In light of the important role of hexyl chains, we further revealed the effect of alkyl chain length on hole transport properties of HTMs in **Chapter 4**. Alkyl chains are common solubilizing groups in organic semiconductors. In addition, manipulating the length of alkyl chains is a widely adopted strategy that can fine tune the properties of organic materials in order to enhance their performance for various applications.[52–57] Yet, a systematic exploration of the influence of chain length on those properties most relevant to highly performing HTMs in PSCs was lacking. Multiscale simulations, along with morphological analyses, uncovered relationships between alkyl chain length and HTM properties that provide important insights for the optimization of future organic materials.

In **Chapter 5**, we explored several potential dopant-free triphenylamine-based hole transport materials for perovskite solar cells by combining two existing design strategies: (1) incorporation of multiple arms for mobility enhancement[58,59] and (2) including Lewis bases that assist in defect passivation.[60] Through multiscale computations along with the analysis of the electronic structure, molecular transport network, and data clustering, we established the relationship among hole mobility, transport parameters, intrinsic molecular properties, and molecular packing. Our results showed that multiarm design can be an effective strategy for four-fold hole mobility enhancement (from 7×10^{-6} to 3×10^{-5} cm^2 V^{-1} s^{-1}) through reducing the reorganization energy and energetic disorder. Furthermore, ionization potential (IP) optimization by changing substituents was performed because the IP decreases with an increasing number of arms. Through the judicious choice of substituents, the IP approaches the minus valence band maximum of MAPbI$_3$ and the hole mobility is further increased ~three-fold. The simulated mobility is in fair agreement with that obtained from field-effect transistors, supporting our computational protocols.

In the second half, **Chapter 6** and **Chapter 7**, two novel computational analysis tools are proposed to evaluate the contributions from molecular building blocks to the reorganization energy and the electronic coupling.

Chapter 6 presents a fragment-based reorganization energy decomposition analysis tool (FB-REDA). This tool delivers insights on how to rationally design low-λ organic semiconductors. The contribution of the fragment vibrational modes to the reorganization energy is exploited to identity the individual contributions of the molecular building blocks. The usefulness of the approach is demonstrated by offering three strategies to reduce the reorganization energy of a promising dopant-free hole transport material (TPA1PM, $\lambda = 213$ meV). A reduction of nearly 50% (TPD3PM, $\lambda = 108$ meV) is achieved.

The proposed design principles are likely transferable to other organic semiconductors exploiting common molecular building blocks.[61]

Following the reorganization decomposition scheme, we proposed a fragment-based electronic coupling decomposition analysis tool (FB-ECDA) in **Chapter 7**. The total electronic coupling can be partitioned into fragment-fragment electronic coupling terms ($V_{frag\text{-}frag}$). As a proof of concept, we investigated multiarm and acene core length effect on triphenylamine(TPA)-based HTMs using FB-ECDA. All molecules were partitioned into a core and one or several arm(s) fragments. For multiarm series, we showed that the number of arms has no significant effect on total electronic coupling, in terms of both distribution and the percolation behavior. This originates from a balance of two contrasting effects: the arm-arm electronic coupling increases while the core-core coupling decreases. On the other hand, we observed molecular aggregation through π–π interactions between pentacene cores as the core length increased, as revealed in the percolation plot based on the core-core electronic coupling term. In addition, we proposed a molecular dimer composition analysis based on $V_{frag\text{-}frag}$, which provides a direct link between the molecular packing and the charge transport network properties. Overall, our analysis tool and computational protocols can provide useful insights into the SPPR, boosting the searching pace of promising organic semiconductors.

Finally, the general conclusions and future outlook are presented in **Chapter 8**.

Chapter 2 Theory

This chapter provides an overview of the theoretical background relevant to the material presented in this thesis. The first section introduces various existing charge transport theories to deal with the sophisticated charge transport behavior of organic semiconductors, which can be partitioned into three different regimes:[39] the band transport, the hopping transport and the intermediate regime. Since this thesis focuses on charge transport in amorphous materials, which are well described by the hopping transport model, we place more emphasis on this model. The next section introduces the practical simulation protocols for charge mobility prediction based on the hopping model. The third section is dedicated to the computational workflow of multiscale simulations in the framework of the Versatile Object-oriented Toolkit for Coarse-graining Applications (VOTCA) package,[40,45–47] which is a powerful tool to investigate the charge dynamics of a system. The practical computational aspects and theoretical background of simulated morphology, charge transfer rate and the associated charge transport parameters and kinetic Monte Carlo (kMC) technique are also discussed in this section. Finally, we introduce the concept and the associated methods of fragment-based decomposition of charge transport parameters, which is the theoretical foundation of **Chapter 6** and **Chapter 7**.

2.1. Charge Transport Theory in Organic Semiconductors

Since charge mobility is one of the most targeted properties in organic semiconductors, the development of *in-silico* techniques capable of predicting it accurately and efficiently has become a research focus.[62,63] From the theoretical perspective, this prediction often requires a physical model that describes well the charge transport behavior of organic semiconductors.[39] To date, however, a unified model that can describe the different charge transport behaviors of any kind of small-molecule organic semiconductors is lacking.[39,64] Unlike charge transport in many inorganic semiconductors, which is well described using the band transport model, transport in organic semiconductors can be classified into three regimes: the two extremes of hopping (polaronic) transport and band transport, and the intermediate regime.

2.1.1. Band Transport Regime

The fundamental basis of band theory is Bloch's theorem, which describes the behavior of electrons in a periodic potential.[65] Due to this inherent limitation, the band transport model is restricted to periodic systems (crystals) and is not suited for disordered or amorphous systems. In the band transport regime, the excess charge (electron or hole) is assumed to be delocalized in the periodic carrier band. Therefore, the band structure, $\varepsilon_p(\mathbf{k})$, which is the dispersion relation of electron energy eigenstate in band p, determines the charge transport properties of the material. For example, the acceleration of the charge carrier due to an electric field follows a Newtonian equation of motion:[65]

$$qF_i = \left(\frac{1}{m_p^*}\right)_{ij}^{-1} \frac{dv_{g,j}}{dt} \tag{2.1}$$

where m_p^* is the effective mass of charge carrier with charge q in band p, F_i is the magnitude of the electric field in direction i and $v_{g,j}$ is the group velocity of the charge carrier wave packet in direction j. The equation above analogizes the charge carrier transport in a periodic potential to the transport of a free charge carrier. The effect of periodic potential acting upon the charge carrier is taken into account in the effective mass, which is the second derivative of the dispersion relation $\varepsilon_p(\mathbf{k})$ under the harmonic approximation:

$$\left(\frac{1}{m_p^*}\right)_{ij} = \frac{1}{\hbar^2} \frac{\partial^2 \varepsilon_p(\mathbf{k})}{\partial k_i \partial k_j} \tag{2.2}$$

In real systems, the charge carrier interacts not only with the electric field, but also with the vibrational motions (phonon) and the defects and impurities present in the material. One of the most widely adopted models to take these effects into account is the Boltzmann transport equation. This equation describes the change in carrier distribution function f with respect to time in terms of the changes in f from different physical origins — electric field, diffusion and collision (with phonons, impurities and other defects):[66]

$$\frac{\partial f}{\partial t} = \left(\frac{\partial f}{\partial t}\right)_{field} + \left(\frac{\partial f}{\partial t}\right)_{diffusion} + \left(\frac{\partial f}{\partial t}\right)_{collision} \tag{2.3}$$

$$= -\frac{\partial \mathbf{k}}{\partial t} \cdot \nabla_k f - \frac{\partial \mathbf{r}}{\partial t} \cdot \nabla_r f + \left(\frac{\partial f}{\partial t}\right)_{collision}$$

where the explicit form of the collision term is less trivial. One simple treatment of the collision term is to assume a linear form of relaxation right after the removal of the electric field to the equilibrium charge distribution f^0 with a relaxation time τ:[66]

$$\left(\frac{\partial f}{\partial t}\right)_{collision} = \frac{f^0 - f}{\tau} \tag{2.4}$$

This is known as the relaxation-time approximation (RTA). Within this approximation, the charge mobility μ can be expressed as:[67]

$$\mu = \frac{q\tau}{m_p^*} \tag{2.5}$$

Here, we omit the index of the tensor for simplicity, but the charge mobility, the effective mass and the relaxation time are all second-order tensors. Only two parameters, m_p^* and τ are necessary for calculating μ. The former can be computed relatively straightforwardly from the band structure of the material using equation 2.2, while the latter is less trivial, as it requires macroscopic information (concentration of impurities and defects), the long range order and elastic properties of the material.[39]

2.1.2. Hopping Transport Regime

In the hopping model, the excess charge is assumed to be localized on one site, which can involve one molecule, several molecules or a segment in a polymer chain.[68–70] Different mechanisms can lead to localization of charge carriers. First, the charge carriers can be localized due to large static disorder and extrinsic charge traps (e.g., dopants) present in the materials, which is especially true for disordered or amorphous materials.[71] Even in ordered systems without defects or traps, the interaction between charge carrier and intramolecular (local electron-phonon coupling, Holstein-type)[72] and intermolecular vibrations (nonlocal electron-phonon coupling, Peierls-type)[73] can lead to charge localization.[74]

During the charge transport process, the charge carrier hops from one site to another, which can be considered as a series of outer-sphere electron transfer process[75,76] from a chemical viewpoint:

$$M_i^+ + M_j \rightarrow M_i + M_j^+ \tag{2.6}$$

where M^+ and M are cationic and neutral molecules, respectively. Under the harmonic approximation, this process can be represented by two parabolas as illustrated in **Figure 2.1**, where the x-axis is the reaction coordinate of the charge transfer process.[77] The two parabolas, with their minima at R_i and R_j, represent two diabatic states of the charge complex system (initial state $[M_i^+ + M_j]$ and finale state $[M_i + M_j^+]$), describing the energy variation along the reaction coordinate. The point (R_{TS}) where two diabatic states cross is the transition state (TS) and the activation free energy ($\Delta G^\dagger$) is defined by the free energy difference between the TS and the minimum of initial state. The driving force for the charge transfer reaction (ΔG^0) is the free energy difference between the minima of final and initial states. Finally, the reorganization energy (λ) is the relaxation energy from the vertical charge excitation[78] (the Frank-Condon point) to the minimum of the final state.

If the nuclear motion is treated classically, the charge transfer rate (k) can be expressed using the semiclassical transition state theory (TST):[79]

$$k = \nu_{eff}\kappa_{el}\Gamma_n exp\left(-\frac{\Delta G^\dagger}{k_B T}\right)$$

(2.7)

where ν_{eff} is the effective vibrational frequency along the reaction coordinate, κ_{el} is the electronic transmission coefficient and Γ_n is the nuclear tunneling factor. ν_{eff} can be regarded as the number of attempt per unit of time made to cross the barrier and κ_{el} and Γ_n as correction factors for ν_{eff}. At room temperature, the nuclear tunneling effect is small and Γ_n is usually set as 1. If we omit the adiabatic correction factor (valid for the nonadiabatic limit),[80] it is not difficult to show that $\Delta G^\dagger$ can be expressed in terms of λ and ΔG^0 through the relation of the two parabolas:

$$\Delta G^\dagger = \frac{(\lambda + \Delta G^0)^2}{4\lambda}$$

(2.8)
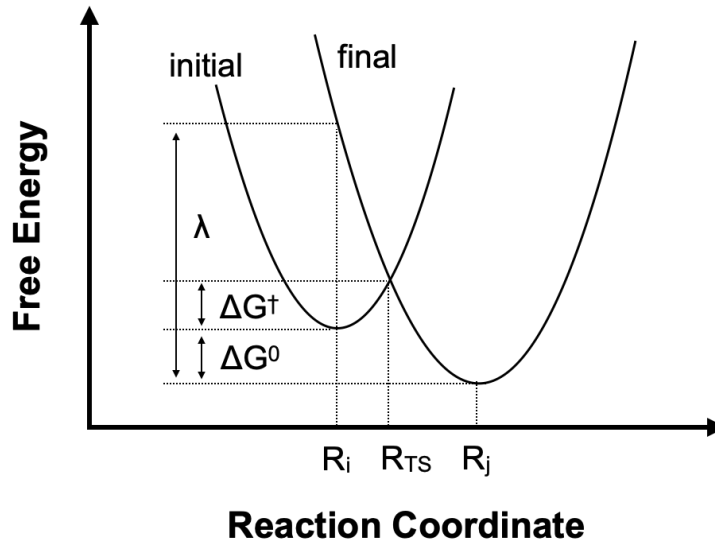
Figure 2.1 Illustration of the two-state charge transfer model. The x-axis is the reaction coordinate, which is a collective variable of all nuclear coordinates R. Initial and final diabatic states are described by two parabolas.

Within Landau-Zener (LZ) theory,[81–83] κ_{el} can be expressed as:

$$\kappa_{el} = \begin{cases} \dfrac{2P_{LZ}}{1 + P_{LZ}} & if \ \Delta G^\dagger \geq -\lambda \\ 2P_{LZ}(1 - P_{LZ}) & if \ \Delta G^\dagger < -\lambda \end{cases}$$

(2.9)

$$P_{LZ} = 1 - exp(-2\pi\gamma)$$

(2.10)

$$2\pi\gamma = \frac{\pi^{3/2}\langle V_{ij}^2\rangle_{TS}}{h\nu_{eff}\sqrt{\lambda k_B T}}$$

(2.11)

where P_{LZ} is the LZ transition probability for a single crossing of the transition region, V_{ij} is the electronic coupling between two states, and $\langle\rangle_{TS}$ denotes the dynamical averaging over nuclear configurations of TS.

In the nonadiabatic limit (small V_{ij} and large λ), which is usually the case for SMAOS, P_{LZ} can be simplified to $2\pi\gamma$ and the overall charge transfer rate becomes:

$$k_{ij} = \frac{2\pi}{\hbar} \frac{\langle V_{ij}^2 \rangle_{TS}}{\sqrt{4\pi\lambda k_B T}} exp\left[-\frac{(\Delta G^0 + \lambda)^2}{4\lambda k_B T}\right] \tag{2.12}$$

which is the Marcus rate equation.[75] The charge transfer rate in this limit becomes independent of v_{eff} and is fully determined through three material-specific charge transport parameters: V_{ij}, λ and ΔG^0 (also known as site energy difference). In the adiabatic limit (large V_{ij} and small λ), P_{LZ} is close to 1 and the charge transfer rate reduces to a standard Arrhenius form:

$$k_{ij} = v_{eff} exp\left(-\frac{\Delta G^\dagger}{k_B T}\right) \tag{2.13}$$

In this case, the charge transfer rate only depends on v_{eff} and $\Delta G^\dagger$. The v_{eff} can be expressed in terms of normal-mode frequency (v_i) and Huang−Rhys factor S_i through mode-average:[84,85]

$$v_{eff} = \sum_i v_i \frac{S_i}{\sum_j S_j} \tag{2.14}$$

2.1.3. Intermediate Regime

Between the two limiting regimes, there is an intermediate regime where both models fail to accurately describe transport behavior.[39] For example, one intrinsic criterion for the hopping model to be valid is charge localization. From a two-state model as shown in **Figure 2.1**, the free energy barrier $\Delta G^\dagger$ should be at least larger than 0 to separate the initial state from the final one. If we assume a zero site energy difference ($\Delta G^0 = 0$), it can be shown that this criterion is equivalent to:[39]

$$V_{ij} < \frac{1}{2}\lambda \tag{2.15}$$

Equation (2.15) indicates that for organic semiconductors with large electronic coupling or small reorganization energy, the hopping transport model is not applicable. In fact, many organic semiconductors lie in this region, as revealed in a recent virtual screening of around 10,000 organic semiconductors from the Cambridge Structural Database.[86] The threshold value ($\lambda/2$) for V_{ij} is even smaller if we go beyond the two-state model, considering a one-electron tight-binding model with N sites for the 1D, 2D and 3D cubic lattice cases.[87] It can be shown that the charge carrier would be localized only if:

$$V_{ij} < \frac{1}{2d}\lambda \tag{2.16}$$

where d denotes the dimensionality of the lattice. Since most organic crystals are 3D materials, the reduced threshold value ($\lambda/6$) indicates that more organic crystals are not well described by the hopping model than that considered using merely a two-state model ($\lambda/2$).

In addition to the energy barrier, the hopping model also assumes that the system returns to equilibrium after each hop, indicating that the hopping rate must be much slower than the vibrational relaxation. Based on a 1D lattice model, Troisi showed that an upper limit of charge mobility exists for the hopping model to be valid:[88]

$$\mu < \frac{2\pi c\tilde{\delta}qL^2}{k_B T} = \mu_{hop} \tag{2.17}$$

where c is the speed of light, $\tilde{\delta}$ is the Raman line broadening and L is the lattice constant.

In the other limit, the band model assumes a full delocalization of the charge carrier, neglecting the electron-phonon coupling effect. This is not the case in the intermediate regime, where a large polaron forms with charge carrier delocalizing over several molecules (partial delocalization).[39] Besides, the validity of band model lies in the existence of delocalized Bloch states, indicating that the mean free path of charge carrier should be much larger than the lattice spacing ($\langle l_{scatter} \rangle > $ L). Similar to the hopping regime, we can derive a lower limit of charge mobility from this inequality:

$$\mu > \frac{Lq}{v_g m^*} = \mu_{band} \tag{2.18}$$

Many different methods have been developed to simulate charge transport behavior in the intermediate regime. For example, the polaronic band theories take into account the local and nonlocal electron-phonon coupling in the model Hamiltonian. Via the polaron transformation, the new polaronic electron bands contain the electron-phonon couplings and the relations and tools developed within the framework of band theory can be adopted to evaluate the charge mobility. In addition, direct extraction of charge mobility via charge dynamics simulations can include the sophisticated electron-phonon interactions in this regime. Techniques for propagation of charge carrier wave-packets such as Ehrenfest-based mean field dynamics[89] and Tully surface-hopping[90] have been applied to investigate excited-state and charge dynamics of various systems.[91–94]

2.2. Dimer Model vs Multiscale Simulations in the Hopping Transport Regime

Having chosen the hopping model to describe the charge transport mechanism, the second step is to simulate the real morphology of a given system. For most of the newly (especially *in-silico*) designed organic semiconductors, however, information on morphology and crystalline structure is unavailable and thus a simple dimer model is often exploited.[39,95,96] Under this approximation, the simulated charge mobility is usually computed based on molecular dimer structures, which are either prototypical dimer configurations (e.g., cofacial and edge-to-face stacking for planar molecules)[97] or taken from molecular dynamics simulations[98] performed on the dimer. Using the Einstein relation, the charge mobility based on a single hop (μ_{sh}) is:

$$\mu_{sh} = \frac{qD}{k_B T} = \frac{q k_{ij} d^2}{k_B T} \qquad (2.19)$$

where k is the charge transfer rate, D is the diffusion coefficient and d is the distance between two molecules. In addition to charge mobility, the physical nature of intermolecular interactions can be revealed using energy decomposition analysis, offering useful insights for the rational design of novel organic semiconductors.[95,99] However, the estimated mobility based on the dimer model considers only the elementary charge hopping step, which inherently neglects the effect of disorder (site energy and electronic coupling)[100–102] and the spatial connectivity present in bulk morphology, leading to overestimated charge mobility. For this reason, recent progress has been made toward the use of multiscale simulations to compute charge mobility, which involve a simulated morphology which mimicks the real one.

The whole process of a typical multiscale charge dynamics simulation is divided into two different steps (scales).[103] (i) The simulated morphology is generated using crystal-structure prediction methods (for crystals) or classical molecular dynamics (MD)/Monte-Carlo (MC) computational protocols resulting in disordered molecular packing (for amorphous materials). The latter techniques are usually based on force-field or semi-empirical level of theory. (ii) The charge transport is evaluated by performing kinetic Monte-Carlo (kMC) simulations based on the morphology obtained from step (i). Recent work by Andrienko *et al.* has shown that simulated hole mobilities of SMAOS extracted from multiscale simulations agree reasonably well with the experimental ones obtained from rigorous space-charge-limited-current measurements.[104]

In this thesis, the multiscale charge transport simulations were performed using the VOTCA package, where the time evolution of charge carriers is simulated using kMC.[40] In the following section, the theoretical details of kMC simulations, the simulated morphology, the charge transfer rate and the charge transport parameters will be discussed.

2.3. Workflow of the Multiscale Simulations in VOTCA

The typical workflow of charge transport simulations with VOTCA is shown in **Figure 2.2**. At the beginning, the morphology of the material, as generated by simulations or obtained from experimental results (in the case of crystals), is transformed into hopping sites and pairs. To perform kMC simulations, the charge transfer rate for each pair needs to be evaluated, which requires computations of associated charge transport parameters (the reorganization energy, electronic coupling and site energy in the case of Marcus rate). This is achieved by utilizing the built-in calculators or quantum chemistry packages. The master equation that describes the time evolution of the charge carrier is then solved using kMC simulations. Each step is discussed in greater detail in the following sections.
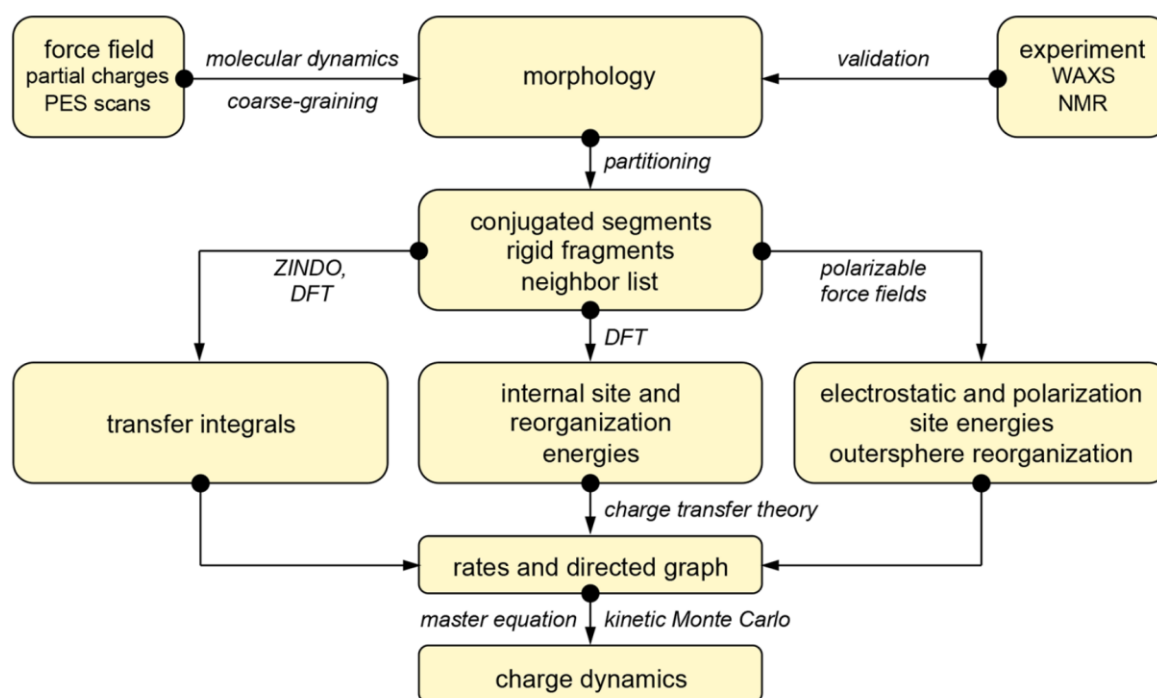
Figure 2.2 Workflow for Microscopic Simulations of Charge Transport Using VOTCA. Reprinted with permission from ref 2 Copyright 2011 American Chemical Society.

2.3.1. Simulated Morphology

The morphology of disordered organic semiconductors can be simulated through MD simulations similar to the "melt-and-quench" computational techniques widely used in the field of inorganic amorphous materials.[105] Initially, the organic molecules are randomly placed and oriented in the simulation box. The simulation box is then heated up above the glass transition temperature of the material, and then rapidly quenched to the room temperature.[106,107] The high-temperature disordered molecular packing is preserved at room temperature due to the high quenching rate, where molecules are trapped in local minima. This mimics the fast quenching caused by evaporation of the solvent in solution-processed deposition methods. Several MD simulations with different initial conditions may be necessary to reach good statistics.

Alternatively, MC simulations have also been used to generate the morphology of disordered organic semiconductors. For example, an MC protocol that mimics the physical vapor deposition process has been developed.[108] At each deposition step, a new molecule is randomly placed on top of the as-deposited surface. The newly-deposited molecule is allowed to move on the surface via basin hopping schemes comprised of several simulated annealing simulations. This avoids molecules being trapped at local minima of the rugged potential energy surface caused by the rough partially-formed surface.

The simulated morphology is then transformed into sites (individual molecules) and pairs (molecular dimers) for kMC simulations. A cutoff distance is usually set to neglect the charge hopping between two distant sites, which is reasonable considering the exponential decay of electronic coupling with intermolecular distance. Furthermore, a mapping procedure that substitutes molecular fragments in the MD snapshot with those optimized using QM methods is performed to remove the bond length fluctuation introduced by MD simulations. This is necessary if this effect is already integrated out in the derivation of the rate expression.

2.3.2. Charge Transfer Rate

Within the framework of kMC simulations, charge transfer rates for all pairs of molecules within the cutoff distance must be evaluated. Several expressions of charge transfer rate, with different degrees of approximation, have been adopted in the literature, from the very simple Miller-Abrahams (MA) hopping rate,[109] where no material-specific information is needed, to the full quantum treatment[110] of the charge transfer rate, in which nuclear motion is treated quantum-chemically. In between, the semiclassical Marcus hopping rate[75] has been widely used:

$$k_{ij} = \frac{2\pi}{\hbar} \frac{V_{ij}^2}{\sqrt{4\pi\lambda k_B T}} exp\left[-\frac{(\Delta E_{ij} + \lambda)^2}{4\lambda k_B T}\right] \tag{2.20}$$

where V_{ij} is the electronic coupling (also known as the transfer integral) between molecules in a dimer, λ is the reorganization energy and ΔE_{ij} is the difference in site energy. The equation above is a simplified version of equation (2.12), where the free energy terms that require ensemble averages are replaced with electronic energies.

On one hand, the Marcus rate expression offers a link between the chemistry and electronic structure of molecules and the molecular packing (morphology) to charge dynamics via the charge transport parameters (λ, V_{ij} and ΔE_{ij}), which is not the case in the oversimplified MA expression. On the other hand, the simulated charge mobility based on the Marcus charge transfer rate is computationally efficient and reasonably accurate as compare to that obtained from the full quantum treatment.[110] The physical meaning and the computational methods of the parameters that appear in this equation will be discussed in the following sections.

2.3.3. Reorganization Energy

The reorganization energy is the nuclear relaxation energy directly following the vertical charge excitation. It is composed of two parts: (1) inner-sphere reorganization energy, which originates from the nuclear relaxation of the charge transfer complex; (2) outer-sphere reorganization energy, coming from the nuclear relaxation of the environment (e.g., solvent or solid environment). For most of the time, the former (on the order of 100 meV) is much larger than the latter (on the order of 1 meV) in organic molecular solid.[40,111] Therefore, neglecting the outer-sphere reorganization energy and only focusing on the inner-sphere part is a reasonable approximation. This is not uncommon in the literature. In this thesis, an emphasis was placed on inner-sphere reorganization energy only, which is simply referred to as reorganization energy from now on.

Rigorously speaking, the computations of reorganization energy should not only include the charge transfer complex (molecular dimer) but also the surrounding molecules. This is because the surrounding molecules in the condensed phase can restrict certain degrees of freedom of nuclear motions, leading to lower inner-sphere reorganization energy.[8] To take this effect into account, one efficient method, despite serving as a lower-bound of true reorganization energy, is to apply the so-called frozen dihedral approximation,[8] where the dihedral angle is fixed during the geometry optimization, which restricts soft-mode vibrations. A further improvement of the interaction between the charge-transfer complex and its surrounding molecules may be achieved using the QM/MM method, in which the MM part uses a polarizable force field.[112] To reduce the computational cost, it is very common to consider the charge-transfer complex alone. The reorganization energy based on charge-transfer complex serves as an upper bound of the true reorganization energy.

A difficulty arises, however, from computing λ based on a molecular dimer: it is necessary to localize the excess charge on the assigned monomer at the vertical charge excitation point, which is usually unachievable with normal DFT. The constrained DFT (CDFT) approach,[113] which forces the excess charge on the desired atoms, is beneficial in this situation. Alternatively, we can assume the intermolecular interactions are identical or nearly the same at the vertical charge excitation (E') and the equilibrium of the product state (E''):

$$E_v = E_{M_1}^{nC} + E_{M_2}^{cN} + E' \tag{2.21}$$

$$E_p = E_{M_1}^{nN} + E_{M_2}^{cC} + E'' \tag{2.22}$$

$$\lambda = E_v - E_p = \left(E_{M_1}^{nC} + E_{M_2}^{cN}\right) - \left(E_{M_1}^{nN} + E_{M_2}^{cC}\right) + \left(E' - E''\right) \tag{2.23}$$

$$\approx \left(E_{M_1}^{nC} + E_{M_2}^{cN}\right) - \left(E_{M_1}^{nN} + E_{M_2}^{cC}\right)$$

where E_v and E_p are the energy of the dimer at vertical excitation and product state, respectively. E_{M1} and E_{M2} denote the energy of the isolated monomers M_1 and M_2. The letters "C" and "N" stand for

cationic and neutral, respectively. Letters in lowercase denote the charge state of the molecule, while uppercase letters indicate the corresponding ground state molecular geometry of that charge state. Under this assumption, we can compute the reorganization energy based on individual monomers (the monomer approximation) and normal DFT can be used in this case. Due to the simplicity and reasonable accuracy, it is not surprising that computing λ based on the monomer approximation is very common in the literature.

In the context of the monomer approximation, there are three computational ways to evaluate the reorganization energy. The first method is known as Nelsen's 4-point method, where λ is calculated using four points on the adiabatic potential energy surfaces of the neutral and cation state of a molecule. The reorganization energy can be represented in a form similar to Equation 2.23 :

$$\lambda = \lambda_N + \lambda_C = (E_{cN} - E_{nN}) + (E_{nC} - E_{cC}) \tag{2.24}$$

where λ_N and λ_C are the reorganization energy from the neutral and cationic adiabatic potential energy surface, as shown in **Figure 2.3**.

The second approach is based on the harmonic approximation, consisting of a normal mode analysis (NM), in which the reorganization energy is the sum of the potential energy of harmonic oscillators defined as:

$$\lambda = \lambda_N + \lambda_C = \sum_i \lambda_i^N + \sum_j \lambda_j^C = \sum_i \frac{1}{2} k_i^N \left(\Delta Q_i^N\right)^2 + \sum_j \frac{1}{2} k_j^C \left(\Delta Q_j^C\right)^2 \tag{2.25}$$

where $\lambda_i^N / \lambda_j^C$ is the reorganization energy contribution from the ith/j^{th} mode of the neutral/cationic ground state and k_i^N / k_j^C is the eigenvalue of the mass-weighted Hessian matrix for the neutral/cationic ground state (N/C). $\Delta Q_i^N / \Delta Q_j^C$ is the projection of the eigenvector of the normal mode (N/C) onto the Cartesian coordinate difference between the cationic and neutral ground states, which is defined as:[114]

$$\Delta Q_i^N = \left(C_i^N\right)^T m^{1/2}(R_C - R_N) \tag{2.26}$$

$$\Delta Q_j^C = \left(C_j^C\right)^T m^{1/2}(R_N - R_C) \tag{2.27}$$

where C_i^N / C_j^C is the eigenvector of the normal mode, m is the mass matrix and R_N/R_C is vector of the Cartesian coordinate of neutral/cation ground state geometry. Since large bending and torsional motions are quite common in the charge transfer process of the SMAOS, the curvilinear coordinate is a good choice to compute the $\Delta Q_i^N / \Delta Q_j^C$ as compared to Cartesian one, following the protocol proposed by Reimers.[115]

The third method is also based on the harmonic approximation. Within this context, the site energy ϵ can be expanded in powers of molecular normal-mode coordinates (Q_i):

$$\epsilon(Q) = \epsilon^0 + \sum_i v_i Q_i + higher\ order\ terms \tag{2.28}$$

where ϵ^0 is the site energy at the ground state equilibrium geometry, and the v_i terms are the linear electron-phonon coupling constants.[116] Assuming the normal modes in the cationic and neutral states are identical, the reorganization energy can be calculated in terms of v_i terms:

$$\lambda = \lambda_N + \lambda_C = 2\sum_i \lambda_i = 2\sum_i \frac{v_i^2}{2\hbar\omega_i} \tag{2.29}$$

where ω_i denotes the frequency of the normal mode i. A practical way to compute the v_i terms is to calculate the numerical differentiation of site energy (ionization energy for hole; electron affinity for electron) with respect to all normal-mode coordinates.[117,118]
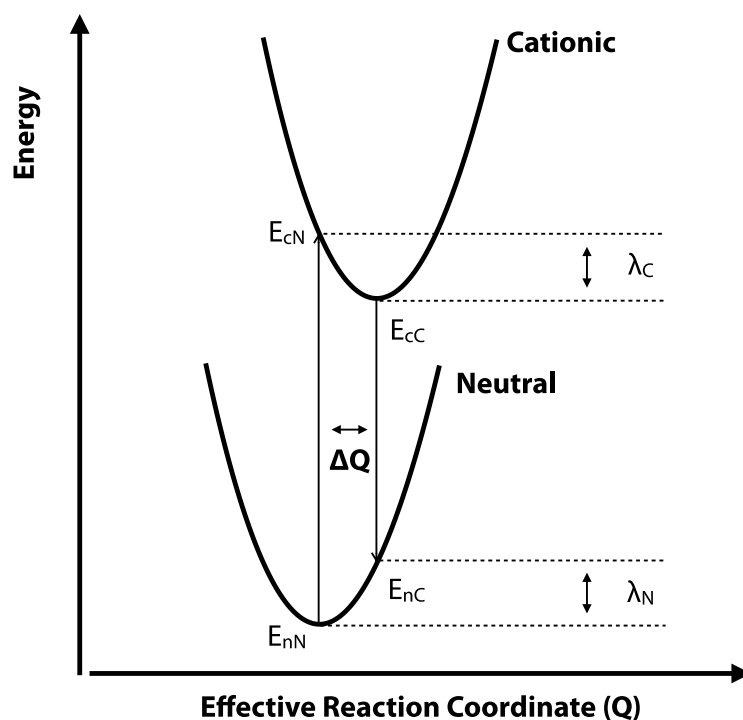
Figure 2.3 Sketch of the potential energy surface of the neutral and cationic molecular states. The relationships between the four points (E_{nN}, E_{cN}, E_{cC} and E_{nC}), λ_N, λ_C and ΔQ on the potential energy surface are depicted.

2.3.4. Electronic Coupling

The electronic coupling V_{ab} for the hole transfer between molecules in a dimer is defined as:

$$V_{ab} = \langle \Psi_a | \hat{H} | \Psi_b \rangle \tag{2.30}$$

where $\hat{H}$ is the Hamiltonian of the molecular dimer, and $|\Psi_a\rangle$ and $|\Psi_b\rangle$ are the diabatic states before and after charge transfer.[39] Since obtaining the diabatic states is generally not a trivial task, computing V_{ab}

based on several approximations is more common. There are many different methods to compute V_{ab}, such as the energy splitting method,[94] the generalized Mulliken−Hush,[119] the constrained density-functional,[120] the fragment-orbital (FO)[121] and the frozen density embedding method,[122] to name a few.[39,123,124] Among these methods, the FO method is very popular because it is cost-effective and reasonably accurate. In particular, FO is widely used in the investigation of charge transport properties in amorphous morphologies, where electronic couplings of a huge number of dimer pairs ($>10^3$) need to be evaluated.[125,126]

In the context of the FO method, the highest occupied molecular orbital (HOMO) splitting in the dimer system is assumed to result from the interaction of the HOMOs of each monomer only.[127] We can then define the one-electron dimer state ($|\varphi\rangle$) using HOMOs of two monomers ($|\phi_A\rangle$ and $|\phi_B\rangle$):

$$|\varphi\rangle = c_1|\phi_A\rangle + c_2|\phi_B\rangle \tag{2.31}$$

where the expansion coefficient c_1 and c_2 can be found by solving the secular equation:

$$(\mathbf{H} - E\mathbf{S})\mathbf{C} = 0 \tag{2.32}$$

$$\mathbf{H} = \begin{bmatrix} e_A & V_{AB} \\ V_{AB} & e_B \end{bmatrix} \tag{2.33}$$

$$\mathbf{S} = \begin{bmatrix} 1 & S_{AB} \\ S_{AB} & 1 \end{bmatrix} \tag{2.34}$$

where $\mathbf{H}$ is the system Hamiltonian, $\mathbf{S}$ is the overlap matrix and $\mathbf{C}$ is the coefficient matrix. The matrix elements in $\mathbf{H}$ and $\mathbf{S}$ are defined as:

$$e_A = \langle \phi_A|\hat{H}|\phi_A\rangle \qquad e_B = \langle \phi_B|\hat{H}|\phi_B\rangle \tag{2.35}$$

$$V_{AB} = \langle \phi_A|\hat{H}|\phi_B\rangle \qquad S_{AB} = \langle \phi_A|\phi_B\rangle$$

e_A/e_B and V_{AB} basically have the same physical meaning as the site energy and the transfer integral in the tight-binding model. In general, $|\phi_A\rangle$ and $|\phi_B\rangle$ are not orthogonal to each other, while an orthogonal basis set is used to construct the Hamiltonian matrix in the tight-binding model. To make them equivalent, a common task is to perform the Löwdin transformation, transforming the original basis set into an orthogonal one, preserving as much as possible the initial local character. The effective electronic coupling V_{AB}^{eff} in the new basis set becomes:

$$V_{AB}^{eff} = \frac{V_{AB} - \frac{1}{2}(e_A + e_B)S_{AB}}{1 - S_{AB}^2} \tag{2.36}$$

The V_{AB} term can be obtained by using the projection of monomer orbitals on dimer orbitals (DIPRO) method.[128] The counterpoise (CP) basis set, which extends the atomic orbitals of each monomer into that of the dimer, and the trick of the resolution of identity based on the dimer MO basis set $|\psi_i\rangle$ are used, which leads to:

$$V_{AB} = \sum_{ij} \langle\phi_A|\psi_i\rangle \langle\psi_i|\hat{H}|\psi_j\rangle \langle\psi_j|\phi_B\rangle = \sum_i \langle\phi_A|\psi_i\rangle \varepsilon_i \langle\psi_i|\phi_B\rangle \tag{2.37}$$

$$\langle\phi_{A/B}|\psi_i\rangle = \sum_m \alpha_m^{A/B} \langle\varphi_m| \sum_n \alpha_n^i |\varphi_n\rangle = \sum_{m,n} \langle\varphi_m|\varphi_n\rangle \alpha_m^{A/B} \alpha_n^i \tag{2.38}$$

$$= \sum_{m,n} s_{mn} \alpha_m^{A/B} \alpha_n^i$$

where ε_i is the ith MO energy of the dimer, $|\varphi_{m/n}\rangle$ is the CP atomic orbital basis set, s_{mn} is the overlap matrix element of atomic orbitals, $\alpha_m^{A/B}$ and α_n^j are the expansion coefficient of the HOMOs of monomer A/B and the ith MO of the dimer.

2.3.5. Site Energy

The site energy is the ionization energy (IE) of the molecule for the hole hopping process. Due to intermolecular interactions, the IE of molecule i in the condense phase (IE_i^c) can significantly differ from that in the isolated gas phase (IE_i^g). This shift in IE is historically called polarization energy (P_i),[41] which is defined as:

$$P_i = IE_i^c - IE_i^g \tag{2.39}$$

The polarization energy and the site energy (IE_i^c) are thus the important target properties in describing hole transfer process in organic condense phase, which is crucial for many optoelectronic applications.[129–133]

Since most organic semiconducting molecules possess non-zero dipole moments, computing IE_i^c in an amorphous morphology involves a large number of molecules, due to the slow convergence of monopole (cation)-dipole interactions. In this context, full *ab initio* methods such as the Kohn-Sham density functional scheme are too expensive in terms of computational resources. For this reason, one common approximation is that of zero intermolecular overlap, where molecules interact with each other only through classical electrostatic interactions. This approximation allows us to assign a net integer (+1) charge on one molecule and to neglect the fragmental charge due to intermolecular charge transfer. The energy of a zero intermolecular-overlap system can be written as a functional of charge densities of the composing molecules $\{\rho_i\}$:[41]

$$U[\{\rho_i(r)\}] = \sum_i E_i[\rho_i(r), \phi_i(r)] - \frac{1}{2} \int \rho_i(r)\phi_i(r)dr \qquad (2.40)$$

$$\phi_i(r) = \sum_{j \neq i} \int \frac{\rho_j(r')}{|r - r'|} dr' \qquad (2.41)$$

where ϕ_i is the electrostatic potential acting on molecule i exerted by all other molecules j and the second term is to avoid double counting the interactions. Different treatments of the explicit form of E_i and ρ_i lead to a variety of methods[43,134–136] (with different levels of accuracy) to compute site energies. For all of these methods, a self-consistent iteration process is usually required to minimize the system energy with respect to $\{\rho_i\}$.

Since the intermolecular (non-covalent) interactions in organic semiconductors are often weak as compared to the intramolecular (covalent) ones, the charge density of molecule i in the condense phase can be written as a perturbation ($\delta\rho_i$) to the charge density of molecule in the isolated gas phase (ρ_i^g) :

$$\rho_i(r) = \rho_i^g(r) + \delta\rho_i(r) \qquad (2.42)$$

In this context, the polarization energy of molecule i can be partitioned into two parts based on their physical origin of the polarization:

$$P_i = E_i^E + E_i^I \qquad (2.43)$$

The first term denotes the contribution from intermolecular interactions between the charge densities of molecules in the gas phase to the polarization energy. The second term is the induction contribution to the polarization energy, including all contributions originating from the electron density perturbation ($\delta\rho_i$) induced by intermolecular interactions. The site energy of molecule i (E_i) for hole transfer can thus be expressed as:

$$E_i = IE_i^c = IE_i^g + P_i = IE_i^g + E_i^E + E_i^I \qquad (2.44)$$

If we are only interested in computing the charge transfer rate, the site energy difference (ΔE_{ij}), rather than the individual site energy, is needed. In this case, the ΔIE_i^g is often approximated as the difference in the HOMOs of two molecules.[116]

In VOTCA, the ρ_i^g term is approximated as the sum of atomic charges (q_{ia}^g) or expanded in terms of multipoles in the molecule i. In the case of atomic charges (monopoles), the ρ_i^g becomes:

$$\rho_i^g(r) = \sum_{a \in i} q_{ia}^g \, \delta(r - r_{ia}) \qquad (2.45)$$

where r_{ia} is the nuclear position. For the $\delta\rho_i$ term, VOTCA adopts the Thole model,[137] which is a modified induced dipole scheme. The induced dipole model proposed by Applequist *et al.*[138] treats the polarization with the distributed polarizability, where the molecular polarizability is described in terms of isotropic atomic polarizability. Thole modified this model by reformulating the dipole-dipole interaction in terms of the interaction between smeared charge densities (ρ).[137] This modification allows for damping of the dipole-dipole interaction, which avoids the so-called "polarization catastrophe" at short range. For the smeared charge density, VOTCA takes the form used in the AMOEBA force field:[139]

$$\rho = \frac{3a}{4\pi}\exp(-au_{ij}^3) \tag{2.46}$$

$$u_{ij} = \frac{R_{ij}}{(\alpha_i\alpha_j)^{1/6}} \tag{2.47}$$

where u_{ij} is the effective distance as a function of the atomic polarizability of site i (α_i) and site j (α_j), R_{ij} is the distance between two polarizable sites and a is the smearing exponent (default = 0.39).

The intermolecular interaction energy (E_{inter}) based on the permanent multipole and the distributed polarizability (without Thole damping) can then be expressed using Stone's notation:[140]

$$E_{inter} = E_m + E_f \tag{2.48}$$

$$= -\frac{1}{2}\sum_{a\in i}\Delta Q_t^a \sum_{b\in j}^{j\neq i} T_{ab}^{tu}(Q_u^b + \Delta Q_u^b) + \frac{1}{2}\sum_{a\in i}\sum_{b\in j}^{j\neq i}(Q_t^a + \Delta Q_t^a)T_{ab}^{tu}(Q_u^b + \Delta Q_u^b)$$

$$= \frac{1}{2}\sum_{a\in i}\sum_{b\in j}^{j\neq i} Q_t^a T_{ab}^{tu} Q_u^b + \frac{1}{2}\sum_{a\in i}\sum_{b\in j}^{j\neq i} \Delta Q_t^a T_{ab}^{tu} Q_u^b$$

where E_m is the positive internal energy required to distort the charge distribution (from Q to Q+ΔQ) and E_f is the interaction energy including both permanent and induced multipole moments. Q_t^a and ΔQ_t^a are the multipole and induced multipole moments, respectively, and T_{tu}^{ab} is the interaction matrix. The first term on the final line of the above equation is the intermolecular energy through interaction between permanent multipoles of different molecules (E_i^E), and the second term is the induction energy (E_i^E). The induced moments can be solved via self-consistent iterations:

$$\Delta Q_t^a = -\sum_{B\neq A}\alpha_{tt'}^{aa'} T_{t'u}^{a'b}(Q_u^b + \Delta Q_u^b) \tag{2.49}$$

where $\alpha_{tt'}^{aa'}$ is the polarizability tensor. With Thole damping, the interaction tensor in the terms involving the induced multipole moments should be replaced with the damped version.[141]

Finally, the contribution from the external electric field (**F**) is considered in site energy difference as:

$$\Delta E_{ij}^{ext} = q\boldsymbol{F} \cdot \boldsymbol{r}_{ij} \qquad (2.50)$$

where $\mathbf{r}_{ij}$ is the vector connecting site i and j. For a typical intermolecular distance (on the order of 1 nm) and moderate electric field ($< 10^8$ V/m), this term is smaller than 0.1 eV.[40]

2.3.6. Kinetic Monte Carlo

As discussed previously, the hopping transport model describes the overall charge transport process as a series of multiple incoherent charge transfer steps. In this context, the kinetic Monte Carlo simulation is a useful technique to solve the master equation that describes the time evolution of a given system. For a system with only one charge carrier in the simulation box, the master equation can be written as:[40]

$$\frac{\partial p_i}{\partial t} = \sum_j p_j k_{ji} - \sum_j p_i k_{ij} \qquad (2.51)$$

where p_i and k_{ij} are site occupation probabilities and the charge transfer rates, respectively. The rejection-free kMC algorithm[39,142] for the single charge carrier case proceeds as following:

(1) Compute all charge transfer rates k_{ij} for each site i.

(2) Randomly pick a site as a starting point (the first charge localization site).

(3) For each step, determine the next hopping site j from the current site i in the following manner. First, generate a random number R_1 between 0 and Σk_{ij}. The next hopping site will be site b if:

$$\sum_{j=1}^{b} k_{ij} \leq R_1 < \sum_{j=b}^{b+1} k_{ij} \qquad (2.52)$$

(4) The simulation time needs to be updated from t to t+Δt after determining the hopping process i → b. Generate a second random number R_2 between 0 and 1 and the waiting time Δt is expressed as:

$$\Delta t = -\frac{\ln(R_2)}{\Sigma\, k_{ij}} \qquad (2.53)$$

(5) Return to step (1) after updating the hopping site from i to b and the simulation time from t to t+Δt.

The charge mobility tensor μ_{ij} is then calculated using the average charge velocity $\langle v \rangle_i$ and the electric field E_j:

$$\mu_{ij} = \frac{\langle v \rangle_i}{E_j} \tag{2.54}$$

In most cases, we are only interested in the diagonal terms μ_{ii} in the charge mobility tensor. Moreover, in isotropic materials (e.g., amorphous materials), the three diagonal matrix elements in the simulated mobility tensor are very close to each other. For good statistics, the charge mobilities are usually averaged over several kMC trajectories and MD snapshots.

2.4. Fragment-based Decomposition of Charge Transport Parameters

Common design strategies for functional organic materials involve combining various molecular building blocks with desirable properties.[143–145] This relies on understanding the target properties of molecular building blocks individually and in combination with one another.[10,146] However the tools used to analyze and to decompose the charge transport parameters into the contributions from individual molecular building blocks are still lacking. The concept of fragment (local) decomposition analysis has been widely adopted for evaluating various quantities. For example, the molecular orbital analysis,[48] the functional group symmetry-adapted perturbation theory[49,50] and the fragment-based excited-state analysis[51] provide useful insight into molecular design and enable a better understanding of the target molecular systems. For this reason, we developed the Fragment-Based Reorganization Energy Decomposition Analysis (FB-REDA) and Fragment-Based Electronic Coupling Decomposition Analysis (FB-ECDA) tools.

2.4.1. Reorganization Energy Decomposition (FB-REDA)

Currently, there are two existing methods that serve to partition the reorganization energy or vibronic coupling constant into local contributions. However, these two methods inevitably introduce the inter-fragment cross terms, which sophisticate the decomposition procedure as explained in the Introduction of **Chapter 6**. Thus, this motivates us to develop fragment-based reorganization energy decomposition analysis (FB-REDA) tool that avoids the generation of cross terms, as detailed in the following and use in **Chapter 6**.

Within the NM method, the reorganization energy can be further partitioned into individual fragment contributions via the fragment mode analysis. Following the protocol proposed by Huix-Rotllant and Ferré,[147] the modes for each fragment are obtained by first partitioning the total mass-weighted Hessian matrix H_{tot} into fragment submatrices H_f. The eigenvectors of the fragment modes C_f are then obtained by diagonalizing these submatrices. These eigenvectors form a complete orthonormal basis set to expand the total normal modes:

$$C_{tot,i} = \sum_j \sum_k d_{jk}^i C_{frag,jk} \tag{2.55}$$

$$d_{jk}^i = C_{tot,i}^T C_{frag,jk} \tag{2.56}$$

where $C_{tot,i}$ is the eigenvector of the total normal mode i, $C_{frag,jk}$ is the eigenvector of the mode j of fragment k and d_{jk}^i is the coefficient of the expansion. The expansion into fragment modes gives access to the fragment contributions to λ.

For convenience, the following derivation is based on λ_N, but the conclusion is the same for λ_C. Inserting Equation (2.26), (2.55) and (2.56) into equation (2.25) leads to an expression for λ_N in which the diagonal terms come from the same fragment mode $(d_1^i \Delta q_{f,1}^N)^2$ whereas the non-diagonal terms originates from two different fragment modes $(d_1^i d_2^i \Delta q_{f,1}^N \Delta q_{f,2}^N)$ (see Equation (2.57)-(2.60)).

$$\lambda_N = \sum_N \frac{1}{2} k_i^N \left(\Delta q_{f,k}^N \sum_j d_{jk}^i \right)^2 = \sum_N \frac{1}{2} k_i^N \left(\Delta q_{f,k}^N d_k^i \right)^2 \tag{2.57}$$

$$= \sum_N \frac{1}{2} k_i^N \left\{ \left[(d_1^i \Delta q_{f,1}^N)^2 + (d_2^i \Delta q_{f,2}^N)^2 + \cdots \right] \right.$$

$$+ \left[(d_1^i d_2^i \Delta q_{f,1}^N \Delta q_{f,2}^N) + (d_1^i d_3^i \Delta q_{f,1}^N \Delta q_{f,3}^N) + \cdots \right] \right\}$$

$$= \sum_N \frac{1}{2} k_i^N [(square\ terms) + (cross\ terms)]$$

$$\Delta q_{f,jk}^N = \left(C_{frag,jk}^N \right)^T m^{1/2} (R_C - R_N) \tag{2.58}$$

$$\Delta q_{f,k}^N = \sum_j \Delta q_{f,jk}^N \tag{2.59}$$

$$d_k^i = \sum_j d_{jk}^i \tag{2.60}$$

The cross-terms involve contributions from two fragments, which are not necessarily small in comparison to the square terms. However, there is no trivial way to divide these cross terms into individual fragment contributions, complicating the decomposition analysis.

To avoid the non-diagonal terms, we thus define the contribution of the mode j of fragment k adopting a relatively different strategy:

$$\lambda_{jk}^i = w_{jk}^i \lambda^i = d_{jk}^i{}^2 \lambda^i \tag{2.61}$$

where λ_{jk}^i is the reorganization energy of the normal mode j for fragment k and the total normal mode i, λ^i is the reorganization energy arising from the total normal mode i and w_{jk}^j is the weight. According to this definition, we can further define the reorganization energy of fragment k arising from the total normal mode i (λ_k^i) and the sum of λ_k^i over all total normal modes (fragment reorganization energy, λ_k) as:

$$\lambda_k^i = \sum_j \lambda_{jk}^i \tag{2.62}$$

$$\lambda_k = \sum_i \lambda_k^i \tag{2.63}$$

Since these fragment modes form a complete orthonormal basis, the following relation holds:

$$\sum_{jk} {d_{jk}^i}^2 = 1 \tag{2.64}$$

$$\sum_k \lambda_k = \sum_i \lambda^i \sum_{jk} {d_{jk}^i}^2 = \sum_i \lambda^i = \lambda_N \tag{2.65}$$

The equation above shows that the sum of the reorganization energies of all fragments is equal to the total reorganization energy, justifying our definition of λ_k.

In addition to the fragment reorganization energy, we also define the fragment mode reorganization energy (λ_{jk}), to identify crucial fragment modes:

$$\lambda_{jk} = \sum_i \lambda_{jk}^i \tag{2.66}$$

In **Chapter 6**, we demonstrate the usefulness of this analysis in terms of λ_{frag}, while targeting the identification of low-λ organic molecules.

2.4.2. Electronic Coupling Decomposition (FB-ECDA)

To our best knowledge, there is no existing electronic coupling decomposition scheme. This drives us to extend our scope from λ to V, developing the fragment-based electronic coupling decomposition analysis (FB-ECDA). Our methodology is detailed as following and apply in **Chapter 7**.

The electronic coupling can be decomposed into fragment-fragment terms using the CP atomic basis set. Instead of computing V_{AB} first using Equation (2.37) and then obtaining the final V_{AB}^{eff} with Equation

(2.36), we directly compute V_{AB}^{eff} using the transformed orthonormal HOMOs of two monomers $|\phi_{A/B}^{LD}\rangle$ in terms of the CP atomic basis set:

$$V_{AB}^{eff} = \sum_i \langle \phi_A^{LD}|\psi_i\rangle \varepsilon_i \langle \psi_i|\phi_B^{LD}\rangle \tag{2.67}$$

$$\langle \phi_{A/B}^{LD}|\psi_i\rangle = \sum_m \beta_m^{A/B} \langle \varphi_m| \sum_n \alpha_n^i |\varphi_n\rangle = \sum_{m,n} s_{mn}\beta_m^{A/B}\alpha_n^i \tag{2.68}$$

where $\beta_m^{A/B}$ is the expansion coefficient of the transformed HOMO of monomer A/B. A simple measure to decompose V_{AB}^{eff} into fragment-fragment contributions is by grouping the CP atomic orbitals of $|\phi_{A/B}^{LD}\rangle$ belonging to the same fragment together. For example, if we define two fragments, a core and an arm group, for each monomer (A and B), the contribution of coreA-coreB, coreA-armB, armA-coreB and armA-armB can be defined as:

$$V_{coreA-coreB}^{eff} = \sum_i \varepsilon_i \sum_{m\in coreA;\, n} s_{mn}\beta_m^A\alpha_n^i \sum_{p\in coreB;\, q} s_{mn}\beta_p^B\alpha_q^i \tag{2.69}$$

$$V_{coreA-armB}^{eff} = \sum_i \varepsilon_i \sum_{m\in coreA;\, n} s_{mn}\beta_m^A\alpha_n^i \sum_{p\in armB;\, q} s_{mn}\beta_p^B\alpha_q^i$$

$$V_{armA-coreB}^{eff} = \sum_i \varepsilon_i \sum_{m\in armA;\, n} s_{mn}\beta_m^A\alpha_n^i \sum_{p\in coreB;\, q} s_{mn}\beta_p^B\alpha_q^i$$

$$V_{armA-armB}^{eff} = \sum_i \varepsilon_i \sum_{m\in armA;\, n} s_{mn}\beta_m^A\alpha_n^i \sum_{p\in armB;\, q} s_{mn}\beta_p^B\alpha_q^i$$

However, following this definition, the sum of these four terms is not equal to V_{AB}^{eff}. The reason behind is that the coefficients of the CP atomic orbitals of the other monomer (B/A) is small but not zero in $|\phi_{A/B}^{LD}\rangle$, resulting in this inequality. Fortunately, the sum of $V_{fragA\text{-}fragB}^{eff}$ and V_{AB}^{eff} are highly linearly correlated (as shown in **Figure 2.4**), implying that corrections for the differences can be easily made through a linear equation.
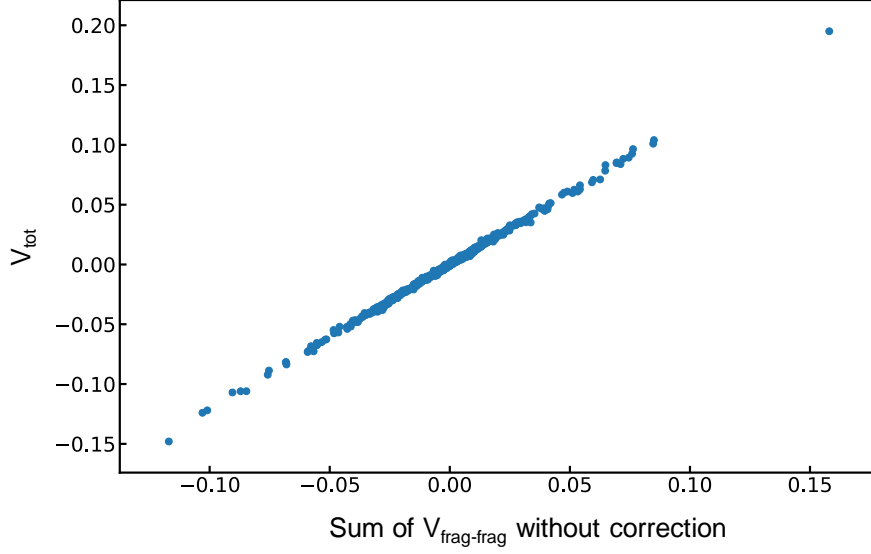
Figure 2.4 Sum of electronic coupling of all fragment-fragment contributions without correction and V_{tot}.

Alternatively, we can enforce this equality at the beginning by equally dividing these nonzero coefficients into all fragments. Following this definition, $V^{eff}_{coreA\text{-}coreB}$; for example, becomes:

$$V^{eff}_{coreA-coreB} = \sum_i F_i \varepsilon_i G_i \tag{2.70}$$

$$F_i = \sum_{m \in coreA;\, n} s_{mn} \beta^A_m \alpha^i_n + \frac{1}{2} \sum_{m \in B;\, n} s_{mn} \beta^A_m \alpha^i_n \tag{2.71}$$

$$G_i = \sum_{p \in coreB;\, q} s_{mn} \beta^B_p \alpha^i_q + \frac{1}{2} \sum_{p \in A;\, q} s_{mn} \beta^B_p \alpha^i_q$$

where the 1/2 comes from the equal partitioning of atomic orbitals from the other monomer into 2 fragments (core and arm in this case). The situation for n fragments case can be easily derived following the same procedure (in this case, the coefficient is 1/n). The results presented in **Chapter 7** all follow this definition.

Chapter 3 A Rising Star: Truxene as a Promising Hole Transport Material in Perovskite Solar Cells

This chapter is published as:

[†]These authors contribute equally.

For all supporting information mentioned in this chapter, please refer to the supporting information of the original paper.

3.1. Introduction

Due to their high power conversion efficiency (PCE), solution processability, and relatively low production cost,[148,149] organic-inorganic metal halide perovskite solar cells (PSCs) are tremendously attractive. Efficient light absorbing perovskites such as methylammonium lead iodide (MAPbI$_3$), exhibit wide absorption ranges over the complete visible solar spectrum.[150] While bare perovskite materials display ambipolar transport, high charge carrier mobility, and long charge carrier lifetimes that facilitate the design of hole/electron transport layer (HTL/ETL) free PSCs,[151–153] their corresponding PCE have not exceeded 14%. On the other hand, PSCs containing hole transport layers have reached PCEs over 20%.[154] Clearly, HTLs are highly beneficial, if not necessary for high-performing PSCs[24,29] making it crucial to design and test suitable hole transport materials (HTMs).[155,156]

Since Grätzel and Park's incorporation of Spiro-OMeTAD into the first solid-state PSC in 2012,[157] it has become the prevalent HTM choice. However, its high synthetic cost (~\$600g^{-1}) and complicated purification procedure prevent large-scale commercial production.[158,159] In addition, pristine Spiro-OMeTAD suffers from relatively poor hole mobility ($\mu=2\times10^{-5}$–2×10^{-4}cm^{2}V^{-1}s^{-1}).[160–163] In practical PSC device fabrication, Spiro-OMeTAD and other HTMs with low hole mobilities are usually doped with ionic additives such as bis- (trifluoromethylsulfonyl)imide lithium salt (Li-TFSI) to increase their conductivity and enhance the overall PSC performance.[161,164] Yet these additives are detrimental to the long-term stability of PSCs due to their deliquescent nature.[165] Consequently, dopant-free HTMs with high hole mobility arise as an appealing alternative, affording high PCE without simultaneously sacrificing the device stability.[159,165–171]

Among the dopant-free HTMs reported to date, truxene-based HTMs are promising candidates exhibiting a much higher hole mobility and similar glass transition temperature (T_g) compared to Spiro-OMeTAD, leading to PSCs with high PCE and good thermal stability.[170,172,173] Following its first reported synthesis in 1894, truxene and its derivatives have been exploited for diverse applications - non-linear optics, two-photon absorption, transistors, organic light-emitting diodes, molecular resistors, lasers, liquid crystals, supercapacitors, and photovoltaics – thanks to the feasibility and variety of peripheral functionalizations.[170,174,175] However, in contrast to other applications, only a surprising small number of truxene HTMs have been investigated for PSCs applications[170,172,173,176–179] despite the virtually infinite number of structural possibilities. The purpose of this work is thus to address this gap and establish the key features of truxene-based materials that lead to promising HTMs for PSCs.
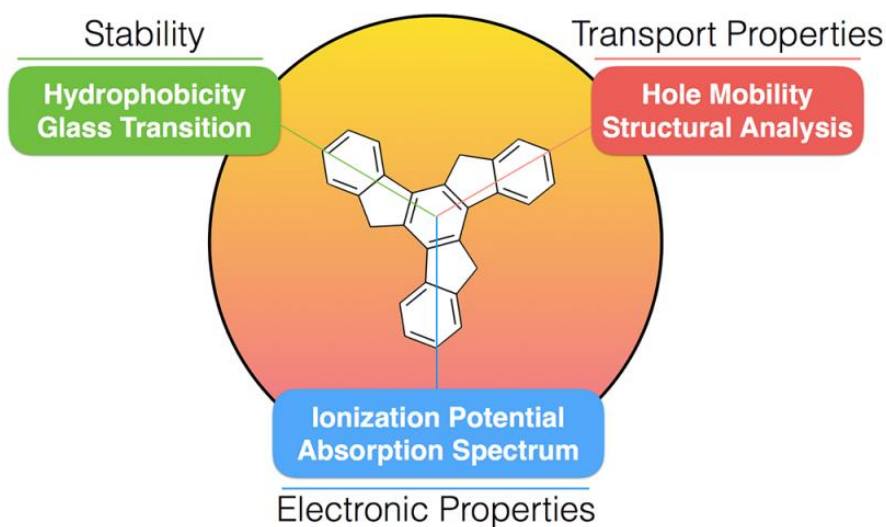
Figure 3.1 Critical properties for hole transport materials in perovskite solar cell.

An ideal HTM for a PSC should fulfill several requirements[180] that can be categorized into three main aspects: electronic properties, hole transport properties and stability (also see **Figure 3.1**), discussed below.

(1) Electronic properties: (a) A suitable energy level alignment between the perovskite and the HTL would facilitate the hole injection and suppress the recombination at the interface, ultimately maximizing the open circuit voltage (V_{oc}).[168,181,182] To fulfill this requirement, the HTM should possess an ionization potential (IP; sometimes approximated as minus HOMO) close to, but not higher than the IP, (sometimes referred to as minus valence band maximum, VBM) of a given perovskite material:[183,184]

$$\Delta IP = IP_{HTM} - IP_{Perovskite} > 0 \tag{3.1}$$

A too large ΔIP would reduce the efficiency of the hole injection and result in a poor PCE.[167,185] Alternatively, a large negative ΔIP leads to a low V_{oc} that decreases the PCE. (b) An HTM should exhibit

a reduced absorption in the visible spectrum to minimize parasitic absorption and improve the solar power conversion efficiency.[186,187]

(2) Hole transport properties: The injection into the HTL at the perovskite/HTL interface is followed by the free hole carrier transport to the anode.[23] Accordingly, an ideal dopant-free HTM should possess a high intrinsic hole mobility ($>10^{-4}$ $cm^2V^{-1}s^{-1}$) that facilitates hole transport and prevents charge recombination at the interface.[26] High hole mobility may also lead to higher short-circuit current density which enhances the PCE.[188] Note that the mobility of an organic crystal is generally superior to its amorphous phase. However, the latter produces a uniform perovskite/HTM interface that results in a more efficient hole injection, especially in the mesoporous-structured PSCs.[172,180] Hence, previously reported mobilities are mainly based on the amorphous morphology of a given organic molecule.[26] Only the amorphous phase will thus be considered herein.

 (3) Stability: (a) Highly hydrophobic HTMs are beneficial as they act as a protective layer boosting overall stability by retarding the ingress of moisture and, in turn, slowing the degradation of the perovskite.[167,189–193] Experimentally, the degree of hydrophobicity can be measured by a water contact angle (WCA).[170,192,194] The higher the WCA, the larger the hydrophobicity and the better the protection of the underlying perovskite layer. (b) Aside from perovskite degradation in the presence of water, the inherent thermal instability of the HTMs comes as another source of possible degradation. Because of their amorphous nature, organic HTMs can undergo a second order phase transition at the glass transition temperature T_g. Since operation temperatures ranging from 60-80 °C are not unusual for practical solar cells, HTMs with relatively low T_g may suffer from significant thermal stress that might eventually deteriorate the performance of the PSC device.[195] Therefore, identifying high-T_g HTMs is also of great importance.

In this work, the truxene core has been selected owing to its inherent high mobility, which eliminates the need for additives and makes truxene molecules efficient dopant-free HTMs in high-performance PSCs.[170,172,178] Analysis of these truxene derivatives revealed structure-property relationships that are highly relevant to PSCs possessing both high performance and high stability. Our computational results agree well with the recent experimental findings by Huang *et al.,* who have shown that TruxC-hex-2 (Trux-OMeTAD) is a very promising HTM, with a 18.2% PCE.[170] To the best of our knowledge, this is the first computational work in which nearly every key intrinsic property of HTMs for PSCs have been thoroughly analyzed. Our results provide key insights into the rational design of truxene-based HTMs and, moreover, deliver a broad design strategy with an accompanying comprehensive computational protocol that for rationally developing HTMs and PSCs with superior performance.

3.2. Results

3.2.1. Molecular Design

The examined truxene derivatives are displayed in **Figure 3.2** with the nomenclature used thorough. The truxene core carrying three methoxydiphenylamine groups (OMeDPA) on substitution sites 3, 8, 13, is named TruxC. The effect of the heteroatom substitution is investigated by considering heterotruxenes such as triazatruxene (nitrogen, TruxN) and thiatruxene (sulfur, TruxS), which have been synthesized and considered as potential candidates in organic electronics.[196,197] We anticipate that altering the heteroatom in the truxene core will tune the ionization potential (IP) and ultimately lead to a desirable V_{oc}. In fact, it has been demonstrated that superior hole transport properties can be achieved via substitution of two heteroatoms.[198,199] Even though truxene derivatives without alkyl chains are already solution processable,[200] alkyl chains have found wide use as solubilizing moieties in organic solvents. However, addition of alkyls chains can modify the molecular packing and has sizable effect on charge transport.[201,202] For this reason, their influence on each of the properties is also of interest. A methylene unit was thus replaced with a C-2(hexyl) and an N-hexyl to form the TruxC-hex and TruxN-hex structures. Finally, inspired by the work by Zhang *et al.*[203] regarding the 3D molecular structural effect on the overall PSC performance, we altered the substitution sites of OMeDPA from 3, 8, 13 to 2, 7, 12, thereby creating TruxC-hex-2. The computational estimates of the transport properties of these derivatives require extensive multiscale simulations, which are detailed in the computational detail section.
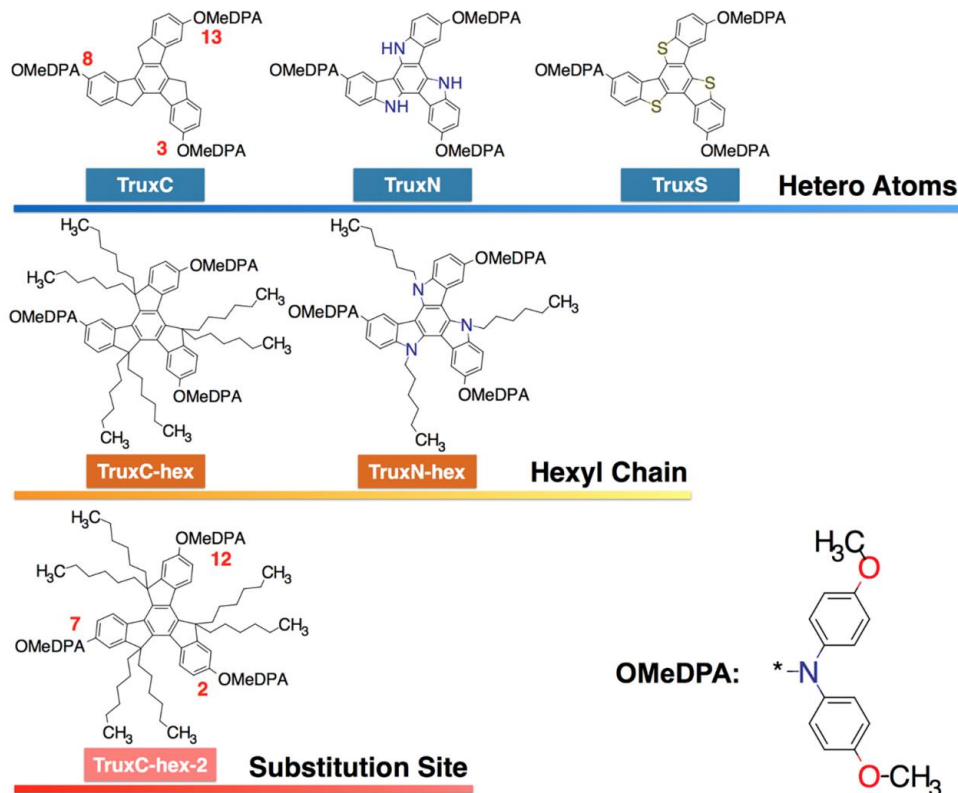
Figure 3.2 Truxene derivatives considered in this work.

3.2.2. Electronic Properties

Ionization potentials were computed using ΔSCF method with different density functionals and methods suggested by Li *et al.*[204,205] of which ΔSCF method with B3LYP functional and methods suggested by Li *et al.* had an excellent agreement with experiment (see ESI). For simplicity, discussions on IP refer to results by ΔSCF method with B3LYP functional. The energy level alignments shown in **Figure 3.3** illustrate the effect of the IP tuning through heteroatom substitution. Swapping C for N decreases the IP by 0.13 eV, while sulfur increases in to 5.35 eV, close to MAPbI₃ (5.43 eV). The hexyl chains enlarge the IPs by ~0.1 eV for both TruxN and TruxC, aligning the HOMO of TruxC-hex nearly perfectly with the valence band maximum of MAPbI₃. A closer inspection of the geometries of TruxC-hex and TruxN-hex reveals that the relative proximity between the hexyl chains and the neighboring OMeDPA groups influence the dihedral angles between the phenyl groups of OMeDPA and the planar truxene core. This geometrical constrain directly correlates with the increase in IP (see ESI). Yet, the benefit associated with the incorporation of alkyl-chains is lost if the substitution sites of OMeDPA are varied (TruxC-hex → TruxC-hex-2, IP=5.14 eV). Overall, these truxene variants outperform Spiro-OMeTAD in terms of ΔIP. Among them, TruxS and TruxC-hex exhibit the most promising energy alignment with the perovskite layer suggestive of a high V_{oc}.
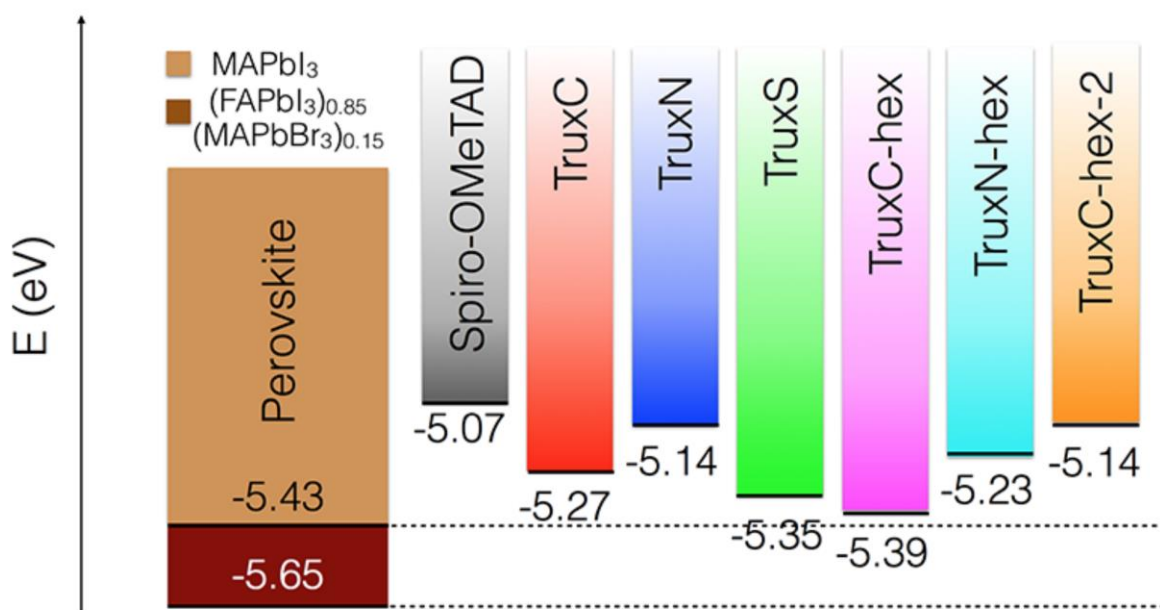
Figure 3.3 Energy level diagram for perovskite,[165,206] Spiro-OMeTAD and truxenes. The numerical values of Spiro-OMeTAD and truxenes are minus computed IPs the B3LYP/6-31G(d,p) level.

UV-Visible absorption spectra were computed using linear response time-dependent density functional theory (see computational details) for Spiro-OMeTAD and truxenes (**Figure 3.4**). The extent of overlap between the two spectra (absorption and solar irradiance) is indicative of parasitic loss. Small spectral overlap is preferred since only little amount of solar energy would be wasted (see Figure S5). The

computed spectra are in reasonable agreement with experimental results (Table S4). In the visible range, Spiro-OMeTAD shows a larger overlap with the solar spectral irradiance as compared to truxenes. Moreover, the ionic additives create a number of oxidized Spiro-OMeTAD molecules, which enlarge the absorption in the visible range and result in a larger parasitic loss (Figure S5).[187,207] In the truxene series, the heteroatom substitution increases the spectral overlap, especially for the nitrogen case (larger peaks at 368 nm). Altering the OMeDPA sites induces a higher absorption peak at 385 nm, which makes TruxC-hex-2 the largest overlap with the solar spectrum among all of our truxene derivatives. Overall, truxenes considered here show smaller overlap with solar spectrum as compared to Spiro-OMeTAD. Furthermore, dopant-free truxenes can avoid introducing additional cation species, leading to lower parasitic loss in visible range.   This makes them promising HTM candidates in inverted or tandem PSC design in terms of lower parasitic loss.
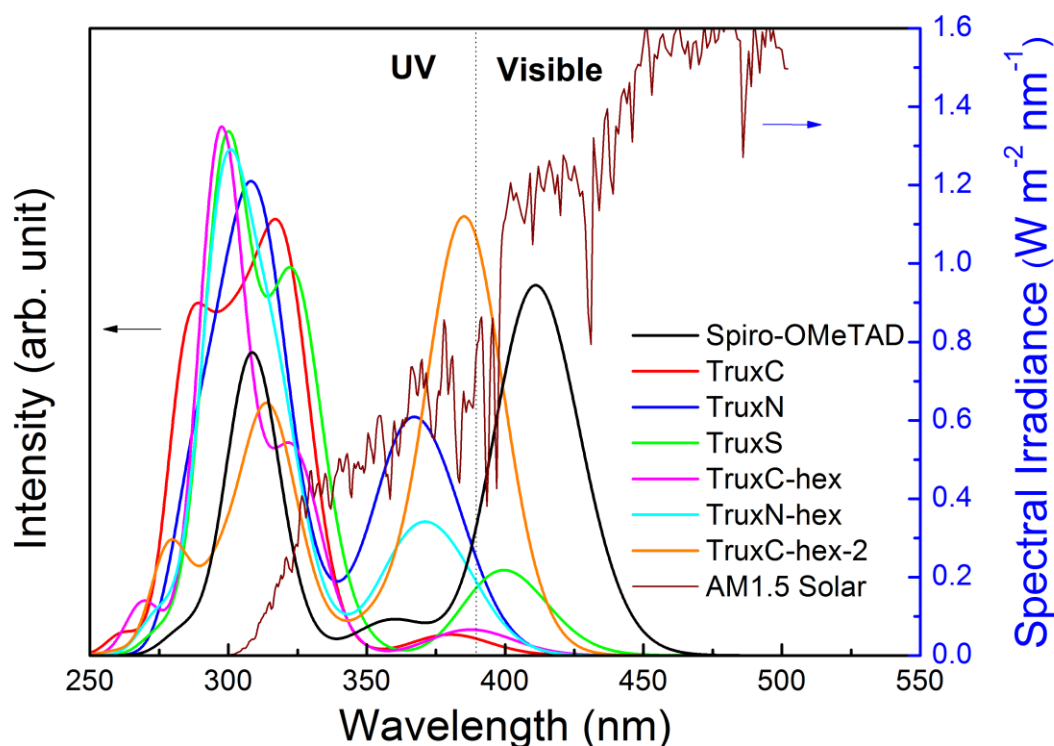
Figure 3.4 Computed UV-visible absorption spectrum of each molecule at the TD-B3LYP/6-31G(d,p) level and the standard AM1.5 solar spectral irradiance (ASTM G-173; Global Tilt).[208]

3.2.3. Hole Transport Properties

Hole transport properties were computed for the amorphous phase of truxenes using a multiscale approach that combines classical molecular dynamics simulations, kinetic Monte Carlo techniques and electronic structure computations (see Computational Details). Non-adiabatic semi-classical Marcus charge-transfer theory[75,209] was applied to evaluate hole transport mobility, in which the high-temperature limit the hopping rate between different sites is defined as:

34

$$\omega_{ij} = \frac{J_{ij}^2}{\hbar} \sqrt{\frac{\pi}{\lambda k_B T}} \exp\left[-\frac{(\Delta E_{ij} - \lambda)^2}{4\lambda k_B T}\right] \qquad (3.2)$$

where T is the temperature, J_{ij} is the transfer integral between sites i and j, ΔE_{ij} is the site energy difference (*i.e.*, $E_i - E_j$) and λ the reorganization energy. Equation (3.2) shows that, taken together, a smaller reorganization energy (λ) and a larger transfer integral (J) result in faster hole transport. Likewise, smaller energy disorder (σ; spread of the hopping site energy differences) also leads to higher hole mobility.[34,210] Hole mobility along with all these related components of the truxene derivatives are presented in **Figure 3.5**. Energy disorder did not show sizable variation upon structural modification. However, a large increase in reorganization energy occurs upon inclusion of hexyl chains (**Figure 3.5 (a)**). Varying the substitution sites of OMeDPA can attenuate the unfavorable enhancement in reorganization energy.
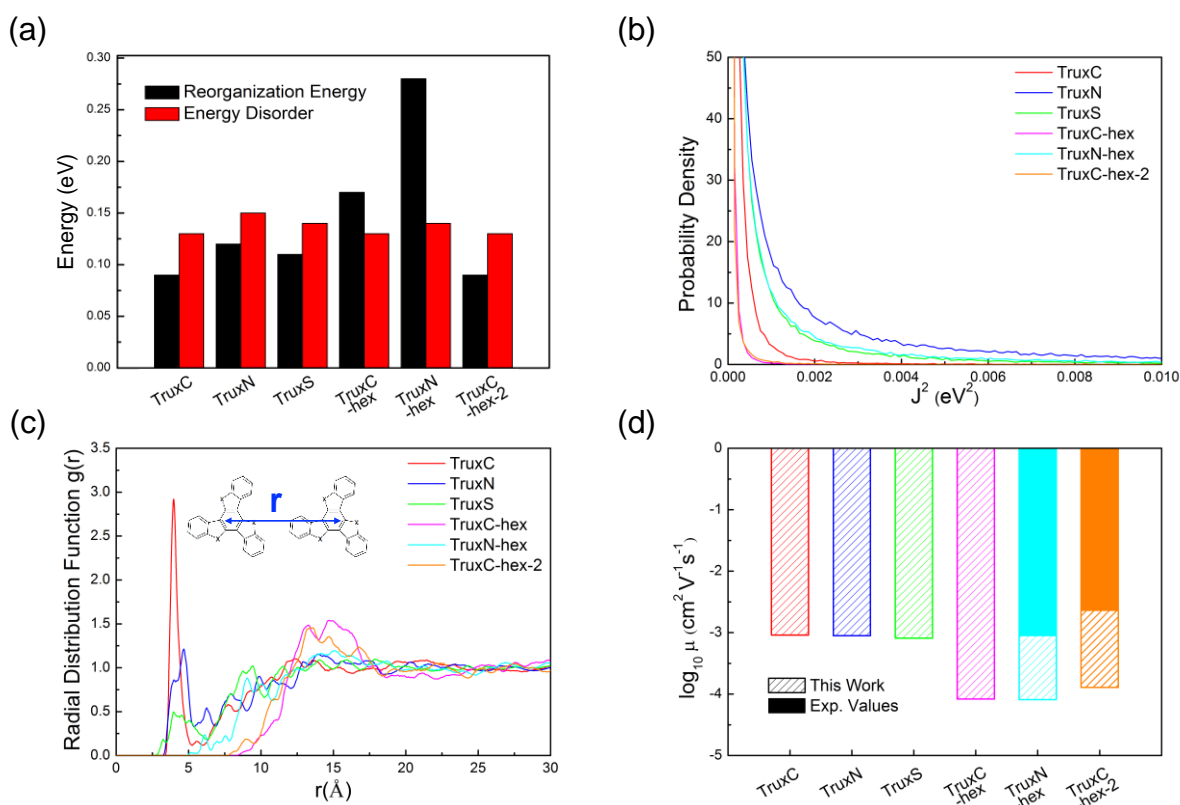
Figure 3.5 (a) Energy disorder vs. reorganization energy plot, (b) probability density distribution of transfer integral square, (c) radial distribution function between centers of geometry of truxene cores and (d) averaged hole mobility of amorphous phase of each molecule.

The distribution function of the squared transfer integral (**Figure 3.5 (b)**) gives a good description of the high value region (10^{-3}~10^{-2} eV^2) that significantly contributes to hole mobility. The effect of the heteroatom is pronounced as illustrated by the largest spread of TruxN, followed by TruxS and TruxC. The hexyl chains deteriorate the electronic coupling between the cores lowering the distribution curve

significantly. This deterioration becomes clear when analyzing the radial distribution function (RDF) between the centers of geometry (COG) of the truxene cores as depicted in **Figure 3.5 (c)**. The first peaks for the bare truxene are located in the 4-5 Å range. In sharp contrast, the substituted truxenes show no peak in this region with a sizable band appearing only at larger distances (≥10 Å), which is associated with significantly lower transfer integrals.
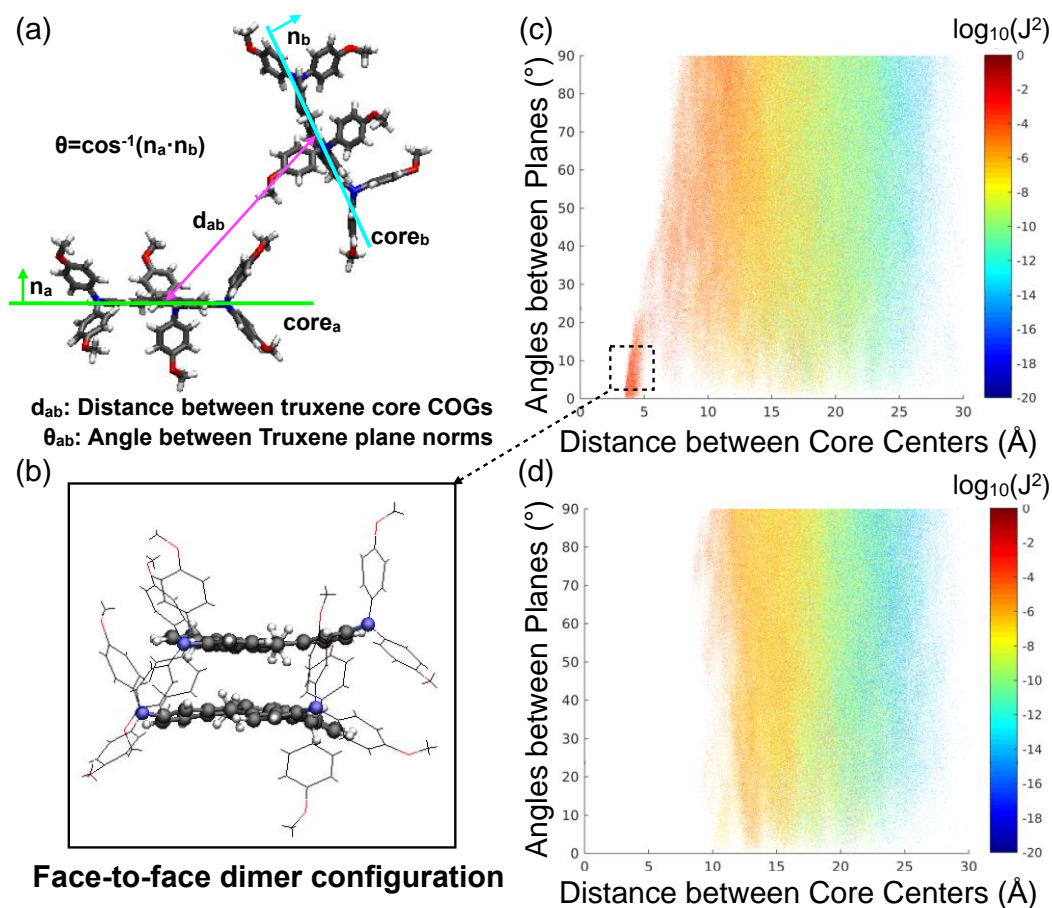
Figure 3.6 (a) Two descriptors used in 2D color map. (b) Face-to-face dimer configuration of truxene molecules. The 2D map colored with transfer integral square for (c) TruxC and (d) TruxC-hex.

The relative arrangement of truxene molecules is best represented by the 2D color maps shown in **Figure 3.6**, S10 and S11. Two descriptors, the distance between the COG of the truxene cores (d_{ab}) and the angle between the normal truxene planes (θ_{ab}) are used for the x- and y-axis in **Figure 3.6 (a)**. Each color-coded dot depicts the occurrence of a given configuration along the molecular dynamic trajectory (see computational details) with the color denoting the value of the square of the transfer integral (**Figure 3.6 (c) and (d)**). Comparisons of the 2D color maps reveals the presence of a region associated with face-to-face dimer configurations of TruxC, which are absent in TruxC-hex. These face-to-face configurations possess large J_{ij}^2 *values* (order of 10^{-2}), which promote hole mobility. After examining each case in Figure S10 and S11, it becomes clear that the presence of hexyl chains prevents the favorable face-to-face truxene arrangement. Further analysis of **Figure 3.5 (b)** and Figure S10, clarifies

36

the wide-spread transfer integrals of TruxN, which arises not only from the higher overall populations around 5 Å, but also from the higher transfer integral ($\sim 10^{-1}$ eV^2) at the same (distance, angle) configurational space compared to TruxC and TruxS. A similar reasoning applied to the comparison of TruxN-hex and TruxC-hex.

The hole mobilities for each molecule are then computed on the basis of all the properties discussed above (**Figure 3.5 (d)**). The computed mobilities are systematically one order of magnitude lower than the experimental results, which is consistent with the known underestimation of the transfer integral by the ZINDO method (see computational details).[211]

In the absence of hexyl chains, truxene and heterotruxenes show remarkably similar hole mobilities in the order of 10^{-3} cm^{2}V^{-1}s^{-1}. In contrast, the substituted truxene derivatives exhibit mobilities one order of magnitude lower than the bare analogues in line with the absence of face-to-face arrangements (*vide supra*). Considering the underestimation of the computed hole mobilities, values in the $10^{-3} \sim 10^{-2}$ cm^{2}V^{-1}s^{-1} range are likely to be measured experimentally for the core lacking alkyl chains. Assuming that other conditions remain unchanged, they would outperform the PCE of their counterpart bearing alkyl chains. Also noteworthy is the increase in hole mobility brought about by modifying the OMeDPA position, which originates from a reduction of the reorganization energy giving a nearly 1.5-fold enhancement (Table S5).

3.2.4. Stability

Hydrophobicity was evaluated by computing the water contact angles of Spiro-OMeTAD and the truxene series, as illustrated in **Figure 3.7**. Both intrinsic (dopant free) Spiro-OMeTAD and TruxC-hex-2 show good agreement with experimental observations (70°~74.5°[160,191] and 90.4°[170], respectively), which justifies the method utilized here (see Computational Details and ESI). The WCA ordering for the truxenes without hexyl chains is: TruxC > TruxS > TruxN. The extent of hydrophobicity can be adjusted by incorporating heteroatoms, which leads to differences as large as 13.1° (TruxC vs. TruxN). The inclusion of hexyl chains increases the WCA considerably: by 24.5° for TruxC and 22.8° for TruxN, as expected from the hydrophobic nature of the alkyl chains. Modification of OMeDPA substitution site was found to decrease WCA by ~10°.

Estimations of the *glass transition temperature* are shown in **Figure 3.8**. In comparison with the known experimental values, our T_gs are systematically ~40°C higher for Spiro-OMeTAD and TruxC-hex-2, due to the much faster cooling rate adopted in molecular dynamic simulations.[212] Despite this overestimation, the qualitative comparisons among the truxene derivative is valuable. The heteroatom substitution from C to N and C to S leads to a serious decrease in T_g of 28°C and 36°C, respectively. Adding hexyl chains also reduced T_g by 28°C for TruxC and 10°C for TruxN. A decrease in T_g upon inclusion of long alkyl chains has been previously observed.[213] For small organic molecules, this phenomenon can be explained by the concept of free volume (V_{free}), which has been invoked to elucidate the influence of the chain

length (n) on T_g for poly-(n-alkyl methacrylates) polymers.[214] The longer the alkyl chains, the further the molecular separation. This free volume facilitates the molecular motions, which in turn, lower T_g. V_{free} was evaluated by subtracting the average volume of a molecule in the amorphous phase (V_a) by the volume of molecule in the gas phase (V_g):

$$V_{free} = V_a - V_g \qquad (3.3)$$

Our result confirms that the addition of hexyl chains increases V_{free} by 182 Å³/molecule for TruxC and 214 Å³/molecule for TruxN. Changing the substitution sites of OMeDPA as in TruxC-hex-2 also lower T_g in comparison to TruxC.
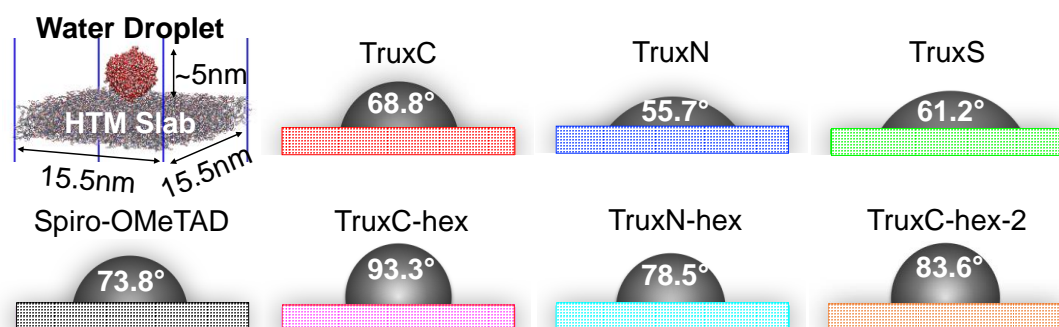
Figure 3.7 Molecular dynamics simulation cell and computed water contact angle for intrinsic Spiro-OMeTAD and truxenes.
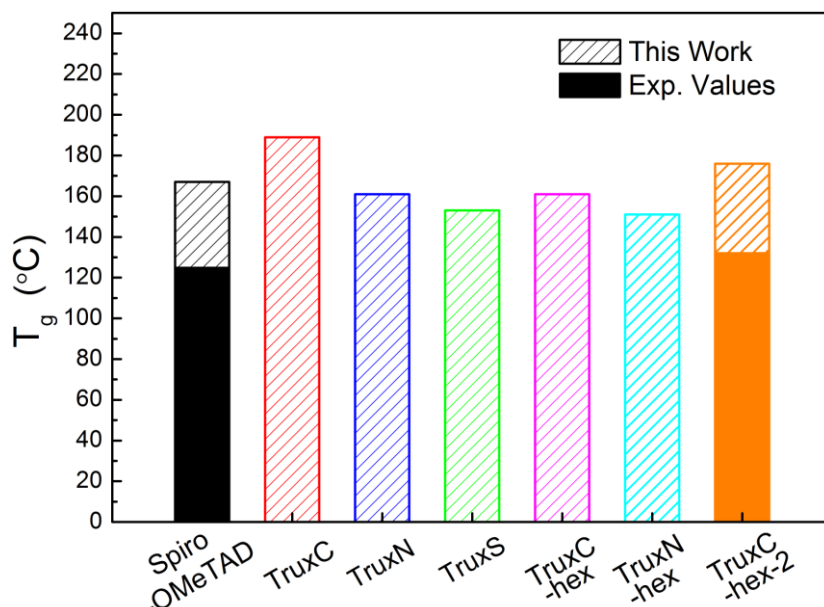
Figure 3.8 Computed and experimental glass transition temperature. The experimental value of intrinsic Spiro-OMeTAD are taken from ref [195]. The experimental Tg of TruxC-hex-2 is approximated by that of TruxC-propane-2 in ref [173] since it is not available.

It should be noted that the computed WCA and T_g of Spiro-OMeTAD are the intrinsic one. We want to stress that since, in practical applications, Spiro-OMeTAD is always doped to compensate for its poor hole mobility, a comparison between dopant free truxenes and doped Spiro-OMeTAD is more reasonable. In this respect, all truxenes considered here outperform the doped Spiro-OMeTAD in terms of both water contact angle (56°)[189] and glass transition temperature (<100°C).[195]

3.2.5. Solubility

Solution-processable HTMs should be soluble in common organic solvents. For this reason, the Hildebrand[215] and Hansen[216] solubility parameters were computed for chlorobenzene to evaluate their relative tendency of the truxenes to dissolve.[217,218] The cores free of hexyl chains tend to dissolve more easily in chlorobenzene than the substituted species (Table S7), likely because the hexyl chains hinder the solvent access and prevent the formation of favorable solute/solvent π -π interactions. At the first glance, this result might appear counter-intuitive since the addition of alkyl chains generally enhances compound solubility in organic solvents. Yet, the factors governing the solubility of a solute in a given solvent are rather complexes and various (e.g., molecular structures, polarity and types of interaction between solute and solvent). If one considers hexane (i.e., alkyl chains) rather than benzene-like solvent, the trends are opposite to that of chlorobenzene following the "like dissolve like" rule.   Overall, since TruxC-hex-2 and TruxN-hex have already been shown to be solution processable in common benzene-like organic solvent (chlorobenzene and toluene),[170,172] it is envisioned that other truxenes without hexyl chains will also be processable in these solvents.

3.3. Summary

The electronic, structural features, hole transport properties and stabilities of the investigated truxenes and the reference Spiro-OMeTAD (intrinsic and doped) are summarized in **Figure 3.9**. The following structure-property relationships emerge from the examination of the different derivatives.

Comparison of TruxC, TruxN and TruxS illustrates the effect of the heteroatom on the IP (increase for TruxS, decrease for TruxN) and parasitic loss (slight increase). The hole mobility remains virtually unchanged but the hydrophobicity and glass transition temperature decrease for TruxS and TruxN. The lower hydrophobicity of the heteroatomic truxenes arises from the enhanced local polarizability induced by the heteroatoms, making the HTM more hydrophilic. This is in line with the various degree of hydrophilic behavior among their small molecule analogues. The solubility in water is pyrrole > thiophene > cyclopentadiene, which corresponds to the order of the WCAs.[219]

The alkyl chains influence every property investigated herein. They act as solubilizing groups (increasing the hydrophobicity) and, somewhat unexpectedly, they decrease the IP of both TruxC and TruxN because of geometrical distortions. The inclusion of hexyl chains also decreases the hole mobility by nearly one order of magnitude (compare TruxC, TruxN with their chain-containing counterparts).

The side chains prevent the truxene cores from adopting a face-to-face dimer configurations, associated with a high transfer integral. Finally, the larger hydrophobicity of the substituted truxene is accompanied by an unfavorable decrease in T_g. Based on these observations, we can conclude that adding alkyl chains may be beneficial for the properties of truxene as an HTM, but further studies should to identify the optimal chain length are necessary.
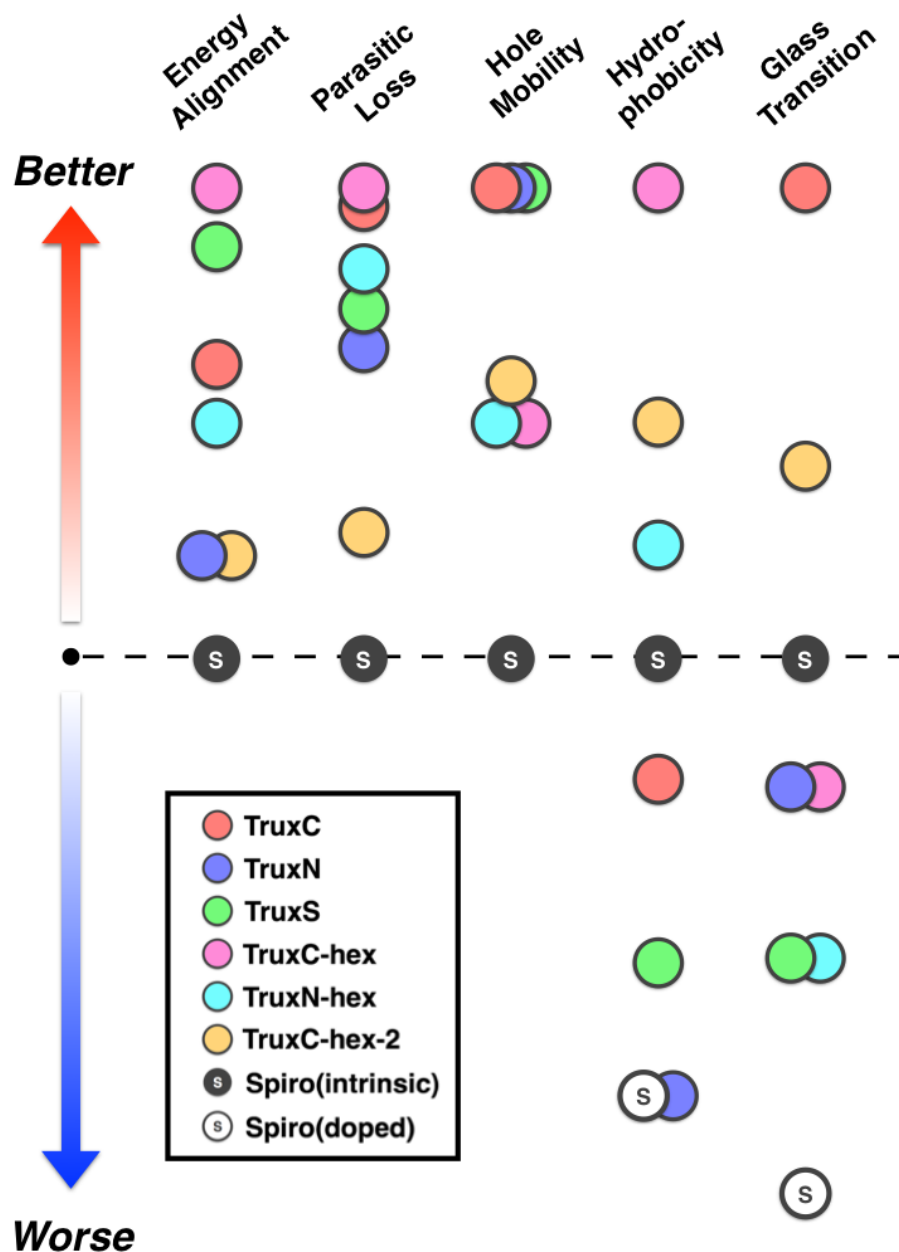
Figure 3.9 Relative trends in the normalized computed electronic properties, transport properties and stability. The mobility of intrinsic Spiro-OMeTAD[163] and all the properties of doped Spiro-OMeTAD[189,195] are taken from experiment. The maximum point is set with the best truxene in each property and zero point with intrinsic Spiro-OMeTAD. Other points are scaled based on these two references (see SI).

Varying the position of OMeDPA (TruxC-hex vs. TruxC-hex-2) decreases the IP and red-shifts the absorption spectrum. It does reduce the reorganization energy by half while retaining a similar energy disorder and transfer integrals. All this leads to a 1.5-fold larger hole mobility. Furthermore, the change in substitution site does not deteriorate T_g significantly, but still preserves a high hydrophobicity. These comparisons demonstrate the influence of a substituent and emphasize the impact of the 3D molecular shape on the properties and morphology of the amorphous phase.

Overall, if only the power conversion efficiency of PSCs is considered, TruxS would be the best candidate tested herein owing to its excellent energy alignment and high hole mobility. However, PCE is not the only criterion necessary to create an ideal perovskite solar cell. In terms of stability, TruxC and TruxC-hex-2 would be promising hole transport materials. In addition to their suitable energy level alignment and hole mobility similar to TruxS, TruxC displays a mild hydrophobicity and high thermal stability. TruxC-hex-2, on the other hand, shows a larger ΔIP, medium hole mobility and possesses both high hydrophobicity and thermal stability. As compared to the intrinsic Spiro-OMeTAD, each of these two molecules exhibit a better performance in every facet. Thus, these molecules represent promising alternatives. Acknowledging that Spiro-OMeTAD must be doped in practical applications, all of the proposed truxene derivatives represent superior alternatives. Simulation protocols such as those discussed in this contribution, rationalize the outstanding performance of TruxC-hex-2 (Trux-OMeTAD)[170] through investigation from a molecular viewpoint by providing concrete structure-property relationship that can serve to identify additional candidates (TruxC and TruxS) for use in perovskite solar cell applications.

3.4. Conclusions

We have employed sophisticated multiscale modeling techniques to derive structure-property relationships for several truxene derivatives. The resulting trends in the electronic, transport properties and stability criteria, crucial for achieving the high-performance perovskite solar cell, illustrate the effects of the heteroatom substitution, alkyl chain addition and site alteration.

As a result of this work, several promising HTM candidates were identified as alternatives to Spiro-OMeTAD. A perovskite solar cell with a TruxS HTM, for example, would exhibit high PCE due to good energy alignment and high hole mobility. Furthermore, to ensure long-term performance a compromise between performance and stability is required. In this case, both TruxC and TruxC-hex-2 show great promise, as recently demonstrated by experiment (TruxC-hex-2).[170] Finally, the computational methodology and protocol employed here are broadly applicable for rationally developing HTMs and PSCs with superior performances. Within this context, in the future we intend to complement this rational design strategy with high-throughput screening of the electronic properties of various commonly used cores.

3.5. Computational Details

3.5.1. Electronic Properties

Molecular Geometry

All the geometries of the neutral and cationic molecules were optimized using B3LYP-[220,221]D3BJ[222] in conjunction with the 6-31G(d) all-electron basis set. Computations related to the following section were performed with Gaussian09.[223]

Ionization Potential

The ionization potential (IP) were computed using a ΔSCF (delta self-consistent field) procedure in conjunction with different density functionals and the 6-31G(d,p) basis set (Table S1):

$$IP = \Delta SCF = E_{cN} - E_{nN} \tag{3.4}$$

where E_{nN}/E_{cN} is the total energy of the neutral/charged molecule in neutral geometry.

UV-visible Absorption Spectrum

The UV-vis absorption spectra were computed at the TD-B3LYP/6-31G(d,p) level with the conductor-like polarized continuum (C-PCM)[224] solvent model using tetrahydrofuran. Gaussian broadening with a 0.13 eV σ was adopted to generate the absorption spectrum.

3.5.2. Hole Mobility

Amorphous Structure Construction

The amorphous assemblies were constructed from a unit cell containing 64 molecules using Packmol.[225] The molecules were first minimized using conjugate gradient algorithm and then equilibrated in the NPT ensemble (500K, 1bar) by performing classical molecular dynamics (MD) simulation. This equilibrated system was then extended to a 2x2x2 supercell with 512 molecules. Further equilibration (500K, 1bar) was performed for 5ns. Finally, a 10ns equilibration in the NPT ensemble (300K, 1bar) followed by another 10 ns for production run serve to generate 1000 snapshots. The simulations were performed under periodic boundary condition using GROMACS package[226,227,228] and the CGenFF[229,230] force field along with charges obtained by the restrained electrostatic potential (RESP)[231] procedure based on HF/6-31G(d,p). The temperature and pressure control used velocity rescaling with a stochastic term[232] (T = 300K, τ_T = 1.0 ps) and an isotropic coupling for the pressure from a Berendsen barostat (P_0 = 1 bar, χ = 4.5 × 10^{-5} bar^{-1}, τ_P = 1.0 ps). The time step used in all simulation was 1 fs. Bonds involving H atoms were constrained using Linear Constraint Solver (LINCS) algorithm. A cutoff of 12 Å was

applied to the van der Waals interaction through the force-switch mode. As for electrostatic interactions, the particle mesh Ewald (PME) method was employed with a 0.12 nm Fourier spacing.

Hole Mobility Computation

The hole mobilities of the HTMs were computed according to the semi-classical Marcus charge-transfer theory on 200 frames extracted from previous MD trajectories using the VOTCA package.[211,233] Within this formalism, the charges are assumed to be localized on a single molecule and each molecule is considered as a hopping site. The charge transfer process thus takes place through the hopping between different sites. The high-temperature, which limit the hopping rate between different sites is defined as Equation (3.2). The reorganization energy was computed by a 4-point method at the B3LYP-D3BJ/6-31G*level:

$$\lambda = E_{nC} - E_{nN} + E_{cN} - E_{cC} \qquad (3.5)$$

where E_{nN} (E_{cC}) is the total energy of the neutral (charged) molecule in neutral (charged) geometry and E_{nC} (E_{cN}) is the energy of the neutral (charged) molecule in charged (neutral) geometry. The Thole model was used to compute site energy (E_i or E_j), which includes contributions from electrostatic interactions, polarization and external electric field.[211] The partial charges needed in this model for neutral and charged state were generated via CHelpG method[234]. The transfer integral J_{ij} was evaluated considering the HOMO and HOMO-1 simultaneously[126] for every molecular pair ij in the neighbor list. This neighbor list was established for every molecular pair having a distance between their nearest fragments within 7 Å. Once all the parameters necessary to calculate the hopping rate are computed, a 1 ms kinetic Monte Carlo (KMC) simulation was performed using a 10^5 Vcm^{-1} electric field to obtain the hole mobility. For a given snapshot (structure), the KMC simulations were conducted with the electric field in three different directions resulting in a total simulation time that correspond to three times the number of snapshots. Figure S6 illustrates that 200 snapshots (600 KMC simulations) are already sufficient to obtain a statistically meaningful distribution of hole mobility.

Structural Analysis

The construction of the 2Ds map was based on the molecular pairs found in the neighbor list established in for the hole mobility computations. Molecular pairs with a distance between COGs of truxene cores larger than 3 nm was not observed.

3.5.3. Hydrophobicity and Glass Transition Temperature

Water Contact Angle

We employed soft-confined method to create an amorphous organic solid surface preventing uncontrollable roughness on the surface.[235] The whole simulation procedure is illustrated in Scheme S1.

Starting from a supercell with x=y=155.0580 Å and z=310.1160 Å, two xenon crystal walls were placed 120 Å apart. Using Packmol, 512 molecules were then placed between these two walls leading to a sandwich structure. The NVT simulation was then performed at 500K, while gradually decreasing the distance between the two walls until reaching the targeted density for the middle amorphous slabs. For each given specie, the targeted density was chosen as the bulk density. Once the desired density was reached, the system was equilibrated in the NVT ensemble at 300K for 10 ns with fixed walls. Finally, the xenon walls were removed, leaving the amorphous slab ready for further simulations.

The water droplet to put atop the amorphous slab was created from a water cube with 1500 water molecules and equilibrated in the NPT ensemble (300K, 1bar) using the simple point charge model (SPC).[236] This equilibrated cube was then placed into a 110 Å side cubic supercell and equilibrated in the NVT ensemble at 300K to obtain a water droplet. This droplet was placed on the amorphous slab and equilibrated in the NVT ensemble at 300K with fixed slab for 10 ns. The simulation details are similar to *Amorphous Structure Construction* section. The Particle Mesh Ewald approach with the slab correction 3dc was adopted to compute the long-range Coulombic interactions.[237] The readers can refer to the supporting information to read more about the method employed to extract the WCA from the MD trajectory.

Glass Transition Temperature

Starting from the previous structures with 512 molecules equilibrated under (500K, 1bar), the system was cooled down from 500K to 300K stepwise at 10K intervals under a constant pressure (1bar). For each temperature step, the step size was 2ns, and the final 500 ps was used to collect statistics at a frequency of 0.20 ps. The cooling rate between the successive temperatures was 0.33 K/ps. The simulation details are similar to *Amorphous Structure Construction* section. The T_g is obtained from the intersection of two fitted lines in specific volume-temperature plot. For details, please refer to the supporting information.

The volume of a molecule in the gas phase V_g is the volume enclosed by the electron density isosurface with an isovalue of 0.001 electrons/Bohr^3 computed using B3LYP/6-31G(d,p).

3.5.4. Solubility Parameters

The Hildebrand solubility parameter (δ_T) is defined as the square root of cohesive energy density (CED). However, this single parameter can only give reasonable prediction for non-polar or slightly polar molecules. In order to broaden its applicability, Hansen further divided the cohesive energy into three intermolecular contributions: dispersive interactions (δ_D), dipole-dipole interactions (δ_P), and hydrogen-bonding interactions (δ_H) as shown in Equation (3.6):

$$\delta_T = \sqrt{CED} = \sqrt{\delta_D^2 + \delta_P^2 + \delta_H^2} \tag{3.6}$$

44

The Hildebrand and Hansen solubility parameter were extracted from the MD simulations. Given that contribution from the hydrogen bond energy is not straightforward,[218] we only reported the contribution from overall Coulombic interaction δ_Q, with the relation:

$$\delta_Q = \sqrt{\delta_P^2 + \delta_H^2} \tag{3.7}$$

The distance between the truxenes (solute) and chlorobenzene (solvent) in Hansen parameter space is an index for solubility, which is approximated by:

$$R^2 = 4(\delta_{D1} - \delta_{D2})^2 + (\delta_{P1} - \delta_{P2})^2 + (\delta_{H1} - \delta_{H2})^2$$
$$\approx 4(\delta_{D1} - \delta_{D2})^2 + (\delta_{Q1} - \delta_{Q2})^2 \tag{3.8}$$

Chapter 4 How does alkyl chain length modify the properties of triphenylamine-based hole transport materials?

4.1. Introduction

Hole transport materials (HTMs) based on phenylamine are commonly used in various optoelectronic applications - organic light emitting diodes[238–241], solid-state dye sensitized solar cell[242–245] and perovskite solar cells (PSCs)[26,169,170,246] – predominately because of their good transport properties, stability, and suitable ionization potential.[247] Specifically, diphenylamine (DPA) and triphenylamine (TPA) are extensively used as building blocks in high-performance or/and dopant-free HTMs of perovskite solar cells.[98,247,248] Spiro-OMeTAD, the current state-of-the-art, possesses four DPA groups substituted onto two fluorene units that are connected through the carbon spiro center.[157] However, the rather poor hole mobility and high cost of Spiro-OMeTAD has prompted searches for promising dopant-free DPA- or TPA-based HTMs that lead to PSCs with high power conversion efficiency (PCE) and long-term stability.[159,169,192,195,246,249–251] The exploration and ultimate identification of novel HTMs for PSCs relies upon establishing relevant structure-property relationships and fulfilling several requirements:

(1) **Energy alignment:** A suitable alignment of energy levels between the perovskite and hole transport layer (HTL) is required to achieve efficient hole injection. This reduces the recombination rate and increases open circuit voltage (V_{oc}).[181,182]

(2) **Optical properties:** The absorption of light falling within the range of the solar spectrum (parasitic loss) should be minimized in order to avoid competition with the perovskite active layer.[186,187]

(3) **Hole mobility:** Promising dopant-free HTMs should possess high intrinsic hole mobility (10^{-4} to 10^{-3} $cm^2V^{-1}s^{-1}$), which facilitates hole transport and reduces recombination at the perovskite/HTL interface.[26]

(4) **Hydrophobicity:** Highly hydrophobic HTMs protect the underlying perovskite layer by slowing the invasion of moisture, which leads to better long-term device performance.[167,189,191–193,252] Hydrophobic HTMs also influence the perovskite grain growth in inverted PSCs, giving rise to a perovskite layer with large grain and long carrier diffusion length.[170,194]

(5) **Oxygen resistance:** Oxygen-induced degradation is a main source of operational instability in methylammonium lead iodide PSC.[253,254] Thus, exploiting HTL as a barrier layer against O_2 diffusion[255] is beneficial.

In general, modifying the length of alkyl chains is a widely-employed approach for tuning the properties of organic materials such as: ionization potential,[52] absorption spectrum,[53] charge transport properties,[53–57] hydrophobicity[256,257] and oxygen diffusion properties.[258–261] The relationship between chain length and each of these properties is, however, not trivial and also depends on the size (small molecule or polymer) and shape (rod-shape, star shape, butterfly-shape and etc.) of molecules as well as the phase of the material (crystal or amorphous). Our previous investigation on truxene derivatives found that transport properties deteriorate when hexyl side chains were present, although hydrophobicity was increased.[262] The contrasting effects brought about by the presence of hexyl chains on these two key properties demonstrate the importance of chain length optimization for improving HTM performance. Here, we elucidate relationships between side chain length and overall HTM performance using our previously established computational protocol.[262]
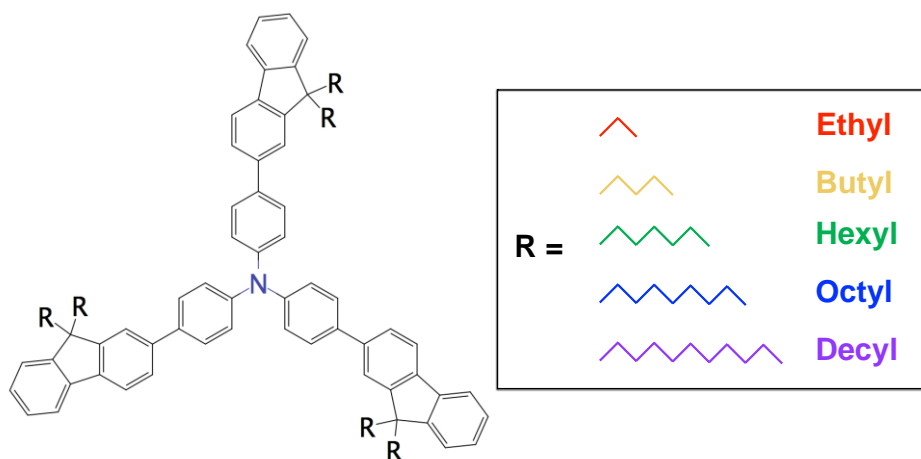
Figure 4.1 The TPA based molecule (TPAF-R) considered in this work.

We selected tris[4-(9,9-dialkylfluoren-2-yl)phenyl]amine (TPAF-R), which consists of three dialkyl-substituted fluorene moieties attached to a TPA core (**Figure 4.1**), as a model system because of its

suitable ionization potential (IP; 5.2 eV) and adequate hole mobility (10^{-4} cm^{2}V^{-1}s^{-1} for the butyl substituted case).[213] Five TPAF derivatives with different chain lengths for the dialkyl component [ethyl (TPAF-E), butyl (TPAF-B), hexyl (TPAF-H), octyl (TPAF-O), and decyl (TPAF-D)] were tested by first examining the ionization potential and absorption spectra. This is followed by combining the investigation of fundamental transport quantities with a morphological analysis of amorphous HTMs. Finally, hydrophobicity and oxygen resistance are evaluated. Computational details can be found in the Supporting Information (SI).

4.2. Results and Discussion

4.2.1. Ionization Potentials and Absorption Spectra

For TPAF-R molecules, it has been experimentally shown that alkyl chain length (ethyl, butyl and hexyl groups) only negligibly affects electronic properties such as ionization potentials (IP) and absorption spectra.[213] Our computations reproduce this finding and show minimal variation with respect to chain length (see Table S1). The IP and absorption spectra trends extracted for TPAF-R molecules stand in stark contrast to substituted truxene cores, which show pronounced differences upon elongation of aliphatic groups attached to the core.[262] The observed differences can be traced to the location of the substitution sites: in truxene, significant structural distortion occurs that disrupts the π-conjugated truxene cores, an influence, which is negligible in TPAF-R molecules. Thus, by choosing a proper substitution site, it is possible to retain the electronic and optical properties of the core, while fine-tuning other properties of interest.

4.2.2. Hole Mobility

Hole mobility is a critically important property that is required for promising HTMs in high performance PSCs. Here, the hole transport process is described by the hopping model, where the hopping rates between two sites are computed using non-adiabatic semi- classical Marcus charge-transfer theory. The high-temperature limit of the hopping rate between different sites is defined as:

$$\omega_{ij} = \frac{J_{ij}^2}{\hbar} \sqrt{\frac{\pi}{\lambda k_B T}} \exp\left[-\frac{\left(\Delta E_{ij} - \lambda\right)^2}{4\lambda k_B T}\right] \qquad (4.1)$$

where T is temperature, J_{ij} is the transfer integral between i and j site, ΔE_{ij} is the site energy difference $E_i - E_j$ and λ is the reorganization energy. Analyzing disorders present in a material is essential to uncover the influence of chain length on transport properties. On one hand, *dynamic disorder*, which arises from atomic thermal fluctuations and is time-dependent, leads to a time variation of the transfer integrals and site energies. On the other hand, *static disorder* (time-independent), which originates in deviations from the perfect crystalline phase, causes the spreading of site energy values

(energetic static disorder) and transfer integrals (positional static disorder).[263] Both dynamic and static disorders can dramatically reduce hole mobility of an amorphous HTM (**Scheme S1**).[263]

The dynamic disorder of the square of the transfer integrals (J^2) is described by the coefficient of variation (C_{J^2}), as defined in the supplementary materials [**Figure 4.2 (a)**]. Varying the length of the alkyl chains produces similar C_{J^2} values (within the error bars), principally because the transfer integrals are often dominated by atomic fluctuations of the π-conjugated moieties (TPA and fluorene) that are unaffected by varying the chain length. The comparable fluctuating behavior of the TPA and fluorene cores is seen by their invariant root mean square fluctuations (RMSF) [black for TPA and red for fluorene, **Figure 4.2 (b)**]. Likewise, the dynamic energetic disorder, given by the standard deviation of site energy difference with time (σ_D), are also roughly similar when the error bars are considered for the different TPAF-R derivatives [**Figure 4.2 (c)**]. This behavior is expected considering that the computation of site energies is dominated by electrostatic contributions involving the π-conjugated cores (see supplementary information).
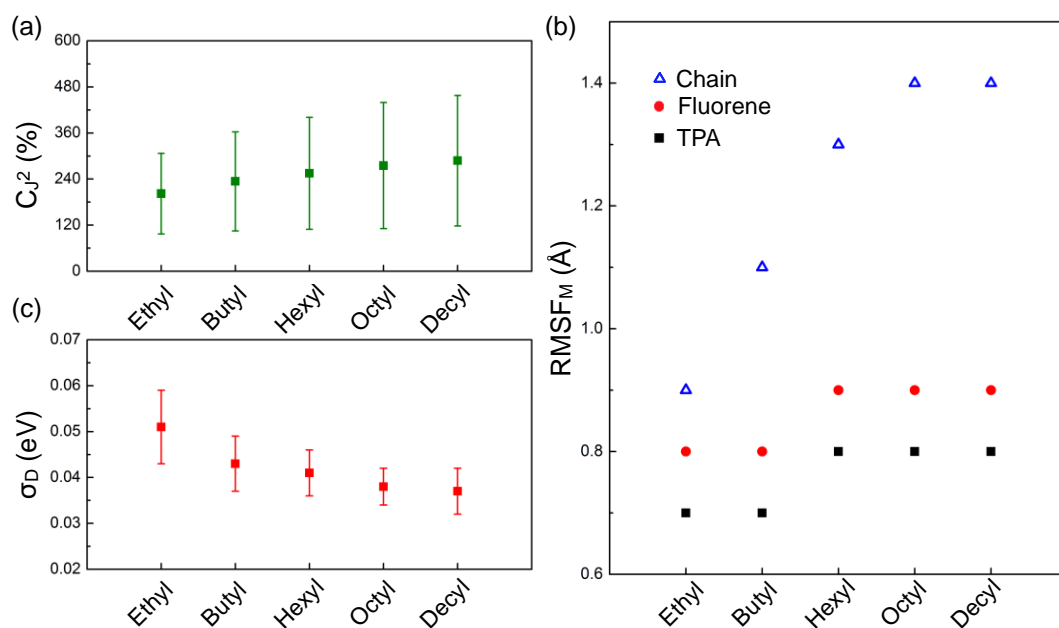
Figure 4.2 (a) C_J^2, (b) RMSF$_M$ (RSMF of a given molecular building block, *i.e.*, alkyl chains, fluorene or TPA and (c) dynamic energetic disorder of the TPAF-R derivatives.

In all cases, the positional static disorder dominates dynamic disorder for the transfer integrals. Therefore, the trend associated with positional static disorder can be approximated by evaluating the total disorder of J^2 (see SI). Longer chains exhibit a broader distribution that extends into the low J^2 region (left-shifted) and lower populations in the high J^2 region [**Figure 4.3 (a)**], relative to their short chain counterparts. Examination of the radial distribution functions (RDF) reveals the origin of the distinct J^2 distributions between the nitrogen atoms (amines) that characterize the morphologies of TPAF-R. The first peak, located at ~6Å, is higher for shorter chain lengths. Elongation of the aliphatic

50

side chains inhibits close contact between the amine groups located at the center of each molecule, which causes a reduction in the first nearest neighbor (FNN) population. In turn, the smaller FNN results in a population decline in the high transfer integral region of TPAF-R for the lengthier alkyl chains. The energetic static disorder (σ_S), determined using Bredas's method,[263] is much higher than its dynamic counterpart [**Figure 4.3 (b)(c)**] dropping from 0.144 eV to 0.116 eV with increasing chain length. The decline in energetic static disorder may arise from the considerable expansion in volume that accompanies longer chains (*vide infra*), as rationalized by the correlated Gaussian disorder model.[37]
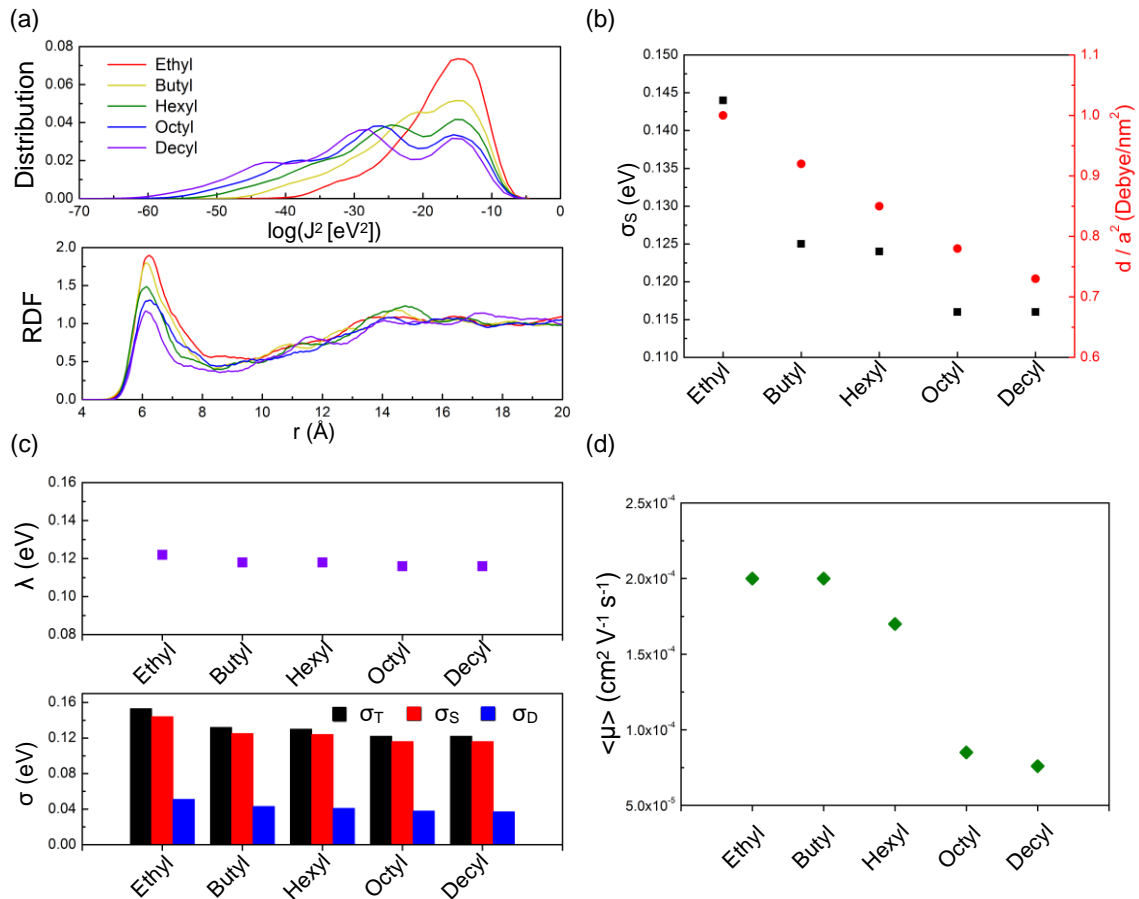
Figure 4.3 (a) (above) Transfer integral square distribution and (below) radial distribution function between central amine atoms, (b) static energetic disorder σ_S (black squares) and d/a^2 (red circles) and, (c) reorganization energy and energetic disorders [dynamic, static and total] and (d) hole mobility of TPAF-R molecules with different alkyl chain lengths.

Taken together, high transfer integrals, low reorganization energy, and small energetic disorder lead to high hopping rates (Equation 1) and large hole mobility. In order to decipher how chain length affects this key property, we examined each of the fundamental transport quantities individually. Interestingly, the reorganization energies are nearly the same in all case [**Figure 4.3 (c)**], whereas increasing the chain length causes a corresponding decrease in the transfer integrals [**Figure 4.3 (a)**] and energetic disorder. Because of these subtle balances, TPAF-E and TPAF-B are characterized by similar hole mobilities

$(2.0 \times 10^{-4}$ cm^{2}V^{-1}s^{-1}), as shown in **Figure 4.3 (d)**. Traversing the series from butyl to decyl shows hole mobility reduced from 2.0×10^{-4} to 7.6×10^{-5} cm^{2}V^{-1}s^{-1} which is dominated by the transfer integrals [**Figure 4.3 (a)**]. Note that our computed hole mobility for TPAF-B agrees well with experiment $(1 \times 10^{-4}$ cm^{2}V^{-1}s$^{-1})$,[213] which further validates our computational approach.

4.2.3. Hydrophobicity

In order to maximize long-term performance in perovskite solar cell, it is crucial to eliminate any sources of instability (*e.g.*, H$_2$O and O$_2$) present within the device. Water invasion can be mitigated through incorporation of hydrophobic HTMs into the PSCs. The hydrophobicity of any HTM can be evaluated by determining the *water contact angle* (WCA) schematically shown in **Figure 4.4**. Longer alkyl groups, which are strongly hydrophobic, lead to higher WCAs, which rise from 83.6° (for ethyl) to 101.9° (for decyl). Influence of the chain length was gauged by computing the ratio of the area occupied by the alkyl chains within 5 Å of the surface layer to the total square area. No aggregation of the alkyl moieties occurs, as they appear homogeneously distributed on the surface. Increasing the length of the aliphatic groups also results in greater surface coverage, which correlates well with larger computed water contact angles for the longest alkyl moieties tested. However, the increase in both WCA and area ratio appears to be nearing a plateau between the octyl to decyl groups, which implies that only marginal improvements in hydrophobicity are expected by further increasing the length of the alkyl chains. Also note that further lengthening of the alkyl moieties could modify the packing behavior of the molecules, potentially leading to a reduction in the WCA.[256,257]
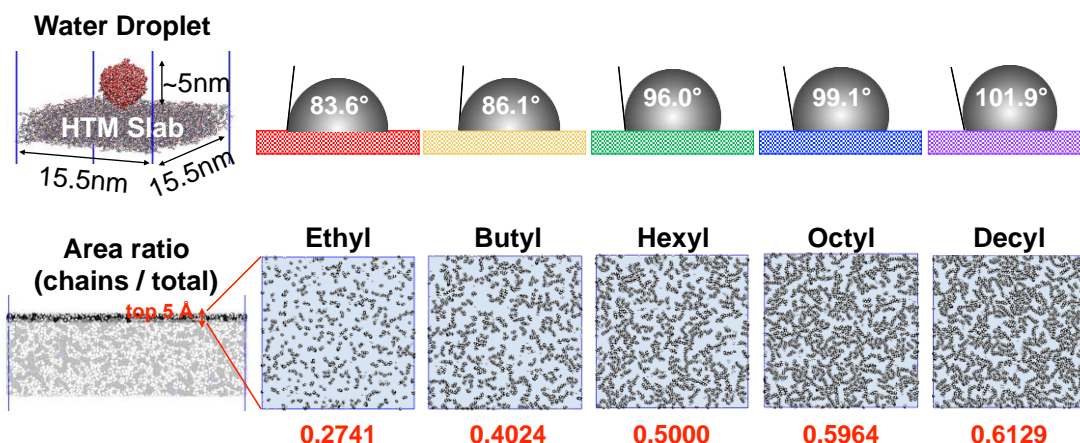
Figure 4.4 (above) Simulation cell and water contact angles; (bottom) the area ratio of alkyl chains to whole square area for TPAFL with different chain lengths. The VDW radii of carbon and hydrogen taken from previous work by Bondi[52] and Rowland et al.[53], respectively.

4.2.4. Oxygen Resistance

The degree of O_2 resistance of an HTM can be assessed by its O_2 diffusion coefficient. In principle, the increasing free volume associated with longer chain lengths implies that O_2 should diffuse more freely in TPAF-R molecules appended with lengthy aliphatic groups [**Figure 4.5 (a)**]. In reality, however, our results indicate that O_2 diffusion behavior is much more sophisticated [**Figure 4.5 (a)**]. The diffusion constants decrease when moving from ethyl to hexyl, increase from hexyl to octyl, and then decrease again between octyl to decyl, which seems quite puzzling. Indeed, while longer alkyl chains provide larger free volumes, their enhanced flexibility [**Figure 4.5 (b)**] can produce traps and barriers that ultimately retard diffusion, as seen by computed root mean square displacement (RMSD) for O_2 trajectories (Figures S5-S14). From these RMSD plots, O_2 diffusion behavior can be characterized as either trapped or trap-free, as shown in **Figure 4.5 (b)**. Due to opposing trends in free volume and flexibility, O_2 is statistically more likely to be trapped in TPAF-H (Figure S9 and S10). In addition, assuming a trap-free pattern, short alkyl groups (ethyl and butyl) tend to have larger RMSDs at the end of their trajectories compared to lengthy alkyl group (hexyl, octyl and decyl), which implies a larger O_2 diffusion barrier for the long chain cases. Since the free volume is larger for longer chain TPAF molecules, a possible origin for the higher diffusion barrier is that the alkyl chains physically obstruct O_2 molecules from diffusing. Practically speaking, tuning the length of the alkyl chains in TPAF molecules can reduce O_2 diffusion constants by up to 50% (ethyl vs. hexyl), indicating that chain length engineering can be used to improve the resistance of HTMs to O_2 ingress.
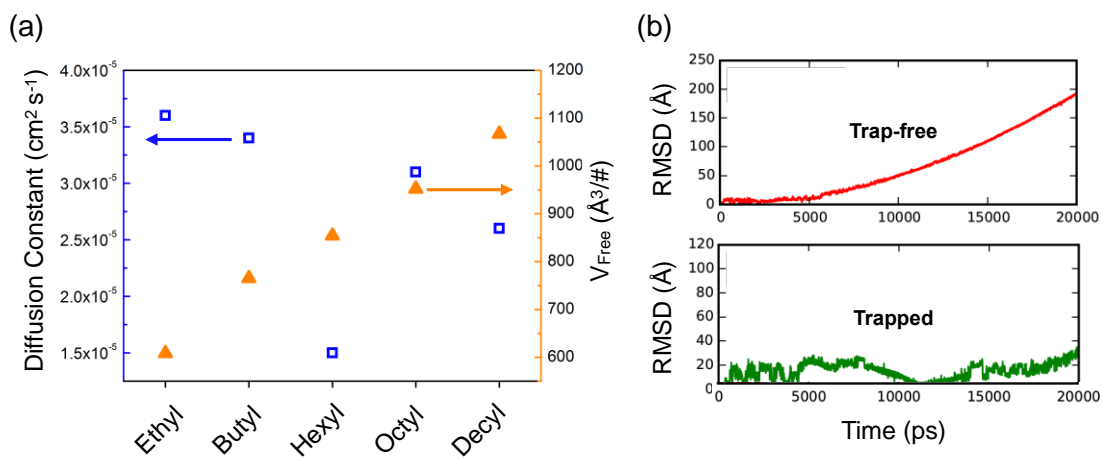
Figure 4.5 (a) Diffusion constant and free volume [in amorphous matrix; volume per molecule] for each case and (b) characteristic of RMSD for trap-free (red line) and trapped (green line) case.

4.3. Conclusions

In summary, we probed different properties of TPAF-R molecules in order to uncover the influence brought about by tuning the length of the alkyl chains that strongly influence HTM performance. Overall, modifying the chain length negligibly affects electronic properties but does decrease hole mobility. The

degree of hydrophobicity can also be enhanced through the incorporation of longer aliphatic groups into the TPAF molecules, which remain homogeneously distributed on the surface. Concerning oxygen diffusion, the longer alkyl chains introduce more free volume which generally permits oxygen to move more freely although these groups also can serve as barriers and traps to retard oxygen diffusion. Our results show that the O_2 diffusion constant can be cut by half by finely tuning the length of the alkyl chains. Considering a holistic picture including each of the properties, TPAF-H appears to be the most promising HTM due to its highest oxygen resistance, relatively high hole mobility and water contact angle. Further elongation of the alkyl chains beyond six carbon atoms results in marginal improvement in hydrophobicity, but significant deterioration in hole mobility and oxygen resistance. In contrast, shorter chains provide slightly ameliorated hole mobility, but worse hydrophobicity as well as high oxygen diffusivity. Although the optimal chain length may be different for other amorphous HTMs, the general trends regarding chain length dependence and the rationalization from a molecular viewpoint utilized here will be beneficial for future rational designs. Moreover, this computational protocol can easily be adopted for computationally-guided design, which should increase the discovery pace of new HTMs. It should be noted that the conclusion we reach here are based on alkyl chains with even number of C and we are aware that odd-even effect of alkyl substituents can be crucial for some organic systems.[54] We will investigate this effect in the future.

Chapter 5 Multiarm and Substituent Effects on Charge Transport of Organic Hole Transport Materials

5.1. Introduction

Organic–inorganic hybrid perovskite solar cells (PSCs) are considered as one of the most promising candidates to meet the increasing energy demand. Since their emergence in 2009, their power conversion efficiency (PCE) has increased from 3.8% to more than 22%.[264,265] To further improve PCE, it is essential to identify the ideal material for each device component. The most important layer in the PSC device is the active perovskite, which is responsible for absorbing sunlight and generating free charge carriers. In addition to the main active perovskite, the hole transport (selective) layers play a crucial role in reducing interfacial electron-hole recombination and serve as a protective coating that retards moisture.[247,266–268] As a result, considerable effort has been directed toward discovering promising hole transport materials (HTMs), especially small organic molecule-based HTMs.[58,269–274]

The desired HTMs properties in perovskite solar cell are well-defined: (a) a suitable ionization potential (IP) and (b) a high hole mobility (μ). A suitable ionization potential (IP) facilitates hole injection and maximizes the open circuit voltage (V_{oc}), while a high hole mobility (μ) affords efficient hole transport from the perovskite layer to the electrode, leading to a high fill factor (FF).[180,275,276] In addition, HTMs with high μ can serve as dopant-free HTMs, avoiding introducing deliquescent salts such as Li-TFSI which is detrimental to long-term stability. Despite recent effort in the field,[59,277–285] the current understanding of the "chemical structure"-property (*i.e.*, hole mobility) relationship for amorphous HTMs is still murky. This lack of knowledge hampers the discovery pace of promising HTMs and, for this reason, systematic investigations of the influence of molecular structure on the hole mobility are beneficial.[275,286] Correspondingly, computer simulations undertaken at the molecular level are powerful

tools in revealing this non-trivial relationship, as demonstrated by Andrienko and Wetzelaer *et. al.*,[287] who compared the hole transport parameters and mobility of five common organic amorphous semiconductors with those obtained by experiments.

Because of the limited understanding of the structure-mobility relationship, current searches for new HTMs tend to rely on trial-and-error approaches. For example, Son *et al.*[58] and Dai *et al.*[59] considered the effect of the number of triphenylamine (TPA) moieties attached to the central core on PSC performance, finding that the HTM hole mobility increases with the number of TPA arms. Another relevant example involved increasing the PCE by introducing more Lewis bases, from zero (TPAC0M) to three methoxy groups (TPAC3M) in order to reduce electron-hole recombination.[60] Thus, a legitimate question is can these two strategies be combined with one another? Assuming we retain the ability of defect passivation by controlling the number of -MeO, can hole mobility be enhanced by introducing additional arms? How do these molecular modifications alter the IP? Starting from TPAC3M (referred to as TPA1C3M later), which is already a promising dopant-free HTM leading to a PSC with ~16% PCE,[60] here, we consider derivatives with increasing numbers of 9-(4-methoxyphenyl)carbazole arms (MPCB arms, as shown in **Figure 5.1**), which are investigated through a multi-scale computational protocol. The relationship between the most critical charge transport parameters and the properties are investigated using electronic structure computations, molecular transport network and dimer-configuration clustering. Our results demonstrate that hole mobility increases with the number of MPCB arms attached to the TPA core. However, introducing more arms leads to an unfavorable decrease in IP, which can be adjusted through careful chemical modification. The simulations of two of the best performing HTMs are compared with field-effect transistor measurements, showing good agreement between experimental and simulated hole mobilities. This finding highlights the relevance of our strategy that has the potential for applications stretching beyond the field of perovskite solar cells.
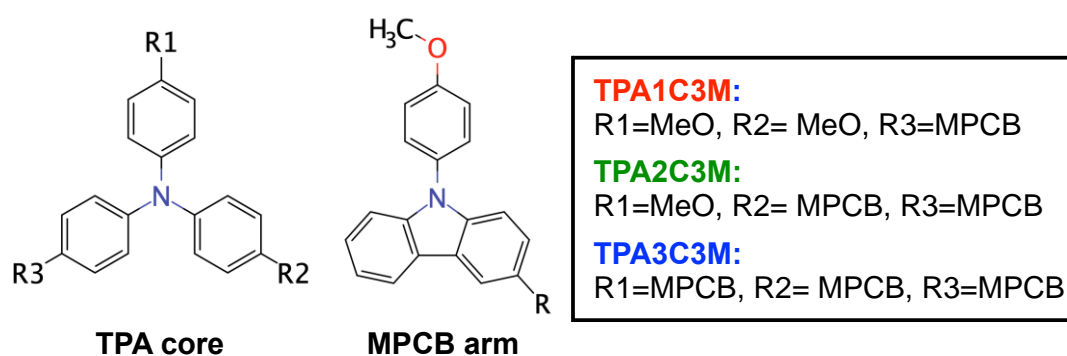
Figure 5.1 The molecular structure of the TPA core, the MPCB arm, the MeO group, as well as the TPA1C3M, TPA2C3M and TPA3C3M molecules.

5.2. Results and Discussion

5.2.1. Multiarm Effect on Charge Transport Properties

Hole mobility is obtained from kinetic Monte Carlo (kMC) simulations, for which the input is the hole hopping rates calculated for each molecular pair ij (molecular dimer) using non-adiabatic semi-classical Marcus charge transfer theory.[75] Each of the charge transport parameters given in the computational details (*e.g.*, reorganization energy λ, transfer integrals J_{ij} and site energy difference ΔE_{ij} in **Equation 5.4**) are discussed below.

The Reorganization energy, (computed with the 4-point method) decreases from 213 meV to 156 meV while increasing the number of MPCB arms (**Figure 5.2 (a)**). Since low reorganization energies lead to high charge transfer rates, increasing the number of MPCB arms attached to the TPA core is an effective strategy that might underpin the outstanding performance of existing multiarm HTMs.[288–290] At room temperature, the charge transfer rate of TPA3C3M is two times that of TPA1C3M, assuming a zero site-energy difference ($\Delta E_{ij} = 0$) and the same transfer integrals (as shown in Equation 5.1).

$$\frac{\omega_{TPA3C3M}}{\omega_{TPA1C3M}} = \sqrt{\frac{\lambda_{TPA1C3M}}{\lambda_{TPA3C3M}}} \exp\left[-\frac{\lambda_{TPA3C3M} - \lambda_{TPA1C3M}}{4k_B T}\right] \approx 2.03 \qquad (5.1)$$

The reason for the significant decrease in λ is extended conjugation, as visualized (**Figure S1**) by the HOMO becoming more spatially delocalized through the MPCB arms when moving from TPA1C3M to TPA3C3M. Thus, it is not surprising that the trend in reorganization energy has been noted for similar molecules such as oligoacene, thienoacenes and oligothiophenes.[291,292]
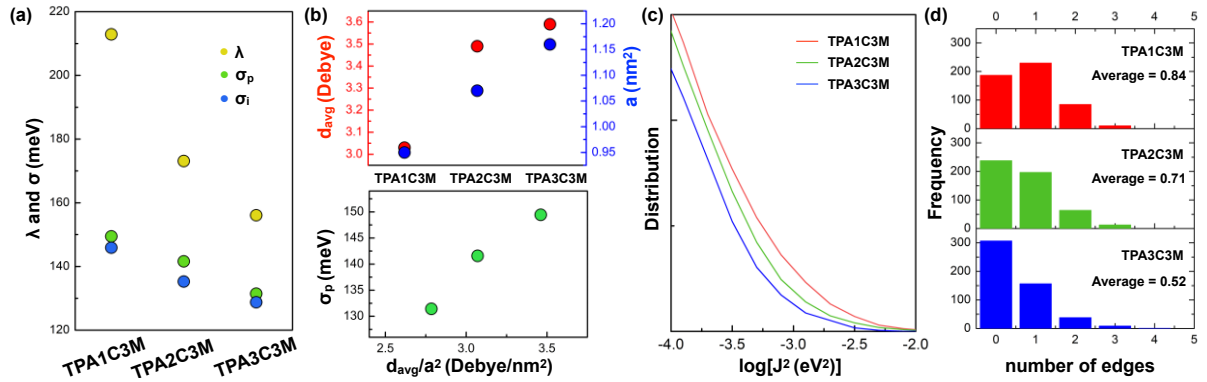
Figure 5.2 (a) Reorganization energy [λ, computed using four-point method at the B3LYP/6-31G(d,p) level], energetic disorder (electrostatic and polarization component, σ_p), and intrinsic energetic disorder (σ_i). (b) Average molecular dipole moment davg and lattice parameter a (top) and a plot of $\sigma_p - d_{avg}/a^2$. (c) Overall transfer integral square distribution. (d) Histogram of the number of edges for each hopping site with a threshold of 10^{-4} eV^2 for TPA1C3M, TPA2C3M, and TPA3C3M molecules.

The origin of the decreasing λ can be further investigated by a partitioning into each contributing vibrational mode using normal model analysis (NM). The reorganization energy determined through

this method is 218 meV, 173 meV and 162 meV for TPA1C3M, TPA2C3M and TPA3C3M, respectively. The good agreement between λ obtained from NM and 4-point method indicates the anharmonic effect is insignificant in our case. Since the behavior and sums of the vibrational mode contributions for all three molecules are similar for λ_1 and λ_2 (see computational details, **Figure 5.3** and **Table S1**), the following discussion focuses only on λ_1. The key contributing normal modes are nearly the same for each of the three molecules (see arrows in **Figure 5.3** and the corresponding vibrational modes in **Figure S3-S5**). Interestingly, with the exception of the first band, TPA1C3M is always characterized by the largest contributions. Given that the relevant frequencies are the same for all molecules, the larger λ_1 contribution of TPA1C3M arises from a larger displacement (ΔQ_i^2, as shown in **Figure S3 to S5**). Overall, introducing more arms does not alter the major vibrational modes that contribute to the local electron-phonon coupling, but rather reduce the reorganization energy by attenuating the geometrical response between the charged and neutral state (*i.e.*, ΔQ_i^2 of these modes).
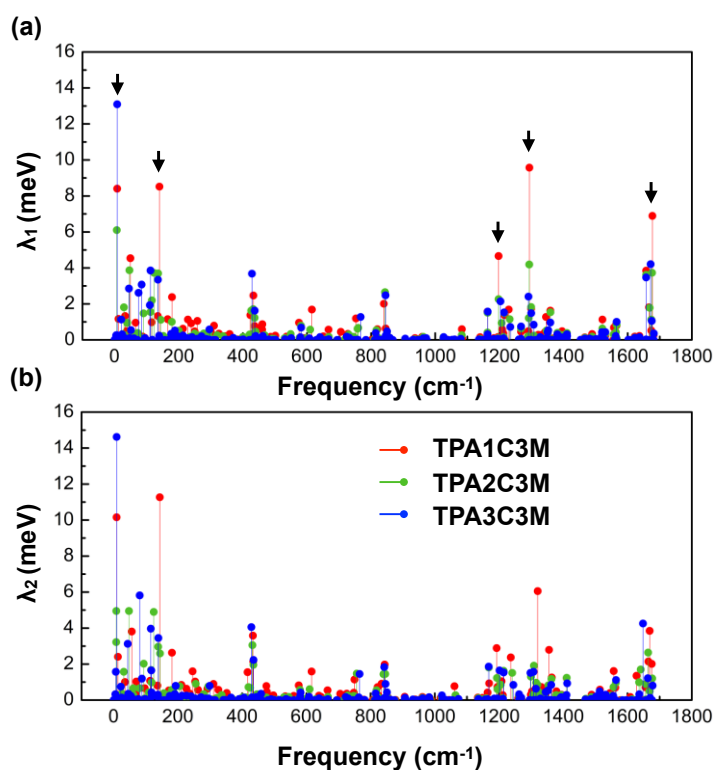
Figure 5.3 Frequency dependence reorganization energy computed using NM method B3LYP/6-31G(d,p) level for (a) neutral (λ_1) and (b) cationic (λ_2) geometry upon hole transfer process for TPA1C3M, TPA2C3M and TPA3C3M. The black arrows indicate the frequencies that make major contribution to reorganization energy.

Energetic disorder: In organic amorphous materials, the lack of translational symmetry leads to a Gaussian or exponential distribution of the site energies, where the molecules with a site energy centered at the tail of the density of states serve as potential charge traps that hamper charge transport.[293] The dependence of charge mobility on the energetic disorder is described by a lattice model:[210,294]

$$\mu \propto \exp[-(C\beta\sigma)^2]$$ (5.2)

where C is a coefficient that depends upon the model used and β is the inverse of temperature ($1/k_BT$). The exponential dependence emphasizes the crucial role of σ. The physical origin of the energetic disorder can be understood from the partitioning:[295]

$$\sigma_{tot}^2 = \sigma_p^2 + \sigma_i^2$$ (5.3)

were σ_{tot} is the total energetic disorder, σ_p the electrostatic and induction component and σ_i is the intrinsic component. σ_i arises from the molecular conformational disorder present in disordered organic materials, which leads to HOMO variation. On the other hand, σ_p results from the electrostatic interactions and the induction between a molecule (site) and its surrounding environment.

As shown in **Figure 5.2 (a)**, σ_p decreases with an increase in the number of MPCB arms, from 149 meV to 131 meV. This can be explained by the correlated Gaussian disorder model (CGDM), which describes the energetic disorder using a dipole glass model (simple cubic lattice, for which the sites are occupied by randomly oriented dipoles).[296] The origin of σ in this model is purely electrostatic, with σ being proportional to the molecular dipole moment (d) and the inverse of the square of the cubic lattice parameter ($1/a^2$). We compute the average molecular dipole moment d_{avg} and effective lattice parameter a for each compound (see page 11 in the supporting information). Although both d_{avg} and a increase by a similar percentage (~20%) when going from 1 to 3 arms, the inverse square dependence of σ on a leads to an overall decrease in d_{avg}/a^2 (**Figure 5.2 (b)**). The good correlation between σ_p and d_{avg}/a^2 indicates that the multiarm design strategy can successfully reduce σ_p if the increase in molecular dipole moment is not significant compared to the increase in molecular size.

Similar to σ_p, the intrinsic energetic disorder also decreases from 146 meV to 129 meV when increasing the number of MPCB arms from one to three. Previous work by Wenzel *et al.* showed that σ_i correlates rather well with the variation in HOMO energy with respect to the easily-rotatable dihedral angles.[295] Similar correlations are observed between the HOMO of the molecule considered here and the dihedral angle between the carbazole group in MPCB and the benzene in the TPA core (**Figure S7**). The HOMO variation decreases with an increase in the number of arms, akin to the σ_i. trend. Since both σ_p and σ_i follow the same trend, the total energetic disorder follows the order TPA1C3M > TPA2C3M > TPA3C3M.

Transfer integrals also exhibit a broad distribution in disordered organic materials. As shown in **Figure 5.2 (c)**, the population in the high transfer integral region [10^{-4}~10^{-2} eV^2] follows the trend TPA1C3M > TPA2C3M > TPA3C3M, suggesting that there are more molecular dimers with high transfer integrals in TPA1C3M than in its multiarmed counterpart. Apart from the magnitude of the transfer integrals, the connectivity of the molecular transport network is also crucial for rationalizing charge mobility.[297,298]

We examined the transport network using two measures: (1) the average number of edges per site (E_{avg}) and (2) the Kirchoff transport index (K, see computational details).[299]

For a threshold value of 10^{-4} eV^2, the majority of the number of edges per site is either 0 or 1 for all three molecules. Going from TPA1C3M to TPA3C3M, the frequency of 1 and 2 edges gradually decreases while that of 0 edges increases. Overall, the average number of edges per hopping site decreases as the number of MPCB arms increases, from 0.84 to 0.52. Similar trends are observed for threshold values of 10^{-5} and 10^{-6} eV^2 (**Figure S8** and **Table S3**). The Kirchoff transport index (**Table S3**) correlates well with E_{avg}, suggesting better transport network properties for TPA1C3M.

In short, TPA1C3M outperforms its counterparts in terms of both the overall distribution and the spatial connectivity of the transfer integrals. Generally, two factors determine the magnitude of the transfer integrals for hole transfer: (1) the intrinsic molecular property (HOMO) and (2) the molecular packing (dimer geometry).[292] Here,, the molecular shape varies from linear (TPA1C3M), to bent (TPA2C3M) to star shape (TPA3C3M), which naturally results in very different molecular packing (dimer configurations) (**Figure 5.4** and **Figure 5.5**). Insightful information can be extracted from the relationship between the molecular packing and the transfer integrals for each amorphous organic material even though the intrinsic change in HOMO also comes into play. The relations are analyzed via data clustering in an N-dimensional space where N is the number of geometrical descriptors used to describe the representative dimer configurations for each molecule (see computational details and SI).
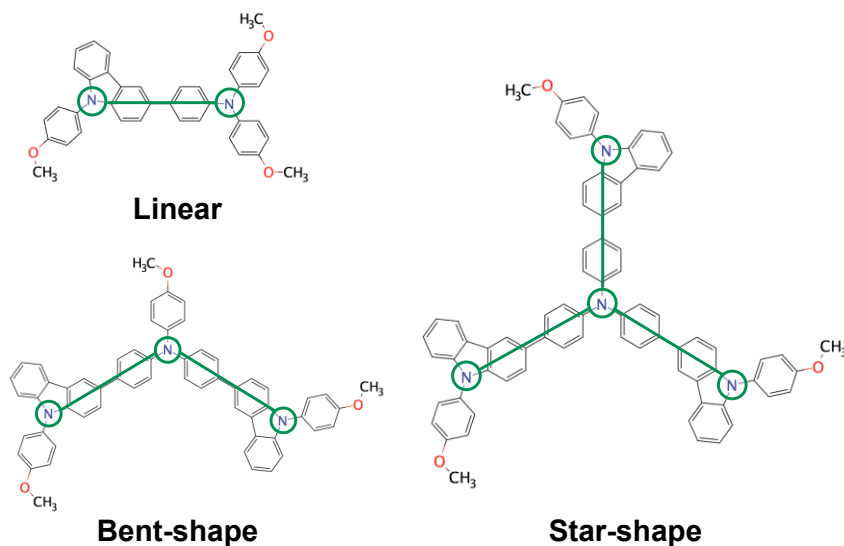
Figure 5.4 The molecular shape of TPA1C3M, TPA2C3M and TPA3C3M molecules.
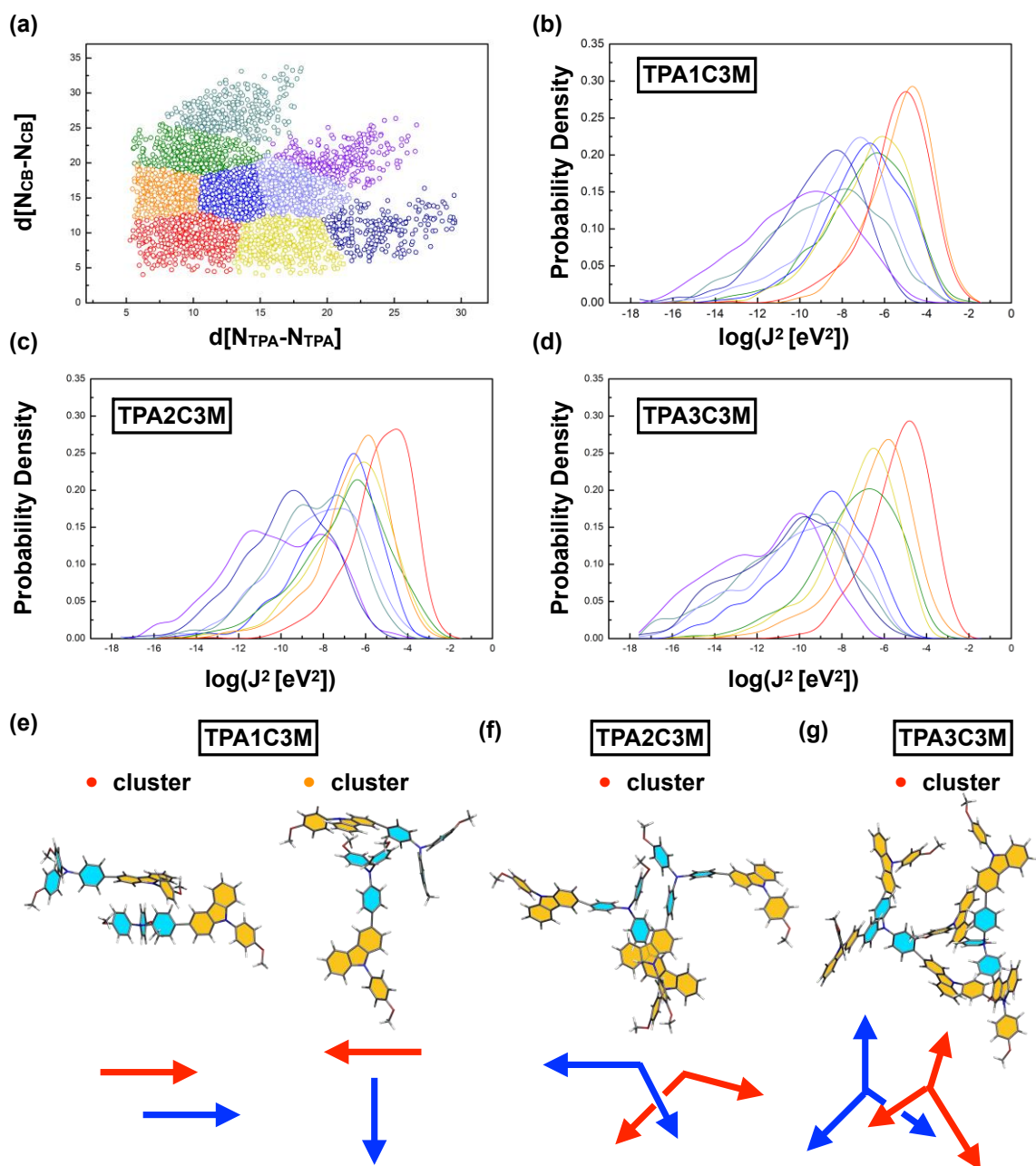
Figure 5.5 (a) Clustering of a 2D configurational space for TPA1C3M into 9 clusters (specified by color), each dot represents a molecular dimer. The $d[N_{TPA}-N_{TPA}]$ stands for the distance between two nitrogen atoms on TPA cores of two molecules and the $d[N_{CB}-N_{CB}]$ represents the distance between two nitrogen atoms on carbazole (CB) arms; the probability density of transfer integral square for the corresponding cluster (with the same color) for (b) TPA1C3M, (c) TPA2C3M and (d) TPA3C3M; the prototypical dimer configuration (centroid of each cluster) for (e) TPA1C3M, (f) TPA2C3M and (g) TPA3C3M. The arrow is a sketch for the prototypical dimer configurations, pointing from nitrogen atom of TPA core (light blue) to that of MPCB arms (light orange).

The TPA1C3M dimer configurations can be represented by points with coordinates ($d[N_{TPA}-N_{TPA}]$, $d[N_{CB}-N_{CB}]$) in a 2-dimensional (2D) configurational space, as shown in **Figure 5.5 (a)**. We plotted the

probability density of the square of the transfer integral for each cluster on the 2D configurational space (**Figure 5.5 (b)**). Clusters located at the bottom left of **Figure 5.5 (a)**, represent close-contact dimer configurations, possess distributions with peaks positioned at higher J^2 region compared to their top right counterparts. Among all the clusters, two (red and orange) possess a J^2 distribution with a peak at $10^{-5} \sim 10^{-4}$ eV^2, which make major contributions to the overall J^2 distribution in the high transfer integral region (**Figure 5.2 (c)**). The prototypical dimer configurations of these two clusters, which are characterized by "parallel" and "T-shape" arrangements, are shown in **Figure 5.5 (e)** (for other clusters, see **Figure S11 to S13**). It is not surprising that these two types of molecular packing lead to high transfer integrals. Furthermore, the prototypical dimer configurations for the orange and yellow clusters, which are roughly symmetric with respect to the diagonal of 2D configurational space, are both "T-shaped" and differ that the moieties involved at the branch point of "T" are different (TPA group for orange cluster and MPCB group for yellow cluster). This results in a difference in the degree of π-π overlap, where the former has two phenyl groups in close contact with the other molecule at the branch point, while the latter has only one, which leads to a left-shifted peak in J^2 distribution for the yellow cluster.

Using the same treatment for TPA2C3M/TPA3C3M as for TPA1C3M, the probability density of transfer integral square for each cluster is shown in **Figure 5.5 (c)** and **(d)**. Unlike TPA1C3M, only one cluster (red) possess a J^2 distribution with a peak at $10^{-5} \sim 10^{-4}$ eV^2, with the corresponding characteristic dimer configurations being shown in **Figure 5.5 (f)** and **(g)**. In the region of $10^{-6} \sim 10^{-5}$ eV^2, TPA2C3M possesses two clusters (orange and yellow) with peaks located in this range, while TPA3C3M only has one cluster (orange) in the same region. Since the number of dimer configurations for each cluster is quite similar, the difference in J^2 probability distribution explains the observed trend in the distribution in the high J^2 region: TPA1C3M > TPA2C3M > TPA3C3M (**Figure 5.2 (c)**).

Hole mobility: To sum up, the reorganization energy, total energetic disorder and transfer integrals all decrease when the number of MPCB arms is increased. Reducing the first two parameters favors high hole mobility, while decreasing the last has the opposite effect. Overall, the simulated hole mobility of TPA1C3M, TPA2C3M and TPA3C3M are 7.34×10^{-6}, 1.49×10^{-5} and 3.09×10^{-5} cm^{2}V^{-1}s^{-1}, respectively (**Figure 5.8**) indicating that the gain from lowering the reorganization energy and energetic disorder surpasses the loss from the lower transfer integrals when more MPCB arms are introduced. This 4.2 fold enhancement in hole mobility proves that the multiarm design strategy is effective for this molecule. Although the totality of multiarm design principles should be examined for other molecules, the computational protocol and the analysis adopted here is broadly applicable to future systematic investigations.

5.2.2. Optimization of the Ionization Potential

The computed ionization potentials of HTMs in isolated gas phase ($IP_{iso)}$ and with solid state correction (IP_{solid}) are shown in **Figure 5.6**. Although the hole mobility is augmented by the number of MPCB arms, the IP_{solid} decreases from 5.10 eV to 4.96 eV, which is unfavorable to the V_{oc}. Thus, it would be

beneficial to adjust the IP via chemical modification while preserving (or even improving) the hole mobility. The strategy is to alter the molecular structure of TPA3C3M minimally, conserving the defect passivation ability (*e.g.*, the number of Lewis bases) by replacing the methoxyphenyl groups located on the MPCB arms with stronger electron-withdrawing groups or alternative substitution site. Since IP_{iso} and IP_{solid} show similar trends, we use the cost-effective IP_{iso} as a preliminary screening criterion, followed by IP_{solid} computations for the potential HTMs.
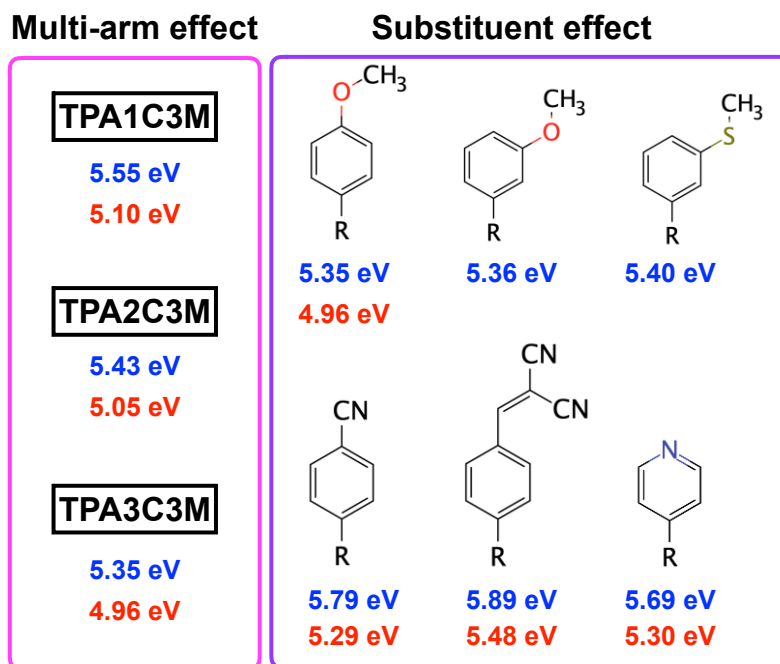
Figure 5.6 Ionization potential of TPA1C3M, TPA2C3M, TPA3C3M and the derivatives of TPA3C3M in isolated gas state ($IP_{iso,}$ blue) and with solid-state correction ($IP_{solid,}$ red).

Seok *et al.* showed that by displacing half of the methoxy groups on Spiro-OMeTAD from the para (electron-donating) to the meta ((electron-withdrawing) position increased the IP by ~0.1 eV.[284] In our case, this modification only raises the IP_{iso} from 5.35 eV to 5.36 eV. Further enhancement can be achieved through heteroatom substitution and replacing m-MeO with m-MeS groups,[300] leading to an IP of 5.40 eV. Given that these two strategies are not sufficient, we introduced stronger electron-withdrawing groups (*e.g.*, benzonitrile, benzylidenemalononitrile and pyridine) that are traditionally used for tuning the IP of HTMs (**Figure 5.6**).[301–303] The IP_{iso} effectively increases from 5.35 eV (methoxyphenyl) to 5.79 eV (benzonitrile; TPA3C3CN), 5.89 eV (benzylidenemalononitrile; TPA3C6CN) and 5.69 eV (pyridine; TPA3C3PD). Further examination shows that their IP_{solid}, 5.29 eV, 5.48 eV and 5.30 eV, approach the value of the minus valance band maximum of MAPbI$_3$.[276]

5.2.3. Substituent Effect on Charge Transport Properties

Analogous to the previous sections, we now discuss substituent effects from TPA3C3M to TPA3C3CN, TPA3C6CN and TPA3C3PD, on each transport parameters: λ, σ and J_{ij}.

Reorganization energy: The reorganization energy (using the 4-point method, see **Table S2** for the NM results) marginally increases from 156 meV to 168 meV (TPA3C3CN), 181 meV (TPA3C6CN) and 168 meV (TPA3C3CN) (**Figure 5.7 (a)**) when stronger electron-withdrawing substituents are introduced. Overall, this effect is less significant than varying the number of arms (25 meV vs 57 meV from TPA1C3M to TPA3C3M). A crude estimation using **Equation 1** suggests that the influence of the reorganization energy change on charge transport by introducing different substituents is minor, with a transfer rate 0.73/0.86 times that of TPA3C3M for TPA3C6CN/TPA3C3CN.

Energetic disorder: σ_p (**Figure 5.7 (a)**) increases from 131 meV to 146 meV (TPA3C3CN) and 179 meV (TPA3C6CN). Yet, replacing the methoxyphenyl by pyridine groups strongly reduces σ_p (by 51 meV). This contrast essentially originates from the molecular dipole moment, as shown in **Figure 5.7 (b)**. Introducing benzylidenemalononitrile groups raises the average molecular dipole moment from 3.59 to 9.60 Debye. The intrinsic energetic disorder follows a similar trend, with the exception of the σ_i of TPA3C3PD, which is larger than that of TPA3C3M. The total energetic disorder evolves as: TPA3C6CN > TPA3C3CN > TPA3C3M > TPA3C3PD.
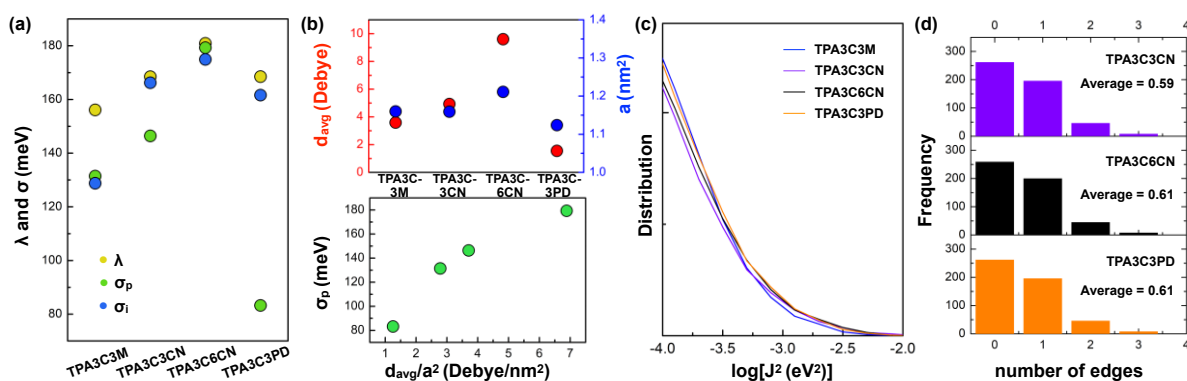
Figure 5.7 (a) Reorganization energy [λ, computed using the four-point method at the B3LYP/6-31G(d,p) level], energetic disorder (electrostatic and polarization component, σ_p), and intrinsic energetic disorder (σ_i). (b) Average molecular dipole moment d_{avg} and lattice parameter a (top) and a plot of $\sigma_p - d_{avg}/a^2$. (c) Overall transfer integral square distribution. (d) Histogram of the number of edges for each hopping site with a threshold of 10^{-4} eV^2 for TPA1C3M, TPA2C3M, and TPA3C3M molecules.

Transfer integrals: All systems exhibit a similar square of the transfer integral distribution in the region where the transfer integral is highest [10^{-4}~10^{-2} eV^2] (**Figure 5.7 (c)**), indicating that both the variations in the HOMO (**Figure S2**) and changes in molecular packing are only slightly affected by the substituent. This is confirmed from the average connectivity plot of the three molecules examined in **Figure 5.7 (d)** (very similar and slightly better than that of TPA3C3M), the Kirchoff transport index (**Table S3**) and the clustering analysis (**Figure S14),** which each show that substituent modification leads to a similar molecular packing and better molecular transport network.
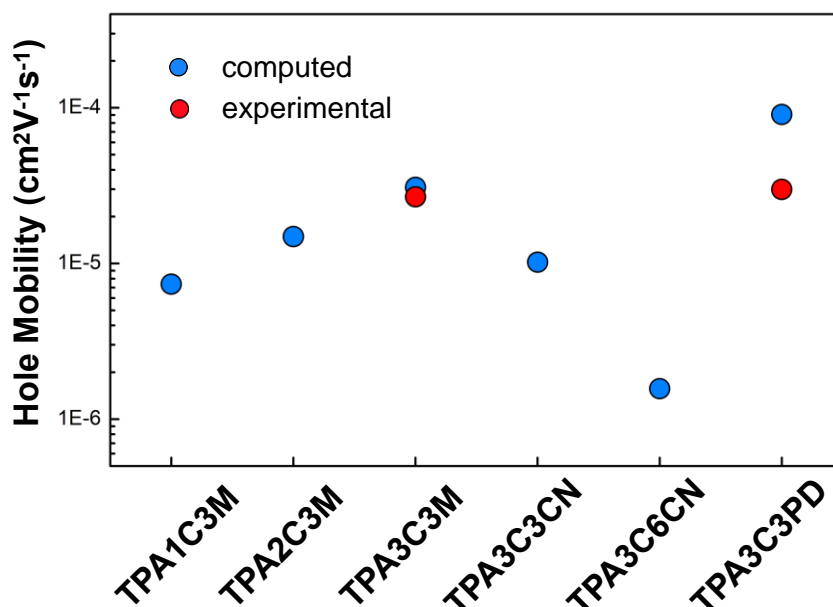
Figure 5.8 The computed and experimentally measured hole mobility (average result from four transistors) for all molecules.

Hole mobility: The hole mobility of TPA3C3CN, TPA3C6CN and TPA3C3PD is predominantly determined by the reorganization energy and the total energetic disorder (1.02×10^{-5}, 1.57×10^{-6} and 9.07×10^{-5} $cm^2V^{-1}s^{-1}$, respectively, **Figure 5.8**). Modifying the substituents from TPA3C3M to TPA3C6CN decreases hole mobility by more than an order of magnitude, whereas TPA3CPD is increased by ~3 times. On the basis of the previous evaluation of the reorganization energy contribution, we can conclude that the energetic disorder, (especially σ_p) is the main source for the variation in hole mobility. This highlights the crucial role of the molecular dipole moment as a design principle. To verify our simulated results, we measured the hole mobility of TPA3C3M and TPA3C3PD, showing highest simulated hole mobility, using bottom contact bottom gate field effect transistors (FETs) prepared by solution processing (**Figure 5.8**). Our predictions are in fair agreement with the experimental mobility of TPA3C3M. The larger computed TPA3C3PD mobility may arise from the hole concentration effect: the FET mobility is extracted at high charge-carrier concentration, while the simulations are performed with a single charge carrier. The trap filling effect at high carrier concentration makes the hole mobility less sensitive to the energetic disorder, which is the parameter most responsible for the difference in the simulated hole mobility of TPA3C3M and TPA3C3PD. For devices operating at lower hole concentrations (*e.g.*, perovskite solar cell), we expect better charge transport for TPA3C3PD than for TPA3C3M.

5.3. Summary

In summary, we investigated multiarm and substituent effects in TPA-based HTMs using multi-scale simulations involving density functional theory computations, classical forcefield molecular dynamics, and kMC simulations. The effect of molecular modifications on crucial transport parameters, the reorganization energy, the energetic disorder and the transfer integrals were evaluated through electronic structure analysis, graph theory and data clustering. The reorganization energy, the energetic disorder and the transfer integrals all decrease when the number of MPCB arms is increased. Yet, the effect of reorganization energy and energetic disorder dominate the transfer integrals, which leads to an overall enhancement of the hole mobility. Despite the effectiveness of the multiarm design strategy on hole transport, the IP decreases when the number of arms is increased, which is unfavorable in terms of V_{oc}. Further optimization of the IP was then undertaken in order to retain the high mobility of TPA3C3M while maintaining the original molecular structure as much as possible to minimize changes in molecular packing. Specifically, modification of the substituents attached to carbazole arms can be used to tune the IP where values can approach the minus valance band maximum of MAPbI$_3$. However, it should be noted that this design strategy may, at the same time, result in HTMs with large molecular dipole moments (TPA3C3CN, TPA3C6CN), which may lead to significant energetic disorder and lower hole mobility. A clever choice of substituents that yields a reduced molecular dipole moment and an enhancement of mobility is TPA3C3PD. From a practical point of view, TPA3C3PD and TPA3C3CN proposed in this work are better than our initial prototypical molecule, TPA1C3M, in terms of both IP and hole mobility. Our results show that promising HTMs can be achieved by modifying each transport parameters through multiarm and substituent optimization, which can be adopted for the future design of HTMs or amorphous organic semiconductors. The simulated results show reasonable agreement with the mobility measured using FET devices for two HTMs with the highest hole mobility, which supports our computational protocols.

From a general viewpoint, the multiarm effect influences all transport parameters at the same time, where the hole mobility is a subtle interplay between these parameters. Hence, the universality of this design strategy should be further examined. However, the transfer integrals and effective lattice parameter, the multi-molecule properties, can remain nearly unchanged through minimally modifying the molecular structures. Modifying substituents thus serves as an effective and efficient strategy to further enhance the hole mobility via minimizing the molecular dipole moment (a single-molecule property). We believe that both our computational protocols and our analysis highlighted here will be useful for future work aimed at investigating the structure-mobility relationship of amorphous organic semiconductors.

5.4. Methodology

5.4.1. Computational Details

Model for amorphous morphology

The amorphous morphology was generated starting from a unit cell with 64 randomly-placed molecules using Packmol. The system was minimized using the conjugate gradient algorithm and then equilibrated in the NPT ensemble (700K, 1bar) by performing classical molecular dynamics (MD) simulation. The equilibrated system was then extended into a 2x2x2 supercell with 512 molecules followed by equilibration (700K, 1bar) for 5 ns. Equilibration in the (300K, 1bar) NPT ensemble was then performed until the density reached equilibrium (~50 ns). A final 10-ns production run generated 1000 structures (snapshots) used in the kinetic Monte Carlo simulations.

The MD simulations were performed under periodic boundary condition with the Gromacs package[226,227,228] and CGenFF[229,230] force field along with charge obtained by restrained electrostatic potential (RESP)[231] procedure based on HF/6-31G**. The temperature and pressure control were using velocity rescaling with a stochastic term[232] (τ_T = 1.0 ps) and an isotropic coupling for the pressure from a Berendsen barostat (P_0 = 1 bar, χ = 4.5 × 10^{-5} bar^{-1}, τ_P = 1.0 ps). The time step used in all simulations was 1 fs and bonds involving H atoms were constrained using the Linear Constraint Solver (LINCS) algorithm. A cutoff of 12 Å was applied to the van der Waals interaction through force-switch mode. As for electrostatic interactions, the particle mesh Ewald (PME) method was employed with a 0.12 nm Fourier spacing.

Charge transport simulations

For amorphous organic materials, the charge transport is well described by the hopping model, where a charge (electron/hole) is assumed to be instantaneously localized on one molecule (or a hopping site). The charge hopping rate between molecules can be evaluated using non-adiabatic semi-classical Marcus charge transfer theory:[75]

$$\omega_{ij} = \frac{J_{ij}^2}{\hbar} \sqrt{\frac{\pi}{\lambda k_B T}} \exp\left[-\frac{(\Delta E_{ij} - \lambda)^2}{4\lambda k_B T}\right] \tag{5.4}$$

where T is the temperature, J_{ij} is the transfer integral (sometimes referred to as electronic coupling) between the i and j sites, ΔE_{ij} is the site energy difference $E_i - E_j$ and λ is the reorganization energy. From the equation above, it is clear that high transfer integral and low reorganization energy lead to a high hopping rate between two sites, which, in turn, leads to high charge mobility. In addition to J_{ij} and λ, the spread of the site energy in an amorphous material is crucial.

The reorganization energy associated with the hole transfer process is related to the local electron-phonon coupling, which can be evaluated in two ways.[114,304] The first is the adiabatic potential energy surface method (the 4-point method), where reorganization energy is expressed as:

$$\lambda = \lambda_1 + \lambda_2 = (E_{nC} - E_{nN}) + (E_{cN} - E_{cC}) \tag{5.5}$$

where E_{nN} (E_{cC}) is the total energy of the neutral (cationic) molecule in neutral (cationic) geometry and E_{nC} (E_{cN}) is the energy of the neutral (cationic) molecule in cationic (neutral) geometry. The second method is the normal-mode (NM) analysis, which partitions the total reorganization energy into contribution from each vibrational mode. As such, the reorganization energy is expressed as:

$$\lambda = \lambda_1 + \lambda_2 = \sum_i \lambda_{1_i} + \sum_j \lambda_{2_j} = \sum_i \frac{1}{2} k_i \Delta Q_i^2 + \sum_j \frac{1}{2} k_j \Delta Q_j^2 \qquad (5.5)$$

where $\lambda_{1_i}/\lambda_{2_j}$ is the contribution to reorganization energy from the vibrational mode i/j of the neutral/cationic geometry, k_i/k_j is the eigenvalue of mass-weighted Hessian matrix of neutral/cationic molecule and $\Delta Q_i/\Delta Q_j$ represents the displacement along the ith/jth mode coordinate between the equilibrium positions of neutral and cationic states. We compute the reorganization energy using the two methods at the B3LYP[220,221]/6-31G(d,p) level with D3BJ[222] correction and Gaussian16 software[305]. The NM analysis was performed using DUSHIN and Gaussian16 in tandem.

Site energies are computed using the Thole model, where the correction terms resulting from the electrostatic and polarization effects from the environment (surrounding molecules and external electric field) are added to the HOMO of an isolated gas molecule.[137,211,306,307] The partial charges needed in this model for the neutral and cationic states were generated via CHelpG.[234] We extract the energetic disorder present in HTMs using the Gaussian disorder model, where the energetic disorder (σ) is obtained from fitting the histogram of energy difference (ΔE_{ij}) to the Gaussian distribution.[211,308]

In order to efficiently compute the transfer integral of every molecular pair ij in the neighbor list, we adopted ZINDO-based Molecular Orbital Overlapping (MOO) method.[126,309] The results obtained from this method have been shown to be in reasonable agreement with those computed at the B3LYP/6-31G(d) level.[310] We only take HOMO into consideration when evaluating transfer integral since the energy difference between HOMO and HOMO-1 is large enough (0.6~0.8 eV) for the molecules considered here. The neighbor list was established for every molecular pair having a distance between their nearest fragments within 7 Å. After all parameters defined for each hopping site and each molecular pair appear in **Equation 1** were computed, kinetic Monte Carlo (kMC) simulation was performed with 10 ms simulation time and a 10^5 Vcm^{-1} electric field. The hole mobility was determined from an average charge velocity.[306] For each molecule, 100 snapshots of an MD trajectory were taken for kMC simulations to reach better statistics. For a given MD snapshot, KMC simulations with electric field of six different directions (x, y, z, -x, -y, and -z) were conducted resulting in 600 kMC simulations for each molecule.

Molecular transport network

The connectivity of the molecular transport network was investigated based on a graph constructed for each molecule, where the vertices are the molecular centers of mass and the edges are the square of transfer integrals equal to or higher than a certain threshold value (see SI).[311] The connectivity is evaluated by examining the histogram of the number of edges (connections) of each hopping site. The

average number of edges per hopping site serves as a quantitative descriptor for the connectivity of the molecular network. The threshold values of J^2 are from 10^{-6} to 10^{-4} eV^2. For a threshold above 10^{-4} eV^2, almost all hopping sites possess 0 edge. Yet, J^2 values smaller than 10^{-6} eV^2 have a negligible contribution to the effective hole transport. The histograms for the different MD snapshots are very similar and the results shown here are thus from one MD snapshot and the total counts of a histogram sum to 512 (total number of molecules in a simulation box). For more information, please see the supporting information.

Clustering of dimer configurations

The dimer configurations of an HTM were clustered through defining a cartesian coordinate system, where each dimer configuration can be represented as a point with coordinates. The k-means clustering algorithm, which is a reasonable choice for our task,[312] was used in junction with the elbow method to find the optimal number of clusters (**Figure S10**). For more information, please see the supporting information.

Ionization potential

The ionization potentials of the solid-state amorphous HTMs were computed using a computational protocol proposed by Andrienko et. al.,[287] which has shown a good agreement between computed and experimental IPs. Correction terms based on the Thole model were added to the isolated gas phase IP to account for the solid state effect (electrostatic and induction effect from surrounding molecules). The isolated gas phase IP was computed using the ΔSCF procedure in conjunction with B3LYP functional and the 6-31G(d,p) basis set.

$$IP_{\text{solid}} = IP_{\text{iso}} + E_{\text{corr}} - 2\sigma \tag{5.6}$$

$$IP_{\text{iso}} = \Delta SCF = E_{\text{cN}} - E_{\text{nN}} \tag{5.7}$$

where $IP_{\text{solid}}/IP_{\text{iso}}$ is the ionization potential of an HTM in solid state/isolated gas phase, E_{corr} is the IP correction term from electrostatic and induction effect, σ is the standard deviation of the site energy distribution, and $E_{\text{nN}}/E_{\text{cN}}$ is the total energy of the neutral/cationic molecule in a neutral geometry.

5.4.2. Experimental Details

Hole mobility measurement

The hole mobility of TPA3C3M and TPA3C3PD was measured by field effect transistors with a bottom gate bottom contact (BGBC) configuration. The BGBC transistor substrates are purchased from Fraunhofer Institute for Photonic Microsystems. N-doped silicon wafer and a SiO$_2$ layer (230 nm) are

utilized as bottom gate electrode and dielectric layer, respectively. A 30 nm Au is applied as source and drain electrodes, and a 10 nm ITO layer is used to improve the adhesion of Au on SiO_2. The channel length (L) and width (W) of the BGBC transistor substrate are 2.5 μm and 10 mm, respectively. The substrate was washed by water, acetone and isopropanol before use. TPA3C3M and TPA3C3PD were dissolved in chloroform with a concentration of 5 mg mL^{-1}. A 50 nm thin film of TPA3C3M or TPA3C3PD was deposited on the transistor substrate by spin coating the solution at 1000 rpm. After spin-coating, the substrates were annealed at 100 °C. The current-voltage (I-V) characteristics of the transistors were measured in nitrogen glovebox using a custom-built probe station and a Keithley 2612A dual-channel source measure unit. The electron mobility of the transistors was extracted from saturation regime according to the equation:

$$\mu = 2 \left(\frac{\partial \sqrt{I_{D,sat}}}{\partial V_{GS}} \right)^2 \frac{L}{WC_i} \tag{5.8}$$

where L and W are the channel length and width, respectively. $I_{D,sat}$ is the current between source and drain electrode at saturation, and V_{GS} is the gate-source voltage. C_i (1.4×10^{-8} F cm^{-2}) is the capacity of the dielectric layer.

Synthesis of HTMs

The general synthetic information of TPA3C3M and TPA3C3PD molecules can be found in supporting information.

Chapter 6 FB-REDA: Fragment-Based Decomposition Analysis of the Reorganization Energy for Organic Semiconductors

This chapter is published as:

6.1. Introduction

Organic semiconductors based on small molecules are exploited in various optoelectronic applications owing to their well-defined chemical structures (monodispersity), low cost, flexibility and low-temperature and solution processability.[95,313] In the spirit of "molecular LEGOs,"[10,146] their properties are easily tuneable with the charge mobility being the most relevant target[262,314–319] for rational design. Relevant examples include the incorporation of hole transport materials with high hole mobility into photovoltaics or organic light-emitting diodes with low hole-electron recombination rate.[25,26,320]

Reorganization energy (λ) is one of the key parameters determining the efficiency of charge transport in both the hopping transport and the band transport (related to electron-phonon coupling term) regime.[39,321] Organic semiconductors with smaller reorganization energy (assuming the other parameters fixed) in general show a higher charge mobility.[322] Therefore, understanding the relationship between molecular structures and reorganization energy is the key to a successful rational design.[95,199]

A molecule's reorganization energy is generally computed using Nelsen's 4-point method or the normal mode (NM) analysis.[115,322,323] In order to assess the role played by each molecular building block, it is insightful to decompose the overall reorganization energy into the individual molecular fragment contribution (λ_{frag}). However, analysis tools giving direct access to the fragment contribution are still lacking. There are currently two existing analysis that serve to evaluate the atomic or fragment contributions to λ or the vibronic coupling constant (V).

The first approach, developed by Shuai, Coropceanu *et al.* based on the NM analysis, expresses the displacements along the normal modes in terms of molecular internal coordinates.[324,325] The total reorganization energy is then equal to a sum of internal coordinate contributions (see **Equation S1** in the ESI). Using this approach, the authors were able to demonstrate the influence of substituents and substitution sites on the overall reorganization energy of indolo [3,2-b]carbazole derivatives. While such an analysis tool is useful to identify the substituent leading to the lowest λ, it is less convenient to evaluate the fragment contributions to λ in a "molecular LEGOs" framework. First, the reorganization energy in the internal coordinate representation contains cross terms involving two different internal coordinates, which are not necessarily small in comparison to the square terms (see **Equation S1** in the ESI). However, there is no trivial way to divide these cross terms into internal coordinate contributions or to partition internal coordinates involving more than one fragment.

The second method developed by Sato *et. al.*, is associated with the concept of atomic vibronic coupling constant (AVCC).[326,327] They investigated the chain-length dependence of the reorganization energy for oligofluorenes and oligothiophenes by evaluating the change in local degree of vibronic coupling when increasing the length of the oligomer. Because the sum of all AVCC is equal to the total vibronic coupling constant (see **Equation S2** in the ESI), the fragment vibronic coupling constants can be defined as a sum over all the AVCC of the corresponding atoms within a fragment. However, given that the total reorganization energy is proportional to the square of the total vibronic coupling constant, the representation of λ in terms of AVCC inevitably leads to cross terms involving two different atomic vibronic constants (coupled contributions from different atoms).

This work proposes an alternative strategy to decompose the reorganization energy into local contributions. The approach is inspired by the idea of Huix-Rotllant *et al.*,[147] who decomposed the molecular normal modes in terms of local fragment modes. Instead of first decomposing λ into internal coordinates or atomic contributions, we avoid the generation of cross terms by computing the fragment contributions directly from the fragment modes. The equations and associated details are discussed in the methodology section.

As a proof of concept, we use the proposed fragment reorganization decomposition analysis to identify organic hole transport materials (HTM) with low reorganization energy. We start with TPA1PM[328] that has proved to be an efficient dopant-free HTM good for defect-passivation. The molecule (shown in **Figure 6.1 (a)**) is composed of a triphenylamine core (TPA), a phenyl-substituted carbazole arm (PCZ) and methoxy (M) substituent groups. The chosen strategy for reducing the reorganization energy is established based on the fragment-based decomposition analysis. Three molecular design approaches were successively adopted and their effects on the total hole reorganization energy (λ_{tot}) and the fragment contributions (divided into core (λ_{core}), arm (λ_{arm}) and substituent (λ_{sub}) contributions) are discussed. The three strategies are: (1) introducing multiarm, (2) non-covalent lock

and (3) core rigidification. The usefulness of the computational approach is demonstrated by the reduction by half of the reorganization energy compared to TPA1PM (from 213 to 108 meV).

6.2. Computational Details

Geometry optimization, electronic structure and frequency computations of the neutral and cationic molecules were performed at the B3LYP-[220,221]D3BJ[222] level in conjunction with the 6-31G(d,p) basis set. All DFT computations were performed with Gaussian16.[223] The NM analysis was performed using our in-house code, DUSHIN[115] and Gaussian16 in tandem.

To evaluate the validity of harmonic approximation, the reorganization energies were computed using both the 4-point method and NM analysis (**Figure S1**). Our results show that the reorganization energies obtained from these two methods are very similar, justifying the use of the harmonic approximation.

6.3. Results and Discussion

6.3.1. Analysis of TPA1PM

We first compute the reorganization energy of the parent TPA1PM molecule (211 meV) prior to its decomposition into three fragments: (1) a TPA core (Core), (2) a PCZ arm (Arm), and (3) three methoxy substituents (Sub), as shown in **Figure 6.1 (a).** The fragment reorganization energy (in meV) of the core (91), Arm (80) and Sub (40) are obtained via equation (6). The $\lambda_{\text{frag}}/\lambda_{\text{tot}}$ ratio for each fragment is represented in the pie chart (**Figure 6.1 (b)**). The core contributes the most (43.0%) to total reorganization energy. The contribution from the arm is slightly less significant (37.9%), with Sub contributing the least (19.1%).

The normal modes that are dominating the reorganization energy are plotted in **Figure 6.1 (c)** with λ_i^N /λ_j^C representing the contribution for each normal mode i and j. Given the large number of normal modes in each system, we define the spectral density $\lambda_{N/C}(\omega)$ to facilitate the analysis:[329,330]

$$\lambda_N(\omega) = \sum_i \lambda_i^N \, \delta(\omega - \omega_i) \qquad (6.1)$$

$$\lambda_C(\omega) = \sum_j \lambda_j^C \, \delta(\omega - \omega_j)$$

where ω is the vibrational frequency and the Dirac δ function is approximated by a Gaussian broadening distribution with $\sigma = 10$ cm^{-1} (**Figure 6.1 (c)**). Because $\lambda_N(\omega)$ and $\lambda_C(\omega)$ exhibit the same features and that the magnitude of λ_N and λ_C are very close (104 and 107 meV respectively) the discussion on the spectral density will focus on the neutral case $\lambda_N(\omega)$.

The 10 most contributing peaks in $\lambda_N(\omega)$ are shown in **Figure 6.1 (c)** and the composition in terms of their fragment modes is shown in **Table S1**. Overall, several fragment modes recurrently contribute to these 10 important peaks and those with $\lambda_{jk} > 1.2$ meV (10 cm^{-1}) are listed in **Table S2**. More specifically, the two most relevant fragment modes correspond to in-plane bond-stretching and angle-bending in the Core (**Figure 6.2**). Considering the fact that the Core is the largest contributor to the reorganization energy, an efficient strategy to reduce λ consist in spreading the HOMO away from the TPA core. As shown in our former work,[322] this objective can be achieved by introducing additional PCZ arms.
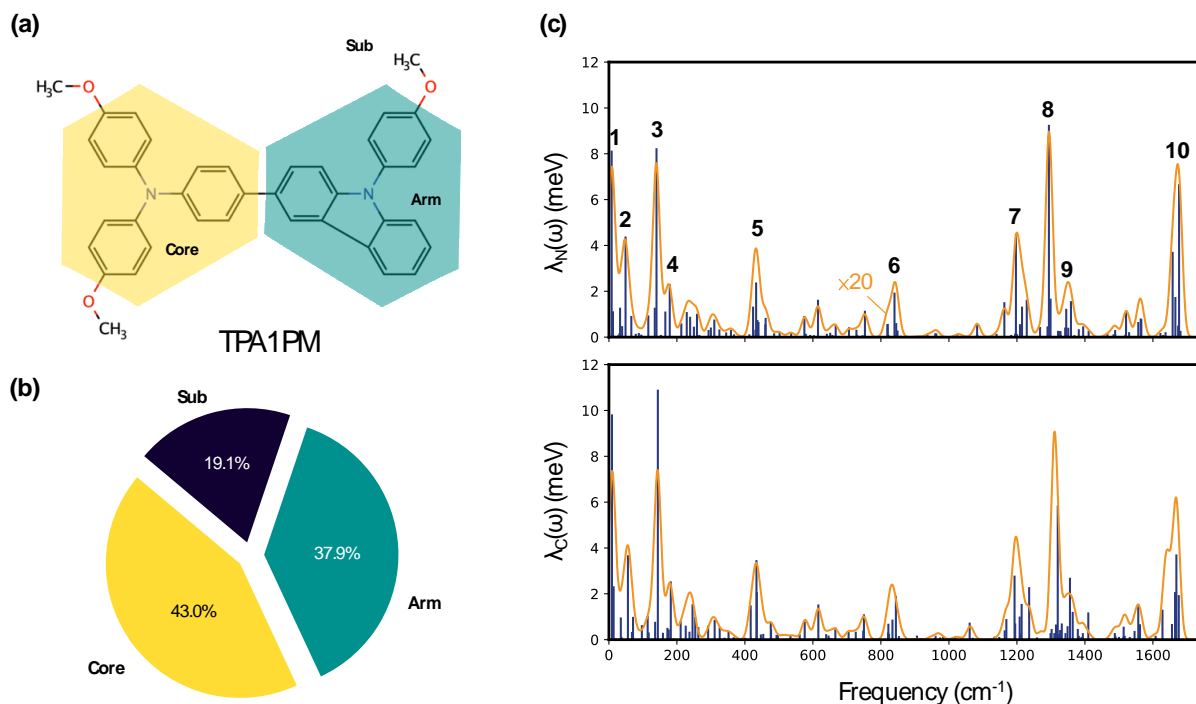
Figure 6.1 (a) Illustration of the decomposition of TPA1PM into Core, Arm and Sub fragments. (b) The ratio of the fragment to the total reorganization energy for each fragment. (c) The spectral density plot, blue lines are $\lambda_i^N / \lambda_j^C$ and orange lines are $\lambda_N(\omega)$ and $\lambda_C(\omega)$ with intensity multiplied by 20. The 10 most important peaks are indexed.

6.3.2. Introducing Multiarm

The first strategy to reduce the reorganization energy of TPA1PM is thus to increase the number of PCZ arms, as exemplified in **Figure 6.3 (a)**. Given that the methoxy groups serve as a Lewis base passivating defects in the perovskite layer,[328] the number of methoxy substituents are kept constant. They are inserted either directly on the core or on the arms depending on their number.

The design strategy is efficient as the total reorganization energy decreases by up to ~20% with increasing the number of PCZ arms, from 213, 173 to 156 meV (**Figure 6.3 (b)**). As expected, the highest occupied molecular orbitals (HOMO) spread through the PCZ arms (**Figure S2**). The contribution from Core and Sub to the HOMO (evaluated using natural atomic orbital analysis (NAO)

Figure 6.3 (c)) decreases from ~80% to ~72% for Core and from ~7% to ~0% for Sub respectively, while that of Arm increases. These trends are in line with the decrease of λ_{core} and λ_{sub}, which contrasts with the λ_{arm} increase from 80 to 101 meV. Overall, it is clear that the redistribution of the HOMO is the dominant factor affecting λ and that the largest contribution comes from the arms **Figure 6.3 (d)**.

7.85 meV   4.10 meV
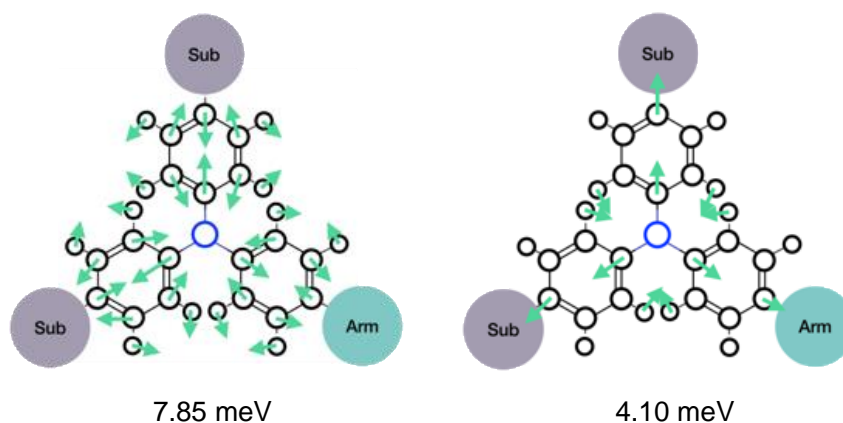
Figure 6.2 Illustration of the two most contributing fragment modes and their corresponding fragment reorganization energies in TPA1PM.

The spectral density of the Total, Core, Arm and Sub contribution plotted in **Figure 6.3 (e)** illustrates how does the number of arms alter the fragment contribution. The overall features of $\lambda_{tot}(\omega)$ are very similar for the three molecules with the exception of an additional peak (marked with*) appearing in the low frequency range of the TPA3PM spectrum, (composition shown in **Table S3**).

The 1st peak originates from three degenerated (by symmetry) Arm fragment modes, featuring inter-fragment rotation between each Arm and the TPA Core (see **Figure 6.4 (a)**). As the number of arms increases, a larger number of "arm" atoms contribute to the normal mode, leading to a larger ΔQ_i^N. Yet, the eigen frequency of this mode changes negligibly upon the addition of arms, leading to a larger λ_i^N in line with **Equation 2.25**. Except for the first peak, the intensity of nearly all peaks decreases as the number of arm increases. The 5th and 6th peaks that remain unchanged between TPA1PM and TPA3PM constitute another exception.

Unsurprisingly, the decrease of most peaks in $\lambda_{tot}(\omega)$ comes from the fact that the relevant normal modes involve the Core and Sub fragments whose contribution is reduced. The main fragment modes present in the unchanged 5th and 6th peaks feature an out-of-plane torsion of benzene rings (**Figure 6.4 (b)**) that
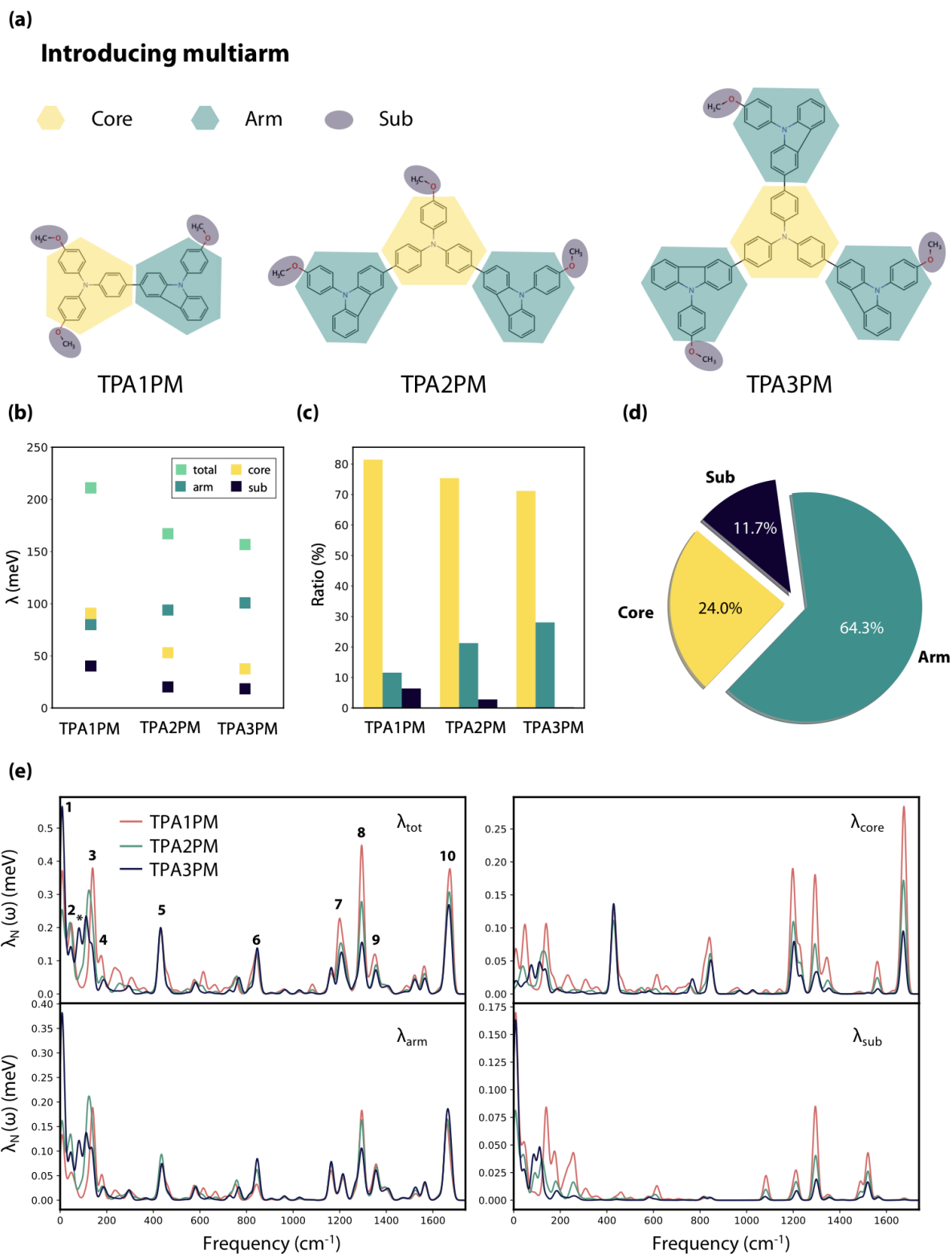
Figure 6.3 (a) The TPA1PM, TPA2PM and TPA3PM molecules and their fragments. (b) Total reorganization energy, fragment reorganization energy, (c) contribution to the HOMO from the NAO analysis and (d) the ratio of λ_{frag} to λ_{tot} of each fragment. (e) Spectral density plots for λ_{frag} and λ_{tot} for TPA1PM, TPA2PM and TPA3PM.

negligibly change across the TPA1PM to TPA3PM series. The multiarm strategy is thus unable to efficiently reduce the vibronic coupling caused by this modes.

The fragment modes with $\lambda_{jk} > 1.2$ meV (10 cm^{-1}) for TPA3PM (given in **Table S4**) show that the two most important contributions comes from the Arm and Sub fragments and correspond to inter-fragment rotational motions (**Figure 6.4 (a,c)**). Interestingly, both these modes are present in the 1st peak via their coupling with the Arm and Core rotations around the C-C bridging bond. These results suggest that freezing the relative rotational motion between the Core and the Arm can further reduce λ by elimination of the 1st peak. Taking TPA3PM as our new starting point, the second strategy is thus to quench this inter-fragment rotational motion by introducing "non-covalent locks" that force the planarity between the benzene in the TPA Core and the carbazole in the PCZ Arm.[331] We expect that locking the out-of-plane mode will partially eliminate the contribution from the 1st peak (see next section).
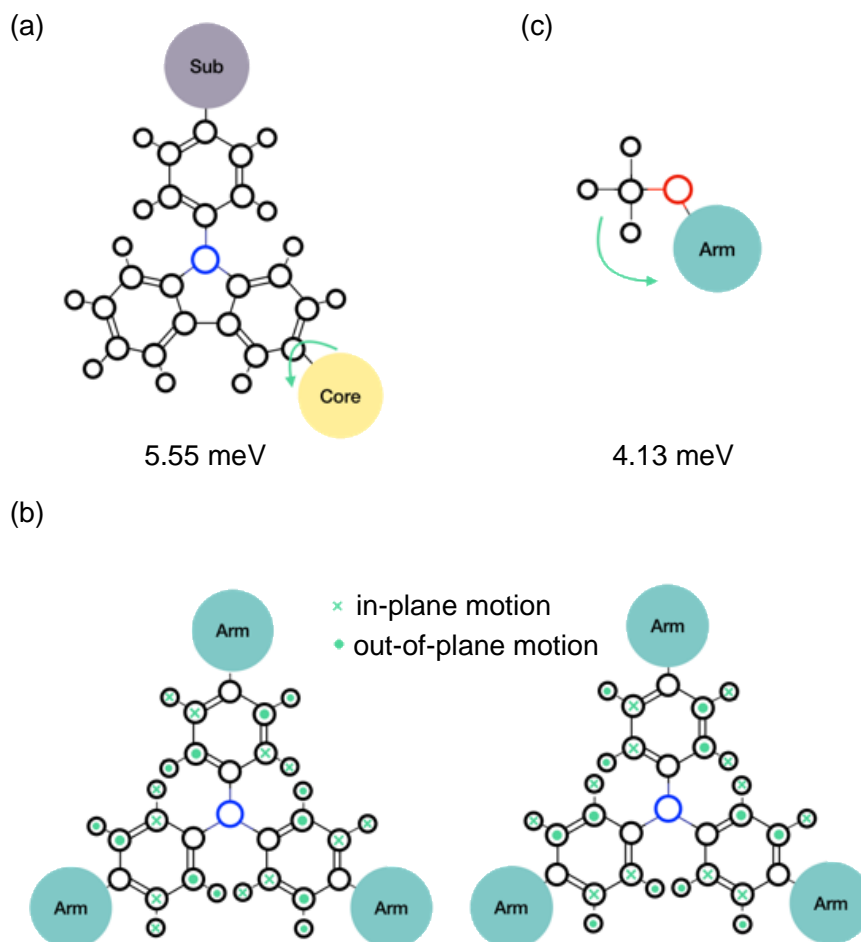
Figure 6.4 Illustration of (a) the inter-fragment rotational modes present in the 1st peak and (b) the two dominant Core fragment modes present in the 5th and the 6th peak of TPA3PM. (a,c) The two most contributing fragment modes in TPA3PM.

An alternative strategy consists in reducing the contribution from the 5th and 6th peaks that are not affected by the number of arms. As discussed previously, the corresponding Core fragment modes

correspond to an out-of-plane torsion in three benzene groups (**Figure 6.4 (b)**). This type of vibrational motion can be significantly restricted by introducing covalent bond between nearby benzene moieties. An example would be to substitute TPA by PCZ or indolo[3,2,1-jk]carbazole moiety (ICZ). This alternative will be discussed in the "Core Rigidification" section.

6.3.3. Non-covalent Lock

The non-covalent locks are introduced to restrict the inter-moiety rotational motion between the Core and Arm in order to further reduce λ. In **Figure 6.5 (a)**, the benzene rings of the core are replaced by 1 or 3 pyrimidine rings able to form 2 pairs of N$\cdots$H noncovalent interaction for each pyrimidine-carbazole pair.

The total reorganization energy decreases with increasing the number of pyrimidine in the Core (MPD3PM and TPD3PM), from 156, 144 to 108 meV (**Figure 6.5 (b)**). A further ~31% reduction in reorganization energy is achieved, demonstrating the efficiency of this strategy. The overall fragment contributions, λ_{core}, λ_{arm} and λ_{sub} decrease with increasing the number of pyrimidine. By restricting the contribution to the first peak, one expects the reduction in λ_{arm} and λ_{sub}. However, λ_{core} also decreases from 36, 35 to 30 meV. Since all the fragment reorganization energies decrease, the λ_{frag} to λ_{tot} ratio for each fragment of TPD3PM does not change significantly compared to TPA3PM (**Figure 6.5 (c)**). The arms are still the largest contributors (62.9%) followed by Core (28.3%) and Sub (8.8%).

The spectral density in **Figure 6.5 (d)** provides several explanations to the observed trends: first, the 1st peak indeed decreases with increasing the number of pyrimidine and almost disappear in the TPD3PM spectra of $\lambda_{tot}(\omega)$, $\lambda_{arm}(\omega)$ and $\lambda_{sub}(\omega)$. Interestingly, the 2nd peak, although less intense, follows a similar trend. The fragment mode analysis indicates that the 2nd peak contains an arm-based fragment modes associated with inter-moiety bending motions (**see Table S3**). Those are also being restricted by the non-covalent locker.

Finally, the unexpected decrease in λ_{core} is shown to essentially arises from the significant reduction of the 5th peak (in $\lambda_{core}(\omega)$). As mentioned earlier, the 5th peak of TPA3PM is dominated by the benzene out-of-plane torsion. When the pyrimidine rings are introduced, the motion is attenuated by the intramolecular non-covalent interactions, (**Figure 6.6**). The 5th peak of $\lambda_{arm}(\omega)$ follows a very similar trend to that of $\lambda_{core}(\omega)$ owing to the key Arm fragment mode featuring analogue out-of-plane torsional motion of the carbazole in the PCZ Arm, as shown in **Table S3**. This movement is also restricted by the non-covalent locks (**Figure 6.6**).

Overall, this section demonstrates that the non-covalent lockers reduce the contribution from the fragment modes dominated by out-of-plane inter-moieties motions involving the Core and Arm fragments. This strategy can be applied to other systems. For instance, Malagoli and Brédas showed that the reorganization energy of N,N,'-diphenyl-N,N'-bis(3-methylphenyl)-(1,1'-biphenyl)-4,4'-diamine
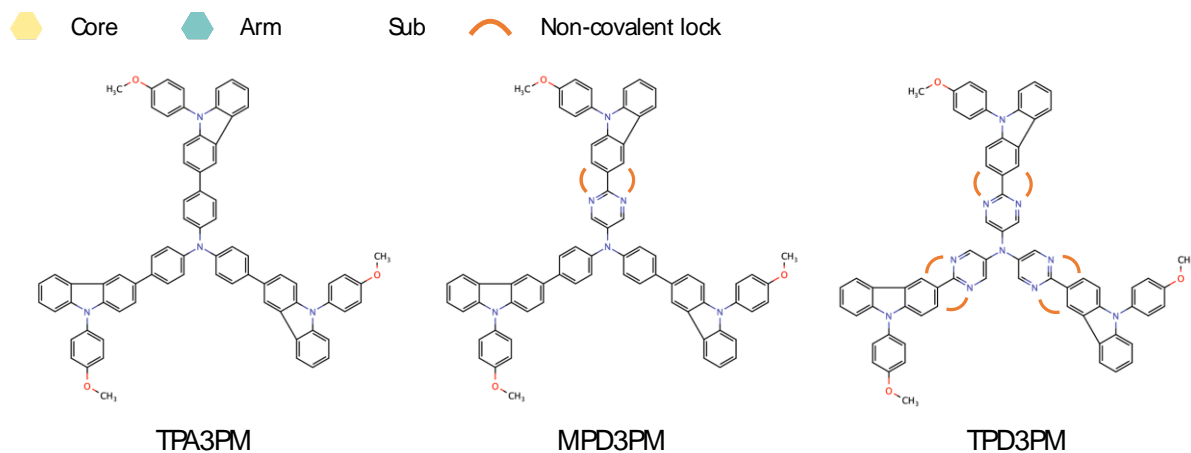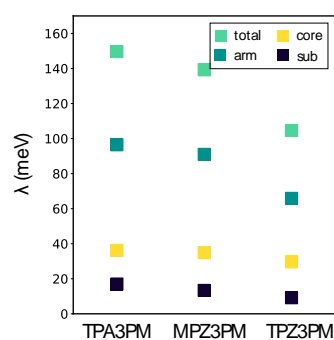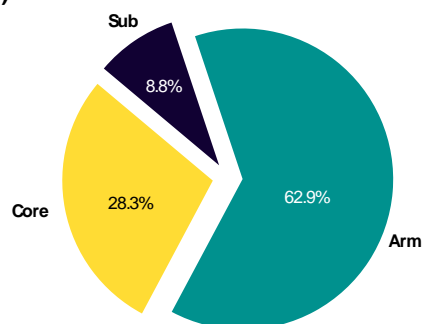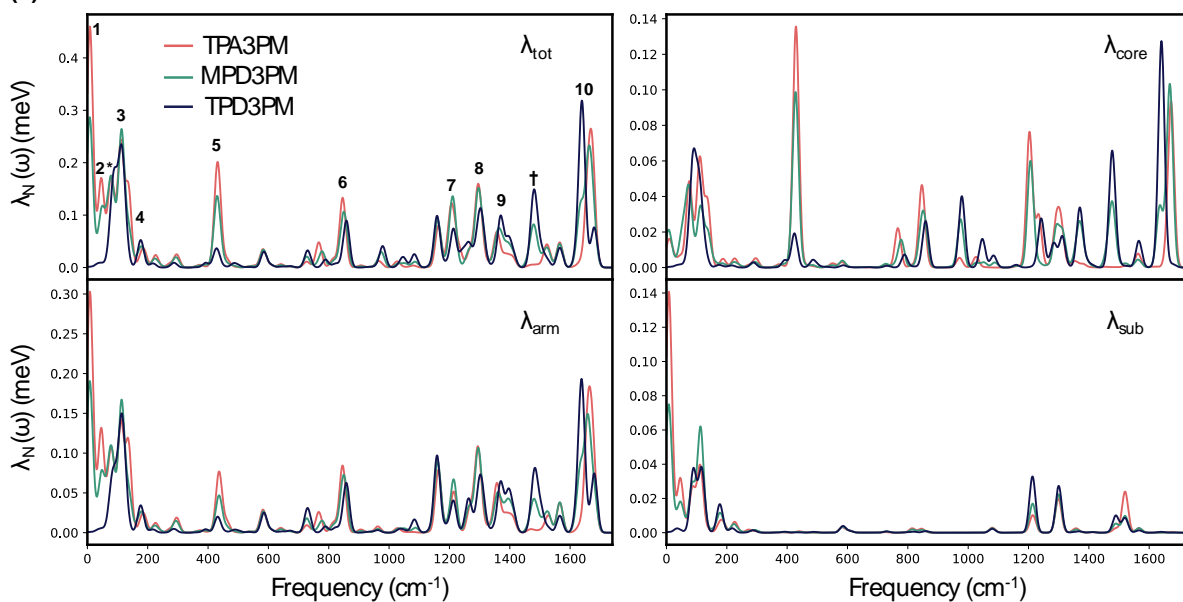
Figure 6.5 (a) The TPA3PM, MPD3PM and TPD3PM molecules and their fragments. (b) Total reorganization energy, fragment reorganization energy, (c) the ratio of λ_{frag} to λ_{tot} of each fragment, and (d) Spectral density plots for λ_{frag} and λ_{tot} for TPA3PM, MPD3PM and TPD3PM.

(TPD), a widely used hole transport material for organic light-emitting diodes, is more than twice of that of its monomer (TPA).[61] They found that λ of TPD is dominated by the central biphenyl fragment, which may be due to the huge change in the inter-ring dihedral angle between neutral and cation ground state geometry. We anticipate the reorganization energy of TPD to be largely reduce upon introduction of non-covalent locks between the two phenyl groups.

Core fragment mode
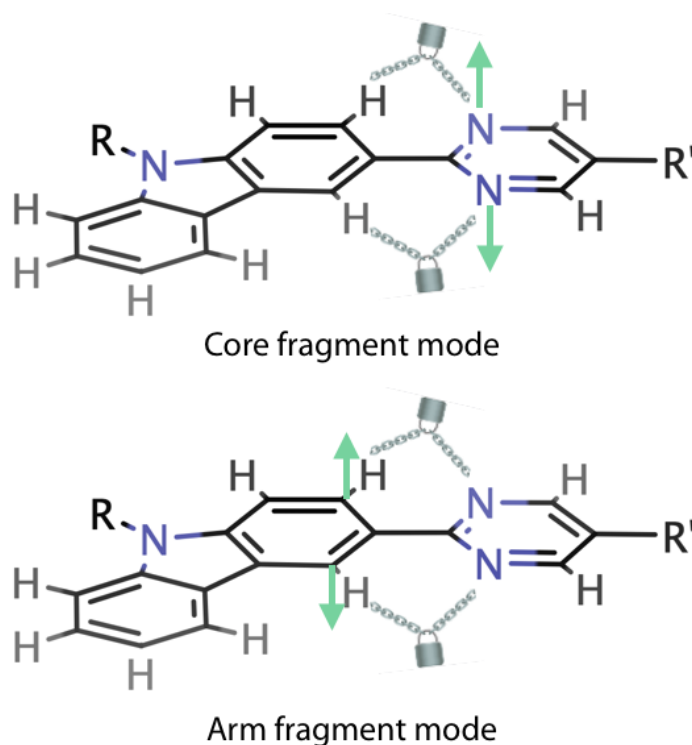
Arm fragment mode

Figure 6.6 The fragment modes of TPD3PM features out-of-plane torsions involving atoms in the non-covalent interaction pairs (only the motion of non-H atoms near the non-covalent interaction pairs is shown with the green arrows).

6.3.4. Core Rigidification

As mentioned in the "Multiarm" section, the alternative strategy to reduce the reorganization energy of TPA3PM is to restrict the out-of-plane torsion of the benzene moieties in the TPA Core. To achieve this goal, the core can be "rigidified" by introducing covalent bonds between the neighboring benzene moieties transforming TPA into to a PCZ (1 bond) or a ICZ Core (2 bonds) shown in **Figure 6.8 (a)**.

Overall, the core rigidification is relatively efficient and leads to up a 28% reduction in total reorganization energy from 156 to 112 meV (**Figure 6.8 (b)**). As expected, the value of λ_{core} goes down but more surprisingly λ_{arm} and λ_{sub} also decreases upon replacement of TPA by ICZ. Given that the reorganization energy of every fragment decreases, the λ_{frag} to λ_{tot} ratios of TPD3PM is very similar to those of TPA3PM (**Figure 6.8 (c)**).

The spectral density of $\lambda_{tot}(\omega)$ and $\lambda_{core}(\omega)$ (**Figure 6.8 (d)**) indicates that the intensity of the 5th and 6th peaks decreases from TPA to ICZ. In addition, the * and 3rd peaks in $\lambda_{core}(\omega)$ decreases upon core-rigidification. Since their dominant Core modes involve relative motions between the TPA benzene rings (**Figure 6.7**), it is not surprising that the contribution from these modes is attenuated by the core-rigidification.

The unexpected decrease in λ_{arm} and λ_{sub} originates from the reduced contributions in the low-frequency region, $\omega < 200$ cm^{-1}. In the case of $\lambda_{arm}(\omega)$, this region features relative motions (rotational and translational) between Arms and Core shown in **Table S3**. Given that ICZ3PM undergoes less geometrical reorganization in relevant internal coordinates (defined in **Figure S3**) upon oxidation, ΔQ and thus the reorganization energy are smaller (see **Table S5**). The 1st peak in $\lambda_{sub}(\omega)$ decreases upon binding covalently the benzene rings because of the smaller dihedral angle change between the Core and Arm in ICZ3PM, which cause the reduction of the contribution from the Sub rotational modes to which they are coupled (*vide supra*).
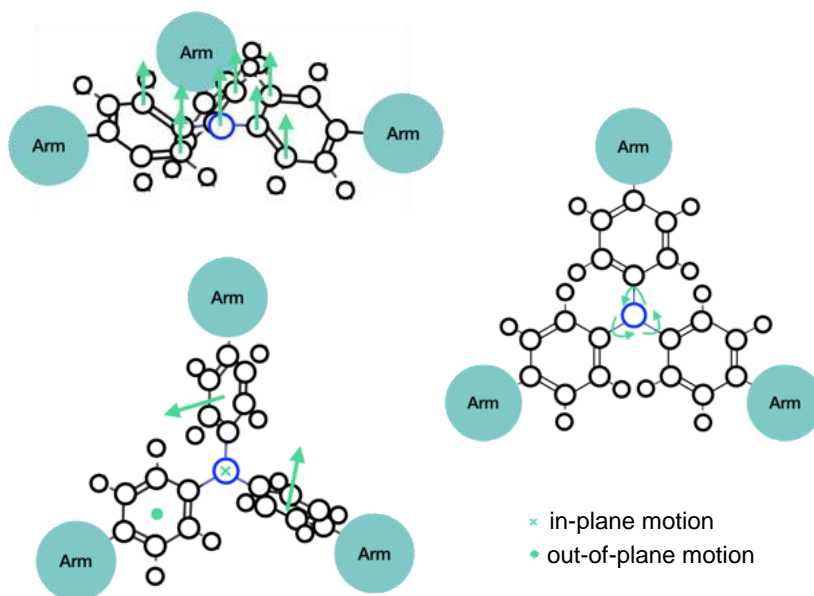
Figure 6.7 The main Core fragment modes of TPA3PM present in the * and the 3rd peaks.

This section demonstrated that ICZ is a promising building block in organic semiconductors if the goal is to lower the reorganization energy. Interestingly, a recent work by Jiang, Wang and collaborators concluded that perovskite solar cells exploiting ICZ-based HTMs exhibited outstanding performance.[332] As a building block, the use of the ICZ core is, however, scarce and our work calls for a more systematic analysis of the performance of HTMs for PSCs involving this core fragment.
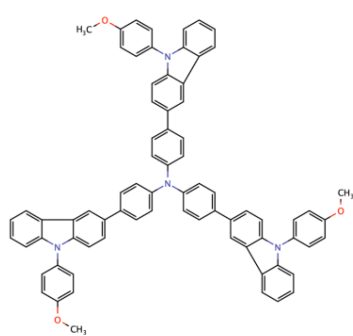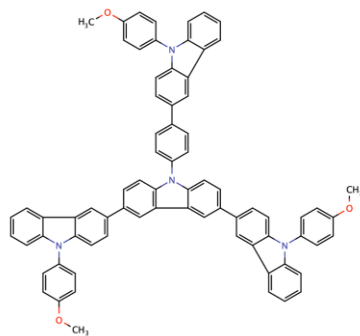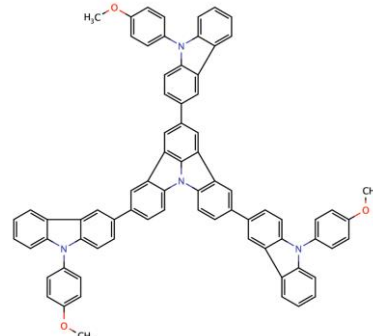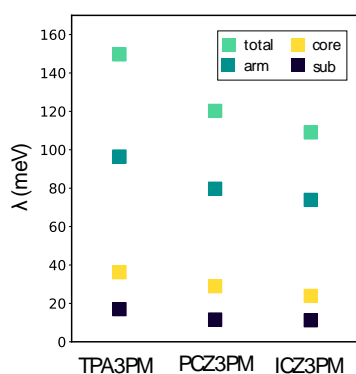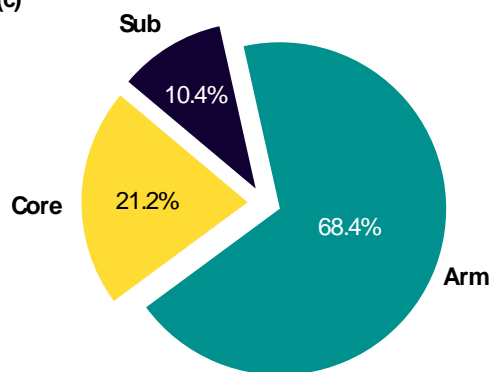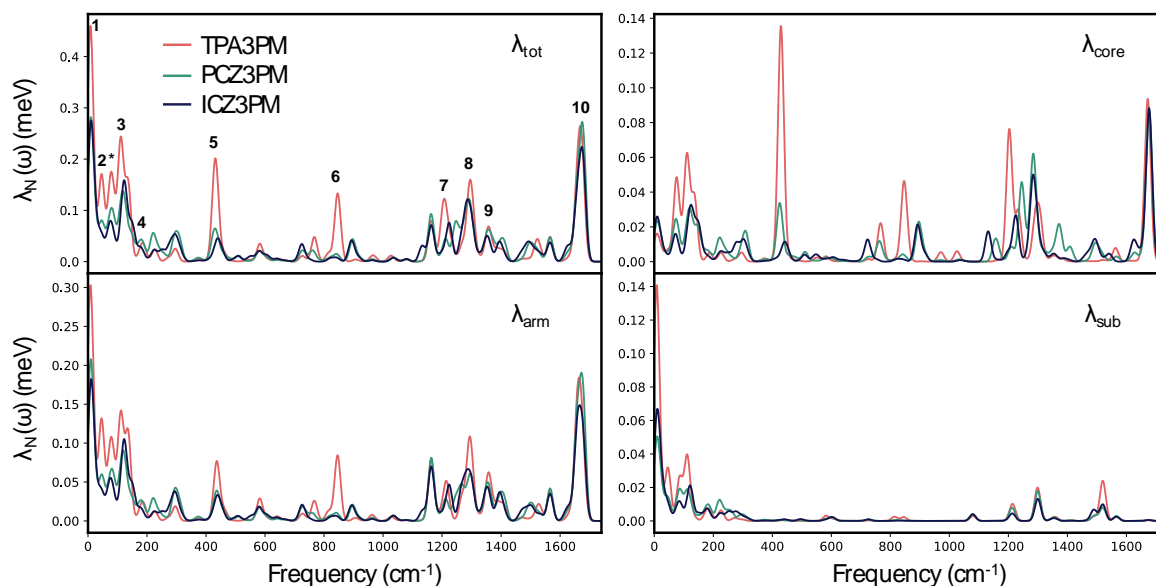
Figure 6.8 (a) The TPA3PM, PCZ2PM and ICZ3PM molecules and their fragments. (b) Total reorganization energy, fragment reorganization energy, (c) the ratio of λ_{frag} to λ_{tot} of each fragment, and (d) Spectral density plots for λ_{frag} and λ_{tot} for TPA3PM, PCZ3PM and ICZ3PM.

6.4. Conclusions

We developed a fragment-based decomposition analysis tool for the reorganization energy and demonstrated its usefulness by rationally designing low λ organic HTMs. Starting from the promising dopant-free TPA1PM HTM composed of triphenyl amine and carbazole building blocks, three design strategies were adopted to lower the reorganization energy of TPA1M (λ= 213 meV): multiarm, non-covalent lock, and core rigidification. The introduction of multiple arms reduces λ by extending the π-conjugation away from the core. The lower λ of TPA3PM (156 meV) originates from diminishing the contributions from the TPA core that arises from two types of modes: (1) the Arm/Core rotational motions around the C-C bridge and (2) the out-of-plane torsions of the core benzene rings. We attenuated the former by introducing non-covalent locks at the Core and Arm bridging point. The intramolecular non-covalent interactions constrain the reorganization of the nuclei, which allows for a ~31% reduction in the λ of TPD3PM (108 meV). On the other hand, the out-of-plane motion of the benzene rings is constrained by the insertion of covalent bonds between the benzene rings, which leads to a nearly 28% decrease in λ (ICZ3PM, 112 meV). Given the extensive use of triphenylamine and carbazole building blocks in organic semiconductors, we expect the two types of aforementioned fragment modes to largely contribute to their organization energies. For this reason the proposed strategies should be transferable to a variety of systems, such as, for instance, TPD (a common HTM for organic light emitting diodes). As such, we believe that the precise insight brought by our computational analysis tools has significant potential for facilitating and accelerating the search for novel low-λ organic semiconductors.

Chapter 7 FB-ECDA: Fragment-Based Electronic Coupling Decomposition Analysis for Organic Amorphous Semiconductors

7.1. Introduction

The versatility of synthetic organic chemistry offers possibilities of tailoring organic materials for specific applications. Within this context, amorphous organic semiconductors have attracted tremendous attention, especially in the field of energy-related applications and optoelectronic devices.[39,95,333–337] The amorphous nature of these materials enables fabrication of homogeneous large-scale thin films, which is beneficial for commercialization.[338] However, their disordered molecular packing usually results in much lower charge mobilities as compared to those of the organic crystals counterpart. In most applications; charge mobility is in fact one of the most important target properties as it significantly influences the performance of the devices. [339,340] Instead of boosting the charge mobility of amorphous organic semiconductors over those of crystalline ones, massive efforts have been generally placed into searching amorphous materials featuring excellent film-forming ability and reasonable charge mobility ($10^{-4} - 10^{-3}$ cm^{2}V^{-1}s^{-1}).[26]

Understanding the structure-packing-property relationships (SPPR) help accelerating the discovery pace of promising organic molecules.[33] Despite recent efforts in the field,[203,336,341] our understanding is still very limited and few effective rational design strategies are adopted. One reason for this limitation is the complex charge transport behavior resulting from the disordered molecular packing. This complexity prevents the direct experimental probing of the distribution of charge transport parameters, reorganization energy (λ), electronic coupling (V), site energy (E), and individual molecular conformation.[342] Instead, effective parameters for the whole morphology are extracted by performing numerical fitting of charge mobility data using phenomenological model (*e.g.*. Gaussian disorder model),[342] leading to obscure SPPR.

Conveniently, multiscale simulation protocols and toolkits enables molecular level investigations of charge transport phenomenon in amorphous organic materials[40–44] that lead to insightful SPPR.[8,45,287,343,344] Our own work constitutes a relevant example in which we established SSSR for

HTMs incorporated into perovskite solar cells between molecular modifications (hetero atoms, alkyl chain length and multiarm effect) and charge transport parameters.[322,345,346]

Common design strategies for functional organic materials involve combining various molecular building blocks with desirable properties.[143–145] This approach relies on understanding the evolution of the target properties based on the individual molecular building blocks and on the molecule as a whole.[10,146] However, tools for decomposing the charge transport parameters into the individual contributions from the building blocks are still lacking. The concept of fragment(local) decomposition analysis has provided useful insights and has been widely adopted for evaluating various quantities such as molecular orbital analysis,[48] functional group symmetry-adapted perturbation theory[49,50] and fragment-based excited-state analysis.[51] Within the context of molecular design, we recently developed a fragment-based reorganization energy decomposition analysis (FB-REDA) scheme and demonstrated its usefulness for the rational design of potential low-λ organic semiconductors.[347] This work extends our scope from the reorganization energy to the electronic coupling and introduces the fragment-based electronic coupling decomposition analysis (FB-ECDA).

As a proof of concept, we demonstrate that FB-ECDA provides new insight into the SPPR of organic semiconductors, especially useful for disordered systems. We investigate the hole transport properties of two series of molecules (shown in **Figure 7.1**). We first focus on a triphenylamine core (TPA) and a 9-(4-methoxyphenyl)-9H-carbazole arm (PCZ) (*i.e.*, 1ARM)[328] and gradually increase the number of PCZ arms attached to the central TPA core from 1 to 2 (2ARM) and 3 (3ARM). The second series starts from another HTM (BEN)[348] composed of two PCZ arms and a benzene core. The acene core length is extend from benzene to anthracene (ANT) and pentacene (PEN). Combining molecular transport network analysis (graph theory), percolation theory and FB-ECDA, we show that the relative size and nature of the conjugated building blocks has a large impact on their contributions to the network properties of total electronic coupling.

7.2. Methodology

For the methodology of FB-ECDA, please refer to **Section 2.4.2.**

7.2.1. Molecular Transport Network

The molecular transport network of amorphous morphology is investigated based on a graph constructed for each compound, where the vertices are the molecular centers of mass and the edges are the electronic couplings equal to or higher than a certain threshold value V_{th} (see SI).[311]

The percolation curve is constructed based on the established graph. For each V_{th}, we searched for the largest cluster present in the morphology, in which each node is at least connected by one other node. The function ρ is defined as the ratio of the size of the largest cluster to the size of the whole system

(512 nodes in our case). The ρ-log$|V_{th}|$ plot is the so-called percolation curve, which usually exhibits a characteristic step-like behavior indicating a distinct transition at a certain threshold value V_p (percolation threshold). Conventionally, the V_p is defined as the point where ρ reaches 0.5. In addition to V_p, we define the onset of percolation (V_{on}) as ρ reaches 0.05, corresponding to a stage where the largest connected cluster is composed of 25 nodes (molecules).

Multi-arm Effect

| 1ARM | 2ARM | 3ARM |

Core-length Effect

| BEN | ANT | PEN |
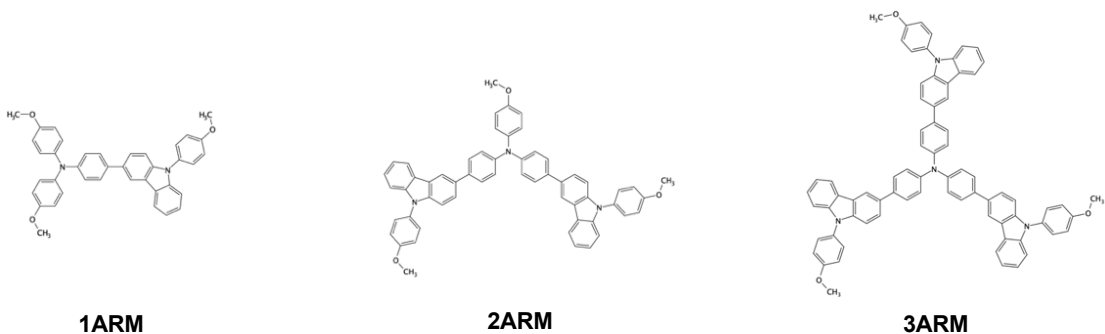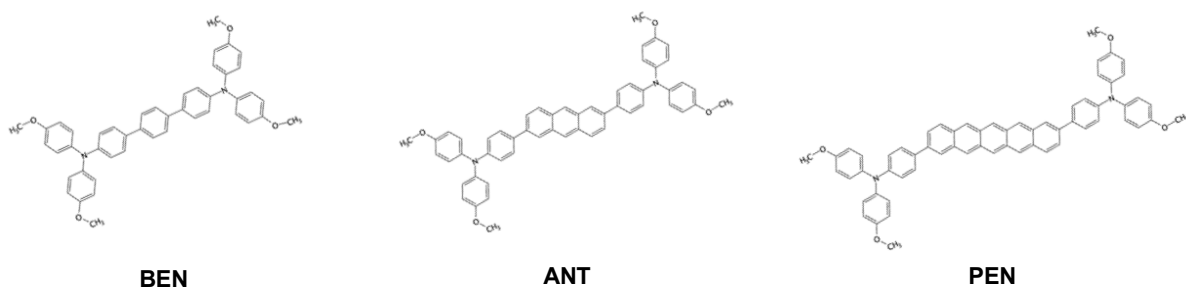
Figure 7.1 Two series of molecules investigated in this work. The blue circles represent the core units and the green ones represent arm units.

7.2.2. Composition Analysis of Dimer Configurations

Since the largest connected network (molecular cluster) present at the percolation threshold is of great importance, understanding the corresponding dimer configurations of edges linking the nodes within the cluster provides useful insight for future molecular design. For each edge (electronic coupling), we constructed a n×n matrix **V** and the matrix element V_{ij} is defined as:

$$V_{ij} = V^{eff}_{\text{fragi,A}-\text{fragj,B}} \tag{7.1}$$

where $V^{eff}_{fragi,A\text{-}fragj,B}$ is the electronic coupling between i[th] fragment of molecule A and j[th] fragment of molecule B and n is the number of fragments. This matrix represents an unique fingerprint for the dimer, where we can classify the dimer configurations. For details of classification, please see **Section 7.5**.

7.2.3. Computational Details

The computation of electronic coupling and fragment-based electronic coupling decomposition analysis are performed using ZINDO method with Gaussian16 in tandem with our in-house code to effectively evaluate electronic couplings of thousands of dimers.[223] The trends obtained from ZINDO method have been shown to be in reasonable agreement with those computed at the B3LYP/6-31G(d) level.[310]

The simulated amorphous morphology of molecules in multiarm series are taken from our previous work.[322] For molecules in acene series, their morphologies were generated starting from a unit cell with 64 randomly-placed molecules using Packmol. The system was minimized using the conjugate gradient algorithm and then equilibrated in the NPT ensemble (700K, 1bar) by performing classical molecular dynamics (MD) simulation. The equilibrated system was then extended into a 2x2x2 supercell with 512 molecules followed by equilibration (700K, 1bar) for 5 ns. Equilibration in the (300K, 1bar) NPT ensemble was then performed until the density reached equilibrium (~50 ns), where the last MD snapshot was used for FB-ECDA analysis. The dimers used for further analysis are chosen that the shortest distance between two monomers are within 0.7 nm. For monomers far away from each other are less important in contributing charge transport. The MD simulations were performed under periodic boundary condition with the Gromacs package[226,227,228] and GAFF force field[349] along with charge obtained by AM1-BCC method.[350,351] The temperature and pressure control were using velocity rescaling with a stochastic term[232] (τ_T = 1.0 ps) and an isotropic coupling for the pressure from a Berendsen barostat (P_0 = 1 bar, χ = 4.5 × 10^{-5} bar^{-1}, τ_P = 1.0 ps). The time step used in all simulations was 1 fs and bonds involving H atoms were constrained using the Linear Constraint Solver (LINCS) algorithm. A cutoff of 12 Å was applied to the van der Waals interaction through force-switch mode. As for electrostatic interactions, the particle mesh Ewald (PME) method was employed with a 0.12 nm Fourier spacing.

7.3. Results and Discussion

7.3.1. Multiarm Effect

We recently investigated the multiarm effect on each charge transport parameter and computed the hole mobility for these three molecules. The fragment contributions to the reorganization energy were analyzed using our FB-REDA decomposition scheme, which showed that introducing more arms reduces λ_{core} at the cost of increasing λ_{arm}. Following our former fragment definition, TPA and PCZ are assigned as the core and arm units, respectively. Accordingly, there are 4 (2×2), 9 (3×3), and 16 (4×4) V_{F1F2} terms for 1ARM, 2ARM and 3ARM, respectively. By symmetry, the fragment-fragment electronic coupling reduce to 3 quantities:

$$V_{CC} = V_{coreA-coreB}^{eff} \tag{7.2}$$

$$V_{CA} = \sum_i (V_{coreA-\mathrm{armB},i}^{eff} + V_{coreB-\mathrm{armA},i}^{eff})$$

$$V_{AA} = \sum_{ij} V_{armA,i-\mathrm{armB},j}^{eff}$$

$$V_{tot} = V_{CC} + V_{CA} + V_{AA}$$

where V_{tot} is the sum of the three fragment-fragment electronic coupling terms.

The probability distribution function (PDF) of the electronic coupling terms shown in **Figure 7.2** summarizes the sensitivity to the multiarm effect. Upon increasing the number of PCZ arms, the PDF of V_{tot} is slightly right-shifted to low-V region, which essentially results from the opposite PDFs trend of V_{AA} and V_{CC}, which are a direct consequence of the change in molecular packing. The steric hinderance brought by the additional arms increases, preventing close contact between the cores (**Figure S7.1**). Simultaneously, the probability of finding dimers with small arm-arm distance (D_{AA}) increases. Since V decays exponentially with the intermolecular distance, the trend of the inter-fragment distance (D_{CC} and D_{AA}) explains well the evolution of the electronic coupling terms.
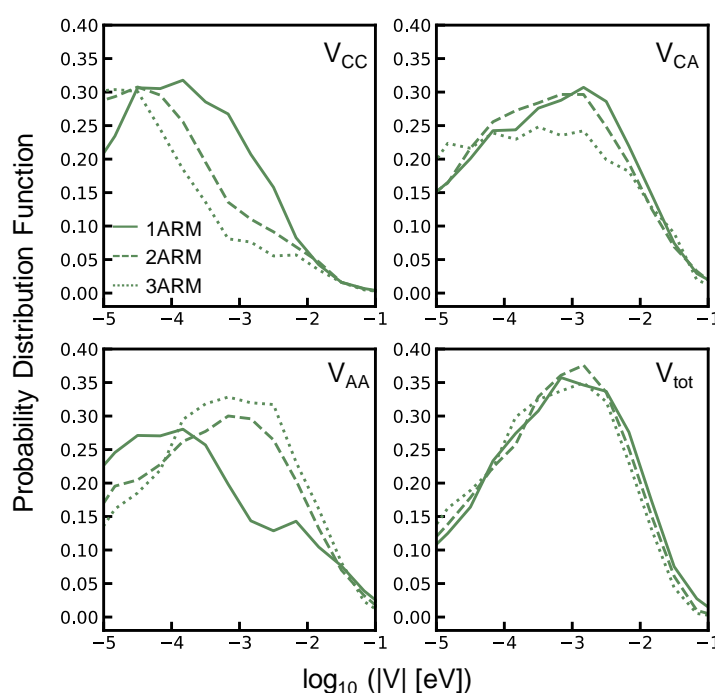
Figure 7.2 The probability distribution functions of $\log_{10}(|V_{CC}|)$, $\log_{10}(|V_{CA}|)$, $\log_{10}(|V_{AA}|)$ and $\log_{10}(|V_{tot}|)$ for 1ARM, 2ARM and 3ARM.

The PDF of D_{CA} (**Figure S7.1**) similar to that of V_{CA}, shows only little variation upon increasing the number of arms. This is somewhat counter-intuitive considering that the V_{CA} of 3ARM is a sum over the contributions from 6 core-arm pairs vs 2 for 1ARM. 3ARM should thus exhibit a higher V_{CA}, which

is not the case (**Figure 7.2**). The reason behind is the electronic structure: the HOMO expands through the arms causing the expansion coefficient of each arm and hence the individual $V^{eff}_{coreA\text{-}armB,i}$ and $V^{eff}_{coreB\text{-}armA}$, terms to decrease accordingly.

While the PDF of the electronic coupling is an insightful statistical metric to analyze the couplings present in the morphology, it does not provide information on the transport network linked to the charge dynamics. The role of the molecular transport network is revealed using graph theory: a graph constructed from vertices represented by the molecular centers of mass and edges being the electronic couplings. Among the various information extractable from this graph, the percolation curve and the critical percolation threshold (V_p) occurring in a given transport network (see **Section 7.2.1** for more details) are the most relevant.

(a) (b)
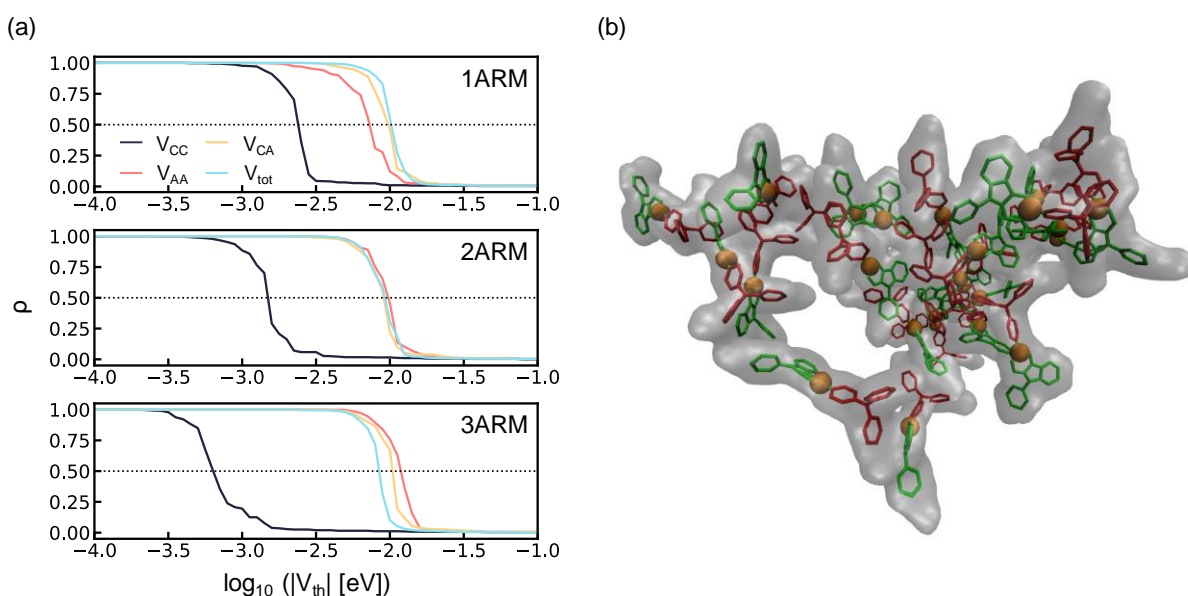
Figure 7.3 (a) Percolation curves of 1ARM, 2ARM and 3ARM based on graphs constructed using $\log_{10}(|V_{CC}|)$, $\log_{10}(|V_{CA}|)$, $\log_{10}(|V_{AA}|)$ and $\log_{10}(|V_{tot}|)$ and (b) the largest connected molecular cluster at the onset of percolation for graph based on V_{CA} of 1ARM. The green and red bonds represents the PCZ arm and the TPA core, respectively, while the orange sphere and gray surface represents the geometrical center and VDW surface of each molecule (node).

The percolation curves of the electronic coupling terms (**Figure 7.3 (a)**) show that the V_{CC} is significantly affected by the addition of arms (*i.e.*, V_p becomes smaller). The trend is opposite for V_{AA} and V_p remains nearly unchanged for V_{CA}. Across the series, the critical percolation threshold for V_{tot} decreases slightly, which indicates a decay in the charge transport due to a reduction of the molecular transport network. This trend correlates well with the PDFs, suggesting that the arm-arm contribution increases at the cost of reducing the core-core contribution. Note however that these two sets of trends (PDF and percolation curve) are not rooted in the same phenomenon:[352] the percolation curves account

for the spatial (network) information thus providing a more complete assessment of the electronic coupling contribution to the charge mobility.
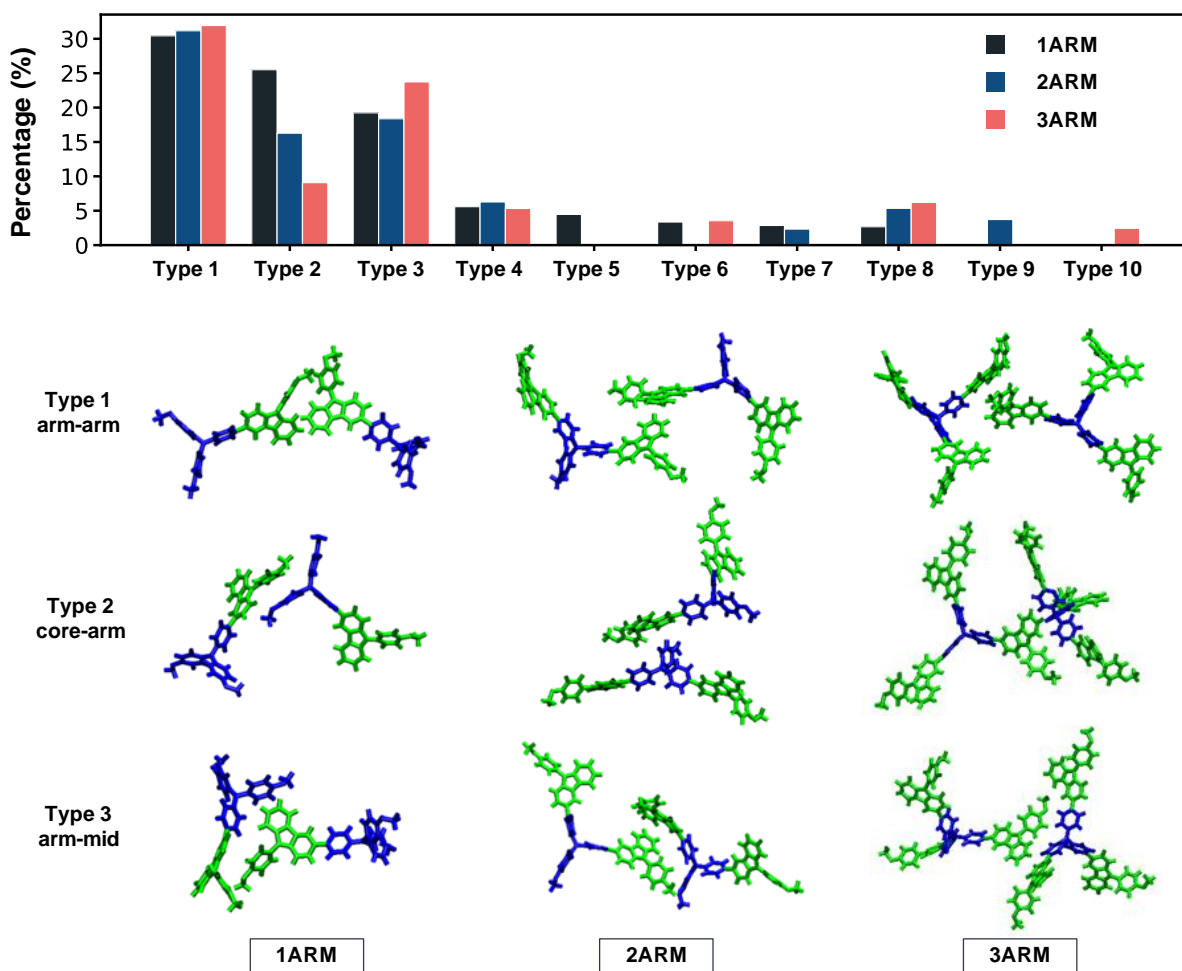
Figure 7.4 The bar plot showing the percentage of different types of dimer configurations present in the largest cluster at percolation threshold and the representative dimer configurations of type 1, type 2 and type 3 for 1ARM, 2ARM and 3ARM. The green and blue bonds represents the PCZ arm and the TPA core, respectively. The gray shaded area is a guide to the eye.

Another relevant feature is observed for V_{CA}, for which the V_p is recurrently high. In particular, V_{CA} is the key contributor to 1ARM. In the high-V_p limit for V_{F1F2}, most nodes (molecules) in the largest cluster would arrange themselves such as to have a close F1-F2 contact. In an amorphous or disordered morphology, not surprisingly, the core-to-arm (or head-to-tail, see **Figure 7.4**, Type 2) packing is the most common. For the graphs based on V_{CC} or V_{AA}, the high-V_p situation is more likely achieved in an ordered molecular packing, *e.g.*, columnar-like stacking (**Figure S7.4**).

The percolation curves based on V_{CC} is reflective of the influence of the chemical features on the electronic coupling. Assuming a similarity between the TPA and PCZ moieties, one would expect comparable percolation behaviors for V_{CC} and V_{AA}. Surprisingly, the percolation threshold for V_{CC} lags

significantly behind that of V_{AA}. This distinction cannot be rationalized by the PDFs of D_{CC} and D_{AA} (see **Figure S7.2**), in which the probabilities of finding dimer configurations of close core-core and arm-arm contact are similar (distance < 7 Å). In sharp contrast, the PDFs of V_{CC} and V_{AA} of 1ARM (**Figure S7.2**) exhibit different characteristics (one-peak vs two-peak distribution). The first small peak associated with V_{AA}, located at high-V region ($\log|V| \sim -2.1$), is relatively close to the percolation threshold. Comparing the type of dimers with close core-core and arm-arm contact (small D_{CC} vs small D_{AA}) reveals that better overlap and thus higher electronic coupling is achieved with the planar carbazole units (*i.e.*, $V_{AA} > V_{CC}$). This implies that the electronic coupling can be improved upon minor tuning of the molecular fragment and that replacing the TPA core with a PCZ fragment in 1ARM may improve the overall molecular transport network properties assuming the similar HOMO distributions.

Identifying the dimer configurations that are most crucial to charge transport is also highly insightful. We argue that the edges connecting nodes within the largest cluster at the percolation limit can be considered as the most important dimer configurations (see detailed on the analysis in **Section 7.5**). **Figure 7.4** summarizes the 10 most recurrent configurations. Among them, Type 1, 2 and 3 are the dominant configurations for all three compounds, which together contribute to more than 60% of the total configurations. It is interesting to note that the relevant types of dimer configurations do not change significantly in function of the molecular shapes. Also, the parallel stacked dimers (1ARM, Type 8, **Figure S7.8**), which are usually the most stable configurations in the gas phase, correspond to less than 3%. This suggests that configurations exhibiting high electronic couplings are relatively rare for these three compounds.

The dimer composition analysis also clarifies the crucial role of the core-arm interactions in 1ARM identified previously using the percolation curves. As shown in **Figure 7.4**, the configurations featuring core-arm close contact (Type 2, 3, 4 and 6, see **Figure S7.8**) correspond to more than 50% of the total dimer configurations. This outcome implies that more emphasis should be placed on maximizing the electronic coupling between core and arm in the design of core-arm type amorphous organic semiconductors.

Overall, adding arms does not improve the charge transport through increasing the electronic coupling. This may seem counter-intuitive as a spatially more delocalized HOMO is usually preferred for organic semiconductors with high hole mobility. However, the V_{AA} increases at the cost of decreasing V_{CC} due to change in molecular packing (D_{CC} vs D_{AA}); meanwhile V_{CA} negligibly change. These contrasting trends cancel out with the consequence that V_{tot} change negligibly. While the electronic coupling trends (V_{AA}, V_{CC} and V_{CA}) might be similar in other multiarm systems, the overall V_{tot} can still be enhanced through judicious choice of molecular building blocks. As demonstrated in our previous work,[288,353] the multiarm strategy can also be exploited to devise organic semiconductors with higher hole mobility through lowering the reorganization energy and the energetic disorder.[322]

7.3.2. Core-length Effect

The second series of molecules investigated herein contains a central acene core moiety and two TPA unit as arms. Within this core/arm definition, there are 9 (3×3) fragment-fragment electronic coupling terms for each molecule. They can be group by symmetry as described above (V_{CC}, V_{CA} and V_{AA}).

Figure 7.5 provides the PDFs of the electronic coupling terms upon increasing the core-length. Overall, the PDF of V_{tot} exhibits a transition from a one- to two-peak distribution going from BEN to PEN, which mainly arises from the V_{CC} term. Additionally, the position of the main peak shifts gradually to the left as observed for V_{AA}. Importantly and unlike for the mutliarm series, the trend observed in the PDFs of V_{CC} and V_{AA} cannot be explained by a simple geometrical descriptor (*i.e.*, D_{CC} and D_{AA}). For instance, the small hump gradually appearing around −2 in the V_{CC} plot is not observed in the PDF of D_{CC} (**Figure S7.3**). Similarly, the marginal left-shifted distribution of the D_{AA} curve upon increasing core-length does not explain the strong left-shift in the PDFs of V_{AA}.
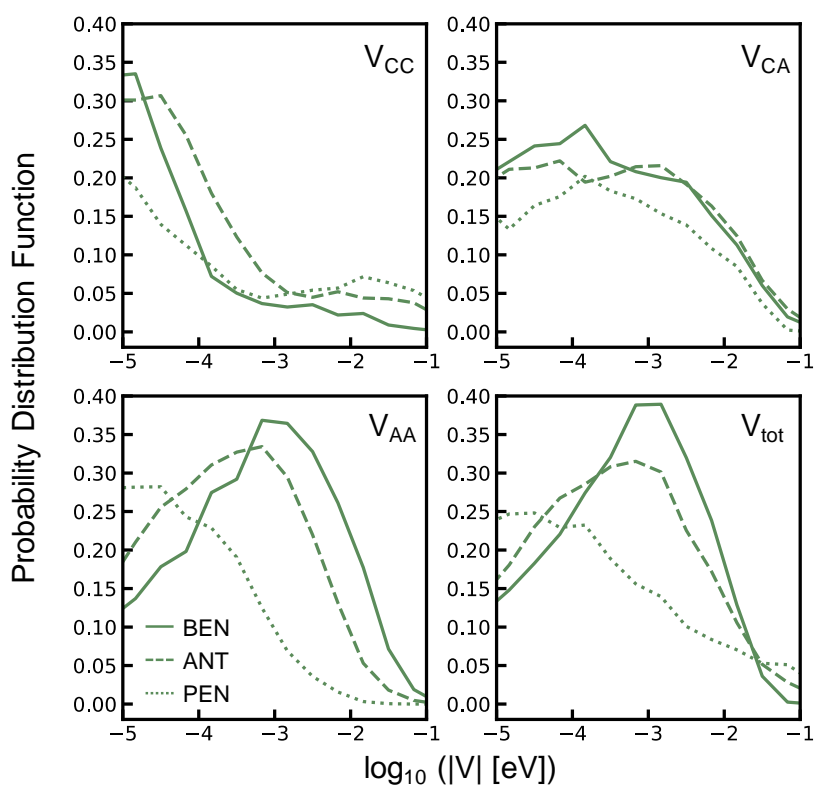
Figure 7.5 The probability distribution functions of $\log_{10}(|V_{CC}|)$, $\log_{10}(|V_{CA}|)$, $\log_{10}(|V_{AA}|)$ and $\log_{10}(|V_{tot}|)$ for BEN, ANT and PEN.

This apparent mismatch is rooted in the electronic structure. With increasing the core length, the HOMO contribution from the atoms in the core increases, whereas that from the arm atoms decreases (see the natural atomic orbital (NAO) analysis in **Figure S7.5**). In other words, even if the packing behavior of the three compounds remains similar, the large difference in HOMO induces changes in the electronic coupling distribution. The significant drop in composition of arm from ANT to PEN may explain the significant peak-shift observed in the PDFs for V_{AA}.
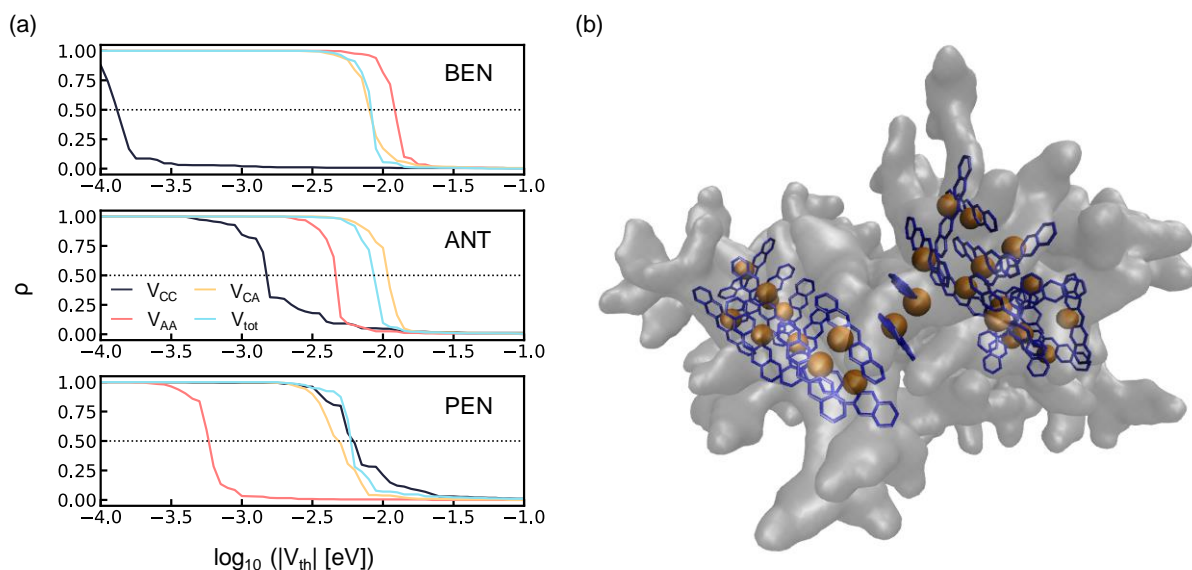
Figure 7.6 (a) The percolation curves of BEN, ANT, PEN based on graphs constructed using $\log_{10}(|V_{CC}|)$, $\log_{10}(|V_{CA}|)$, $\log_{10}(|V_{AA}|)$ and $\log_{10}(|V_{tot}|)$ and (b) the largest connected molecular cluster at the onset of percolation for graph based on V_{CC} of PEN. The blue color represents the pentacene core. And the orange sphere and gray surface represents the center of geometry and VDW surface of each molecule (node).

The percolation threshold for V_{tot} decreases with increasing the acene core length. This originates from the opposite trend for V_{CC} ($V_p \uparrow$) and V_{AA} ($V_p \downarrow$) across the series. The V_p for V_{CA} is more complicated, as it first increases (BEN→ANT) and then decreases significantly (ANT→PEN). The most contributing component (V_{F1F2} with the largest V_p), changes from V_{AA}(BEN) to V_{CA} (ANT) and V_{CC} (PEN). This trend aligns well with the dimer composition analysis shown in **Figure 7.7**. In contrast to the multiarm set, the most common types of dimer configurations vary across the core-length series and this despite their similar molecular shape. For BEN, the prevalent dimer configuration is Type 1, featuring a close arm-arm contact, while Type 2 (core-arm) and Type 7 (core-core, X-shape) dominate for ANT and PEN respectively.

The largest connected cluster at the onset of percolation ($\rho = 0.05$, $V_{on} = -1.85$) for V_{CC} of PEN features a π-π molecular assembly (**Figure 7.6** (b)), which is responsible for the small hump in the PDF of V_{CC} in **Figure 7.5**. However, this molecular aggregate does not efficiently contribute to the overall molecular transport network. As seen in the percolation curve based on PEN V_{tot}, the presence of these assemblies leads to an early onset (-1.75 in log scale). Despite the high V_{on}, the percolation threshold occurs at a relatively low value (-2.25 in log scale). This contrasts with the similar V_p and V_{on} for BEN (-2.07 and -1.92 in log scale). The link between the molecular packing and the large V_{on} and V_p difference for PEN is clearer when looking at the prevalent dimer configurations at V_p in the largest cluster as a function of V_{th} (**Figure S7.14**). At high V_{th}, the cluster is mainly composed of three dimer types (17, 21 and 22, see **Figure S7.13**) which include some parallel-stacking patterns. As V_{th} decreases, the percentages of these

types decrease gradually, while cross-shape dimer configurations leading to smaller V_{tot} contribute the most (types 18, 5 and 7, **Figure S7.13**). The scenario thus involves small π-π stacked molecular assemblies formed at an early stage (early onset) but the packing between these assemblies is less ordered, leading to relatively weak connections between the clusters. These weak connections are rate-limiting in the hole transport process, delaying the percolation transition.
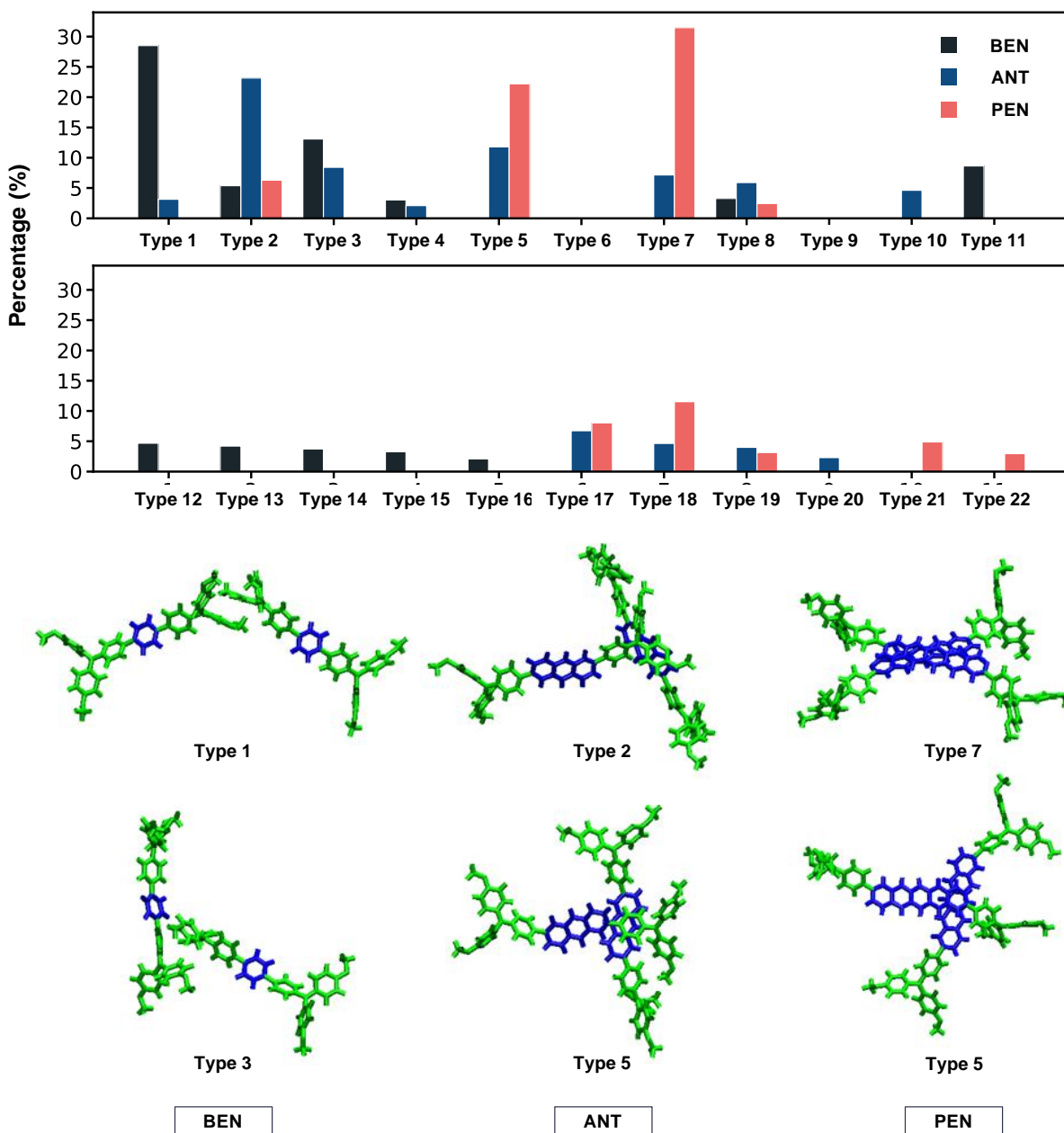
Figure 7.7 The bar plot showing the percentage of different types of dimer configurations present in the largest cluster at percolation threshold and the representative dimer configurations of two most common types for BEN, ANT and PEN. The green and blue bonds represents the TPA arm and the oligoacene core, respectively. The gray shaded area is a guide to the eye.

From the molecular structure perspective, introducing long planar acene core do not sterically hamper the close contact between TPA arms. The comparison between the PDFs of the geometrical descriptors (D_{AA} and D_{CC}) for the multiarm and core-length series, shows that the change in distributions are much more significant for across the former (**Figure S7.1** and **Figure S7.3**). Yet, increasing the acene core-length modifies the fragment-fragment interactions in a more subtle manner, which cannot be probed using the analysis based on simple geometrical descriptors.

7.4. Conclusions

Here we developed a fragment-based electronic coupling decomposition analysis tool, FB-ECDA, which serves to investigate molecular structure-packing-property relationships especially for disordered organic semiconductors. Two series of molecules, multiarm and acene core-length, were investigated using FB-ECDA, natural atomic orbital analysis, graph theory and dimer composition analysis. Introducing more PCZ arms improves the coupling between the arms but worsens the one between the cores (both in distribution and percolation curve) as expected from the fragment-fragment distance (D_{AA} and D_{CC}) trends. Overall adding more arm substituents has no significant effect on the electronic coupling. Yet, FB-ECDA stresses the importance of placing more emphasis on maximizing the electronic coupling between the core and arms in the design of core-arm based amorphous organic semiconductors as V_{CA} remains a key contributors to the total electronic coupling.

Another set of trends arises while increasing the length of the acene core. In contrast to the multiarm case, the composition of the dimer configurations change significantly along this series. In particular, large core of PEN promotes the formation of several small π-π stacking molecular assemblies. Despite their large electronic coupling, these π-π stack dimers are actually not contributing much to the hole transport properties. The limiting factor is shown to be the molecular dimers with lower electronic couplings, bridging the π-π stacked assemblies. Overall, increasing the acene core-length worsen the electronic coupling in terms of molecular transport network, which is especially true for PEN.

An optimal molecular transport network can be achieved through a subtle fine-tuning of the molecular interactions (dimer compositions) and chemical structure (electronic coupling between fragments). Changing the film-processing condition (or simulated process); will enable the tuning the dimer configurations without altering the chemical composition. Alternatively, a minor chemical modification can sensitively affect the electronic coupling, while preserving the original packing pattern under the same processing condition. In either case, our analysis tool and computational protocols can provide insights into the SPPR, boosting the searching pace of promising organic semiconductors.

7.5. Supporting Information
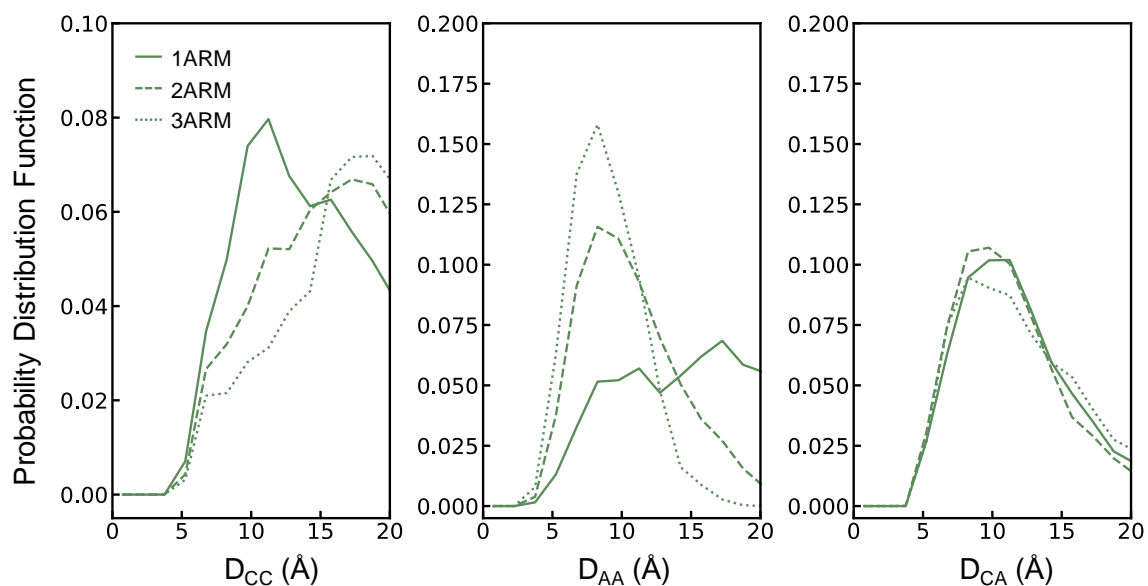
Figure S7.1 The probability distribution functions of distance between cores (D_{CC}, left) and arms (D_{AA}, middle) and core and arm (D_{CA}) for 1ARM, 2ARM and 3ARM. D_{AA} and D_{CA} is the smallest distance between all possible pairs of arms or core-arm. The distance between any pair of fragments is calculated using the distance between N atoms of fragments.
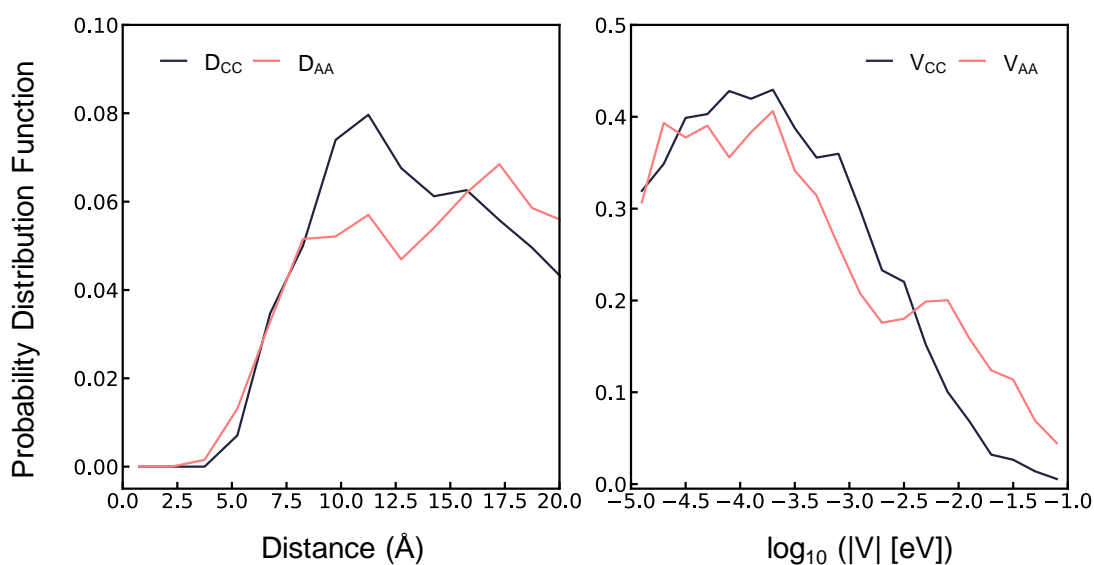
Figure S7.2 The probability distribution functions of D_{CC} and D_{AA} (left) and V_{CC} and V_{AA} (right) of 1ARM.
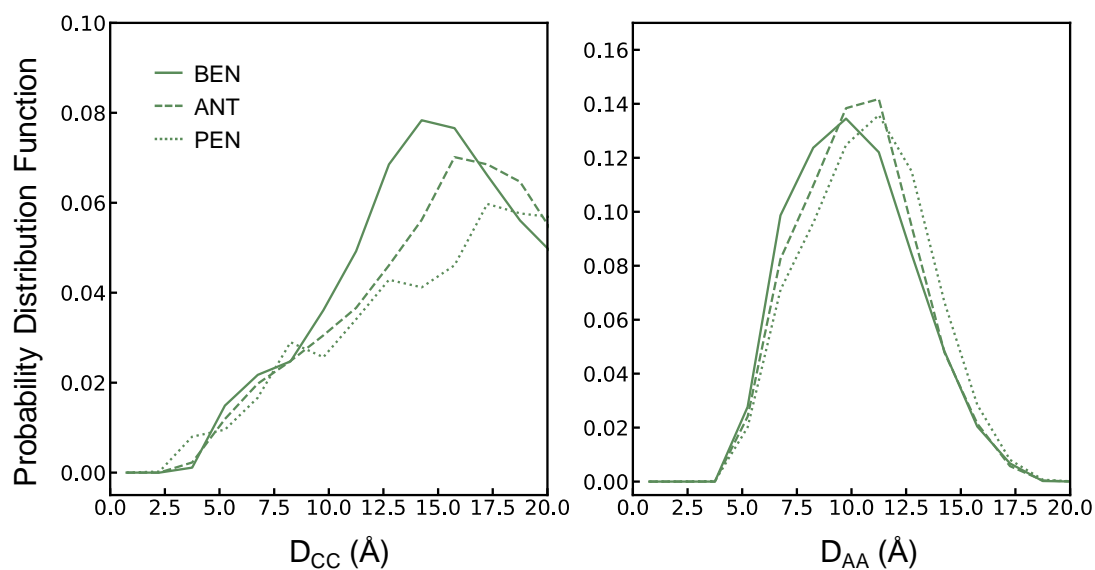
Figure S7.3 The probability distribution functions of distance between cores (D_{CC}, left) and arms (D_{AA}, right) for BEN, ANT and PEN. D_{CC} is calculated using the center of geometry of the acene cores. D_{AA} is the smallest distance between all possible pairs of arms of monomers. The distance between arms is calculated using distance between N atoms of the selected arms.
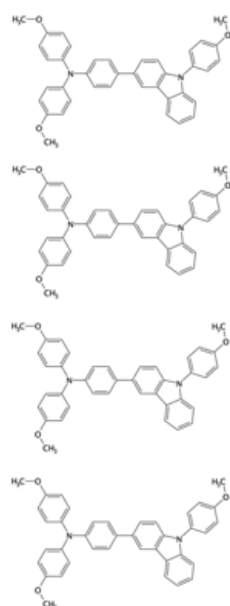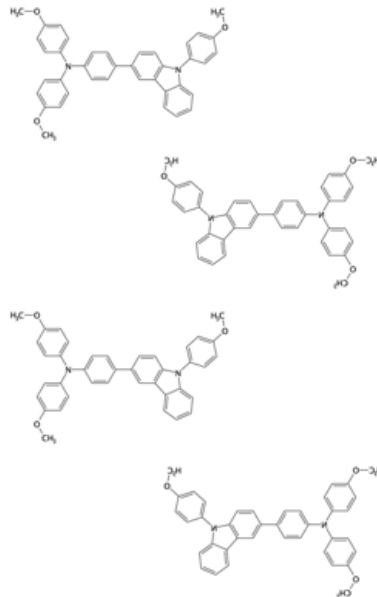
Figure S7.4 Illustration of possible stacking mode featuring high V_p for percolation plot based on V_{AA} and V_{CC}.
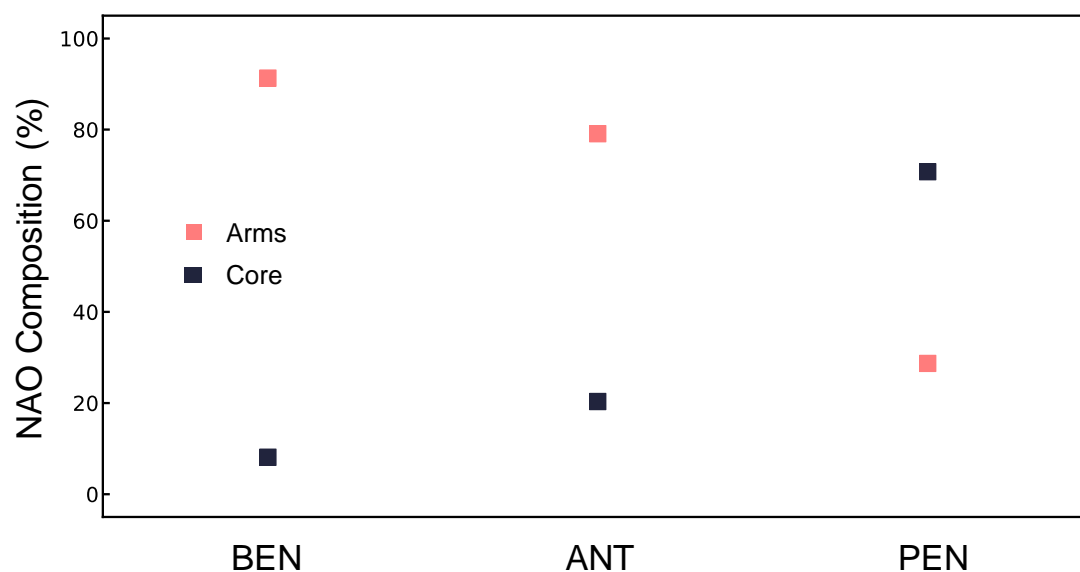
Figure S7.5 The fragment composition of HOMO in terms of natural atomic orbital (NAO) basis for BEN, ANT and PEN. The composition of arms is the sum of contributions from two TPA arms.

7.5.1. Composition Analysis of Dimer Configurations

Given that V_p represents a sharp transition from an unpercolated to percolated state, it is insightful to analyze the dimer con-figurations at this specific point. Our protocol of dimer composition analysis is illustrated in **Figure S7.6**. Our analysis tool has two main advantages. First, the V matrix based on V_{F1F2} terms serves as a good probe for the dimer conformation since electronic coupling is very sensitive to the geometrical relation between molecular fragments. Meanwhile, it extracts the most useful information from the complicated relation present in a dimer conformation (i.e. a N×N distance matrix between monomers with N as the number of atoms in a monomer). Second, classification of molecular dimers using the descriptor rather than V matrix enables the comparison between compounds with different V matrix size. The **V** matrix mentioned in the main article represents an unique fingerprint for the dimer, where we can classify the dimer configurations. For each molecule in this work, the illustration of **V** matrix is constructed as shown in **Figure S7.7**.
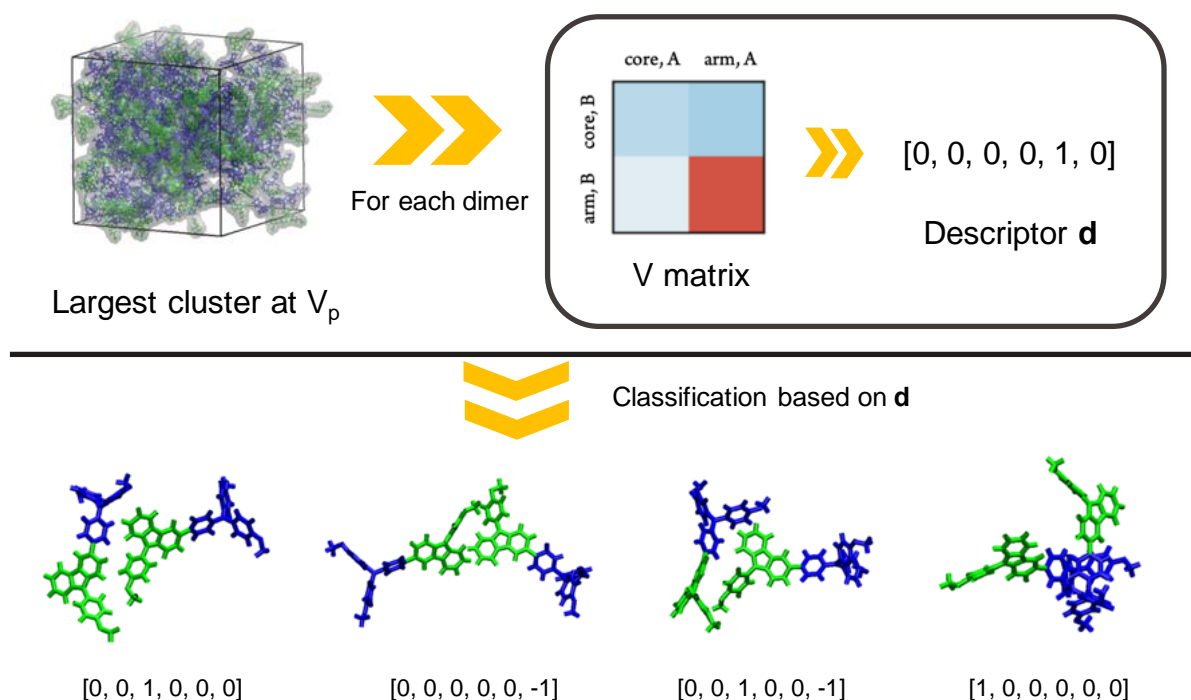
Figure S7.6 Illustration of the protocol of dimer composition analysis.

We classify the matrix by counting the number of element larger than a certain threshold value M. First, we construct a 6×1 vector as a descriptor of the matrix, where the element in the vector is defined as:

$$\mathbf{d} = [p_{CC} \ n_{CC} \ p_{CA} \ n_{CA} \ p_{AA} \ n_{AA}] \tag{S 7.1}$$

where p_{CC}, p_{CA} and p_{AA} are the number of matrix elements corresponding to core-core, core-armi and armi-armj which are positive and larger than the threshold value M. Similarly, n_{CC}, n_{CA} and n_{AA} are the number of matrix elements corresponding to core-core, core-armi and armi-armj which are negative and smaller than minus M. The threshold value M is determined for each molecule in a way that it is the largest value that does not make any matrix classified as [0, 0, 0, 0, 0, 0]. The dimer configurations with the same descriptor are then considered the same type. Due to the arbitrary choice of sign of the HOMO of molecular A and molecular B, **d** is considered to be equivalent to −**d**. The color method is the symmetric logarithmic method in matplotlib, which is useful in a situation that there is positive (red) and negative (blue) data and logarithmic scaling is preferred for both. The parameters are chosen as following: linthresh = 0.0001, linscale = 0.03, vmin = −vmax and vmax is chosen as the maximum of the absolute value of all fragment-fragment electronic coupling terms of all edges. In the following figures, the types showing more than 2% population are shown. For 1ARM, 2ARM and 3ARM, the most appearing dimer configurations (>2%) can be categorized into 10 types based on their descriptors (from **Figure S7.8** to **Figure S7.10**). For BEN, ANT and PEN, we follow the same ordering and nomenclature for the first 10 types as the multiarm case. Similarly, the most appearing dimer configurations (> 2%) is chosen and categorized, resulting in 10 additional types based on their descriptors (from **Figure S7.11** to **Figure S7.13**).
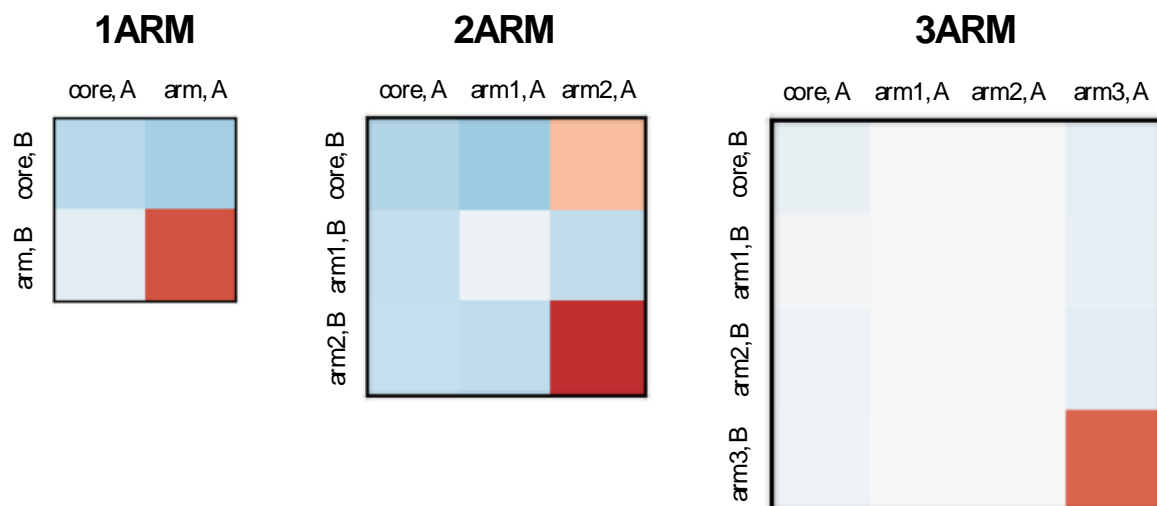
1ARM 2ARM 3ARM

Figure S7.7 The illustration of V matrix for 1ARM, 2ARM and 3ARM. The V matrix of BEN, ANT and PEN are constructed following the same way as that of 2ARM.

1ARM

| Type1 [0,0,0,0,1,0] | Type2 [0,0,1,0,0,0] | Type3 [0,0,1,0,0,-1] | Type4 [0,0,1,0,1,0] |
| 30.43% | 25.50% | 19.24% | 5.59% |

| Type5 [1,0,0,-1,0,0] | Type6 [0,0,2,0,0,-1] | Type7 [1,0,0,0,0,0] | Type8 [1,0,0,-2,1,0] |
| 4.48% | 3.36% | 2.87% | 2.68% |
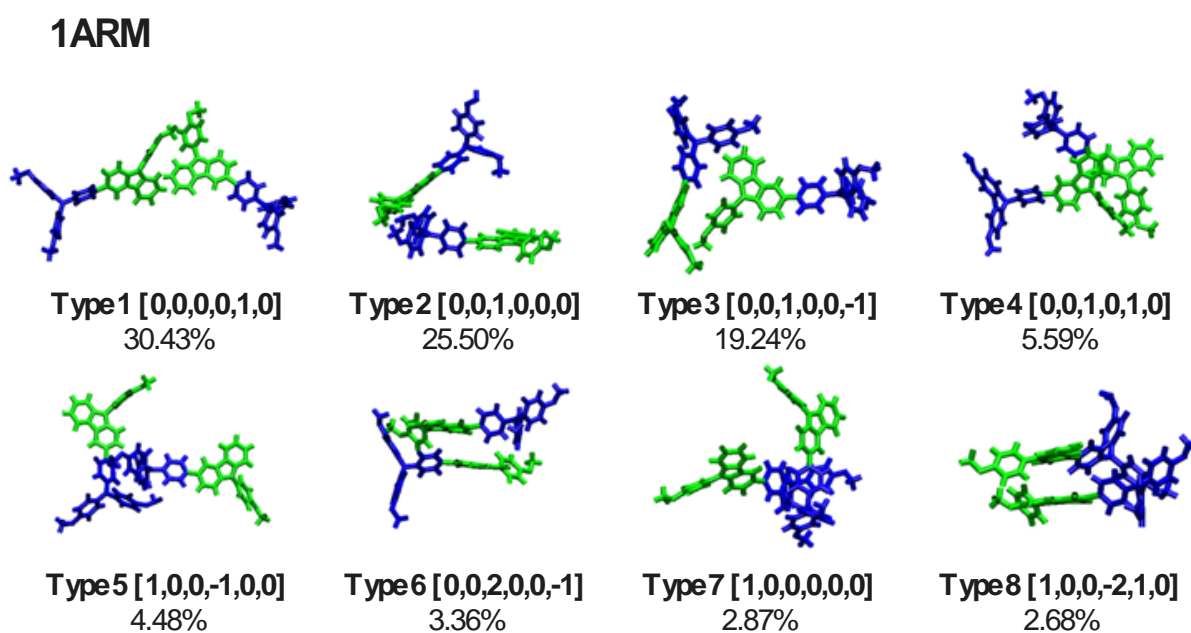
Figure S7.8 Illustration of different types of dimer configurations of 1ARM. The green and blue bonds represents the PCZ arm and the TPA core, respectively.

2ARM

Type 1 [0,0,0,0,1,0]
31.16%

Type 2 [0,0,1,0,0,0]
16.28%

Type 3 [0,0,1,0,0,-1]
18.37%

Type 4 [0,0,1,0,1,0]
6.28%

Type 7 [1,0,0,0,0,0]
2.33%

Type 8 [1,0,0,-2,1,0]
5.35%

Type 9 [0,0,1,-1,1,0]
3.72%
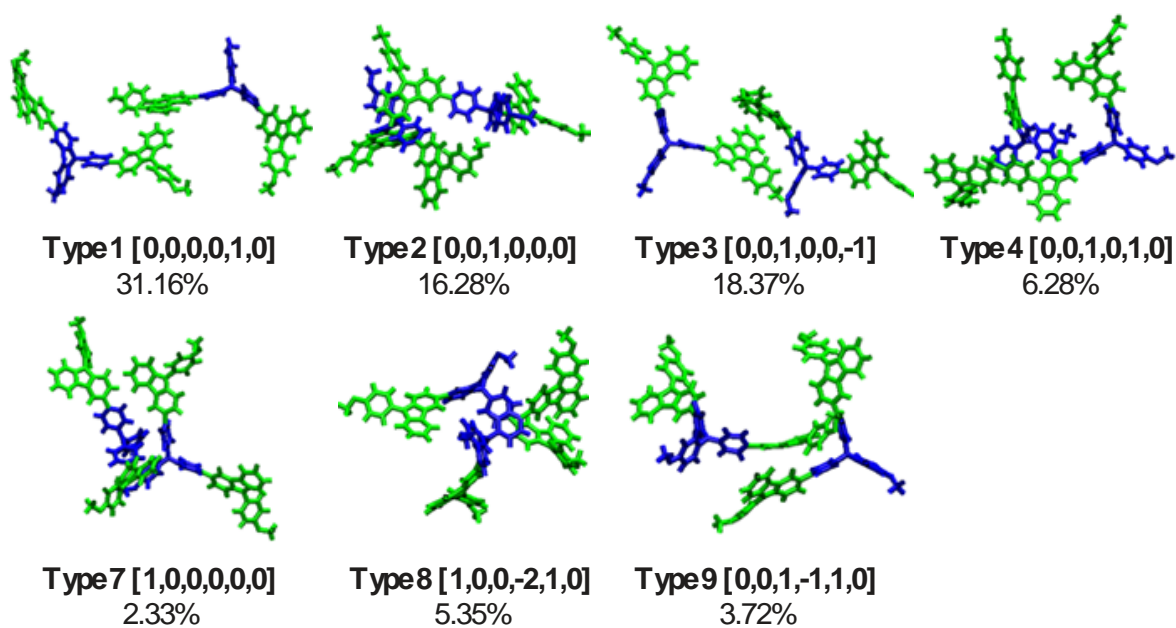
Figure S7.9 Illustration of different types of dimer configurations of 2ARM. The green and blue bonds represents the PCZ arm and the TPA core, respectively.

3ARM

Type 1 [0,0,0,0,1,0]
31.93%

Type 2 [0,0,1,0,0,0]
9.09%

Type 3 [0,0,1,0,0,-1]
23.73%

Type 4 [0,0,1,0,1,0]
5.33%

Type 6 [0,0,2,0,0,-1]
3.55%

Type 8 [1,0,0,-2,1,0]
6.21%

Type 10 [1,0,0,-1,1,0]
2.44%
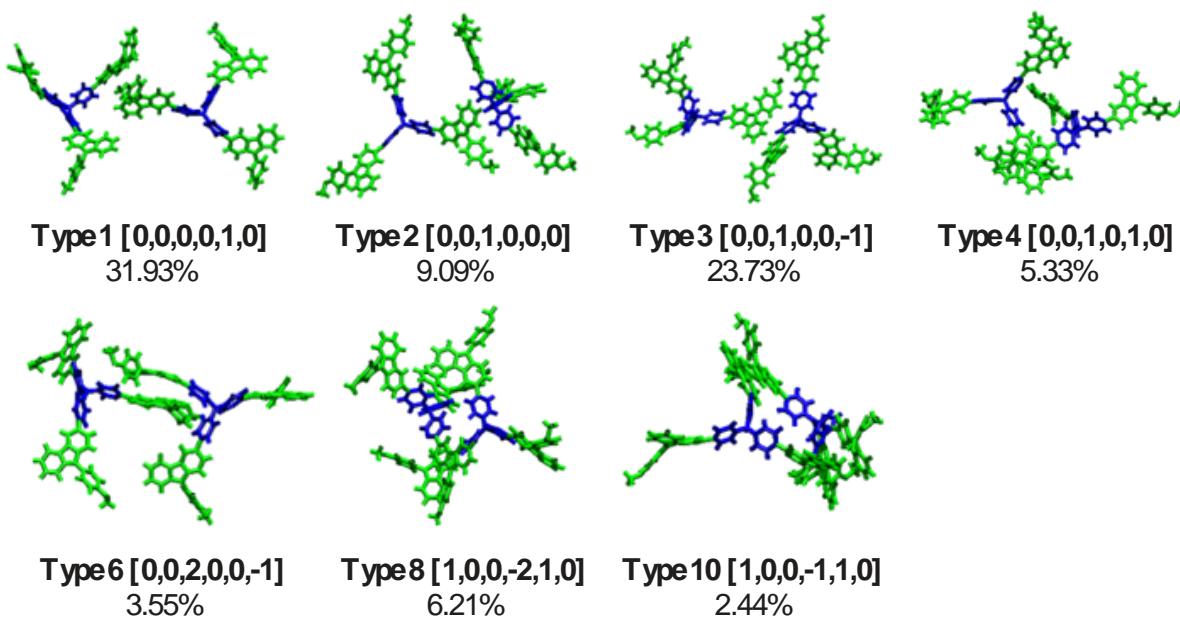
Figure S7.10 Illustration of different types of dimer configurations of 3ARM. The green and blue bonds represents the PCZ arm and the TPA core, respectively.

BEN

Type 1 [0,0,0,0,1,0]
28.51%

Type 2 [0,0,1,0,0,0]
5.38%

Type 3 [0,0,1,0,0,-1]
13.09%

Type 4 [0,0,1,0,1,0]
3.04%

Type 8 [1,0,0,-2,1,0]
3.27%

Type 11 [0,0,0,0,1,-1]
8.64%

Type 12 [0,0,1,0,1,-1]
4.68%

Type 13 [0,0,0,0,2,0]
4.21%

Type 14 [0,0,1,0,0,-2]
3.74%

Type 15 [0,0,1,-1,1,-1]
3.27%

Type 16 [0,0,1,-1,2,0]
2.10%
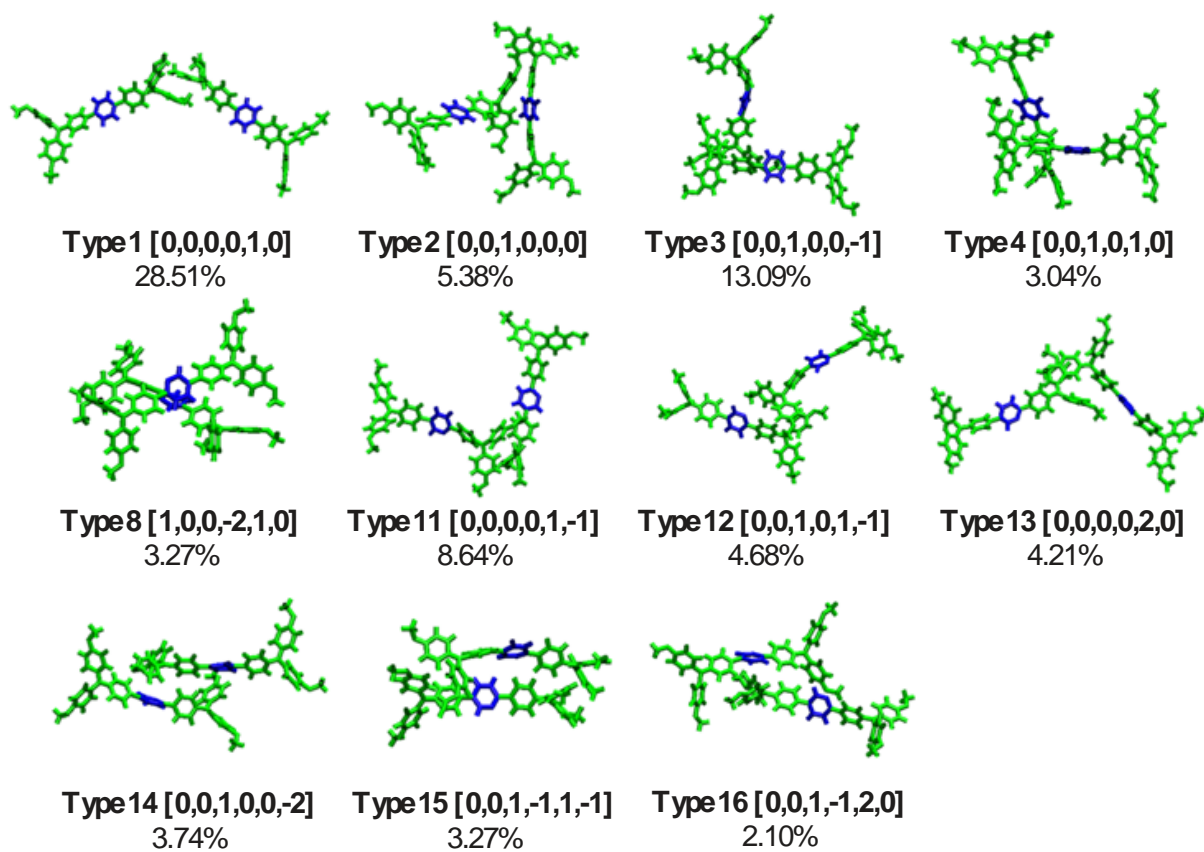
Figure S7.11 Illustration of different types of dimer configurations of BEN. The green and blue bonds represents the TPA arm and the oligoacene core, respectively.

ANT

Type 1 [0,0,0,0,1,0]	Type 2 [0,0,1,0,0,0]	Type 3 [0,0,1,0,0,-1]	Type 4 [0,0,1,0,1,0]
3.15%	23.16%	8.42%	2.1%
Type 5 [1,0,0,-1,0,0]	Type 7 [1,0,0,0,0,0]	Type 8 [1,0,0,-2,1,0]	Type 10 [1,0,0,-1,1,0]
11.79%	7.16%	5.90%	4.63%
Type 17 [1,0,0,-2,0,0]	Type 18 [1,0,1,0,0,0]	Type 19 [1,0,1,-1,0,0]	Type 20 [1,0,0,-1,0,-1]
6.74%	4.64%	4.00%	2.31%
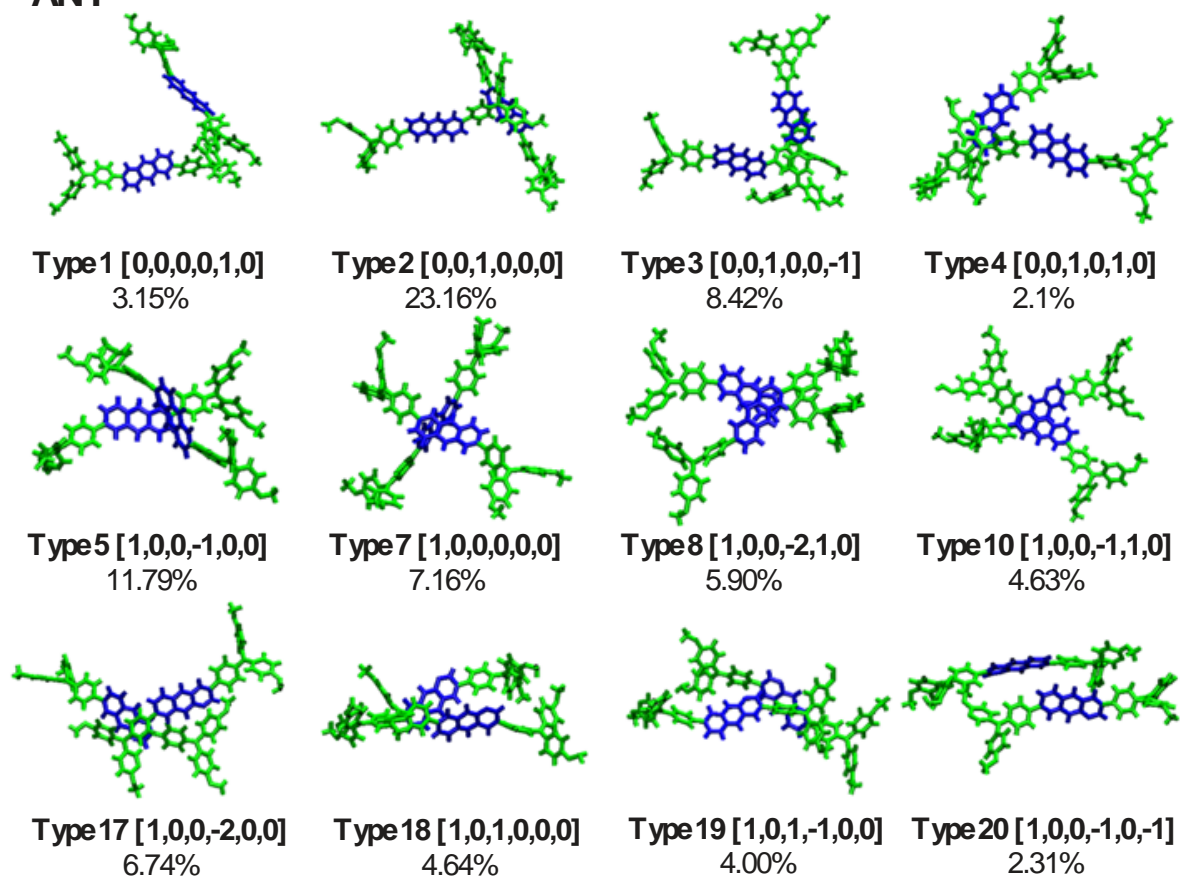
Figure S7.12 Illustration of different types of dimer configurations of ANT. The green and blue bonds represents the TPA arm and the oligoacene core, respectively.

PEN

Type 2 [0,0,1,0,0,0]	Type 5 [1,0,0,-1,0,0]	Type 7 [1,0,0,0,0,0]	Type 8 [1,0,0,-2,1,0]
6.30%	22.20%	31.47%	2.45%
Type 17 [1,0,0,-2,0,0]	Type 18 [1,0,1,0,0,0]	Type 19 [1,0,1,-1,0,0]	Type 21 [1,0,0,-4,1,0]
8.04%	11.54%	4.00%	4.90%

Type 22 [1,0,0,-3,0,0]
2.97%
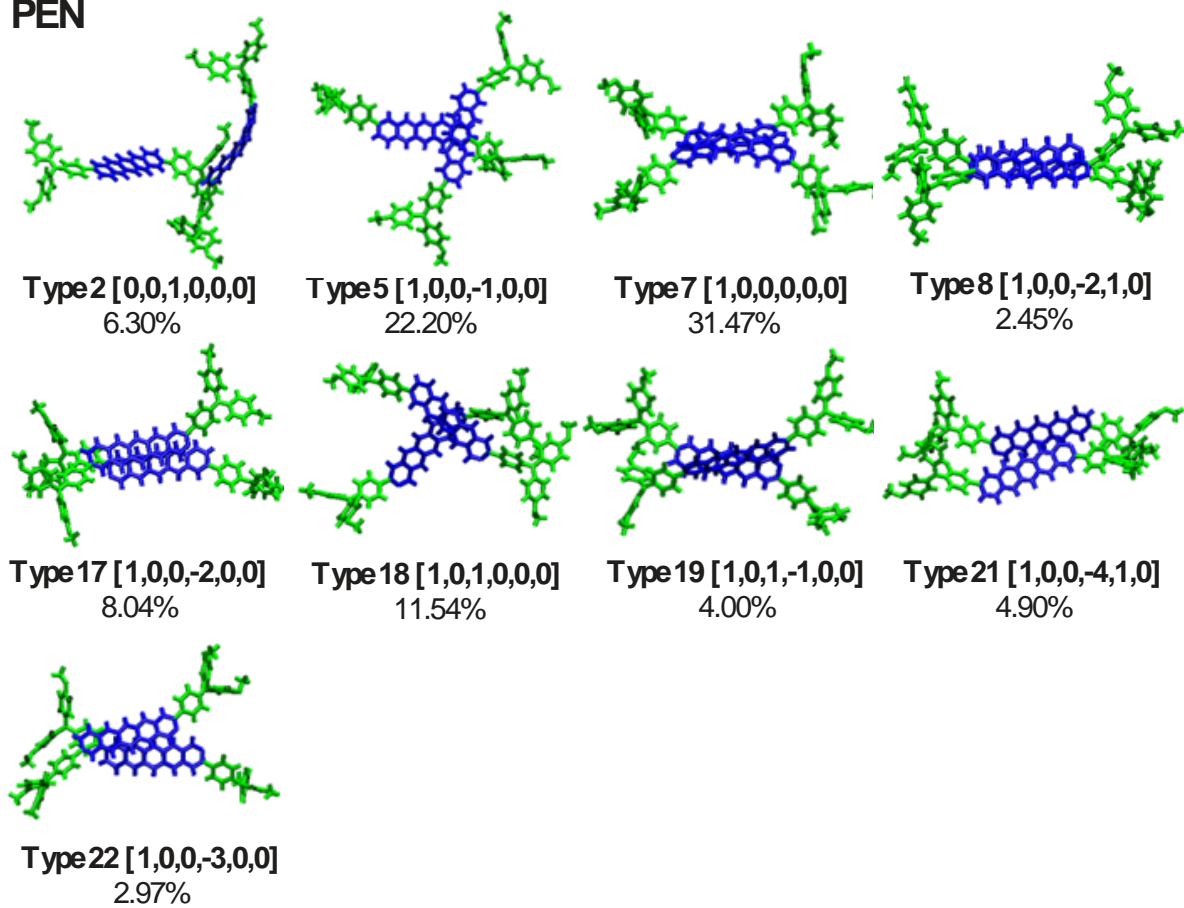
Figure S7.13 Illustration of different types of dimer configurations of PEN. The green and blue bonds represents the TPA arm and the oligoacene core, respectively.
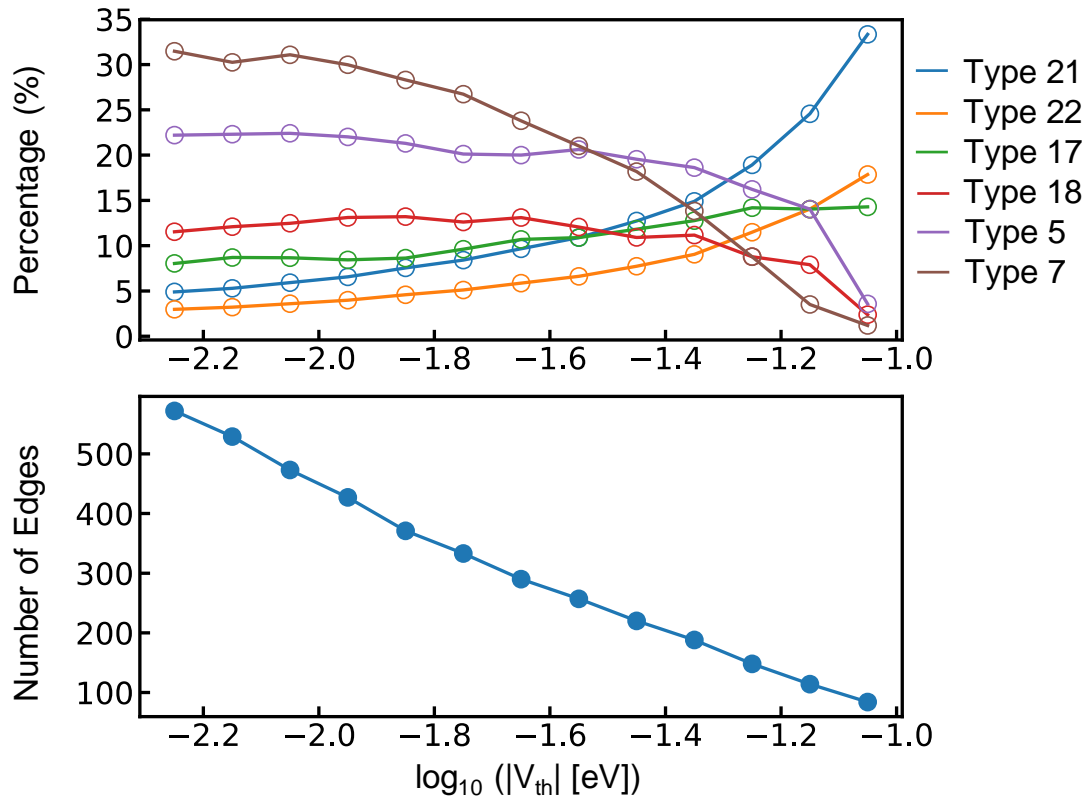
Figure S7.14 (top) The composition of dimer configurations and (bottom)the number of edges in the largest connected cluster as a function of $\log_{10}|V_{th}|$.

Chapter 8 General Conclusions and Outlook

Since the pioneering work by Shirakawa, MacDiarmid and Heeger in 1977, where the first synthesized conductive polyacetylene polymer was reported, the charge transport properties of organic materials have attracted tremendous attention. The flexible and solution-processible nature of organic semiconductors (OSC) makes them perfect candidates for emerging applications where large-scale homogeneous semiconducting thin films are required. While the demand for tailor-made OSCs in various applications is increasing, the search for OSCs of high charge mobility using rational design strategies remains rather limited. This is because the current understanding of the relationship between molecular structure, molecular packing and charge transport properties, upon which rational design strategies rely, is still lacking. In addition to SPPR, little knowledge of contributions from "molecular LEGOs" to charge transport parameters limits the usage of efficient design strategies based on the combination of molecular building blocks (*e.g.*, donor-acceptor type organic dyes). Thus, this thesis aims at offering useful insights into these two aspects, with a specific focus on small-molecule-based amorphous hole transport materials.

The first section was dedicated to revealing the SPPR of HTMs incorporated in perovskite solar cells (PSCs) by performing multiscale charge dynamics simulations. We started with a truxene derivative TruxC-hex-2, a promising dopant-free HTM that results in a perovskite solar cell with 18.2% PCE. Since it was among the best performing dopant-free HTMs at that time, it served as a good starting point for in-depth investigations and further optimizations. The effect of heteroatoms, the presence of hexyl chains and OMeDPA substitution sites on ionization energy, hole mobility, absorption, glass transition temperature and water contact angle were investigated. Taking all these different aspects into account, we suggested that the TruxS and TruxC truxene derivatives without hexyl chains can be promising hole transport materials for PSCs. One interesting finding here was that hexyl chains have a massive negative impact on hole mobility of HTMs, mainly originating from the reduced electronic coupling due to the enhanced intermolecular distance. Moreover, through a 2D color map based on two geometrical descriptors, we clearly identified the absence of high electronic-coupling face-to-face dimer arrangements for truxene derivatives with hexyl chains.

The crucial role of the hexyl chain observed in the first work motivated us to further investigate the effect of alkyl chain length on the properties of interest in PSCs. Alkyl chains are widely used as solubilizing groups in organic semiconductors. Moreover, they are exploited to fine-tune the desired molecular properties through modification of the sophisticated molecular packing behavior. However, how alkyl chain length affects the molecular packing and charge transport properties in SMAOS remains unclear. Our results show that the distribution of electronic coupling is significantly shifted to the low-V^2 region as the chain length increases, which comes from the increased intermolecular distance. On the other hand, the energetic disorder decreases with increasing alkyl chain length due to the same reason, which can be explained using the Correlated Gaussian Disorder Model (CGDM). In this model, the energetic disorder is proportional to the molecular dipole moment and to the inverse of the squared effective lattice constant (which is related to the intermolecular distance). Since alkyl chain substitution has no significant effect on electronic properties (ionization energy, reorganization energy and molecular dipole moment), the enhanced intermolecular distance leads to a smaller energetic disorder with increasing chain length. We suggest that this finding is universal for SMAOS, which indicates that an optimal chain length which maximizes hole mobility can be obtained with short or intermediate alkyl chains.

The contrasting contributions from charge transport parameters to hole mobility observed in the alkyl chain length tuning is not a special case. We showed, in the final work of the first section, that the hole mobility in the multiarm design strategy also exhibits similar characteristics. The multiarm design strategy is an empirical strategy, showing an increase in hole mobility with the number of substituted triphenylamine arms in HTMs. While this strategy has been proven effective, the underlying mechanism remains unknown. From our results, increasing number of arms leads to reduction of all charge transport parameters simultaneously. For the molecules investigated here, this results in increasing hole mobility as the number of arms grows. The origin of the reduced charge parameters were investigated further. The decrease in λ results from the more spatially extended HOMO through the substituted arms. Similar to the alkyl chain length case, the reason for the reduction of σ is the enhanced intermolecular distance due to the enlarged molecular volume. Finally, the slight decrease in electronic coupling, in terms of both the distribution and the transport network, is less trivial as the relationship between the molecule design (number of arms), the molecular packing and the electronic coupling is obscure. This drove us to develop a computational protocol that enables the decomposition of the total electronic coupling into fragment-fragment contributions and the characterization of dimer configurations. Finally, we also demonstrated that through a minimal modification of the molecular structure (i.e. changing substituent groups), we are able to more or less preserve the molecular packing and hence the electronic coupling, while still tuning the ionization potential (IP). In the context of application, we proposed two promising HTM candidates (TPA3C3M and TPA3C3PD) for PSCs which possess suitable IP and high hole mobility.

In the second section of the thesis, we focused on the decomposition of λ and V into contributions from molecular fragments. We started with developing a λ-decomposition tool (FB-REDA) where the fragment reorganization energy λ_{frag} is defined in terms of local fragment modes. With our definition, we avoid the unfavorable cross terms which are inevitable in previous methods, enabling an unambiguous partitioning of λ. The trends regarding λ observed in our previous multiarm work can be explained utilizing λ_{frag}. We find that λ_{core} and λ_{sub} decrease at the cost of a slight increase in λ_{arm}, leading to an overall reduction in total λ with increasing number of arms. To show the usefulness of our tool, we managed to reduce the λ of a promising dopant-free hole transport material (TPA1PM, $\lambda = 213$ meV) by almost 50% (TPD3PM, $\lambda = 108$ meV) through successive molecular design strategies based on the results of FB-REDA. Since the molecular building blocks investigated here are quite common in HTMs, we suggest that the molecular design strategies applied here may be transferable to other similar systems.

Finally, following the development of FB-REDA, we extended the scope of our decomposition analysis to the break-down of electronic coupling into fragment contributions (FB-ECDA). As electronic coupling is defined between two monomers of a charge transfer complex, the fragment decomposition of electronic coupling leads to V_{F1F2} terms involving fragments (F1 and F2) from the two monomers (1 and 2). By comparing the probability distribution function and percolation curves of V_{F1F2}, we show that the slight decrease of electronic coupling observed in our multiarm work is due to the contrasting contributions of core-core (V_{CC}) and arm-arm (V_{AA}) electronic couplings. As the number of arms increases, the arm fragments become statistically closer to one other, while core fragments exhibit an opposite trend. These trends of inter-fragment distance correlate well with the trends observed in V_{CC} and V_{AA}. In contrast, the distance between core and arm show no significant change with respect to the number of arms, which results in a nearly unchanged distribution of V_{CA}. As the trends of inter-fragment distances ($D_{AA} \downarrow$, $D_{CC} \uparrow$, D_{CA} – with increasing number of arms) should be quite general for other multiarm amorphous systems, we suggest that trends of V_{CC}, V_{AA} and V_{CA} observed here would also be transferable to other SMAOS of similar shape and size. Overall, our results imply that electronic coupling is not so strongly affected by the multiarm design. In addition, we developed a composition analysis tool of dimer configurations based on the electronic coupling matrix and the associated descriptor. This tool can be used to characterize the features of molecular packing in condensed phase. In particular, analyzing the dimer composition of the largest cluster at the percolation threshold offers fruitful insights into the relationship between molecular packing and charge transport, as demonstrated by the identification of the role of π–π aggregates present in the simulated morphology of pentacene-based HTMs.

Although the molecules used to showcase our decomposition schemes (FB-REDA and FB-ECDA) all belong to p-type SMAOS, these protocols are generally applicable to any organic semiconductors. Moreover, it has been proven that V and λ, which are parameters in the context of hopping model, are related to transport parameters used in band or polaronic band model. This makes V and λ easy-to-compute descriptors for charge transport mobility, which have been used for high-throughput virtual

screening for high-mobility OSCs.[321] In addition, these decomposition protocols could be easily extended to the investigation of excited state dynamics, where V and λ are also used to describe the exciton transfer process.

The previous paragraphs summarize the main conclusions of this thesis. Several potential research directions can be pursued based on these findings, as outlined in the following sections.

Fragment-based decomposition of energetic disorder

Following the development of the V- and λ-decomposition schemes, it is natural to consider how to decompose site energy (difference) or energetic disorder into fragment contributions. Within the linear electron-vibration and harmonic approximation, it can be shown that[263] the internal energetic disorder (σ_{int}) can be written in terms of reorganization energy:

$$\sigma_{int}^2 = 2\lambda k_B T \tag{8.1}$$

This indicates that we could directly use the FB-REDA to estimate the fragment contributions to the internal energetic disorder. In addition, the fragment reorganization energy could be averaged over all molecules present in the simulated morphology to partially take into account the anharmonicity.

The external energetic disorder, arising from intermolecular interactions, can be evaluated in the framework of the atomic charge and the distributed polarizability. In this context, all intermolecular interactions are pairwise and it would be straightforward to define the inter-fragment contribution to the site energy by grouping the corresponding pairwise terms together, in a similar fashion to FB-ECDA.

Effect of dopants on charge carrier dynamics

In many practical applications, dopants are added to organic charge transport materials to increase the concentration of charge carriers (n). The charge conductivity (σ) follows the relation:

$$\sigma = ne\mu \tag{8.2}$$

Much evidence has shown that the charge mobility is modified by doping,[354] which is not surprising as (1) addition of dopants may change the morphology of a material under the same processing conditions and (2) dopants are ions that interact strongly with charge carrier via electrostatic forces. However, how dopants interact with charge carrier and how they affect charge mobility remains not fully understood.[355] The computational protocols used here can be extended to reveal the underlying mechanism of the modified charge mobility. One foreseeable challenge is that dopants may not always fully transfer an integer number of charge to the host materials, which makes zero-overlap approximation invalid. In this case, a QM/MM scheme may be utilized to tackle this challenge. Alternatively, machine learning potentials trained on DFT data may be a solution, which has been proven to describe complicated system with good accuracy and reasonable computational cost.[356–358]

Understanding the effect of processing conditions on molecular packing and charge transport

In this thesis, we always follow the same or very similar computational protocols to generate the simulated morphologies of different materials, corresponding to the same experimental processing conditions. However, modifications to the processing conditions are likely to change the charge transport property of a given material. For example, the morphology of a material prepared by spin-coating may differ if different solvents or different spin speeds are used. How to generate a simulated morphology which mimics those obtained experimentally with different processing conditions is a challenge. A close collaboration with experimental groups would be necessary to develop reliable computational protocols which generate "real" morphologies. In addition, we can understand the effect of processing conditions on charge transport properties qualitatively. Recent works showed that for computational protocols mimicking the evaporation deposition process, changing the deposition rate or the substrate temperature has an impact on the simulated morphology and charge mobility.[359] We believe that more insight can be obtained utilizing the computational protocols we developed in this thesis to this end. For example, using the dimer composition analysis and FB-ECDA could help us build a direct link between the molecular packing and the processing conditions.

Bibliography

(1)   Moore, G. E. Cramming More Components onto Integrated Circuits. *Electronics* **1965**, 114–117. https://doi.org/10.1109/n-ssc.2006.4785860.

(2)   Arias, A. C.; MacKenzie, J. D.; McCulloch, I.; Rivnay, J.; Salleo, A. Materials and Applications for Large Area Electronics: Solution-Based Approaches. *Chem. Rev.* **2010**, *110* (1), 3–24. https://doi.org/10.1021/cr900150b.

(3)   Root, S. E.; Savagatrup, S.; Printz, A. D.; Rodriquez, D.; Lipomi, D. J. Mechanical Properties of Organic Semiconductors for Stretchable, Highly Flexible, and Mechanically Robust Electronics. *Chem. Rev.* **2017**, *117* (9), 6467–6499. https://doi.org/10.1021/acs.chemrev.7b00003.

(4)   Lüssem, B.; Keum, C. M.; Kasemann, D.; Naab, B.; Bao, Z.; Leo, K. Doped Organic Transistors. *Chem. Rev.* **2016**, *116* (22), 13714–13751. https://doi.org/10.1021/acs.chemrev.6b00329.

(5)   Hains, A. W.; Liang, Z.; Woodhouse, M. A.; Gregg, B. A. Molecular Semiconductors in Organic Photovoltaic Cells. *Chem. Rev.* **2010**, *110* (11), 6689–6735. https://doi.org/10.1021/cr9002984.

(6)   Hedley, G. J.; Ruseckas, A.; Samuel, I. D. W. Light Harvesting for Organic Photovoltaics. *Chem. Rev.* **2017**, *117* (2), 796–837. https://doi.org/10.1021/acs.chemrev.6b00215.

(7)   Ostroverkhova, O. Organic Optoelectronic Materials: Mechanisms and Applications. *Chem. Rev.* **2016**, *116* (22), 13279–13412. https://doi.org/10.1021/acs.chemrev.6b00127.

(8)   Friederich, P.; Meded, V.; Poschlad, A.; Neumann, T.; Rodin, V.; Stehr, V.; Symalla, F.; Danilov, D.; Lüdemann, G.; Fink, R. F.; Kondov, I.; von Wrochem, F.; Wenzel, W. Molecular Origin of the Charge Carrier Mobility in Small Molecule Organic Semiconductors. *Adv. Funct. Mater.* **2016**, *26* (31), 5757–5763. https://doi.org/10.1002/adfm.201601807.

(9)   Ostroverkhova, O. Organic Optoelectronic Materials: Mechanisms and Applications. *Chem. Rev.* **2016**, *116* (22), 13279–13412. https://doi.org/10.1021/acs.chemrev.6b00127.

(10)   Kunkel, C.; Schober, C.; Margraf, J. T.; Reuter, K.; Oberhofer, H. Finding the Right Bricks for Molecular Legos: A Data Mining Approach to Organic Semiconductor Design. *Chem. Mater.* **2019**, *31* (3), 969–978. https://doi.org/10.1021/acs.chemmater.8b04436.

(11)   Bronstein, H.; Nielsen, C. B.; Schroeder, B. C.; McCulloch, I. The Role of Chemical Design in the Performance of Organic Semiconductors. *Nat. Rev. Chem.* **2020**, *4* (2), 66–77. https://doi.org/10.1038/s41570-019-0152-9.

(12) Cui, Y.; Wang, Y.; Bergqvist, J.; Yao, H.; Xu, Y.; Gao, B.; Yang, C.; Zhang, S.; Inganäs, O.; Gao, F.; Hou, J. Wide-Gap Non-Fullerene Acceptor Enabling High-Performance Organic Photovoltaic Cells for Indoor Applications. *Nat. Energy* **2019**, *4* (9), 768–775. https://doi.org/10.1038/s41560-019-0448-5.

(13) Meng, L.; Zhang, Y.; Wan, X.; Li, C.; Zhang, X.; Wang, Y.; Ke, X.; Xiao, Z.; Ding, L.; Xia, R.; Yip, H. L.; Cao, Y.; Chen, Y. Organic and Solution-Processed Tandem Solar Cells with 17.3% Efficiency. *Science (80-.).* **2018**, *361* (6407), 1094–1098. https://doi.org/10.1126/science.aat2612.

(14) Ràfols-Ribé, J.; Will, P. A.; Hänisch, C.; Gonzalez-Silveira, M.; Lenk, S.; Rodríguez-Viejo, J.; Reineke, S. High-Performance Organic Light-Emitting Diodes Comprising Ultrastable Glass Layers. *Sci. Adv.* **2018**, *4* (5), 1–10. https://doi.org/10.1126/sciadv.aar8332.

(15) Chen, H. W.; Lee, J. H.; Lin, B. Y.; Chen, S.; Wu, S. T. Liquid Crystal Display and Organic Light-Emitting Diode Display: Present Status and Future Perspectives. *Light Sci. Appl.* **2018**, *7* (3), 17168. https://doi.org/10.1038/lsa.2017.168.

(16) Köhler, A.; Bässler, H. *Electronic Processes in Organic Semiconductors*; Wiley-VCH, 2015.

(17) Kanibolotsky, A. L.; Perepichka, I. F.; Skabara, P. J. Star-Shaped π-Conjugated Oligomers and Their Applications in Organic Electronics and Photonics. *Chem. Soc. Rev.* **2010**, *39* (7), 2695–2728. https://doi.org/10.1039/b918154g.

(18) Cai, Z.; Awais, M. A.; Zhang, N.; Yu, L. Exploration of Syntheses and Functions of Higher Ladder-Type π-Conjugated Heteroacenes. *Chem* **2018**, *4* (11), 2538–2570. https://doi.org/10.1016/j.chempr.2018.08.017.

(19) Gundlach, D. J.; Nichols, J. A.; Zhou, L.; Jackson, T. N. Thin-Film Transistors Based on Well-Ordered Thermally Evaporated Naphthacene Films. *Appl. Phys. Lett.* **2002**, *80* (16), 2925–2927. https://doi.org/10.1063/1.1471378.

(20) Jiang, H.; Hu, W. The Emergence of Organic Single-Crystal Electronics. *Angew. Chemie - Int. Ed.* **2020**, *59* (4), 1408–1428. https://doi.org/10.1002/anie.201814439.

(21) Jhulki, S.; Moorthy, J. N. Small Molecular Hole-Transporting Materials (HTMs) in Organic Light-Emitting Diodes (OLEDs): Structural Diversity and Classification. *J. Mater. Chem. C* **2018**, *6* (31), 8280–8325. https://doi.org/10.1039/c8tc01300d.

(22) Baranovskii, S. D. Theoretical Description of Charge Transport in Disordered Organic Semiconductors. *Phys. Status Solidi Basic Res.* **2014**, *251* (3), 487–525. https://doi.org/10.1002/pssb.201350339.

(23) Ameen, S.; Rub, M. A.; Kosa, S. A.; Alamry, K. A.; Akhtar, M. S.; Shin, H.-S.; Seo, H.-K.; Asiri, A. M.; Nazeeruddin, M. K. Perovskite Solar Cells: Influence of Hole Transporting Materials on Power Conversion Efficiency. *ChemSusChem* **2016**, *9* (1), 10–27. https://doi.org/10.1002/cssc.201501228.

(24) Bakr, Z. H.; Wali, Q.; Fakharuddin, A.; Schmidt-Mende, L.; Brown, T. M.; Jose, R. Advances in Hole Transport Materials Engineering for Stable and Efficient Perovskite Solar Cells. *Nano*

Energy **2017**, *34* (February), 271–305. https://doi.org/10.1016/j.nanoen.2017.02.025.

(25)   Agarwala, P.; Kabra, D. A Review on Triphenylamine (TPA) Based Organic Hole Transport Materials (HTMs) for Dye Sensitized Solar Cells (DSSCs) and Perovskite Solar Cells (PSCs): Evolution and Molecular Engineering. *J. Mater. Chem. A* **2017**, *5* (4), 1348–1373. https://doi.org/10.1039/c6ta08449d.

(26)   Calió, L.; Kazim, S.; Grätzel, M.; Ahmad, S. Hole-Transport Materials for Perovskite Solar Cells. *Angew. Chemie Int. Ed.* **2016**, *55* (47), 14522–14545. https://doi.org/10.1002/anie.201601757.

(27)   Xu, T.; Chen, L.; Guo, Z.; Ma, T. Strategic Improvement of the Long-Term Stability of Perovskite Materials and Perovskite Solar Cells. *Phys. Chem. Chem. Phys.* **2016**, *18* (39), 27026–27050. https://doi.org/10.1039/c6cp04553g.

(28)   Habisreutinger, S. N.; McMeekin, D. P.; Snaith, H. J.; Nicholas, R. J. Research Update: Strategies for Improving the Stability of Perovskite Solar Cells. *APL Mater.* **2016**, *4* (9), 091503. https://doi.org/10.1063/1.4961210.

(29)   Juarez-Perez, E. J.; Wuβler, M.; Fabregat-Santiago, F.; Lakus-Wollny, K.; Mankel, E.; Mayer, T.; Jaegermann, W.; Mora-Sero, I. Role of the Selective Contacts in the Performance of Lead Halide Perovskite Solar Cells. *J. Phys. Chem. Lett.* **2014**, *5* (4), 680–685. https://doi.org/10.1021/jz500059v.

(30)   Rakstys, K.; Igci, C.; Nazeeruddin, M. K. Efficiency: Vs. Stability: Dopant-Free Hole Transporting Materials towards Stabilized Perovskite Solar Cells. *Chem. Sci.* **2019**, *10* (28), 6748–6769. https://doi.org/10.1039/c9sc01184f.

(31)   Rodríguez-Seco, C.; Cabau, L.; Vidal-Ferran, A.; Palomares, E. Advances in the Synthesis of Small Molecules as Hole Transport Materials for Lead Halide Perovskite Solar Cells. *Acc. Chem. Res.* **2018**, *51* (4), 869–880. https://doi.org/10.1021/acs.accounts.7b00597.

(32)   Kim, G. W.; Choi, H.; Kim, M.; Lee, J.; Son, S. Y.; Park, T. Hole Transport Materials in Conventional Structural (n–i–p) Perovskite Solar Cells: From Past to the Future. *Adv. Energy Mater.* **2020**, *10* (8), 1–30. https://doi.org/10.1002/aenm.201903403.

(33)   Niyas, M. A.; Ramakrishnan, R.; Vijay, V.; Hariharan, M. Structure-Packing-Property Correlation of Self-Sorted Versus Interdigitated Assembly in TTF·TCNQ-Based Charge-Transport Materials. *Chem. - A Eur. J.* **2018**, *24* (47), 12318–12329. https://doi.org/10.1002/chem.201705537.

(34)   Bässler, H. Charge Transport in Disordered Organic Photoconductors a Monte Carlo Simulation Study. *Phys. status solidi* **1993**, *175* (1), 15–56. https://doi.org/10.1002/pssb.2221750102.

(35)   Bouhassoune, M.; Mensfoort, S. L. M. va.; Bobbert, P. A.; Coehoorn, R. Carrier-Density and Field-Dependent Charge-Carrier Mobility in Organic Semiconductors with Correlated Gaussian Disorder. *Org. Electron. physics, Mater. Appl.* **2009**, *10* (3), 437–445. https://doi.org/10.1016/j.orgel.2009.01.005.

(36)   Pasveer, W. F.; Cottaar, J.; Tanase, C.; Coehoorn, R.; Bobbert, P. A.; Blom, P. W. M.; De Leeuw, M.; Michels, M. A. J. Unified Description of Charge-Carrier Mobilities in Disordered Semiconducting Polymers. *Phys. Rev. Lett.* **2005**, *94* (20), 1–4. https://doi.org/10.1103/PhysRevLett.94.206601.

(37)   Novikov, S. V; Dunlap, D. H.; Kenkre, V. M.; Parris, P. E.; Vannikov,   a V. Essential Role of Correlations in Governing Charge Transport in Disordered Organic Materials. *Phys. Rev. Lett.* **1998**, *81* (20), 4472–4475. https://doi.org/10.1103/PhysRevLett.81.4472.

(38)   Kwiatkowski, J. J.; Nelson, J.; Li, H.; Bredas, J. L.; Wenzel, W.; Lennartz, C. Simulating Charge Transport in Tris(8-Hydroxyquinoline) Aluminium (Alq3). *Phys. Chem. Chem. Phys.* **2008**, *10* (14), 1852. https://doi.org/10.1039/b719592c.

(39)   Oberhofer, H.; Reuter, K.; Blumberger, J. Charge Transport in Molecular Materials: An Assessment of Computational Methods. *Chem. Rev.* **2017**, *117* (15), 10319–10357. https://doi.org/10.1021/acs.chemrev.7b00086.

(40)   Rühle, V.; Lukyanov, A.; May, F.; Schrader, M.; Vehoff, T.; Kirkpatrick, J.; Baumeier, B.; Andrienko, D. Microscopic Simulations of Charge Transport in Disordered Organic Semiconductors. *J. Chem. Theory Comput.* **2011**, *7* (10), 3335–3345. https://doi.org/10.1021/ct200388s.

(41)   D'Avino, G.; Muccioli, L.; Castet, F.; Poelking, C.; Andrienko, D.; Soos, Z. G.; Cornil, J.; Beljonne, D. Electrostatic Phenomena in Organic Semiconductors: Fundamentals and Implications for Photovoltaics. *J. Phys. Condens. Matter* **2016**, *28* (43). https://doi.org/10.1088/0953-8984/28/43/433002.

(42)   Friederich, P.; Meded, V.; Symalla, F.; Elstner, M.; Wenzel, W. QM/QM Approach to Model Energy Disorder in Amorphous Organic Semiconductors. *J. Chem. Theory Comput.* **2015**, *11* (2), 560–567. https://doi.org/10.1021/ct501023n.

(43)   Ratcliff, L. E.; Grisanti, L.; Genovese, L.; Deutsch, T.; Neumann, T.; Danilov, D.; Wenzel, W.; Beljonne, D.; Cornil, J. Toward Fast and Accurate Evaluation of Charge On-Site Energies and Transfer Integrals in Supramolecular Architectures Using Linear Constrained Density Functional Theory (CDFT)-Based Methods. *J. Chem. Theory Comput.* **2015**, *11* (5), 2077–2086. https://doi.org/10.1021/acs.jctc.5b00057.

(44)   Poelking, C.; Andrienko, D. Long-Range Embedding of Molecular Ions and Excitations in a Polarizable Molecular Environment. *J. Chem. Theory Comput.* **2016**, *12* (9), 4516–4523. https://doi.org/10.1021/acs.jctc.6b00599.

(45)   Vehoff, T.; Baumeier, B.; Troisi, A.; Andrienko, D. Charge Transport in Organic Crystals: Role of Disorder and Topological Connectivity. *J. Am. Chem. Soc.* **2010**, *132* (33), 11702–11708. https://doi.org/10.1021/ja104380c.

(46)   May, F.; Marcon, V.; Hansen, M. R.; Grozema, F.; Andrienko, D. Relationship between Supramolecular Assembly and Charge-Carrier Mobility in Perylenediimide Derivatives: The Impact of Side Chains. *J. Mater. Chem.* **2011**, *21* (26), 9538–9545.

https://doi.org/10.1039/c1jm10500k.

(47)   Lukyanov, A.; Andrienko, D. Extracting Nondispersive Charge Carrier Mobilities of Organic
         Semiconductors from Simulations of Small Systems. *Phys. Rev. B* **2010**, *82* (19), 193202.
         https://doi.org/10.1103/PhysRevB.82.193202.

(48)   WEINHOLD, F.; LANDIS, C. R. Natural Bond Orbitals and Extensions of Localized Bonding
         Concepts. *Chem. Educ. Res. Pr.* **2001**, *2* (2), 91–104. https://doi.org/10.1039/b1rp90011k.

(49)   Parrish, R. M.; Sherrill, C. D. Spatial Assignment of Symmetry Adapted Perturbation Theory
         Interaction Energy Components: The Atomic SAPT Partition. *J. Chem. Phys.* **2014**, *141* (4).
         https://doi.org/10.1063/1.4889855.

(50)   Parrish, R. M.; Parker, T. M.; David Sherrill, C. Chemical Assignment of Symmetry-Adapted
         Perturbation Theory Interaction Energy Components: The Functional-Group SAPT Partition. *J.
         Chem. Theory Comput.* **2014**, *10* (10), 4417–4431. https://doi.org/10.1021/ct500724p.

(51)   Plasser, F. TheoDORE : A Toolbox for a Detailed and Automated Analysis of Electronic
         Excited State Computations. *ChemRxiv.* **2019**.

(52)   Friedel, B.; McNeill, C. R.; Greenham, N. C. Influence of Alkyl Side-Chain Length on the
         Performance of Poly(3-Alkylthiophene)/Polyfluorene All-Polymer Solar Cells. *Chem. Mater.*
         2010, *22* (11), 3389–3398. https://doi.org/10.1021/cm100189t.

(53)   Cadisa, A.; Oosterbaan, W. D.; Vandewal, K.; Bolsée, J. C.; Bertho, S.; D'Haen, J.; Lutsen, L.;
         Vanderzande, D.; Manca, J. V. Effect of Alkyl Side-Chain Length on Photovoltaic Properties
         of Poly(3-Alkylthiophene)/Pcbm Bulk Heterojunctions. *Adv. Funct. Mater.* **2009**, *19* (20),
         3300–3306. https://doi.org/10.1002/adfm.200900797.

(54)   Babel, A.; Jenekhe, S. A. Alkyl Chain Length Dependence of the Field-Effect Carrier Mobility
         in Regioregular Poly(3-Alkylthiophene)S. *Synth. Met.* **2005**, *148* (2), 169–173.
         https://doi.org/10.1016/j.synthmet.2004.09.033.

(55)   Min, J.; Luponosov, Y. N.; Gerl, A.; Polinskaya, M. S.; Peregudova, S. M.; Dmitryakov, P. V.;
         Bakirov, A. V.; Shcherbina, M. A.; Chvalun, S. N.; Grigorian, S.; Kaush-Busies, N.;
         Ponomarenko, S. A.; Ameri, T.; Brabec, C. J. Alkyl Chain Engineering of Solution-Processable
         Star-Shaped Molecules for High-Performance Organic Solar Cells. *Adv. Energy Mater.* **2014**, *4*
         (5), 1–10. https://doi.org/10.1002/aenm.201301234.

(56)   Arikainen, E. 0; Boden, N.; Bushby, R. J.; Clements, J.; Movaghar, B.; Wood, A. Effects of
         Side-Chain Length on the Charge Transport Properties of Discotic Liquid Crystals and Their
         Implications for the Transport Mechanism. *J. Mater. Chem* **1995**, *5* (12), 2161–2165.
         https://doi.org/10.1039/jm9950502161.

(57)   Osaka, I.; Zhang, R.; Sauvé, G.; Smilgies, D.-M.; Kowalewski, T.; McCullough, R. D. High-
         Lamellar Ordering and Amorphous-Like π-Network in Short-Chain
         Thiazolothiazole−Thiophene Copolymers Lead to High Mobilities. *J. Am. Chem. Soc.* **2009**,
         131 (7), 2521–2529. https://doi.org/10.1021/ja801475h.

(58)   García-Benito, I.; Zimmermann, I.; Urieta-Mora, J.; Aragó, J.; Calbo, J.; Perles, J.; Serrano, A.;

Molina-Ontoria, A.; Ortí, E.; Martín, N.; Nazeeruddin, M. K. Heteroatom Effect on Star-Shaped Hole-Transporting Materials for Perovskite Solar Cells. *Adv. Funct. Mater.* **2018**, *28* (31), 1–10. https://doi.org/10.1002/adfm.201801734.

(59)   Liu, X.; Kong, F.; Jin, S.; Chen, W.; Yu, T.; Hayat, T.; Alsaedi, A.; Wang, H.; Tan, Z.; Chen, J.; Dai, S. Molecular Engineering of Simple Benzene-Arylamine Hole-Transporting Materials for Perovskite Solar Cells. *ACS Appl. Mater. Interfaces* **2017**, *9* (33), 27657–27663. https://doi.org/10.1021/acsami.7b06193.

(60)   Park, S. J.; Jeon, S.; Lee, I. K.; Zhang, J.; Jeong, H.; Park, J.-Y.; Bang, J.; Ahn, T. K.; Shin, H.-W.; Kim, B.-G.; Park, H. J. Inverted Planar Perovskite Solar Cells with Dopant Free Hole Transporting Material: Lewis Base-Assisted Passivation and Reduced Charge Recombination. *J. Mater. Chem. A* **2017**, *5* (25), 13220–13227. https://doi.org/10.1039/C7TA02440A.

(61)   Malagoli, M.; Brédas, J. L. Density Functional Theory Study of the Geometric Structure and Energetics of Triphenylamine-Based Hole-Transporting Molecules. *Chem. Phys. Lett.* **2000**, *327* (1–2), 13–17. https://doi.org/10.1016/S0009-2614(00)00757-0.

(62)   Fazzi, D.; Caironi, M.; Castiglioni., C. Quantum-Chemical Insights into the Prediction of Charge Transport Parameters for a Naphthalenetetracarboxydiimide-Based Copolymer with Enhanced Electron Mobility. *J. Am. Chem. Soc.* **2011**, *133* (47), 19056–19059. https://doi.org/10.1021/ja208824d.

(63)   Landi, A. Charge Mobility Prediction in Organic Semiconductors: Comparison of Second-Order Cumulant Approximation and Transient Localization Theory. *J. Phys. Chem. C* **2019**, *123* (31), 18804–18812. https://doi.org/10.1021/acs.jpcc.9b04252.

(64)   Yavuz, I. Dichotomy between the Band and Hopping Transport in Organic Crystals: Insights from Experiments. *Phys. Chem. Chem. Phys.* **2017**, *19* (38), 25819–25828. https://doi.org/10.1039/c7cp05297a.

(65)   Kittel, C. *Introduction to Solid State Physics*, 8th ed.; Wiley, 2004.

(66)   Ziman, J. M. *Principles of the Theory of Solids*; Cambridge University Press, 1972. https://doi.org/10.1017/CBO9781139644075.

(67)   Xi, J.; Long, M.; Tang, L.; Wang, D.; Shuai, Z. First-Principles Prediction of Charge Mobility in Carbon and Organic Nanomaterials. *Nanoscale* **2012**, *4* (15), 4348–4369. https://doi.org/10.1039/c2nr30585b.

(68)   Fornari, R. P.; Troisi, A. Theory of Charge Hopping along a Disordered Polymer Chain. *Phys. Chem. Chem. Phys.* **2014**, *16* (21), 9997–10007. https://doi.org/10.1039/c3cp54661f.

(69)   Greco, C.; Melnyk, A.; Kremer, K.; Andrienko, D.; Daoulas, K. C. Generic Model for Lamellar Self-Assembly in Conjugated Polymers: Linking Mesoscopic Morphology and Charge Transport in P3HT. *Macromolecules* **2019**, *52* (3), 968–981. https://doi.org/10.1021/acs.macromol.8b01863.

(70)   Massé, A.; Friederich, P.; Symalla, F.; Liu, F.; Meded, V.; Coehoorn, R.; Wenzel, W.; Bobbert, P. A. Effects of Energy Correlations and Superexchange on Charge Transport and Exciton

Formation in Amorphous Molecular Semiconductors: An Ab Initio Study. *Phys. Rev. B* **2017**, *95* (11), 1–11. https://doi.org/10.1103/PhysRevB.95.115204.

(71)   Sworakowski, J.; Janus, K.; Nešpůrek, S.; Vala, M. Local States in Organic Materials: Charge Transport and Localization. *IEEE Trans. Dielectr. Electr. Insul.* **2006**, *13* (5), 1001–1015. https://doi.org/10.1109/TDEI.2006.247825.

(72)   Holstein, T. Studies of Polaron Motion. *Ann. Phys. (N. Y).* **1959**, *8* (3), 343–389. https://doi.org/10.1016/0003-4916(59)90003-x.

(73)   Su, W. P.; Schrieffer, J. R.; Heeger, A. J. Solitons in Polyacetylene. *Phys. Rev. Lett.* **1979**, *42* (25), 1698–1701. https://doi.org/10.1103/PhysRevLett.42.1698.

(74)   Xie, X.; Santana-Bonilla, A.; Troisi, A. Nonlocal Electron-Phonon Coupling in Prototypical Molecular Semiconductors from First Principles. *J. Chem. Theory Comput.* **2018**, *14* (7), 3752–3762. https://doi.org/10.1021/acs.jctc.8b00235.

(75)   Marcus, R. a. Electron Transfer Reactions in Chemistry: Theory and Experiment. *Angew. Chemie Int. Ed. English* **1993**, *32* (8), 1111–1121. https://doi.org/10.1002/anie.199311113.

(76)   Beratan, D. N.; Onuchic, J. N. Adiabaticity and Nonadiabaticity in Bimolecular Outer-sphere Charge Transfer Reactions. *J. Chem. Phys.* **1988**, *89* (10), 6195–6203. https://doi.org/10.1063/1.455436.

(77)   Nitzan, A. *Chemical Dynamics in Condensed Phases: Relaxation, Transfer and Reactions in Condensed Matter Molecular Systems*; Oxford University Press, 2006. https://doi.org/10.1002/cphc.200700074.

(78)   Fatayer, S.; Schuler, B.; Steurer, W.; Scivetti, I.; Repp, J.; Gross, L.; Persson, M.; Meyer, G. Reorganization Energy upon Charging a Single Molecule on an Insulator Measured by Atomic Force Microscopy. *Nat. Nanotechnol.* **2018**, *13* (5), 376–380. https://doi.org/10.1038/s41565-018-0087-1.

(79)   Newton, M. Electron Transfer Reactions in Condensed Phases. *Annu. Rev. Phys. Chem.* **1984**, *35* (1), 437–480. https://doi.org/10.1146/annurev.physchem.35.1.437.

(80)   Spencer, J.; Scalfi, L.; Carof, A.; Blumberger, J. Confronting Surface Hopping Molecular Dynamics with Marcus Theory for a Molecular Donor-Acceptor System. *Faraday Discuss.* **2016**, *195*, 215–236. https://doi.org/10.1039/c6fd00107f.

(81)   Landau, L. D. A. Theory of Energy Transfer on Collisions. *Phys. Z. Sowjetunion* **1932**, *1*, 88. https://doi.org/10.1016/B978-0-08-010586-4.50012-2.

(82)   Landau, L. D. A. Theory of Energy Transfer on Collisions II. *Phys. Z. Sowjetunion* **1932**, *2*, 46.

(83)   Zener, C. Non\hyphen Adiabatic Crossing of Energy Levels. *Proc. Roy. Soc. A* **1932**, *33* (1929), 696–702.

(84)   Brédas, J. L.; Beljonne, D.; Coropceanu, V.; Cornil, J. Charge-Transfer and Energy-Transfer Processes in π-Conjugated Oligomers and Polymers: A Molecular Picture. *Chem. Rev.* **2004**, *104* (11), 4971–5003. https://doi.org/10.1021/cr040084k.

(85)   Geng, Y.; Wu, S. X.; Li, H. Bin; Tang, X. D.; Wu, Y.; Su, Z. M.; Liao, Y. A Theoretical

Discussion on the Relationships among Molecular Packings, Intermolecular Interactions, and Electron Transport Properties for Naphthalene Tetracarboxylic Diimide Derivatives. *J. Mater. Chem.* **2011**, *21* (39), 15558–15566. https://doi.org/10.1039/c1jm12483h.

(86)   Schober, C.; Reuter, K.; Oberhofer, H. Virtual Screening for High Carrier Mobility in Organic Semiconductors. *J. Phys. Chem. Lett.* **2016**, *7* (19), 3973–3977. https://doi.org/10.1021/acs.jpclett.6b01657.

(87)   Sosorev, A. Y. Role of Intermolecular Charge Delocalization and Its Dimensionality in Efficient Band-like Electron Transport in Crystalline 2,5-Difluoro-7,7,8,8-Tetracyanoquinodimethane (F2-TCNQ). *Phys. Chem. Chem. Phys.* **2017**, *19* (37), 25478–25486. https://doi.org/10.1039/c7cp04357k.

(88)   Troisi, A. The Speed Limit for Sequential Charge Hopping in Molecular Materials. *Org. Electron.* **2011**, *12* (12), 1988–1991. https://doi.org/10.1016/j.orgel.2011.08.020.

(89)   Li, X.; Tully, J. C.; Schlegel, H. B.; Frisch, M. J. Ab Initio Ehrenfest Dynamics. *J. Chem. Phys.* **2005**, *123* (8). https://doi.org/10.1063/1.2008258.

(90)   Tully, J. C. Molecular Dynamics with Electronic Transitions. *J. Chem. Phys.* **1990**, *93* (2), 1061–1071. https://doi.org/10.1063/1.459170.

(91)   Blancafort, L.; Hunt, P.; Robb, M. A. Intramolecular Electron Transfer in Bis(Methylene) Adamantyl Radical Cation: A Case Study of Diabatic Trapping. *J. Am. Chem. Soc.* **2005**, *127* (10), 3391–3399. https://doi.org/10.1021/ja043879h.

(92)   Plasser, F.; Lischka, H. Semiclassical Dynamics Simulations of Charge Transport in Stacked -Systems. *J. Chem. Phys.* **2011**, *134* (3). https://doi.org/10.1063/1.3526697.

(93)   Tran, T.; Prlj, A.; Lin, K. H.; Hollas, D.; Corminboeuf, C. Mechanisms of Fluorescence Quenching in Prototypical Aggregation-Induced Emission Systems: Excited State Dynamics with TD-DFTB. *Phys. Chem. Chem. Phys.* **2019**, *21* (18), 9026–9035. https://doi.org/10.1039/c9cp00691e.

(94)   Ziogos, O. G.; Giannini, S.; Ellis, M.; Blumberger, J. Identifying High-Mobility Tetracene Derivatives Using a Non-Adiabatic Molecular Dynamics Approach. *J. Mater. Chem. C* **2020**, *8* (3), 1054–1064. https://doi.org/10.1039/c9tc05270d.

(95)   Gryn'Ova, G.; Lin, K. H.; Corminboeuf, C. Read between the Molecules: Computational Insights into Organic Semiconductors. *J. Am. Chem. Soc.* **2018**, *140* (48), 16370–16386. https://doi.org/10.1021/jacs.8b07985.

(96)   Chi, W. J.; Li, Q. S.; Li, Z. S. Exploring the Electrochemical Properties of Hole Transport Materials with Spiro-Cores for Efficient Perovskite Solar Cells from First-Principles. *Nanoscale* **2016**, *8* (11), 6146–6154. https://doi.org/10.1039/c6nr00235h.

(97)   Li, Y.; Gryn'ova, G.; Saenz, F.; Jeanbourquin, X.; Sivula, K.; Corminboeuf, C.; Waser, J. Heterotetracenes: Flexible Synthesis and in Silico Assessment of the Hole-Transport Properties. *Chem. - A Eur. J.* **2017**, *23* (33), 8058–8065. https://doi.org/10.1002/chem.201701139.

(98)   Chi, W.-J.; Li, Q.-S.; Li, Z.-S. Exploring the Electrochemical Properties of Hole Transport Materials with Spiro-Cores for Efficient Perovskite Solar Cells from First-Principles. *Nanoscale* **2016**, *8* (11), 6146–6154. https://doi.org/10.1039/C6NR00235H.

(99)   Gryn'ova, G.; Corminboeuf, C. Implications of Charge Penetration for Heteroatom-Containing Organic Semiconductors. *J. Phys. Chem. Lett.* **2016**, *7* (24), 5198–5204. https://doi.org/10.1021/acs.jpclett.6b02585.

(100)   Illig, S.; Eggeman, A. S.; Troisi, A.; Jiang, L.; Warwick, C.; Nikolka, M.; Schweicher, G.; Yeates, S. G.; Henri Geerts, Y.; Anthony, J. E.; Sirringhaus, H. Reducing Dynamic Disorder in Small-Molecule Organic Semiconductors by Suppressing Large-Amplitude Thermal Motions. *Nat. Commun.* **2016**, *7*, 1–10. https://doi.org/10.1038/ncomms10736.

(101)   Troisi, A. Prediction of the Absolute Charge Mobility of Molecular Semiconductors: The Case of Rubrene. *Adv. Mater.* **2007**, *19* (15), 2000–2004. https://doi.org/10.1002/adma.200700550.

(102)   Giannini, S.; Carof, A.; Ellis, M.; Yang, H.; Ziogos, O. G.; Ghosh, S.; Blumberger, J. Quantum Localization and Delocalization of Charge Carriers in Organic Semiconducting Crystals. *Nat. Commun.* **2019**, *10* (1), 1–12. https://doi.org/10.1038/s41467-019-11775-9.

(103)   Kordt, P.; Van Der Holst, J. J. M.; Al Helwi, M.; Kowalsky, W.; May, F.; Badinski, A.; Lennartz, C.; Andrienko, D. Modeling of Organic Light Emitting Diodes: From Molecular to Device Properties. *Adv. Funct. Mater.* **2015**, *25* (13), 1955–1971. https://doi.org/10.1002/adfm.201403004.

(104)   Kotadiya, N. B.; Mondal, A.; Xiong, S.; Blom, P. W. M.; Andrienko, D.; Wetzelaer, G. J. A. H. Rigorous Characterization and Predictive Modeling of Hole Transport in Amorphous Organic Semiconductors. *Adv. Electron. Mater.* **2018**, *4* (12), 1–7. https://doi.org/10.1002/aelm.201800366.

(105)   Chen, T.-J.; Kuo, C.-L. Structural, Electronic, and Dielectric Properties of Amorphous Hafnium Silicates. *J. Appl. Phys.* **2011**, *110* (11), 114105. https://doi.org/10.1063/1.3664780.

(106)   Alberga, D.; Mangiatordi, G. F.; Lattanzi, G.; Adamo, C.; Fisica, D.; Aldo, B.; Orabona, V.; Bari, I.-; Scienze, F.; Aldo, B.; Orabona, V.; Bari, I.-. Theoretical Investigation of Hole Transporter Materials for Energy Devices. **2015**. https://doi.org/10.1021/acs.jpcc.5b08981.

(107)   Schrader, M.; Christian, K.; Andrienko, D. Charge Transport in Amorphous and Smectic Mesophases of Dicyanovinyl- Substituted Oligothiophenes †. **2012**, 22258–22264. https://doi.org/10.1039/c2jm34837c.

(108)   Neumann, T.; Danilov, D.; Lennartz, C.; Wenzel, W. Modeling Disordered Morphologies in Organic Semiconductors. *J. Comput. Chem.* **2013**, *34* (31), 2716–2725. https://doi.org/10.1002/jcc.23445.

(109)   Miller, A.; Abrahams, E. Impurity Conduction at Low Concentrations. *Phys. Rev.* **1960**, *120* (3), 745–755. https://doi.org/10.1103/PhysRev.120.745.

(110)   De Vries, X.; Friederich, P.; Wenzel, W.; Coehoorn, R.; Bobbert, P. A. Full Quantum Treatment of Charge Dynamics in Amorphous Molecular Semiconductors. *Phys. Rev. B* **2018**,

97 (7), 1–10. https://doi.org/10.1103/PhysRevB.97.075203.

(111)   McMahon, D. P.; Troisi, A. Evaluation of the External Reorganization Energy of Polyacenes. *J. Phys. Chem. Lett.* **2010**, *1* (6), 941–946. https://doi.org/10.1021/jz1001049.

(112)   Loco, D.; Polack, É.; Caprasecca, S.; Lagardère, L.; Lipparini, F.; Piquemal, J. P.; Mennucci, B. A QM/MM Approach Using the AMOEBA Polarizable Embedding: From Ground State Energies to Electronic Excitations. *J. Chem. Theory Comput.* **2016**, *12* (8), 3654–3661. https://doi.org/10.1021/acs.jctc.6b00385.

(113)   Kaduk, B.; Kowalczyk, T.; Van Voorhis, T. Constrained Density Functional Theory. *Chem. Rev.* **2012**, *112* (1), 321–370. https://doi.org/10.1021/cr200148b.

(114)   Geng, H.; Niu, Y.; Peng, Q.; Shuai, Z.; Coropceanu, V.; Brédas, J. L. Theoretical Study of Substitution Effects on Molecular Reorganization Energy in Organic Semiconductors. *J. Chem. Phys.* **2011**, *135* (10). https://doi.org/10.1063/1.3632105.

(115)   Reimers, J. R. A Practical Method for the Use of Curvilinear Coordinates in Calculations of Normal-Mode-Projected Displacements and Duschinsky Rotation Matrices for Large Molecules. *J. Chem. Phys.* **2001**, *115* (20), 9103–9109. https://doi.org/10.1063/1.1412875.

(116)   Coropceanu, V.; Cornil, J.; da Silva Filho, D. A.; Olivier, Y.; Silbey, R.; Brédas, J. L. Charge Transport in Organic Semiconductors. *Chem. Rev.* **2007**, *107* (4), 926–952. https://doi.org/10.1021/cr050140x.

(117)   Sánchez-Carrera, R. S.; Paramonov, P.; Day, G. M.; Coropceanu, V.; Brédas, J. L. Interaction of Charge Carriers with Lattice Vibrations in Oligoacene Crystals from Naphthalene to Pentacene. *J. Am. Chem. Soc.* **2010**, *132* (41), 14437–14446. https://doi.org/10.1021/ja1040732.

(118)   Martinelli, N. G.; Idé, J.; Sánchez-Carrera, R. S.; Coropceanu, V.; Brédas, J. L.; Ducasse, L.; Castet, F.; Cornil, J.; Beljonne, D. Influence of Structural Dynamics on Polarization Energies in Anthracene Single Crystals. *J. Phys. Chem. C* **2010**, *114* (48), 20678–20685. https://doi.org/10.1021/jp105843t.

(119)   Cave, R. J.; Newton, M. D. Generalization of the Mulliken-Hush Treatment for the Calculation of Electron Transfer Matrix Elements. *Chem. Phys. Lett.* **1996**, *249* (1–2), 15–19. https://doi.org/10.1016/0009-2614(95)01310-5.

(120)   Wu, Q.; Van Voorhis, T. Extracting Electron Transfer Coupling Elements from Constrained Density Functional Theory. *J. Chem. Phys.* **2006**, *125* (16). https://doi.org/10.1063/1.2360263.

(121)   Senthilkumar, K.; Grozema, F. C.; Bickelhaupt, F. M.; Siebbeles, L. D. A. Charge Transport in Columnar Stacked Triphenylenes: Effects of Conformational Fluctuations on Charge Transfer Integrals and Site Energies. *J. Chem. Phys.* **2003**, *119* (18), 9809–9817. https://doi.org/10.1063/1.1615476.

(122)   Pavanello, M.; Neugebauer, J. Modelling Charge Transfer Reactions with the Frozen Density Embedding Formalism. *J. Chem. Phys.* **2011**, *135* (23). https://doi.org/10.1063/1.3666005.

(123)   Kubas, A.; Gajdos, F.; Heck, A.; Oberhofer, H.; Elstner, M.; Blumberger, J. Electronic

Couplings for Molecular Charge Transfer: Benchmarking CDFT, FODFT and FODFTB against High-Level Ab Initio Calculations. II. *Phys. Chem. Chem. Phys.* **2015**, *17* (22), 14342–14354. https://doi.org/10.1039/c4cp04749d.

(124) Kubas, A.; Hoffmann, F.; Heck, A.; Oberhofer, H.; Elstner, M.; Blumberger, J. Electronic Couplings for Molecular Charge Transfer: Benchmarking CDFT, FODFT, and FODFTB against High-Level Ab Initio Calculations. *J. Chem. Phys.* **2014**, *140* (10). https://doi.org/10.1063/1.4867077.

(125) Alkan, M.; Yavuz, I. Intrinsic Charge-Mobility in Benzothieno[3,2- b] [1]Benzothiophene (BTBT) Organic Semiconductors Is Enhanced with Long Alkyl Side-Chains. *Phys. Chem. Chem. Phys.* **2018**, *20* (23), 15970–15979. https://doi.org/10.1039/c8cp01640b.

(126) Kirkpatrick, J. An Approximate Method for Calculating Transfer Integrals Based on the ZINDO Hamiltonian. *Int. J. Quantum Chem.* **2008**, *108* (1), 51–56. https://doi.org/10.1002/qua.21378.

(127) Valeev, E. F.; Coropceanu, V.; da Silva Filho, D. A.; Salman, S.; Brédas, J.-L. Effect of Electronic Polarization on Charge-Transport Parameters in Molecular Organic Semiconductors. *J. Am. Chem. Soc.* **2006**, *128* (30), 9882–9886. https://doi.org/10.1021/ja061827h.

(128) Baumeier, B.; Kirkpatrick, J.; Andrienko, D. Density-Functional Based Determination of Intermolecular Charge Transfer Properties for Large-Scale Morphologies. *Phys. Chem. Chem. Phys.* **2010**, *12* (36), 11103–11113. https://doi.org/10.1039/c002337j.

(129) de Silva, P.; Van Voorhis, T. QM/MM Study of Static and Dynamic Energetic Disorder in the Emission Layer of an Organic Light-Emitting Diode. *J. Phys. Chem. Lett.* **2018**, *9* (6), 1329–1334. https://doi.org/10.1021/acs.jpclett.8b00040.

(130) Schwarze, M.; Tress, W.; Beyer, B.; Gao, F.; Scholz, R.; Poelking, C.; Ortstein, K.; Gunther, A. A.; Kasemann, D.; Andrienko, D.; Leo, K. Band Structure Engineering in Organic Semiconductors. *Science (80-.).* **2016**, *352* (6292), 1446–1449. https://doi.org/10.1126/science.aaf0590.

(131) Schwarze, M.; Schellhammer, K. S.; Ortstein, K.; Benduhn, J.; Gaul, C.; Hinderhofer, A.; Perdigón Toro, L.; Scholz, R.; Kublitski, J.; Roland, S.; Lau, M.; Poelking, C.; Andrienko, D.; Cuniberti, G.; Schreiber, F.; Neher, D.; Vandewal, K.; Ortmann, F.; Leo, K. Impact of Molecular Quadrupole Moments on the Energy Levels at Organic Heterojunctions. *Nat. Commun.* **2019**, *10* (1), 1–9. https://doi.org/10.1038/s41467-019-10435-2.

(132) Sun, H.; Ryno, S.; Zhong, C.; Ravva, M. K.; Sun, Z.; Körzdörfer, T.; Brédas, J. L. Ionization Energies, Electron Affinities, and Polarization Energies of Organic Molecular Crystals: Quantitative Estimations from a Polarizable Continuum Model (PCM)-Tuned Range-Separated Density Functional Approach. *J. Chem. Theory Comput.* **2016**, *12* (6), 2906–2916. https://doi.org/10.1021/acs.jctc.6b00225.

(133) Cochrane, K. A.; Schiffrin, A.; Roussy, T. S.; Capsoni, M.; Burke, S. A. Pronounced Polarization-Induced Energy Level Shifts at Boundaries of Organic Semiconductor

Nanostructures. *Nat. Commun.* **2015**, *6*. https://doi.org/10.1038/ncomms9312.

(134) Tsiper, E. V.; Soos, Z. G. Charge Redistribution and Polarization Energy of Organic Molecular Crystals. *Phys. Rev. B - Condens. Matter Mater. Phys.* **2001**, *64* (19), 1–12. https://doi.org/10.1103/PhysRevB.64.195124.

(135) Difley, S.; Wang, L. P.; Yeganeh, S.; Yost, S. R.; Voorhis, T. Van. Electronic Properties of Disordered Organic Semiconductors via QM/MM Simulations. *Acc. Chem. Res.* **2010**, *43* (7), 995–1004. https://doi.org/10.1021/ar900246s.

(136) Friederich, P.; Symalla, F.; Meded, V.; Neumann, T.; Wenzel, W. Ab Initio Treatment of Disorder Effects in Amorphous Organic Materials: Toward Parameter Free Materials Simulation. *J. Chem. Theory Comput.* **2014**, *10* (9), 3720–3725. https://doi.org/10.1021/ct500418f.

(137) Thole, B. T. Molecular Polarizabilities Calculated with a Modified Dipole Interaction. *Chem. Phys.* **1981**, *59* (3), 341–350. https://doi.org/10.1016/0301-0104(81)85176-2.

(138) Applequist, J.; Carl, J. R.; Fung, K. K. An Atom Dipole Interaction Model for Molecular Polarizability. Application to Polyatomic Molecules and Determination of Atom Polarizabilities. *J. Am. Chem. Soc.* **1972**, *94* (9), 2952–2960. https://doi.org/10.1021/ja00764a010.

(139) Ponder, J. W.; Wu, C.; Ren, P.; Pande, V. S.; Chodera, J. D.; Schnieders, M. J.; Haque, I.; Mobley, D. L.; Lambrecht, D. S.; Distasio, R. A.; Head-Gordon, M.; Clark, G. N. I.; Johnson, M. E.; Head-Gordon, T. Current Status of the AMOEBA Polarizable Force Field. *J. Phys. Chem. B* **2010**, *114* (8), 2549–2564. https://doi.org/10.1021/jp910674d.

(140) Stone, A. *The Theory of Intermolecular Forces*; Oxford University Press, 2013. https://doi.org/10.1093/acprof:oso/9780199672394.001.0001.

(141) Ren, P.; Ponder, J. W. Polarizable Atomic Multipole Water Model for Molecular Mechanics Simulation. *J. Phys. Chem. B* **2003**, *107* (24), 5933–5947. https://doi.org/10.1021/jp027815+.

(142) Jansen, A. P. J. *An Introduction to Kinetic Monte Carlo Simulations of Surface Reactions*; Springer, Berlin, Heidelberg, 2012. https://doi.org/10.1007/978-3-642-14382-3_1.

(143) Maula, T. A.; Hatch, H. W.; Shen, V. K.; Rangarajan, S.; Mittal, J. Designing Molecular Building Blocks for the Self-Assembly of Complex Porous Networks. *Mol. Syst. Des. Eng.* **2019**, *4* (3), 644–653. https://doi.org/10.1039/c9me00006b.

(144) Merkle, R. C. Molecular Building Blocks and Development Strategies for Molecular Nanotechnology. *Nanotechnology* **2000**, *11* (2), 89–99. https://doi.org/10.1088/0957-4484/11/2/309.

(145) Bureš, F. Fundamental Aspects of Property Tuning in Push-Pull Molecules. *RSC Adv.* **2014**, *4* (102), 58826–58851. https://doi.org/10.1039/c4ra11264d.

(146) Vela, S.; Krüger, C.; Corminboeuf, C. Exploring Chemical Space in the Search for Improved Azoheteroarene-Based Photoswitches. *Phys. Chem. Chem. Phys.* **2019**, *21* (37), 20782–20790. https://doi.org/10.1039/c9cp03831k.

(147) Huix-Rotllant, M.; Ferré, N. An Effective Procedure for Analyzing Molecular Vibrations in Terms of Local Fragment Modes. *J. Chem. Theory Comput.* **2016**, *12* (10), 4768–4777. https://doi.org/10.1021/acs.jctc.6b00514.

(148) Green, M. A.; Ho-Baillie, A.; Snaith, H. J. The Emergence of Perovskite Solar Cells. *Nat. Photonics* **2014**, *8* (7), 506–514. https://doi.org/Doi 10.1038/Nphoton.2014.134.

(149) Williams, S. T.; Rajagopal, A.; Chueh, C. C.; Jen, A. K. Y. Current Challenges and Prospective Research for Upscaling Hybrid Perovskite Photovoltaics. *J. Phys. Chem. Lett.* **2016**, *7* (5), 811–819. https://doi.org/10.1021/acs.jpclett.5b02651.

(150) Grätzel, M. The Light and Shade of Perovskite Solar Cells. *Nat. Mater.* **2014**, *13* (9), 838–842. https://doi.org/10.1038/nmat4065.

(151) Huang, L.; Sun, X.; Li, C.; Xu, R.; Xu, J.; Du, Y.; Wu, Y.; Ni, J.; Cai, H.; Li, J.; Hu, Z.; Zhang, J. Electron Transport Layer-Free Planar Perovskite Solar Cells: Further Performance Enhancement Perspective from Device Simulation. *Sol. Energy Mater. Sol. Cells* **2016**, *157*, 1038–1047. https://doi.org/10.1016/j.solmat.2016.08.025.

(152) Zhou, H.; Shi, Y.; Dong, Q.; Zhang, H.; Xing, Y.; Wang, K.; Du, Y.; Ma, T. Hole-Conductor-Free, Metal-Electrode-Free TiO2/CH3NH3PbI3 Heterojunction Solar Cells Based on a Low-Temperature Carbon Electrode. *J. Phys. Chem. Lett.* **2014**, *5* (18), 3241–3246. https://doi.org/10.1021/jz5017069.

(153) Stranks, S. D.; Eperon, G. E.; Grancini, G.; Menelaou, C.; Alcocer, M. J. P.; Leijtens, T.; Herz, L. M.; Petrozza, A.; Snaith, H. J. Electron-Hole Diffusion Lengths Exceeding 1 Micrometer in an Organometal Trihalide Perovskite Absorber. *Science.* **2013**, *342* (6156), 341–344. https://doi.org/10.1126/science.1243982.

(154) Dongxue, L.; Liu, Y. Recent Progress of Dopant-Free Organic Hole-Transporting Materials in Perovskite Solar Cells. *J. Semicond.* **2017**, *38* (1), 011005. https://doi.org/10.1088/1674-4926/38/1/011005.

(155) Chi, W.; Sun, P.-P.; Li, Z.-S. A Strategy to Improve the Efficiency of Hole Transporting Materials: Introduction of a Highly Symmetrical Core. *Nanoscale* **2016**, *8* (41), 17752–17756. https://doi.org/10.1039/C6NR06116H.

(156) Saliba, M.; Orlandi, S.; Matsui, T.; Aghazada, S.; Cavazzini, M.; Correa-Baena, J.-P.; Gao, P.; Scopelliti, R.; Mosconi, E.; Dahmen, K.-H.; De Angelis, F.; Abate, A.; Hagfeldt, A.; Pozzi, G.; Graetzel, M.; Nazeeruddin, M. K. A Molecularly Engineered Hole-Transporting Material for Efficient Perovskite Solar Cells. *Nat. Energy* **2016**, *1* (2), 15017. https://doi.org/10.1038/nenergy.2015.17.

(157) Kim, H.-S.; Lee, C.-R.; Im, J.-H.; Lee, K.-B.; Moehl, T.; Marchioro, A.; Moon, S.-J.; Humphry-Baker, R.; Yum, J.-H.; Moser, J. E.; Grätzel, M.; Park, N.-G. Lead Iodide Perovskite Sensitized All-Solid-State Submicron Thin Film Mesoscopic Solar Cell with Efficiency Exceeding 9%. *Sci. Rep.* **2012**, *2* (1), 591. https://doi.org/10.1038/srep00591.

(158) Ganesan, P.; Fu, K.; Gao, P.; Raabe, I.; Schenk, K.; Scopelliti, R.; Luo, J.; Wong, L. H.;

Grätzel, M.; Nazeeruddin, M. K. A Simple Spiro-Type Hole Transporting Material for Efficient Perovskite Solar Cells. *Energy Environ. Sci.* **2015**, *8* (7), 1986–1991. https://doi.org/10.1039/C4EE03773A.

(159) Zhang, F.; Liu, X.; Yi, C.; Bi, D.; Luo, J.; Wang, S.; Li, X.; Xiao, Y.; Zakeeruddin, S. M.; Grätzel, M. Dopant-Free Donor (D)-π-D-π-D Conjugated Hole-Transport Materials for Efficient and Stable Perovskite Solar Cells. *ChemSusChem* **2016**, *9* (18), 2578–2585. https://doi.org/10.1002/cssc.201600905.

(160) Xue, Y.; Wu, Y.; Li, Y. Readily Synthesized Dopant-Free Hole Transport Materials with Phenol Core for Stabilized Mixed Perovskite Solar Cells. *J. Power Sources* **2017**, *344*, 160–169. https://doi.org/10.1016/j.jpowsour.2017.01.121.

(161) Swetha, T.; Singh, S. P. Perovskite Solar Cells Based on Small Molecules Hole Transporting Materials. *J. Mater. Chem. A* **2015**, *00*, 1–16. https://doi.org/10.1039/C5TA02507A.

(162) Poplavskyy, D.; Nelson, J. Nondispersive Hole Transport in Amorphous Films of Methoxy-Spirofluorene-Arylamine Organic Compound. *J. Appl. Phys.* **2003**, *93* (1), 341–346. https://doi.org/10.1063/1.1525866.

(163) Xi, H.; Tang, S.; Ma, X.; Chang, J.; Chen, D.; Lin, Z.; Zhong, P.; Wang, H.; Zhang, C. Performance Enhancement of Planar Heterojunction Perovskite Solar Cells through Tuning the Doping Properties of Hole-Transporting Materials. *ACS Omega* **2017**, *2* (1), 326–336. https://doi.org/10.1021/acsomega.6b00465.

(164) Jeon, N. J.; Lee, J.; Noh, J. H.; Nazeeruddin, K.; Grätzel, M.; Seok, S. Il; Nazeeruddin, M. K.; Grätzel, M.; Seok, S. Il. Efficient Inorganic–Organic Hybrid Perovskite Solar Cells Based on Pyrene Arylamine Derivatives as Hole-Transporting Materials. *J. Am. Chem. Soc.* **2013**, *135* (51), 19087–19090. https://doi.org/10.1021/ja410659k.

(165) Liu, J.; Wu, Y.; Qin, C.; Yang, X.; Yasuda, T.; Islam, A.; Zhang, K.; Peng, W.; Chen, W.; Han, L. A Dopant-Free Hole-Transporting Material for Efficient and Stable Perovskite Solar Cells. *Energy Environ. Sci.* **2014**, *7*, 2963–2967. https://doi.org/10.1039/C4EE01589D.

(166) Kazim, S.; Ramos, F. J.; Gao, P.; Nazeeruddin, M. K.; Grätzel, M.; Ahmad, S. A Dopant Free Linear Acene Derivative as a Hole Transport Material for Perovskite Pigmented Solar Cells. *Energy Environ. Sci.* **2015**, *8* (6), 1816–1823. https://doi.org/10.1039/C5EE00599J.

(167) Kim, G.-W.; Kang, G.; Kim, J.; Lee, G. Y.; Kim, H. Il; Pyeon, L.; Lee, J.; Park, T. Dopant-Free Polymeric Hole Transport Material for Highly Efficient and Stable Perovskite Solar Cells. *Energy Environ. Sci.* **2016**, *9* (7), 2326–2333. https://doi.org/10.1039/C6EE00709K.

(168) Liu, Y.; Chen, Q.; Duan, H.-S.; Zhou, H.; Yang, Y.; Chen, H.; Luo, S.; Song, T.-B.; Dou, L.; Hong, Z.; Yang, Y. A Dopant-Free Organic Hole Transport Material for Efficient Planar Heterojunction Perovskite Solar Cells. *J. Mater. Chem. A* **2015**, *3* (22), 11940–11947. https://doi.org/10.1039/c5ta02502h.

(169) Zhang, F.; Yi, C.; Wei, P.; Bi, X.; Luo, J.; Jacopin, G.; Wang, S.; Li, X.; Xiao, Y.; Zakeeruddin, S. M.; Grätzel, M. A Novel Dopant-Free Triphenylamine Based Molecular

"Butterfly" Hole-Transport Material for Highly Efficient and Stable Perovskite Solar Cells. *Adv. Energy Mater.* **2016**, *6* (14), 1600401. https://doi.org/10.1002/aenm.201600401.

(170) Huang, C.; Fu, W.; Li, C. Z.; Zhang, Z.; Qiu, W.; Shi, M.; Heremans, P.; Jen, A. K. Y.; Chen, H. Dopant-Free Hole-Transporting Material with a C3h Symmetrical Truxene Core for Highly Efficient Perovskite Solar Cells. *J. Am. Chem. Soc.* **2016**, *138* (8), 2528–2531. https://doi.org/10.1021/jacs.6b00039.

(171) Liu, J.; Wu, Y.; Qin, C.; Yang, X.; Yasuda, T.; Islam, A.; Zhang, K.; Peng, W.; Chen, W.; Han, L. A Dopant-Free Hole-Transporting Material for Efficient and Stable Perovskite Solar Cells. *Energy Environ. Sci.* **2014**, *7*, 2963–2967. https://doi.org/10.1039/C4EE01589D.

(172) Rakstys, K.; Abate, A.; Dar, M. I.; Gao, P.; Jankauskas, V.; Jacopin, G.; Kamarauskas, E.; Kazim, S.; Ahmad, S.; Grätzel, M.; Nazeeruddin, M. K. Triazatruxene-Based Hole Transporting Materials for Highly Efficient Perovskite Solar Cells. *J. Am. Chem. Soc.* **2015**, *137* (51), 16172–16178. https://doi.org/10.1021/jacs.5b11076.

(173) Wang, J.; Chen, Y.; Liang, M.; Ge, G.; Zhou, R.; Sun, Z.; Xue, S. A New Thermal-Stable Truxene-Based Hole-Transporting Material for Perovskite Solar Cells. *Dye. Pigment.* **2016**, *125*, 399–406. https://doi.org/10.1016/j.dyepig.2015.11.004.

(174) Goubard, F.; Dumur, F. Truxene: A Promising Scaffold for Future Materials. *RSC Adv.* **2015**, *5*, 3521–3551. https://doi.org/10.1039/C4RA11559G.

(175) Li, X.-C.; Zhang, Y.; Wang, C.-Y.; Wan, Y.; Lai, W.-Y.; Pang, H.; Huang, W. Redox-Active Triazatruxene-Based Conjugated Microporous Polymers for High-Performance Supercapacitors. *Chem. Sci.* **2017**, *8* (4), 2959–2965. https://doi.org/10.1039/C6SC05532J.

(176) Ramos, F. J.; Rakstys, K.; Kazim, S.; Gratzel, M.; Nazeeruddin, M. K.; Ahmad, S. Rational Design of Triazatruxene-Based Hole Conductors for Perovskite Solar Cells. *RSC Adv.* **2015**, *5* (66), 53426–53432. https://doi.org/10.1039/C5RA06876B.

(177) Petrikyte, I.; Zimmermann, I.; Rakstys, K.; Daskeviciene, M.; Malinauskas, T.; Jankauskas, V.; Getautis, V.; Nazeeruddin, M. K. Efficiency Enhancement of Perovskite Solar Cells via Incorporation of Phenylethenyl Side Arms into Indolocarbazole-Based Hole Transporting Materials. *Nanoscale* **2016**, *8* (16), 8530–8535. https://doi.org/10.1039/C6NR01275B.

(178) Rakstys, K.; Paek, S.; Gao, P.; Gratia, P.; Marszalek, T.; Grancini, G.; Cho, K. T.; Genevicius, K.; Jankauskas, V.; Pisula, W.; Nazeeruddin, M. K. Molecular Engineering of Face-on Oriented Dopant-Free Hole Transporting Material for Perovskite Solar Cells with 19% PCE. *J. Mater. Chem. A* **2017**, *5* (17), 7811–7815. https://doi.org/10.1039/C7TA01718A.

(179) Su, P.-Y.; Huang, L.-B.; Liu, J.-M.; Chen, Y.-F.; Xiao, L.-M.; Kuang, D.-B.; Mayor, M.; Su, C.-Y. A Multifunctional Poly-N-Vinylcarbazole Interlayer in Perovskite Solar Cells for High Stability and Efficiency: A Test with New Triazatruxene-Based Hole Transporting Materials. *J. Mater. Chem. A* **2017**, *5* (5), 1913–1918. https://doi.org/10.1039/C6TA09314K.

(180) Alberga, D.; Mangiatordi, G. F.; Labat, F.; Ciofini, I.; Nicolotti, O.; Lattanzi, G.; Adamo, C. Theoretical Investigation of Hole Transporter Materials for Energy Devices. *J. Phys. Chem. C*

2015, *119* (42), 23890–23898. https://doi.org/10.1021/acs.jpcc.5b08981.

(181) Petrus, M. L.; Bein, T.; Dingemans, T. J.; Docampo, P. A Low Cost Azomethine-Based Hole Transporting Material for Perovskite Photovoltaics. *J. Mater. Chem. A* **2015**, *3* (23), 12159–12162. https://doi.org/10.1039/C5TA03046C.

(182) Ryu, S.; Noh, J. H.; Jeon, N. J.; Kim, Y. C.; Yang, W. S.; Seo, J.; Seok, S. Il. Voltage Output of Efficient Perovskite Solar Cells with High Open-Circuit Voltage and Fill Factor. *Energy Environ. Sci.* **2014**, *7*, 2614–2618. https://doi.org/10.1039/C4EE00762J.

(183) Antoine, K. Fermi Level, Work Function and Vacuum Level. *Mater. Horizons* **2015**, *1* (1), 96. https://doi.org/10.1039/c3mh00043e.

(184) Bredas, J.-L. Mind the Gap! *Mater. Horiz.* **2014**, *1* (1), 17–19. https://doi.org/10.1039/C3MH00098B.

(185) Polander, L. E.; Pahner, P.; Schwarze, M.; Saalfrank, M.; Koerner, C.; Leo, K. Hole-Transport Material Variation in Fully Vacuum Deposited Perovskite Solar Cells. *APL Mater.* **2014**, *2* (8), 081503. https://doi.org/10.1063/1.4889843.

(186) Savva, A.; Burgués-Ceballos, I.; Choulis, S. A. Improved Performance and Reliability of P-i-n Perovskite Solar Cells via Doped Metal Oxides. *Adv. Energy Mater.* **2016**, *6* (18), 1600285. https://doi.org/10.1002/aenm.201600285.

(187) Jiang, Y.; Almansouri, I.; Huang, S.; Young, T.; Li, Y.; Peng, Y.; Hou, Q.; Spiccia, L.; Bach, U.; Cheng, Y.-B.; Green, M.; Ho-Baillie, A. Optical Analysis of Perovskite/Silicon Tandem Solar Cells. *J. Mater. Chem. C* **2016**, *4*, 5679–5689. https://doi.org/10.1039/C6TC01276K.

(188) Chi, W.-J.; Li, Q.-S.; Li, Z.-S. Effects of Molecular Configuration on Charge Diffusion Kinetics within Hole-Transporting Materials for Perovskites Solar Cells. *J. Phys. Chem. C* **2015**, *119* (16), 8584–8590. https://doi.org/10.1021/acs.jpcc.5b02401.

(189) Leijtens, T.; Giovenzana, T.; Habisreutinger, S. N.; Tinkham, J. S.; Noel, N. K.; Kamino, B. A.; Sadoughi, G.; Sellinger, A.; Snaith, H. J. Hydrophobic Organic Hole Transporters for Improved Moisture Resistance in Metal Halide Perovskite Solar Cells. *ACS Appl. Mater. Interfaces* **2016**, *8* (9), 5981–5989. https://doi.org/10.1021/acsami.5b10093.

(190) Zheng, L.; Chung, Y.-H.; Ma, Y.; Zhang, L.; Xiao, L.; Chen, Z.; Wang, S.; Qu, B.; Gong, Q. A Hydrophobic Hole Transporting Oligothiophene for Planar Perovskite Solar Cells with Improved Stability. *Chem. Commun.* **2014**, *50* (76), 11196. https://doi.org/10.1039/C4CC04680C.

(191) Kwon, Y. S.; Lim, J.; Yun, H.-J.; Kim, Y.-H.; Park, T. A Diketopyrrolopyrrole-Containing Hole Transporting Conjugated Polymer for Use in Efficient Stable Organic–Inorganic Hybrid Solar Cells Based on a Perovskite. *Energy Environ. Sci.* **2014**, *7* (4), 1454–1460. https://doi.org/10.1039/c3ee44174a.

(192) Zhang, F.; Zhao, X.; Yi, C.; Bi, D.; Bi, X.; Wei, P.; Liu, X.; Wang, S.; Li, X.; Zakeeruddin, S. M.; Grätzel, M. Dopant-Free Star-Shaped Hole-Transport Materials for Efficient and Stable Perovskite Solar Cells. *Dye. Pigment.* **2017**, *136*, 273–277.

https://doi.org/10.1016/j.dyepig.2016.08.002.

(193) Su, P. Y.; Chen, Y. F.; Liu, J. M.; Xiao, L. M.; Kuang, D. Bin; Mayor, M.; Su, C. Y. Hydrophobic Hole-Transporting Materials Incorporating Multiple Thiophene Cores with Long Alkyl Chains for Efficient Perovskite Solar Cells. *Electrochim. Acta* **2016**, *209*, 529–540. https://doi.org/10.1016/j.electacta.2016.05.122.

(194) Bi, C.; Wang, Q.; Shao, Y.; Yuan, Y.; Xiao, Z.; Huang, J. Non-Wetting Surface-Driven High-Aspect-Ratio Crystalline Grain Growth for Efficient Hybrid Perovskite Solar Cells. *Nat. Commun.* **2015**, *6*, 7747. https://doi.org/10.1038/ncomms8747.

(195) Malinauskas, T.; Tomkute-Luksiene, D.; Sens, R.; Daskeviciene, M.; Send, R.; Wonneberger, H.; Jankauskas, V.; Bruder, I.; Getautis, V. Enhancing Thermal Stability and Lifetime of Solid-State Dye-Sensitized Solar Cells via Molecular Engineering of the Hole-Transporting Material Spiro-OMeTAD. *ACS Appl. Mater. Interfaces* **2015**, *7* (21), 11107–11116. https://doi.org/10.1021/am5090385.

(196) Luo, J.; Zhao, B.; Shao, J.; Lim, K. A.; On Chan, H. S.; Chi, C. Room-Temperature Discotic Liquid Crystals Based on Oligothiophenes—Attached and Fused Triazatruxenes. *J. Mater. Chem.* **2009**, *19* (44), 8327. https://doi.org/10.1039/b913930c.

(197) Kumar, S. Monomeric Discotic Liquid Crystals. In *Chemistry of Discotic Liquid Crystals: From Monomers to Polymers*; Liquid Crystals Book Series; CRC Press, 2010; pp 49–360. https://doi.org/10.1201/b10457-3.

(198) Hutchison, G. R.; Ratner, M. A.; Marks, T. J. Intermolecular Charge Transfer between Heterocyclic Oligomers. Effects of Heteroatom and Molecular Packing on Hopping Transport in Organic Semiconductors. *J. Am. Chem. Soc.* **2005**, *127* (48), 16866–16881. https://doi.org/10.1021/ja0533996.

(199) Gryn'ova, G.; Corminboeuf, C. Implications of Charge Penetration for Heteroatom-Containing Organic Semiconductors. *J. Phys. Chem. Lett.* **2016**, *7* (24), 5198–5204. https://doi.org/10.1021/acs.jpclett.6b02585.

(200) Shelton, S. W.; Chen, T. L.; Barclay, D. E.; Ma, B. Solution-Processable Triindoles as Hole Selective Materials in Organic Solar Cells. *ACS Appl. Mater. Interfaces* **2012**, *4* (5), 2534–2540. https://doi.org/10.1021/am300228w.

(201) Ma, Z.; Geng, H.; Wang, D.; Shuai, Z. Influence of Alkyl Side-Chain Length on the Carrier Mobility in Organic Semiconductors: Herringbone vs. Pi–Pi Stacking. *J. Mater. Chem. C* **2016**, *4* (20), 4546–4555. https://doi.org/10.1039/C6TC00755D.

(202) Cherniawski, B. P.; Lopez, S. A.; Burnett, E. K.; Yavuz, I.; Zhang, L.; Parkin, S. R.; Houk, K. N.; Briseno, A. L. The Effect of Hexyl Side Chains on Molecular Conformations, Crystal Packing, and Charge Transport of Oligothiophenes. *J. Mater. Chem. C* **2017**, *5* (3), 582–588. https://doi.org/10.1039/C6TC04612F.

(203) Zhang, J.; Hua, Y.; Xu, B.; Yang, L.; Liu, P.; Johansson, M. B.; Vlachopoulos, N.; Kloo, L.; Boschloo, G.; Johansson, E. M. J.; Sun, L.; Hagfeldt, A. The Role of 3D Molecular Structural

Control in New Hole Transport Materials Outperforming Spiro-OMeTAD in Perovskite Solar Cells. *Adv. Energy Mater.* **2016**, *6* (19), 1–9. https://doi.org/10.1002/aenm.201601062.

(204) Chi, W.-J.; Li, Q.-S.; Li, Z.-S. Exploring the Electrochemical Properties of Hole Transport Materials with Spiro-Cores for Efficient Perovskite Solar Cells from First-Principles. *Nanoscale* **2016**, *8* (11), 6146–6154. https://doi.org/10.1039/C6NR00235H.

(205) Chi, W.-J.; Sun, P.-P.; Li, Z.-S. How to Regulate Energy Levels and Hole Mobility of Spiro-Type Hole Transport Materials in Perovskite Solar Cells. *Phys. Chem. Chem. Phys.* **2016**, *18*. https://doi.org/10.1039/C6CP03316D.

(206) Rakstys, K.; Paek, S.; Gao, P.; Gratia, P.; Marszalek, T.; Grancini, G.; Cho, K. T.; Genevicius, K.; Jankauskas, V.; Pisula, W.; Nazeeruddin, M. K. Molecular Engineering of Face-on Oriented Dopant-Free Hole Transporting Material for Perovskite Solar Cells with 19% PCE. *J. Mater. Chem. A* **2017**, *5* (17), 7811–7815. https://doi.org/10.1039/C7TA01718A.

(207) Fantacci, S.; Angelis, F. De; Nazeeruddin, M. K.; Grätzel, M. Electronic and Optical Properties of the Spiro- MeOTAD Hole Conductor in Its Neutral and Oxidized Forms : A DFT / TDDFT Investigation. *J. Phys. Chem. C* **2011**, *115* (Ii), 23126–23133. https://doi.org/dx.doi.org/10.1021/jp207968b.

(208) AM1.5 solar spectral irradiance. AM1.5 solar spectral irradiance http://rredc.nrel.gov/solar/spectra/am1.5/ASTMG173/ASTMG173.html (accessed Mar 1, 2017).

(209) Barbara, P. F.; Meyer, T. J.; Ratner, M. a. Contemporary Issues in Electron Transfer Research. *J. Phys. Chem.* **1996**, *100* (31), 13148–13168. https://doi.org/10.1021/jp9605663.

(210) Coehoorn, R.; Pasveer, W. F.; Bobbert, P. A.; Michels, M. A. J. Charge-Carrier Concentration Dependence of the Hopping Mobility in Organic Materials with Gaussian Disorder. *Phys. Rev. B - Condens. Matter Mater. Phys.* **2005**, *72* (15), 1–20. https://doi.org/10.1103/PhysRevB.72.155206.

(211) Rühle, V.; Lukyanov, A.; May, F.; Schrader, M.; Vehoff, T.; Kirkpatrick, J.; Baumeier, B.; Andrienko, D. Microscopic Simulations of Charge Transport in Disordered Organic Semiconductors. *J. Chem. Theory Comput.* **2011**, *7* (10), 3335–3345. https://doi.org/10.1021/ct200388s.

(212) Buchholz, J.; Paul, W.; Varnik, F.; Binder, K. Cooling Rate Dependence of the Glass Transition Temperature of Polymer Melts: Molecular Dynamics Study. *J. Chem. Phys.* **2002**, *117* (15), 7364. https://doi.org/10.1063/1.1508366.

(213) Sonntag, M.; Kreger, K.; Hanft, D.; Strohriegl, P.; Setayesh, S.; de Leeuw, D. Novel Star-Shaped Triphenylamine-Based Molecular Glasses and Their Use in OFETs. *Chem. Mater.* **2005**, *17* (11), 3031–3039. https://doi.org/10.1021/cm047750i.

(214) Rogers, S.; Mandelkern, L. Glass Transitions of the Poly-(n-Alkyl Methacrylates). *J. Phys. Chem.* **1957**, *61* (7), 985–991. https://doi.org/10.1021/j150553a033.

(215) Hildebrand, J. H. The Entropy of Solution of Molecules of Different Size. *J. Chem. Phys.*

1947, *15* (5), 225. https://doi.org/10.1063/1.1746484.

(216) Hansen, C. M. The Three Dimensional Solubility Parameter and Solvent Diffusion Coefficient. Their Importance in Surface Coating Formulation. *J. Paint Technol.* **1967**, *39*, 104.

(217) Tummala, N. R.; Bruner, C.; Risko, C.; Brédas, J.-L.; Dauskardt, R. H. Molecular-Scale Understanding of Cohesion and Fracture in P3HT:Fullerene Blends. *ACS Appl. Mater. Interfaces* **2015**, *7* (18), 9957–9964. https://doi.org/10.1021/acsami.5b02202.

(218) Tummala, N. R.; Mehraeen, S.; Fu, Y.-T.; Risko, C.; Brédas, J.-L. Materials-Scale Implications of Solvent and Temperature on [6,6]-Phenyl-C61-Butyric Acid Methyl Ester (PCBM): A Theoretical Perspective. *Adv. Funct. Mater.* **2013**, *23* (46), 5800–5813. https://doi.org/10.1002/adfm.201300918.

(219) Yalkowsky, S.; He, Y.; Jain, P. *Handbook of Aqueous Solubility Data, Second Edition*; CRC Press, 2010. https://doi.org/10.1201/EBK1439802458.

(220) Stephens, P. J.; Devlin, F. J.; Chabalowski, C. F.; Frisch, M. J. Ab Initio Calculation of Vibrational Absorption and Circular Dichroism Spectra Using Density Functional Force Fields. *J. Phys. Chem.* **1994**, *98* (45), 11623–11627. https://doi.org/10.1021/j100096a001.

(221) Becke, A. D. Density-functional Thermochemistry. III. The Role of Exact Exchange. *J. Chem. Phys.* **1993**, *98* (7), 5648–5652. https://doi.org/10.1063/1.464913.

(222) Grimme, S.; Ehrlich, S.; Goerigk, L. Effect of the Damping Function in Dispersion Corrected Density Functional Theory. *J. Comput. Chem.* **2011**, *32* (7), 1456–1465. https://doi.org/10.1002/jcc.21759.

(223) Frisch, M. J.; Trucks, G. W.; Schlegel, H. B.; Scuseria, G. E.; Robb, M. A.; Cheeseman, J. R.; Scalmani, G.; Barone, V.; Mennucci, B.; Petersson, G. A.; Nakatsuji, H.; Caricato, M.; Li, X.; Hratchian, H. P.; Izmaylov, A. F.; Bloino, J.; Zheng, G.; Sonnenberg, J. L.; Hada, M.; Ehara, M.; Toyota, K.; Fukuda, R.; Hasegawa, J.; Ishida, M.; Nakajima, T.; Honda, Y.; Kitao, O.; Nakai, H.; Vreven, T.; Montgomery Jr., J. A.; Peralta, J. E.; Ogliaro, F.; Bearpark, M.; Heyd, J. J.; Brothers, E.; Kudin, K. N.; Staroverov, V. N.; Kobayashi, R.; Normand, J.; Raghavachari, K.; Rendell, A.; Burant, J. C.; Iyengar, S. S.; Tomasi, J.; Cossi, M.; Rega, N.; Millam, J. M.; Klene, M.; Knox, J. E.; Cross, J. B.; Bakken, V.; Adamo, C.; Jaramillo, J.; Gomperts, R.; Stratmann, R. E.; Yazyev, O.; Austin, A. J.; Cammi, R.; Pomelli, C.; Ochterski, J. W.; Martin, R. L.; Morokuma, K.; Zakrzewski, V. G.; Voth, G. A.; Salvador, P.; Dannenberg, J. J.; Dapprich, S.; Daniels, A. D.; Farkas, Ö.; Foresman, J. B.; Ortiz, J. V; Cioslowski, J.; Fox, D. J. Gaussian 09, Revision D.01. *Gaussian Inc.* **2009**, Wallingford CT. https://doi.org/10.1159/000348293.

(224) Cossi, M.; Rega, N.; Scalmani, G.; Barone, V. Energies, Structures, and Electronic Properties of Molecules in Solution with the C-PCM Solvation Model. *J. Comput. Chem.* **2003**, *24* (6), 669–681. https://doi.org/10.1002/jcc.10189.

(225) Martínez, L.; Andrade, R.; Birgin, E. G.; Martínez, J. M. PACKMOL: A Package for Building Initial Configurations for Molecular Dynamics Simulations. *J. Comput. Chem.* **2009**, *30* (13),

2157–2164. https://doi.org/10.1002/jcc.21224.

(226) Van Der Spoel, D.; Lindahl, E.; Hess, B.; Groenhof, G.; Mark, A. E.; Berendsen, H. J. C. GROMACS: Fast, Flexible, and Free. *J. Comput. Chem.* **2005**, *26* (16), 1701–1718. https://doi.org/10.1002/jcc.20291.

(227) Berendsen, H. J. C.; van der Spoel, D.; van Drunen, R. GROMACS: A Message-Passing Parallel Molecular Dynamics Implementation. *Comput. Phys. Commun.* **1995**, *91* (1–3), 43–56. https://doi.org/10.1016/0010-4655(95)00042-E.

(228) Abraham, M. J.; Murtola, T.; Schulz, R.; Páll, S.; Smith, J. C.; Hess, B.; Lindahl, E. GROMACS: High Performance Molecular Simulations through Multi-Level Parallelism from Laptops to Supercomputers. *SoftwareX* **2015**, *1–2*, 19–25. https://doi.org/10.1016/j.softx.2015.06.001.

(229) Vanommeslaeghe, K.; Hatcher, E.; Acharya, C.; Kundu, S.; Zhong, S.; Shim, J.; Darian, E.; Guvench, O.; Lopes, P.; Vorobyov, I.; Mackerell, A. D. CHARMM General Force Field: A Force Field for Drug-like Molecules Compatible with the CHARMM All-Atom Additive Biological Force Fields. *J. Comput. Chem.* **2009**, *31* (16), NA-NA. https://doi.org/10.1002/jcc.21367.

(230) Yu, W.; He, X.; Vanommeslaeghe, K.; MacKerell, A. D. Extension of the CHARMM General Force Field to Sulfonyl-Containing Compounds and Its Utility in Biomolecular Simulations. *J. Comput. Chem.* **2012**, *33* (31), 2451–2468. https://doi.org/10.1002/jcc.23067.

(231) Bayly, C. I.; Cieplak, P.; Cornell, W.; Kollman, P. a. A Well-Behaved Electrostatic Potential Based Method Using Charge Restraints for Deriving Atomic Charges: The RESP Model. *J. Phys. Chem.* **1993**, *97* (40), 10269–10280. https://doi.org/10.1021/j100142a004.

(232) Bussi, G.; Donadio, D.; Parrinello, M. Canonical Sampling through Velocity Rescaling. *J. Chem. Phys.* **2007**, *126* (1). https://doi.org/10.1063/1.2408420.

(233) Rühle, V.; Junghans, C.; Lukyanov, A.; Kremer, K.; Andrienko, D. Versatile Object-Oriented Toolkit for Coarse-Graining Applications. *J. Chem. Theory Comput.* **2009**, *5* (12), 3211–3223. https://doi.org/10.1021/ct900369w.

(234) Carey, C.; Chirlian, L. E.; Francl, M. M.; Gange, D. M. Beyond CHELP: Improved Potential Derived Charges for Sugars. *Glycoconj. J.* **1997**, *14* (4), 501–505. https://doi.org/10.1023/A:1018511804498.

(235) Liu, H.; Li, Y.; Krause, W. E.; Rojas, O. J.; Pasquinelli, M. A. The Soft-Confined Method for Creating Molecular Models of Amorphous Polymer Surfaces. *J. Phys. Chem. B* **2012**, *116* (5), 1570–1578. https://doi.org/10.1021/jp209024r.

(236) Berendsen, H. J. C.; Postma, J. P. M.; Gunsteren, W. F. van; Hermans, J. *Intermolecular Forces*; Pullman, B., Ed.; Reidel: Dordrecht, 1981.

(237) Hirvi, J. T.; Pakkanen, T. A. Molecular Dynamics Simulations of Water Droplets on Polymer Surfaces. *J. Chem. Phys.* **2006**, *125* (14), 144712. https://doi.org/10.1063/1.2356470.

(238) Kimura, M.; Kuwano, S.; Sawaki, Y.; Fujikawa, H.; Noda, K.; Taga, Y.; Takagi, K. New 9-

132

Fluorene-Type Trispirocyclic Compounds for Thermally Stable Hole Transport Materials in OLEDs. *J. Mater. Chem.* **2005**, *15* (24), 2393. https://doi.org/10.1039/b502268a.

(239) Aonuma, M.; Oyamada, T.; Sasabe, H.; Miki, T.; Adachi, C. Material Design of Hole Transport Materials Capable of Thick-Film Formation in Organic Light Emitting Diodes. *Appl. Phys. Lett.* **2007**, *90* (18), 183503. https://doi.org/10.1063/1.2733627.

(240) Tong, Q. X.; Lai, S. L.; Chan, M. Y.; Lai, K. H.; Tang, J. X.; Kwong, H. L.; Lee, C. S.; Lee, S. T. High Tg Triphenylamine-Based Starburst Hole-Transporting Material for Organic Light-Emitting Devices. *Chem. Mater.* **2007**, *19* (24), 5851–5855. https://doi.org/10.1021/cm0712624.

(241) Jiang, Z.; Ye, T.; Yang, C.; Yang, D.; Zhu, M.; Zhong, C.; Qin, J.; Ma, D. Star-Shaped Oligotriarylamines with Planarized Triphenylamine Core: Solution-Processable, High- T g Hole-Injecting and Hole-Transporting Materials for Organic Light-Emitting Devices. *Chem. Mater.* **2011**, *23* (3), 771–777. https://doi.org/10.1021/cm1018585.

(242) Thelakkat, M. Star-Shaped, Dendrimeric and Polymeric Triarylamines as Photoconductors and Hole Transport Materials for Electro-Optical Applications. *Macromol. Mater. Eng.* **2002**, *287* (7), 442. https://doi.org/10.1002/1439-2054(20020701)287:7<442::AID-MAME442>3.0.CO;2-H.

(243) Leijtens, T.; Ding, I.-K.; Giovenzana, T.; Bloking, J. T.; McGehee, M. D.; Sellinger, A. Hole Transport Materials with Low Glass Transition Temperatures and High Solubility for Application in Solid-State Dye-Sensitized Solar Cells. *ACS Nano* **2012**, *6* (2), 1455–1462. https://doi.org/10.1021/nn204296b.

(244) Planells, M.; Abate, A.; Hollman, D. J.; Stranks, S. D.; Bharti, V.; Gaur, J.; Mohanty, D.; Chand, S.; Snaith, H. J.; Robertson, N. Diacetylene Bridged Triphenylamines as Hole Transport Materials for Solid State Dye Sensitized Solar Cells. *J. Mater. Chem. A* **2013**, *1* (23), 6949–6960. https://doi.org/10.1039/c3ta11417a.

(245) Xu, B.; Sheibani, E.; Liu, P.; Zhang, J.; Tian, H.; Vlachopoulos, N.; Boschloo, G.; Kloo, L.; Hagfeldt, A.; Sun, L. Carbazole-Based Hole-Transport Materials for Efficient Solid-State Dye-Sensitized Solar Cells and Perovskite Solar Cells. *Adv. Mater.* **2014**, *26* (38), 6629–6634. https://doi.org/10.1002/adma.201402415.

(246) Zhao, X.; Zhang, F.; Yi, C.; Bi, D.; Bi, X.; Wei, P.; Luo, J.; Liu, X.; Wang, S.; Li, X.; Zakeeruddin, S. M.; Grätzel, M. A Novel One-Step Synthesized and Dopant-Free Hole Transport Material for Efficient and Stable Perovskite Solar Cells. *J. Mater. Chem. A* **2016**, *4* (42), 16330–16334. https://doi.org/10.1039/C6TA05254A.

(247) Agarwala, P.; Kabra, D. A Review on Triphenylamine (TPA) Based Organic Hole Transport Materials (HTMs) for Dye Sensitized Solar Cells (DSSCs) and Perovskite Solar Cells (PSCs): Evolution and Molecular Engineering. *J. Mater. Chem. A* **2017**, *5* (4), 1348–1373. https://doi.org/10.1039/C6TA08449D.

(248) Zhang, Z.; Hu, W.; Cui, J.; He, R.; Shen, W.; Li, M. Theoretical Insights into the Effect of a

Conjugated Core on the Hole Transport Properties of Hole-Transporting Materials for Perovskite Solar Cells. *Phys. Chem. Chem. Phys.* **2017**, *19* (36), 24574–24582. https://doi.org/10.1039/C7CP04754A.

(249) Wang, Y.-K.; Yuan, Z.-C.; Shi, G.-Z.; Li, Y.-X.; Li, Q.; Hui, F.; Sun, B.-Q.; Jiang, Z.-Q.; Liao, L.-S. Dopant-Free Spiro-Triphenylamine/Fluorene as Hole-Transporting Material for Perovskite Solar Cells with Enhanced Efficiency and Stability. *Adv. Funct. Mater.* **2016**, *26* (9), 1375–1381. https://doi.org/10.1002/adfm.201504245.

(250) Wu, F.; Wang, B.; Wang, R.; Shan, Y.; Liu, D.; Wong, Y. K.; Chen, T.; Zhu, L. Investigation on a Dopant-Free Hole Transport Material for Perovskite Solar Cells. *RSC Adv.* **2016**, *6*, 69365–69369. https://doi.org/10.1039/C6RA07603C.

(251) Tomkute-Luksiene, D.; Daskeviciene, M.; Malinauskas, T.; Jankauskas, V.; Degutyte, R.; Send, R.; Pschirer, N. G.; Wonneberger, H.; Bruder, I.; Getautis, V. Molecular Engineering of the Hole-Transporting Material Spiro-OMeTAD via Manipulation of Alkyl Groups. *RSC Adv.* **2016**, *6* (65), 60587–60594. https://doi.org/10.1039/C6RA09878A.

(252) Zheng, L.; Chung, Y.-H.; Ma, Y.; Zhang, L.; Xiao, L.; Chen, Z.; Wang, S.; Qu, B.; Gong, Q. A Hydrophobic Hole Transporting Oligothiophene for Planar Perovskite Solar Cells with Improved Stability. *Chem. Commun.* **2014**, *50* (50), 11196–11199. https://doi.org/10.1039/c4cc04680c.

(253) Bryant, D.; Aristidou, N.; Pont, S.; Sanchez-Molina, I.; Chotchunangatchaval, T.; Wheeler, S.; Durrant, J. R.; Haque, S. A. Light and Oxygen Induced Degradation Limits the Operational Stability of Methylammonium Lead Triiodide Perovskite Solar Cells. *Energy Environ. Sci.* **2016**, *9* (5), 1655–1660. https://doi.org/10.1039/C6EE00409A.

(254) Aristidou, N.; Sanchez-Molina, I.; Chotchuangchutchaval, T.; Brown, M.; Martinez, L.; Rath, T.; Haque, S. A. The Role of Oxygen in the Degradation of Methylammonium Lead Trihalide Perovskite Photoactive Layers. *Angew. Chemie - Int. Ed.* **2015**, *54* (28), 8208–8212. https://doi.org/10.1002/anie.201503153.

(255) You, J.; Meng, L.; Song, T.-B.; Guo, T.-F.; Yang, Y. (Michael); Chang, W.-H.; Hong, Z.; Chen, H.; Zhou, H.; Chen, Q.; Liu, Y.; De Marco, N.; Yang, Y. Improved Air Stability of Perovskite Solar Cells via Solution-Processed Metal Oxide Transport Layers. *Nat. Nanotechnol.* **2015**, *11* (1), 75–81. https://doi.org/10.1038/nnano.2015.230.

(256) Ishizaki, T.; Saito, N.; SunHyung, L.; Ishida, K.; Takai, O. Study of Alkyl Organic Monolayers with Different Molecular Chain Lengths Directly Attached to Silicon. *Langmuir* **2006**, *22* (24), 9962–9966. https://doi.org/10.1021/la052342u.

(257) Okouchi, M.; Yamaji, Y.; Yamauchi, K. Contact Angle of Poly(Alkyl Methacrylate)s and Effects of the Alkyl Group. *Macromolecules* **2006**, *39* (3), 1156–1159. https://doi.org/10.1021/ma052168g.

(258) Pinnau, I.; Morisato, A.; He, Z. Influence of Side-Chain Length on the Gas Permeation Properties of Poly(2-Alkylacetylenes) †. *Macromolecules* **2004**, *37* (8), 2823–2828.

134

https://doi.org/10.1021/ma0498363.

(259) Pu, G.; Longo, M. L.; Borden, M. a. Effect of Microstructure on Molecular Oxygen Permeation through Condensed Phospholipid Monolayers. *J. Am. Chem. Soc.* **2005**, *127* (18), 6524–6525. https://doi.org/10.1021/ja051103q.

(260) Charati, S. G.; Stern, S. a. Diffusion of Gases in Silicone Polymers: Molecular Dynamics Simulations. *Macromolecules* **1998**, *31* (16), 5529–5535. https://doi.org/10.1021/ma980387e.

(261) Kowert, B. A.; Dang, N. C. Diffusion of Dioxygen in n -Alkanes. *J. Phys. Chem. A* **1999**, *103* (7), 779–781. https://doi.org/10.1021/jp984025k.

(262) Lin, K.-H.; Prlj, A.; Corminboeuf, C. A Rising Star: Truxene as a Promising Hole Transport Material in Perovskite Solar Cells. *J. Phys. Chem. C* **2017**, *121* (39), 21729–21739. https://doi.org/10.1021/acs.jpcc.7b07355.

(263) Tummala, N. R.; Zheng, Z.; Aziz, S. G.; Coropceanu, V.; Brédas, J.-L. Static and Dynamic Energetic Disorders in the C 60 , PC 61 BM, C 70 , and PC 71 BM Fullerenes. *J. Phys. Chem. Lett.* **2015**, *6* (18), 3657–3662. https://doi.org/10.1021/acs.jpclett.5b01709.

(264) Saliba, M.; Correa-Baena, J.-P.; Grätzel, M.; Hagfeldt, A.; Abate, A. Perovskite Solar Cells: From the Atomic Level to Film Quality and Device Performance. *Angew. Chemie Int. Ed.* **2018**, *57* (10), 2554–2569. https://doi.org/10.1002/anie.201703226.

(265) Miyasaka, T.; Kojima, A.; Teshima, K.; Shirai, Y. Organometal Halide Perovskites as Visible-Light Sensitizers for Photovoltaic Cells. *J. Am. Chem. Soc.* **2009**, *131* (17), 6050–6051. https://doi.org/10.1021/ja809598r.

(266) Liu, X.; Zhu, L.; Zhang, F.; You, J.; Xiao, Y.; Li, D.; Wang, S.; Meng, Q.; Li, X. Stable Perovskite Solar Cells Based on Hydrophobic Triphenylamine Hole-Transport Materials. *Energy Technol.* **2017**, *5* (2), 312–320. https://doi.org/10.1002/ente.201600303.

(267) Zheng, L.; Chung, Y. H.; Ma, Y.; Zhang, L.; Xiao, L.; Chen, Z.; Wang, S.; Qu, B.; Gong, Q. A Hydrophobic Hole Transporting Oligothiophene for Planar Perovskite Solar Cells with Improved Stability. *Chem. Commun.* **2014**, *50* (76), 11196–11199. https://doi.org/10.1039/c4cc04680c.

(268) Rodríguez-Seco, C.; Cabau, L.; Vidal-Ferran, A.; Palomares, E. Advances in the Synthesis of Small Molecules as Hole Transport Materials for Lead Halide Perovskite Solar Cells. *Acc. Chem. Res.* **2018**, *51* (4), 869–880. https://doi.org/10.1021/acs.accounts.7b00597.

(269) Zhang, F.; Wang, S.; Zhu, H.; Liu, X.; Liu, H.; Li, X.; Xiao, Y.; Zakeeruddin, S. M.; Grätzel, M. Impact of Peripheral Groups on Phenothiazine-Based Hole-Transporting Materials for Perovskite Solar Cells. *ACS Energy Lett.* **2018**, *3* (5), 1145–1152. https://doi.org/10.1021/acsenergylett.8b00395.

(270) Xiang, F.-X.; Wang, X.-L.; Dou, S.-X. Molecular Engineering of Copper Phthalocyanines: A Strategy in Developing Dopant- Free Hole-Transporting Materials for Efficient and Ambient-Stable Perovskite Solar Cells. *Adv. Energy Mater.* **2018**, *1803287*, 11. https://doi.org/10.1002/)).

(271) Magomedov, A.; Paek, S.; Gratia, P.; Kasparavicius, E.; Daskeviciene, M.; Kamarauskas, E.; Gruodis, A.; Jankauskas, V.; Kantminiene, K.; Cho, K. T.; Rakstys, K.; Malinauskas, T.; Getautis, V.; Nazeeruddin, M. K. Diphenylamine-Substituted Carbazole-Based Hole Transporting Materials for Perovskite Solar Cells: Influence of Isomeric Derivatives. *Adv. Funct. Mater.* **2018**, *28* (9), 1–13. https://doi.org/10.1002/adfm.201704351.

(272) Petrus, M. L.; Schutt, K.; Sirtl, M. T.; Hutter, E. M.; Closs, A. C.; Ball, J. M.; Bijleveld, J. C.; Petrozza, A.; Bein, T.; Dingemans, T. J.; Savenije, T. J.; Snaith, H.; Docampo, P. New Generation Hole Transporting Materials for Perovskite Solar Cells: Amide-Based Small-Molecules with Nonconjugated Backbones. *Adv. Energy Mater.* **2018**, *8* (32), 1–11. https://doi.org/10.1002/aenm.201801605.

(273) Pham, H. D.; Do, T. T.; Kim, J.; Charbonneau, C.; Manzhos, S.; Feron, K.; Tsoi, W. C.; Durrant, J. R.; Jain, S. M.; Sonar, P. Molecular Engineering Using an Anthanthrone Dye for Low-Cost Hole Transport Materials: A Strategy for Dopant-Free, High-Efficiency, and Stable Perovskite Solar Cells. *Adv. Energy Mater.* **2018**, *8* (16), 1–13. https://doi.org/10.1002/aenm.201703007.

(274) Zhang, J.; Xu, B.; Yang, L.; Ruan, C.; Wang, L.; Liu, P.; Zhang, W.; Vlachopoulos, N.; Kloo, L.; Boschloo, G.; Sun, L.; Hagfeldt, A.; Johansson, E. M. J. The Importance of Pendant Groups on Triphenylamine-Based Hole Transport Materials for Obtaining Perovskite Solar Cells with over 20% Efficiency. *Adv. Energy Mater.* **2018**, *8* (2), 1–12. https://doi.org/10.1002/aenm.201701209.

(275) Lin, K. H.; Prlj, A.; Corminboeuf, C. A Rising Star: Truxene as a Promising Hole Transport Material in Perovskite Solar Cells. *J. Phys. Chem. C* **2017**, *121* (39), 21729–21739. https://doi.org/10.1021/acs.jpcc.7b07355.

(276) Urieta-Mora, J.; García-Benito, I.; Molina-Ontoria, A.; Martín, N. Hole Transporting Materials for Perovskite Solar Cells: A Chemical Approach. *Chem. Soc. Rev.* **2018**, *47* (23). https://doi.org/10.1039/C8CS00262B.

(277) Lin, K.-H.; Prlj, A.; Corminboeuf, C. How Does Alkyl Chain Length Modify the Properties of Triphenylamine-Based Hole Transport Materials? *J. Mater. Chem. C* **2018**, *6* (5), 960–965. https://doi.org/10.1039/C7TC05318E.

(278) Chi, W.-J.; Zheng, D.-Y.; Chen, X.-F.; Li, Z.-S. Optimizing Thienothiophene Chain Lengths of D–π–D Hole Transport Materials in Perovskite Solar Cells for Improving Energy Levels and Hole Mobility. *J. Mater. Chem. C* **2017**, *5*, 10055–10060. https://doi.org/10.1039/C7TC03232C.

(279) Sandoval-Torrientes, R.; Zimmermann, I.; Calbo, J.; Aragó, J.; Santos, J.; Ortí, E.; Martín, N.; Nazeeruddin, M. K. Hole Transporting Materials Based on Benzodithiophene and Dithienopyrrole Cores for Efficient Perovskite Solar Cells. *J. Mater. Chem. A* **2018**, *6* (14), 5944–5951. https://doi.org/10.1039/c7ta11314e.

(280) Wang, J.; Wang, S.; Li, X.; Zhu, L.; Meng, Q.; Xiao, Y.; Li, D. Novel Hole Transporting

Materials with a Linear π-Conjugated Structure for Highly Efficient Perovskite Solar Cells. *Chem. Commun.* **2014**, *50* (44), 5829–5832. https://doi.org/10.1039/c4cc01637h.

(281) Wu, Y.; Wang, Z.; Liang, M.; Cheng, H.; Li, M.; Liu, L.; Wang, B.; Wu, J.; Prasad Ghimire, R.; Wang, X.; Sun, Z.; Xue, S.; Qiao, Q. Influence of Nonfused Cores on the Photovoltaic Performance of Linear Triphenylamine-Based Hole-Transporting Materials for Perovskite Solar Cells. *ACS Appl. Mater. Interfaces* **2018**, *10* (21), 17883–17895. https://doi.org/10.1021/acsami.8b02090.

(282) Li, M.; Wang, Z.; Liang, M.; Liu, L.; Wang, X.; Sun, Z.; Xue, S. Low-Cost Carbazole-Based Hole-Transporting Materials for Perovskite Solar Cells: Influence of S,N-Heterocycle. *J. Phys. Chem. C* **2018**, *122* (42), 24014–24024. https://doi.org/10.1021/acs.jpcc.8b09482.

(283) Liu, X.; Kong, F.; Chen, W.; Yu, T.; Huang, Y.; Hayat, T.; Alsaedi, A.; Wang, H.; Chen, J.; Dai, S. Improving the Performance of Arylamine-Based Hole Transporting Materials in Perovskite Solar Cells: Extending π-Conjugation Length or Increasing the Number of Side Groups? *J. Energy Chem.* **2018**, *27* (5), 1409–1414. https://doi.org/10.1016/j.jechem.2017.09.019.

(284) Jeon, N. J.; Lee, H. G.; Kim, Y. C.; Seo, J.; Noh, J. H.; Lee, J.; Seok, S. Il. O-Methoxy Substituents in Spiro-OMeTAD for Efficient Inorganic-Organic Hybrid Perovskite Solar Cells. *J. Am. Chem. Soc.* **2014**, *136* (22), 7837–7840. https://doi.org/10.1021/ja502824c.

(285) Zimmermann, I.; Urieta-Mora, J.; Gratia, P.; Aragï¿½, J.; Grancini, G.; Molina-Ontoria, A.; Ortï¿½, E.; Martï¿½n, N.; Nazeeruddin, M. K. High-Efficiency Perovskite Solar Cells Using Molecularly Engineered, Thiophene-Rich, Hole-Transporting Materials: Influence of Alkyl Chain Length on Power Conversion Efficiency. *Adv. Energy Mater.* **2017**, *7* (6), 1–8. https://doi.org/10.1002/aenm.201601674.

(286) Gryn'ova, G.; Lin, K.-H.; Corminboeuf, C. Read between the Molecules: Computational Insights into Organic Semiconductors. *J. Am. Chem. Soc.* **2018**, *140* (48), 16370–16386. https://doi.org/10.1021/jacs.8b07985.

(287) Kotadiya, N. B.; Mondal, A.; Xiong, S.; Blom, P. W. M.; Andrienko, D.; Wetzelaer, G. J. A. H. Rigorous Characterization and Predictive Modeling of Hole Transport in Amorphous Organic Semiconductors. *Adv. Electron. Mater.* **2018**, *1800366*, 1–7. https://doi.org/10.1002/aelm.201800366.

(288) Liu, X.; Kong, F.; Jin, S.; Chen, W.; Yu, T.; Hayat, T.; Alsaedi, A.; Wang, H.; Tan, Z.; Chen, J.; Dai, S. Molecular Engineering of Simple Benzene–Arylamine Hole-Transporting Materials for Perovskite Solar Cells. *ACS Appl. Mater. Interfaces* **2017**, *9* (33), 27657–27663. https://doi.org/10.1021/acsami.7b06193.

(289) Urieta-Mora, J.; Zimmermann, I.; Aragó, J.; Molina-Ontoria, A.; Ortí, E.; Martín, N.; Nazeeruddin, M. K. Dibenzoquinquethiophene- and Dibenzosexithiophene-Based Hole-Transporting Materials for Perovskite Solar Cells. *Chem. Mater.* **2018**, acs.chemmater.8b04003. https://doi.org/10.1021/acs.chemmater.8b04003.

(290) Kou, C.; Feng, S.; Li, H.; Li, W.; Li, D.; Meng, Q.; Bo, Z. Molecular "Flower" as the High-Mobility Hole-Transport Material for Perovskite Solar Cells. *ACS Appl. Mater. Interfaces* **2017**, *9* (50), 43855–43860. https://doi.org/10.1021/acsami.7b13380.

(291) Atahan-Evrenk, Ş.; Aspuru-Guzik, A. Prediction and Theoretical Characterization of P-Type Organic Semiconductor Crystals for Field-Effect Transistor Applications. In *Journal of Arthropod-Borne Diseases*; 2014; Vol. 12, pp 95–138. https://doi.org/10.1007/128_2013_526.

(292) Watanabe, M.; Chang, Y. J.; Liu, S. W.; Chao, T. H.; Goto, K.; Islam, M. M.; Yuan, C. H.; Tao, Y. T.; Shinmyozu, T.; Chow, T. J. The Synthesis, Crystal Structure and Charge-Transport Properties of Hexacene. *Nat. Chem.* **2012**, *4* (7), 574–578. https://doi.org/10.1038/nchem.1381.

(293) Coropceanu, V.; Cornil, J.; da Silva Filho, D. A.; Olivier, Y.; Silbey, R.; Brédas, J. L. Charge Transport in Organic Semiconductors. *Chem. Rev.* **2007**, *107* (4), 926–952. https://doi.org/10.1021/cr050140x.

(294) Bässler, H. Charge Organic Photoconductors a Monte Carlo Simulation Study. *Phys. Status Solidi B* **1993**, *175*, 15–56. https://doi.org/https://doi.org/10.1002/pssb.2221750102.

(295) Friederich, P.; Meded, V.; Poschlad, A.; Neumann, T.; Rodin, V.; Stehr, V.; Symalla, F.; Danilov, D.; Lüdemann, G.; Fink, R. F.; Kondov, I.; von Wrochem, F.; Wenzel, W. Molecular Origin of the Charge Carrier Mobility in Small Molecule Organic Semiconductors. *Adv. Funct. Mater.* **2016**, *26* (31), 5757–5763. https://doi.org/10.1002/adfm.201601807.

(296) Nikitenko, V. R.; Sukharev, V. M. Transport Level in Disordered Organics: Correlated Energetic Disorder in Dipole Glass Model. *J. Phys. Conf. Ser.* **2016**, *741* (1), 1–5. https://doi.org/10.1088/1742-6596/741/1/012080.

(297) Schrader, M.; Körner, C.; Elschner, C.; Andrienko, D. Charge Transport in Amorphous and Smectic Mesophases of Dicyanovinyl-Substituted Oligothiophenes. *J. Mater. Chem.* **2012**, *22* (41), 22258–22264. https://doi.org/10.1039/c2jm34837c.

(298) Vehoff, T.; Baumeier, B.; Troisi, A.; Andrienko, D. Charge Transport in Organic Crystals: Role of Disorder and Topological Connectivity. *J. Am. Chem. Soc.* **2010**, *132* (33), 11702–11708. https://doi.org/10.1021/ja104380c.

(299) Jackson, N. E.; Savoie, B. M.; Chen, L. X.; Ratner, M. A. A Simple Index for Characterizing Charge Transport in Molecular Materials. *J. Phys. Chem. Lett.* **2015**, *6* (6), 1018–1021. https://doi.org/10.1021/acs.jpclett.5b00135.

(300) Hu, Z.; Fu, W.; Yan, L.; Miao, J.; Yu, H.; He, Y.; Goto, O.; Meng, H.; Chen, H.; Huang, W. Effects of Heteroatom Substitution in Spiro-Bifluorene Hole Transport Materials. *Chem. Sci.* **2016**, *7* (8), 5007–5012. https://doi.org/10.1039/c6sc00973e.

(301) Wu, F.; Shan, Y.; Qiao, J.; Zhong, C.; Wang, R.; Song, Q.; Zhu, L. Replacement of Biphenyl by Bipyridine Enabling Powerful Hole Transport Materials for Efficient Perovskite Solar Cells. *ChemSusChem* **2017**, *10* (19), 3833–3838. https://doi.org/10.1002/cssc.201700973.

(302) Rakstys, K.; Paek, S.; Gao, P.; Gratia, P.; Marszalek, T.; Grancini, G.; Cho, K. T.; Genevicius, K.; Jankauskas, V.; Pisula, W.; Nazeeruddin, M. K. Molecular Engineering of Face-on

Oriented Dopant-Free Hole Transporting Material for Perovskite Solar Cells with 19% PCE. *J. Mater. Chem. A* **2017**, *5* (17), 7811–7815. https://doi.org/10.1039/c7ta01718a.

(303) Steck, C.; Franckevičius, M.; Zakeeruddin, S. M.; Mishra, A.; Bäuerle, P.; Grätzel, M. A-D-A-Type S,N-Heteropentacene-Based Hole Transport Materials for Dopant-Free Perovskite Solar Cells. *J. Mater. Chem. A* **2015**, *3* (34), 17738–17746. https://doi.org/10.1039/c5ta03865k.

(304) Ma, H.; Liu, N.; Huang, J.-D. A DFT Study on the Electronic Structures and Conducting Properties of Rubrene and Its Derivatives in Organic Field-Effect Transistors. *Sci. Rep.* **2017**, *7* (1), 331. https://doi.org/10.1038/s41598-017-00410-6.

(305) Frisch, M. J.; Trucks, G. W.; Schlegel, H. B.; Scuseria, G. E.; Robb, M. A.; Cheeseman, J. R.; Scalmani, G.; Barone, V.; Petersson, G. A.; Nakatsuji, H.; Li, X.; Caricato, M.; Marenich, A. V.; Bloino, J.; Janesko, B. G.; Gomperts, R.; Mennucci, B.; Hratchian, H. P.; J. V. Ortiz; Izmaylov, A. F.; Sonnenberg, J. L.; Williams-Young, D.; Ding, F.; Lipparini, F.; Egidi, F.; Goings, J.; Peng, B.; Petrone, A.; Henderson, T.; Ranasinghe, D.; Zakrzewski, V. G.; Gao, J.; Rega, N.; Zheng, G.; Liang, W.; Hada, M.; Ehara, M.; Toyota, K.; Fukuda, R.; Hasegawa, J.; Ishida, M.; Nakajima, T.; Honda, Y.; Kitao, O.; Nakai, H.; Vreven, T.; Throssell, K.; Montgomery, J. A.; Jr., J. E. P.; Ogliaro, F.; Bearpark, M. J.; Heyd, J. J.; Brothers, E. N.; Kudin, K. N.; Staroverov, V. N.; Keith, T. A.; Kobayashi, R.; Normand, J.; Raghavachari, K.; Rendell, A. P.; Burant, J. C.; Iyengar, S. S.; Tomasi, J.; Cossi, M.; Millam, J. M.; Klene, M.; Adamo, C.; Cammi, R.; Ochterski, J. W.; Martin, R. L.; Morokuma, K.; Farkas, O.; Foresman, J. B.; Fox, D. J. Gaussian 16, Revision B.01. **2016**, Gaussian, Inc., Wallingford CT.

(306) Victor, R.; Lukyanov, A.; May, F.; Schrader, M.; Veho, T.; Kirkpatrick, J.; Andrienko, D.; Rühle, V.; Lukyanov, A.; May, F.; Schrader, M.; Vehoff, T.; Kirkpatrick, J.; Baumeier, B.; Andrienko, D.; Victor, R.; Lukyanov, A.; May, F.; Schrader, M.; Veho, T.; Kirkpatrick, J.; Andrienko, D. Microscopic Simulations of Charge Transport in Disordered Organic Semiconductors. *J. Chem. Theory Comput.* **2011**, *7*, 3335–3345. https://doi.org/10.1021/ct200388s.

(307) D'Avino, G.; Muccioli, L.; Castet, F.; Poelking, C.; Andrienko, D.; Soos, Z. G.; Cornil, J.; Beljonne, D. Electrostatic Phenomena in Organic Semiconductors: Fundamentals and Implications for Photovoltaics. *J. Phys. Condens. Matter* **2016**, *28* (43). https://doi.org/10.1088/0953-8984/28/43/433002.

(308) Lin, J. B.; Darzi, E. R.; Jasti, R.; Yavuz, I.; Houk, K. N. Solid-State Order and Charge Mobility in [5]- to [12]Cycloparaphenylenes. *J. Am. Chem. Soc.* **2019**, *141* (2), 952–960. https://doi.org/10.1021/jacs.8b10699.

(309) Baumeier, B.; Kirkpatrick, J.; Andrienko, D. Density-Functional Based Determination of Intermolecular Charge Transfer Properties for Large-Scale Morphologies. *Phys. Chem. Chem. Phys.* **2010**, *12* (36), 11103–11113. https://doi.org/10.1039/c002337j.

(310) Yavuz, I.; Lin, J. B.; Houk, K. N. Impact of Morphology, Side-Chains, and Crystallinity on Charge-Transport Properties of π-Extended Double Helicenes. *Phys. Chem. Chem. Phys.* **2019**,

21 (2), 901–914. https://doi.org/10.1039/C8CP06982D.

(311) Savoie, B. M.; Kohlstedt, K. L.; Jackson, N. E.; Chen, L. X.; Olvera de la Cruz, M.; Schatz, G. C.; Marks, T. J.; Ratner, M. A. Mesoscale Molecular Network Formation in Amorphous Organic Materials. *Proc. Natl. Acad. Sci.* **2014**, *111* (28), 10055–10060. https://doi.org/10.1073/pnas.1409514111.

(312) Jain, A. K. Data Clustering: 50 Years beyond K-Means. *Pattern Recognit. Lett.* **2010**, *31* (8), 651–666. https://doi.org/10.1016/j.patrec.2009.09.011.

(313) Mishra, A.; Bäuerle, P. Small Molecule Organic Semiconductors on the Move: Promises for Future Solar Energy Technology. *Angew. Chemie - Int. Ed.* **2012**, *51* (9), 2020–2067. https://doi.org/10.1002/anie.201102326.

(314) Yamashita, Y. Organic Semiconductors for Organic Field-Effect Transistors. *Sci. Technol. Adv. Mater.* **2009**, *10* (2), 024313. https://doi.org/10.1088/1468-6996/10/2/024313.

(315) Sun, H.; Gerasimov, J.; Berggren, M.; Fabiano, S. N-Type Organic Electrochemical Transistors: Materials and Challenges. *J. Mater. Chem. C* **2018**, *6* (44), 11778–11784. https://doi.org/10.1039/c8tc03185a.

(316) Kippelen, B.; Brédas, J. L. Organic Photovoltaics. *Energy Environ. Sci.* **2009**, *2* (3), 251–261. https://doi.org/10.1039/b812502n.

(317) Yavuz, I.; Lin, J. B.; Houk, K. N. Impact of Morphology, Side-Chains, and Crystallinity on Charge-Transport Properties of π-Extended Double Helicenes. *Phys. Chem. Chem. Phys.* **2019**, *21* (2), 901–914. https://doi.org/10.1039/c8cp06982d.

(318) Tummala, N. R.; Elroby, S. A.; Aziz, S. G.; Risko, C.; Coropceanu, V.; Brédas, J. L. Packing and Disorder in Substituted Fullerenes. *J. Phys. Chem. C* **2016**, *120* (31), 17242–17250. https://doi.org/10.1021/acs.jpcc.6b05197.

(319) Guo, J.; Zhang, Y.; Cai, W.; Zhang, Z.; He, R.; Shen, W.; Li, M. Effect of Double Bond Conjugation on Hole Mobility of Thiophene-Based Hole Transport Materials in Perovskite Solar Cells. *Mater. Chem. Phys.* **2020**, *240* (July 2019), 122058. https://doi.org/10.1016/j.matchemphys.2019.122058.

(320) Shahnawaz, S.; Sudheendran Swayamprabha, S.; Nagar, M. R.; Yadav, R. A. K.; Gull, S.; Dubey, D. K.; Jou, J. H. Hole-Transporting Materials for Organic Light-Emitting Diodes: An Overview. *J. Mater. Chem. C* **2019**, *7* (24), 7144–7158. https://doi.org/10.1039/c9tc01712g.

(321) Schober, C.; Reuter, K.; Oberhofer, H. Virtual Screening for High Carrier Mobility in Organic Semiconductors. *J. Phys. Chem. Lett.* **2016**, *7* (19), 3973–3977. https://doi.org/10.1021/acs.jpclett.6b01657.

(322) Lin, K. H.; Prlj, A.; Yao, L.; Drigo, N.; Cho, H. H.; Nazeeruddin, M. K.; Sivula, K.; Corminboeuf, C. Multiarm and Substituent Effects on Charge Transport of Organic Hole Transport Materials. *Chem. Mater.* **2019**, *31* (17), 6605–6614. https://doi.org/10.1021/acs.chemmater.9b00438.

(323) Nelsen, S. F.; Blackstock, S. C.; Kim, Y. Estimation of Inner Shell Marcus Terms for Amino

Nitrogen Compounds by Molecular Orbital Calculations. *J. Am. Chem. Soc.* **1987**, *109* (3), 677–682. https://doi.org/10.1021/ja00237a007.

(324)   Geng, H.; Niu, Y.; Peng, Q.; Shuai, Z.; Coropceanu, V.; Brédas, J. L. Theoretical Study of Substitution Effects on Molecular Reorganization Energy in Organic Semiconductors. *J. Chem. Phys.* **2011**, *135* (10). https://doi.org/10.1063/1.3632105.

(325)   Shuai, Z.; Geng, H.; Xu, W.; Liao, Y.; André, J. M. From Charge Transport Parameters to Charge Mobility in Organic Semiconductors through Multiscale Simulation. *Chem. Soc. Rev.* **2014**, *43* (8), 2662–2679. https://doi.org/10.1039/c3cs60319a.

(326)   Sato, T.; Uejima, M.; Iwahara, N.; Haruta, N.; Shizu, K.; Tanaka, K. Vibronic Coupling Density and Related Concepts. *J. Phys. Conf. Ser.* **2013**, *428* (1). https://doi.org/10.1088/1742-6596/428/1/012010.

(327)   Uejima, M.; Sato, T.; Tanaka, K.; Kaji, H. Vibronic Coupling Density Analysis for the Chain-Length Dependence of Reorganization Energies in Oligofluorenes: A Comparative Study with Oligothiophenes. *Phys. Chem. Chem. Phys.* **2013**, *15* (33), 14006–14016. https://doi.org/10.1039/c3cp51592c.

(328)   Park, S. J.; Jeon, S.; Lee, I. K.; Zhang, J.; Jeong, H.; Park, J. Y.; Bang, J.; Ahn, T. K.; Shin, H. W.; Kim, B. G.; Park, H. J. Inverted Planar Perovskite Solar Cells with Dopant Free Hole Transporting Material: Lewis Base-Assisted Passivation and Reduced Charge Recombination. *J. Mater. Chem. A* **2017**, *5* (25), 13220–13227. https://doi.org/10.1039/c7ta02440a.

(329)   Xie, X.; Santana-Bonilla, A.; Fang, W.; Liu, C.; Troisi, A.; Ma, H. Exciton-Phonon Interaction Model for Singlet Fission in Prototypical Molecular Crystals. *J. Chem. Theory Comput.* **2019**, *15* (6), 3721–3729. https://doi.org/10.1021/acs.jctc.9b00122.

(330)   Bednarska, J.; Zaleśny, R.; Bartkowiak, W.; Ośmiałowski, B.; Medved, M.; Jacquemin, D. Quantifying the Performances of DFT for Predicting Vibrationally Resolved Optical Spectra: Asymmetric Fluoroborate Dyes as Working Examples. *J. Chem. Theory Comput.* **2017**, *13* (9), 4347–4356. https://doi.org/10.1021/acs.jctc.7b00469.

(331)   Cheng, Y.; Qi, Y.; Tang, Y.; Zheng, C.; Wan, Y.; Huang, W.; Chen, R. Controlling Intramolecular Conformation through Nonbonding Interaction for Soft-Conjugated Materials: Molecular Design and Optoelectronic Properties. *J. Phys. Chem. Lett.* **2016**, *7* (18), 3609–3615. https://doi.org/10.1021/acs.jpclett.6b01695.

(332)   Ma, X. J.; Zhu, X. D.; Wang, K. L.; Igbari, F.; Yuan, Y.; Zhang, Y.; Gao, C. H.; Jiang, Z. Q.; Wang, Z. K.; Liao, L. S. Planar Starburst Hole-Transporting Materials for Highly Efficient Perovskite Solar Cells. *Nano Energy* **2019**, *63* (June), 103865. https://doi.org/10.1016/j.nanoen.2019.103865.

(333)   Lee, M. M.; Teuscher, J.; Miyasaka, T.; Murakami, T. N.; Snaith, H. J. Efficient Hybrid Solar Cells Based on Meso-Superstructured Organometal Halide Perovskites. *Science (80-.).* **2012**, *338* (6107), 643–647. https://doi.org/10.1126/science.1228604.

(334)   Reineke, S.; Lindner, F.; Schwartz, G.; Seidler, N.; Walzer, K.; Lüssem, B.; Leo, K. White

Organic Light-Emitting Diodes with Fluorescent Tube Efficiency. *Nature* **2009**, *459* (7244), 234–238. https://doi.org/10.1038/nature08003.

(335) Liu, J.; Chen, S.; Qian, D.; Gautam, B.; Yang, G.; Zhao, J.; Bergqvist, J.; Zhang, F.; Ma, W.; Ade, H.; Inganäs, O.; Gundogdu, K.; Gao, F.; Yan, H. Fast Charge Separation in a Non-Fullerene Organic Solar Cell with a Small Driving Force. *Nat. Energy* **2016**, *1* (7), 1–7. https://doi.org/10.1038/nenergy.2016.89.

(336) Drigo, N.; Roldan-Carmona, C.; Franckevičius, M.; Lin, K. H.; Gegevičius, R.; Kim, H.; Schouwink, P. A.; Sutanto, A. A.; Olthof, S.; Sohail, M.; Meerholz, K.; Gulbinas, V.; Corminboeuf, C.; Paek, S.; Nazeeruddin, M. K. Doped but Stable: Spirobisacridine Hole Transporting Materials for Hysteresis-Free and Stable Perovskite Solar Cells. *J. Am. Chem. Soc.* **2020**, *142* (4), 1792–1800. https://doi.org/10.1021/jacs.9b07166.

(337) Weissenseel, S.; Drigo, N. A.; Kudriashova, L. G.; Schmid, M.; Morgenstern, T.; Lin, K. H.; Prlj, A.; Corminboeuf, C.; Sperlich, A.; Brütting, W.; Nazeeruddin, M. K.; Dyakonov, V. Getting the Right Twist: Influence of Donor-Acceptor Dihedral Angle on Exciton Kinetics and Singlet-Triplet Gap in Deep Blue Thermally Activated Delayed Fluorescence Emitter. *J. Phys. Chem. C* **2019**. https://doi.org/10.1021/acs.jpcc.9b08269.

(338) Li, H.; Li, C.; Duan, L.; Qiu, Y. Charge Transport in Amorphous Organic Semiconductors: Effects of Disorder, Carrier Density, Traps, and Scatters. *Isr. J. Chem.* **2014**, *54* (7), 918–926. https://doi.org/10.1002/ijch.201400057.

(339) Kim, G. W.; Choi, H.; Kim, M.; Lee, J.; Son, S. Y.; Park, T. Hole Transport Materials in Conventional Structural (n–i–p) Perovskite Solar Cells: From Past to the Future. *Adv. Energy Mater.* **2020**, *1903403*, 1–30. https://doi.org/10.1002/aenm.201903403.

(340) Kulkarni, A. P.; Tonzola, C. J.; Babel, A.; Jenekhe, S. A. Electron Transport Materials for Organic Light-Emitting Diodes. *Chem. Mater.* **2004**, *16* (23), 4556–4573. https://doi.org/10.1021/cm049473l.

(341) Fuentes Pineda, R.; Troughton, J.; Planells, M.; Sanchez-Molina Santos, I.; Muhith, F.; Nichol, G. S.; Haque, S.; Watson, T.; Robertson, N. Effect of Alkyl Chain Length on the Properties of Triphenylamine-Based Hole Transport Materials and Their Performance in Perovskite Solar Cells. *Phys. Chem. Chem. Phys.* **2018**, *20* (2), 1252–1260. https://doi.org/10.1039/c7cp07682g.

(342) Baranovskii, S. D. Theoretical Description of Charge Transport in Disordered Organic Semiconductors. *Phys. status solidi* **2014**, *251* (3), 487–525. https://doi.org/10.1002/pssb.201350339.

(343) Thompson, I. R.; Coe, M. K.; Walker, A. B.; Ricci, M.; Roscioni, O. M.; Zannoni, C. Microscopic Origins of Charge Transport in Triphenylene Systems. *Phys. Rev. Mater.* **2018**, *2* (6), 25–29. https://doi.org/10.1103/PhysRevMaterials.2.064601.

(344) Schrader, M.; Körner, C.; Elschner, C.; Andrienko, D. Charge Transport in Amorphous and Smectic Mesophases of Dicyanovinyl-Substituted Oligothiophenes. *J. Mater. Chem.* **2012**, *22* (41), 22258–22264. https://doi.org/10.1039/c2jm34837c.

(345) Lin, K. H.; Prlj, A.; Corminboeuf, C. A Rising Star: Truxene as a Promising Hole Transport Material in Perovskite Solar Cells. *J. Phys. Chem. C* **2017**, *121* (39), 21729–21739. https://doi.org/10.1021/acs.jpcc.7b07355.

(346) Lin, K. H.; Prlj, A.; Corminboeuf, C. How Does Alkyl Chain Length Modify the Properties of Triphenylamine-Based Hole Transport Materials? *J. Mater. Chem. C* **2018**, *6* (5), 960–965. https://doi.org/10.1039/c7tc05318e.

(347) Lin, K.-H.; Corminboeuf, C. FB-REDA: Fragment-Based Decomposition Analysis of the Reorganization Energy for Organic Semiconductors. *Phys. Chem. Chem. Phys.* **2020**, 11881–11890. https://doi.org/10.1039/d0cp01722a.

(348) Liu, X.; Kong, F.; Jin, S.; Chen, W.; Yu, T.; Hayat, T.; Alsaedi, A.; Wang, H.; Tan, Z.; Chen, J.; Dai, S. Molecular Engineering of Simple Benzene-Arylamine Hole-Transporting Materials for Perovskite Solar Cells. *ACS Appl. Mater. Interfaces* **2017**, *9* (33), 27657–27663. https://doi.org/10.1021/acsami.7b06193.

(349) Wang, J.; Wolf, R. M.; Caldwell, J. W.; Kollman, P. A.; Case, D. A. Development and Testing of a General Amber Force Field. *J. Comput. Chem.* **2004**, *25* (9), 1157–1174. https://doi.org/10.1002/jcc.20035.

(350) Jakalian, A.; Bush, B. L.; Jack, D. B.; Bayly, C. I. Fast, Efficient Generation of High-Quality Atomic Charges. AM1-BCC Model: I. Method. *J. Comput. Chem.* **2000**, *21* (2), 132–146. https://doi.org/10.1002/(SICI)1096-987X(20000130)21:2<132::AID-JCC5>3.0.CO;2-P.

(351) Jakalian, A.; Jack, D. B.; Bayly, C. I. Fast, Efficient Generation of High-Quality Atomic Charges. AM1-BCC Model: II. Parameterization and Validation. *J. Comput. Chem.* **2002**, *23* (16), 1623–1641. https://doi.org/10.1002/jcc.10128.

(352) Rolland, N.; Franco-Gonzalez, J. F.; Volpi, R.; Linares, M.; Zozoulenko, I. V. Understanding Morphology-Mobility Dependence in PEDOT:Tos. *Phys. Rev. Mater.* **2018**, *2* (4), 1–9. https://doi.org/10.1103/PhysRevMaterials.2.045605.

(353) Park, S.; Heo, J. H.; Yun, J. H.; Jung, T. S.; Kwak, K.; Ko, M. J.; Cheon, C. H.; Kim, J. Y.; Im, S. H.; Son, H. J. Effect of Multi-Armed Triphenylamine-Based Hole Transporting Materials for High Performance Perovskite Solar Cells. *Chem. Sci.* **2016**, *7* (8), 5517–5522. https://doi.org/10.1039/C6SC00876C.

(354) Schloemer, T. H.; Christians, J. A.; Luther, J. M.; Sellinger, A. Doping Strategies for Small Molecule Organic Hole-Transport Materials: Impacts on Perovskite Solar Cell Performance and Stability. *Chem. Sci.* **2019**, *10* (7), 1904–1935. https://doi.org/10.1039/C8SC05284K.

(355) Lüssem, B.; Keum, C.-M.; Kasemann, D.; Naab, B.; Bao, Z.; Leo, K. Doped Organic Transistors. *Chem. Rev.* **2016**, *116* (22), 13714–13751. https://doi.org/10.1021/acs.chemrev.6b00329.

(356) Hellström, M.; Ceriotti, M.; Behler, J. Nuclear Quantum Effects in Sodium Hydroxide Solutions from Neural Network Molecular Dynamics Simulations. *J. Phys. Chem. B* **2018**, *122* (44), 10158–10171. https://doi.org/10.1021/acs.jpcb.8b06433.

(357)   Brickel, S.; Das, A. K.; Unke, O. T.; Turan, H. T.; Meuwly, M.   Reactive Molecular Dynamics for the [Cl–CH 3 –Br] − Reaction in the Gas Phase and in Solution: A Comparative Study Using Empirical and Neural Network Force Fields . *Electron. Struct.* **2019**, *1* (2), 024002. https://doi.org/10.1088/2516-1075/ab1edb.

(358)   Sosso, G. C.; Miceli, G.; Caravati, S.; Behler, J.; Bernasconi, M. Neural Network Interatomic Potential for the Phase Change Material GeTe. *Phys. Rev. B - Condens. Matter Mater. Phys.* **2012**, *85* (17), 1–13. https://doi.org/10.1103/PhysRevB.85.174103.

(359)   Li, Z.; Cheng, Y.; Yao, Y.; Xiong, S.; Zhang, X. Molecular Deposition Condition Dependent Structural and Charge Transport Properties of CBP Films. *Comput. Mater. Sci.* **2020**, *182* (February), 109785. https://doi.org/10.1016/j.commatsci.2020.109785.

Curriculum Vitae

Kun-Han Lin

EPFL SB ISIC LCMD
CH-1015 Lausanne

+41 21 69 39753

kun-han.lin@epfl.ch

Education

2016 – Now **Ph.D. Candidate in Theoretical Chemistry**, EPFL, Lausanne, Switzerland.
Laboratory for Computational Molecular Design (LCMD).
Supervisor: Prof. Clémence Corminboeuf

2013 – 2015 **M.Sc. in Materials Science and Engineering**, National Taiwan University, Taiwan
Master Thesis: Computational Study of the Origins of the Enhanced Li Storage
Capacity and the
Kinetic Behaviors of Li Ions on Reduced Graphene Oxide.
Supervisor: Prof. Chin-Lung Kuo.

2008 – 2012 **B.Sc. in Materials Science and Engineering**, National Taiwan University, Taiwan
Bachelor Project: Investigation on the Effect of Aluminum Ion on Electrodeposition
Behavior of Cr From Cr(III)-Formic Acid Electrolyte.
Supervisor: Prof. Chao-Sung Lin.

Publications

1. **Direct observation of aggregation-induced emission mechanism.**
   J. Guan, A. Prlj, R. Wei, J. Peng, <u>K.-H. Lin</u>, J. Liu, H. Han, Z. Yu, C. Corminboeuf,
   D. Zhao, J. Zheng, *Angew. Chem. Int. Ed.*, DOI: 10.1002/anie.202004318

2. **FB-REDA: fragment-based decomposition analysis of the reorganization energy
   for organic semiconductors.**
   <u>K.-H. Lin</u>, C. Corminboeuf, *Phys. Chem. Chem. Phys.*, **22** (2020), 11881.

3. **Doped but stable: spirobisacridine hole transporting materials for hysteresis-**

free and stable perovskite solar cells.

N. Drigo, C. Roldan-Carmona, M. Franckevicius, <u>K.-H. Lin</u>, R. Gegevicius, H. Kim, P. A. Schouwink, A. A. Sutanto, S. Olthof, M. Sohail, K. Meerholz, V. Gulbinas, C. Corminboeuf, S. Paek, M. K. Nazeeruddin, *J. Am. Chem. Soc.*, **4** (2020), 1792.

4. **Getting the Right Twist: Influence of Donor-Acceptor Dihedral Angle on Exciton Kinetics and Singlet-Triplet Gap in Deep Blue Thermally Activated Delayed Fluorescence Emitter.**

S. Weißenseel, N. Drigo, L. Kudriashova, M. Schmid, T. Morgenstern, <u>K.-H. Lin</u>, A. Prlj, C. Corminboeuf, A. Sperlich, W. Brütting, M. K. Nazeeruddin, V. Dyakonov, *J. Phys. Chem. C*, **123** (2019) 27778.

5. **Multiarm and Substituent Effects on Charge Transport of Organic Hole Transport Materials.**

<u>K.-H. Lin</u>, A. Prlj, L. Yao, N. Drigo, H.-H. Cho, M. K. Nazeeruddin, K. Sivula, C. Corminboeuf, *Chem. Mater.*, **31** (2019) 6605.

6. **Mechanisms of fluorescence quenching in prototypical aggregation-induced emission systems: excited state dynamics with TD-DFTB.**

T. Tran, A. Prlj, <u>K.-H. Lin</u>, D. Hollas, C. Corminboeuf, *Phys. Chem. Chem. Phys.*, **21** (2019) 9026.

7. **Read between the Molecules: Computational Insights into Organic Semiconductors.**

G. Gryn'ova, <u>K.-H. Lin</u>, C. Corminboeuf, *J. Am. Chem. Soc.*, **140** (2018) 16370.

8. **Restriction Enzyme Analysis of Double-Stranded DNA on Pristine Single-Walled Carbon Nanotubes.**

S.-J. Wu, N. Schuergers, <u>K.-H. Lin</u>, A. J. Gillen, C. Corminboeuf, A. A. Boghossian, *ACS Appl. Mater. Interfaces*, **10** (2018) 37386.

9. **How does alkyl chain length modify the properties of triphenylamine-based hole transport materials?.**

<u>K.-H. Lin</u>, A. Prlj, C. Corminboeuf, *J. Mater. Chem. C*, **6** (2018) 960.

10. **A Rising Star: Truxene as a Promising Hole Transport Material in Perovskite Solar Cells.**

<u>K.-H. Lin</u>, A. Prlj, C. Corminboeuf, *J. Phys. Chem. C*, **121** (2017) 21729

11. **Lithiation mechanisms and lithium storage capacity of reduced graphene oxide nanoribbons: a first-principles study.**

<u>K.-H. Lin</u>, C.-L. Kuo, *J. Mater. Chem. A*, **5** (2017) 4912.

12. **Microstructure and properties of carbon–sulfur-containing chromium deposits electroplated in trivalent chromium baths with thiosalicylic acid.**

C.-W. Chien, C.-L. Liu, F.-J. Chen, <u>K.-H. Lin</u>, C.-S. Lin, *Electrochim. Acta*, **72** (2012) 74.

Scientific Presentations

2019   **Poster**: "Mobility Volcano: Interplay of Transport Quantities in Acenes and Thienoacenes Based HTMs", SCS 2019, Lausanne, Switzerland.

2018   **Poster**: "Understanding the Crucial Design of Amorphous Hole Transport Materials in Perovskite Solar Cell", MRS 2018, Boston, USA.

2018   **Poster**: "Understanding the Crucial Design of Amorphous Hole Transport Materials in Perovskite Solar Cell", SCS 2018, Lausanne, Switzerland.

2018   **Poster**: "Revealing the Structure-Property Relationship of Organic Hole Transport Materials in Perovskite Solar Cell", SCS 2018, Lausanne, Switzerland.

2018   **Poster**: "Understanding the Crucial Design of Amorphous Hole Transport Materials in Perovskite Solar Cell", COMDI 2018, Lausanne, Switzerland.

2018   **Poster**: "High-Throughput Screening of Novel 2D Support Materials for Catalysis", COMDI 2018, Lausanne, Switzerland.

2017   **Poster**: "A Rising Star: Truxene as a Promising Hole Transport Material in Perovskite Solar Cells", WATOC 2017, Munich, Germany.

2017   **Poster**: "High-Throughput Screening of Novel 2D Support Materials for Catalysis", STC 2017, Basel, Switzerland.

2015   **Poster**: "Lithiation Mechanism and Origin of Enhanced Lithium Storage Capacity for Functionalized Graphene Nanoribbons: A First-Principles Study", ACCMS-8, Taipei, Taiwan.

2015   **Poster**: "First-Principles Study of Lithiation Mechanism and Origin of Enhanced Lithium Capacity for Reduced Graphene Oxide", MRS-T Annual Meeting, Taipei, Taiwan.

2015   **Talk**: "First-Principles Study of Lithium Storage and Diffusion Mechanisms on Functionalized Graphene Nanoribbons", ICMAT 2015 and IUMRS-ICA 2015, Singapore.

2015   **Talk**: "Lithiation Mechanism and Origin of Enhanced Lithium Storage Capacity for Functionalized Graphene Nanoribbons: A First-Principles Study", ICMAT 2015 and IUMRS-ICA 2015, Singapore.

2014   **Talk**: "Adsorption of Li on Armchair Graphene Nanoribbons Terminated with Different Functional Groups", Annual Conference of the Taiwan Ceramic Society, Taipei, Taiwan

2013   **Poster**: "First-Principles Study of The Electronic Properties of Graphene Adsorbed on The Perfect and Oxygen Deficient HfO2 Surface", MRS-T Annual Meeting, Taoyuan, Taiwan.

Honors and Awards

2018   **SCS Travel Award**, Swiss Chemical Society.

2015   **Graduate Student Scholarship**, Micron Technology Foundation.

2011 – 2012   **College Student Research Scholarship**, National Science Council, Taiwan.

2012   **Honorary Member**, Phi Tau Phi Scholastic Honor Society.

2011   **CSC Educational Foundation Scholarship**, China Steel Cooperation, Taiwan.

Supervision of students

02.2020 – 06.2020   **Bachelor Project of Computational Chemistry**, EPFL, Lausanne

Students: Iwona Swiderska and Helene Wu

Title: Effect of Intramolecular Interactions on the Reorganization Energy of Molecules with Bulky Side Groups

02.2019 – 06.2019   **Bachelor Project of Computational Chemistry**, EPFL, Lausanne

Students: Lionel Rumpf and Matthias Linus

Title: Reducing charge reorganization energy by optimizing intramolecular noncovalent interaction

02.2018 – 06.2018   **Bachelor Project of Computational Chemistry**, EPFL, Lausanne

Students: Thomas Jordan and Colin Jeanguenat

Title: OASIS-20: Benchmarking the Structure, the Stability and the Transport Properties of Organic Molecular Crystals

09.2017 – 12.2017   **Interdisciplinary Project for Master Students**, EPFL, Lausanne

Students: Kevin Jablonka

Title: Theoretical and experimental investigation of Dopant-Free Hole-Transporting Materials for Stable and Efficient Perovskite Solar Cells.

Software and Coding Skills

Quantum Chemistry	Gaussian, ADF, TeraChem, Orca, Q-Chem, Turbomole
Quantum Solid-State	VASP, Quantum Espresso, CP2K
Classical MD	Gromacs, DL_POLY, LAMMPS
Charge Transport	VOTCA_CTP
Coding	bash, Python, Fortran